



**HAL**  
open science

# Connectivity of channelized sedimentary bodies: analysis and simulation strategies in subsurface modeling

Guillaume Rongier

► **To cite this version:**

Guillaume Rongier. Connectivity of channelized sedimentary bodies: analysis and simulation strategies in subsurface modeling. Applied geology. Université de Lorraine; Université de Neuchâtel, 2016. English. NNT : 2016LORR0026 . tel-01754642v2

**HAL Id: tel-01754642**

**<https://hal.science/tel-01754642v2>**

Submitted on 25 Sep 2016

**HAL** is a multi-disciplinary open access archive for the deposit and dissemination of scientific research documents, whether they are published or not. The documents may come from teaching and research institutions in France or abroad, or from public or private research centers.

L'archive ouverte pluridisciplinaire **HAL**, est destinée au dépôt et à la diffusion de documents scientifiques de niveau recherche, publiés ou non, émanant des établissements d'enseignement et de recherche français ou étrangers, des laboratoires publics ou privés.



Distributed under a Creative Commons Attribution 4.0 International License

# Connectivity of channelized sedimentary bodies: analysis and simulation strategies in subsurface modeling

*Connectivité de corps sédimentaires chenalisés :  
stratégies d'analyse et de simulation  
en modélisation de subsurface*

## THÈSE

présentée et soutenue publiquement le 15 mars 2016  
pour l'obtention du grade de

**Docteur de l'Université de Lorraine et  
de l'Université de Neuchâtel**

**Spécialité Géosciences**

par

**Guillaume RONGIER**

### Composition du jury:

<i>Rapporteurs:</i>	Prof. Klaus MOSEGAARD	University of Copenhagen
	Prof. Thierry MULDER	Université de Bordeaux
	Dr. Michael PYRCZ	Chevron
<i>Examineurs:</i>	Dr. Julien STRAUBHAAR	Université de Neuchâtel
	Dr. Vanessa TELES	IFP Energies nouvelles
<i>Directeur de thèse:</i>	Prof. Philippe RENARD	Université de Neuchâtel
<i>Directrice de thèse:</i>	Prof. Judith SAUSSE	Université de Lorraine
<i>Co-directrice de thèse:</i>	Dr. Pauline COLLON	Université de Lorraine
<i>Invités:</i>	Prof. Gregoire MARIETHOZ	Université de Lausanne
	Dr. Sebastien STREBELLE	Chevron



## IMPRIMATUR POUR THESE DE DOCTORAT

---

**La Faculté des sciences de l'Université de Neuchâtel  
autorise l'impression de la présente thèse soutenue par**

**Monsieur Guillaume RONGIER**

Réalisée en cotutelle avec

L'Université de Lorraine, France

Titre :

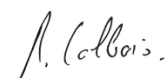
**« Connectivity of channelized sedimentary  
bodies: analysis and simulation strategies in  
subsurface modeling »**

**sur le rapport des membres du jury:**

- Prof. Philippe Renard, Université de Neuchâtel, directeur de thèse
- Prof. Judith Sausse, Université de Lorraine, directrice de thèse
- Dr Pauline Collon, Université de Lorraine, co-directrice de thèse
- Prof. Klaus Mosegaard, Université de Copenhague, Danemark
- Prof. Thierry Mulder, Université de Bordeaux, France
- Dr Michael Pycrz, Chevron, USA
- Dr Julien Straubhaar, Université de Neuchâtel
- Dr Vanessa Teles, IFPEN, France

Neuchâtel, le 1<sup>er</sup> avril 2016

Le Doyen, Prof. B. Colbois





« Son petit visage en forme de cœur paraissait dur  
sous le voile de deuil que formait ses cheveux noirs. »

**PHILIP K. DICK**

Le Bal des schizos, 1972



# Abstract

**Keywords** turbiditic channel connectivity connected component stochastic simulation Lindenmayer system channel migration

Channels are the main sedimentary structures for sediment transportation and deposition from the continents to the ocean floor. The significant permeability of their deposits enables fluid circulation and storage. As illustrated with turbiditic systems, those channel fill is highly heterogeneous. Combined with the spatial organization of the channels, this impacts significantly the connectivity between the permeable deposits. The scarcity of the field data involves an incomplete knowledge of these subsurface reservoir architectures. In such environments, stochastic simulations are used to estimate the resources and give an insight on the associated uncertainties. Several methods have been developed to reproduce these complex environments. They raise two main concerns: how to analyze and compare the connectivity of a set of stochastic simulations? How to improve the representation of the connectivity within stochastic simulations of channels and reduce the uncertainties?

The first concern leads to the development of a method to objectively compare realizations in terms of connectivity. The proposed approach relies on the connected components of the simulations, on which several indicators are computed. A multidimensional scaling (MDS) representation facilitates the realization comparison. The observations on the MDS are then validated by the analysis of the heatmap and the indicators. The application to a synthetic case study highlights the difference of connectivity between several methods and parameter values to model channel/levee complexes. In particular, some methods are far from representing channel-shaped bodies.

Two main issues derive from the second concern. The first issue is the difficulty to simulate a highly elongated object, here a channel, conditioned to well or seismic-derived data. We rely on a formal grammar, the Lindenmayer system, to stochastically simulate conditional channel objects. Predefined growth rules control the channel morphology to simulate straight to sinuous channels. That



## Abstract

morphology conditions the data during its development thanks to attractive and repulsive constraints. Such constraints ensure the conditioning while preserving at best the channel morphology. The second issue arises from the limited control on the channel organization. This aspect is addressed by taking into account the evolution processes underlying channel organization. An initial channel is simulated with a Lindenmayer system. Then that channel migrates using sequential Gaussian simulation or multiple-point simulation. This process reproduces the complex relationships between successive channels without relying on partially validated physical models with an often constraining parameterization.

The applications of those various works to synthetic cases highlight the potentiality of the approaches. They open up interesting prospects to better take into account the connectivity when stochastically simulating channels.

# Résumé

**Mots-clefs** chenal turbiditique connectivité composante connexe simulation stochastique système de Lindenmayer migration de chenaux

Les chenaux sont des structures sédimentaires clefs dans le transport et le dépôt de sédiments depuis les continents jusqu'aux planchers océaniques. Leurs dépôts perméables permettent la circulation et le stockage de fluides. Comme illustré avec les systèmes turbiditiques, le remplissage de ces chenaux est très hétérogène. Son impact sur la connectivité des dépôts perméables est amplifié par les variations d'organisation spatiale des chenaux. Mais du fait de l'aspect lacunaire des données, l'architecture de ces structures souterraines n'est que partiellement connue. Dans ce cas, les simulations stochastiques permettent d'estimer les ressources et les incertitudes associées. De nombreuses méthodes ont été développées pour reproduire ces environnements. Elles soulèvent deux questions capitales : comment analyser et comparer la connectivité de simulations stochastiques ? Comment améliorer la représentation de la connectivité dans les simulations stochastiques de chenaux et réduire les incertitudes ?

La première question nous a conduits à développer une méthode pour comparer objectivement des réalisations en se concentrant sur la connectivité. L'approche proposée s'appuie sur les composantes connexes des simulations, sur lesquelles sont calculés plusieurs indicateurs. Une représentation par positionnement multidimensionnel (MDS) facilite la comparaison des réalisations. Les observations faites grâce au MDS sont ensuite validées par une carte de chaleur et les indicateurs. L'application à un cas synthétique de complexes chenaux/levées montre les différences de connectivité entre des méthodes et des valeurs de paramètres différentes. En particulier, certaines méthodes sont loin de reproduire des objets avec une forme de chenaux.

La seconde question amène deux principaux problèmes. Premièrement, il apparaît difficile de conditionner des objets très allongés, comme des chenaux, à des données de puits ou dérivées de sismiques. Nous nous appuyons sur une grammaire formelle, le système de Lindenmayer, pour simuler stochasti-

## Résumé

quement des objets chenaux conditionnés. Des règles de croissance prédéfinies contrôlent la morphologie du chenal, de rectiligne à sinueuse. Cette morphologie conditionne les données au fur et à mesure de son développement grâce à des contraintes attractives ou répulsives. Ces contraintes assurent le conditionnement tout en préservant au mieux la morphologie. Deuxièmement, l'organisation spatiale des chenaux apparaît peu contrôlable. Nous proposons de traiter ce problème en intégrant les processus qui déterminent l'organisation des chenaux. Un premier chenal est simulé avec un système de Lindenmayer. Puis ce chenal migre à l'aide d'une simulation gaussienne séquentielle ou d'une simulation multipoints. Cette approche reproduit les relations complexes entre des chenaux successifs sans s'appuyer sur des modèles physiques partiellement validés et au paramétrage souvent contraignant.

L'application de ces travaux à des cas synthétiques démontre le potentiel de ces approches. Elles ouvrent des perspectives intéressantes pour mieux prendre en compte la connectivité dans les simulations stochastiques de chenaux.

# Aperçu à l'usage des francophones

Les fluides et leur circulation sont des éléments fondamentaux en géologie. D'une part ils sont liés à la formation et l'évolution de nombreuses structures géologiques. D'autre part ces fluides peuvent être eux-mêmes des ressources exploitables ou aboutir à la formation de ressources exploitables. De ce point de vue les systèmes chenalisés fluviatiles et turbiditiques sont des structures majeures. Parmi les dépôts liés à ces systèmes, certains ont une perméabilité élevée autorisant la circulation et le stockage de fluides, comme de l'eau, du pétrole et du gaz [p. ex. [Fitterman et al., 1991](#), [Mayall et al., 2006](#), [Braathen et al., 2012](#)]. Un élément architectural fondamental de ces systèmes est le chenal.

Dans le cas des systèmes turbiditiques, les chenaux assurent le transport des sédiments depuis la marge continentale jusqu'au bassin océanique. Mais ces chenaux sont eux-mêmes le siège de dépôts de sédiments, dont des dépôts perméables à fort potentiel réservoir. Ceci explique le fort intérêt qui leur est porté. Le remplissage de ces chenaux n'est pas homogène [p. ex. [Labourdette, 2007](#), [McHargue et al., 2011](#)]. Ils contiennent également des dépôts plus argileux qui peuvent bloquer la circulation de fluides entre deux chenaux, donc compartimenter le réservoir et compliquer son exploitation. Cet aspect est encore amplifié par sa combinaison à l'organisation spatiale des chenaux [p. ex. [Labourdette, 2007](#), [Mayall et al., 2006](#)]. En effet les chenaux résultent d'une longue évolution composée de migrations continues ou abruptes et d'avulsions [p. ex. [Abreu et al., 2003](#), [Kolla, 2007](#)]. L'architecture qui en résulte est donc particulièrement complexe, avec un impact significatif sur la connectivité des dépôts perméables et la compartimentation du réservoir (figure 1).

Ces structures étant enfouies au moment de leur exploitation potentielle, leur architecture ne peut être connue complètement par des observations directes. Différents types de données – données de puits ou données sismiques notam-

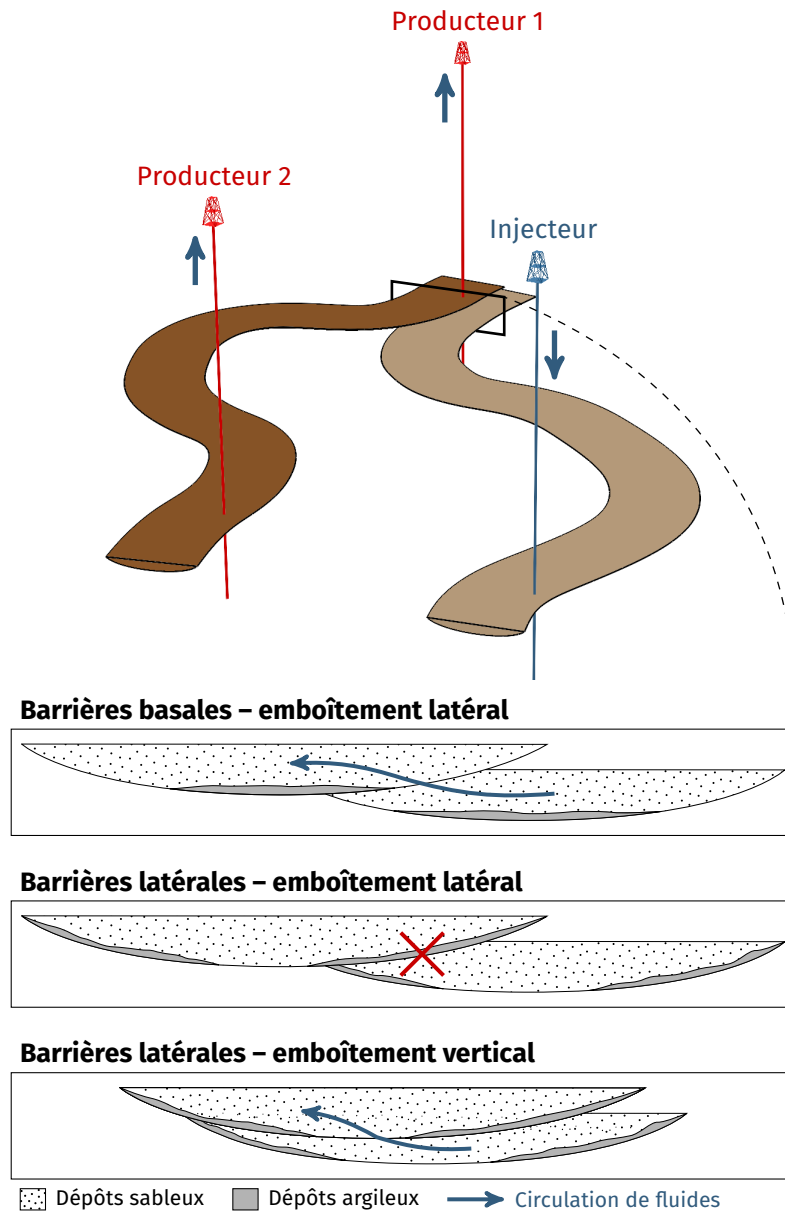


**FIGURE 1** Effet du remplissage et de l'organisation spatiale de chenaux, plus ou moins emboîtés les uns dans les autres, sur la circulation des fluides. Lors de l'implantation d'un puits producteur, le problème est d'estimer si celui-ci sera bien connecté au puits injecteur. Ici suivant le type de barrières argileuses et l'emboîtement des chenaux, le puits producteur 2 peut ne pas être connecté à l'injecteur. Le producteur 1 est certain d'être connecté à l'injecteur, mais son rendement concernant la récupération de pétrole risque d'être moins intéressant.

ment – donnent une image extrêmement lacunaire de cette architecture et de la connectivité associée. De ce point de vue, les simulations stochastiques permettent de reconstituer un ensemble d'architectures probables en prenant en compte les données disponibles. Elles donnent ainsi accès à l'incertitude autour des modèles simulés. Plusieurs méthodes se sont attaquées à la simulation de chenaux [p. ex. [Viseur, 2001](#), [Strebelle, 2002](#), [Pyrz et al., 2009](#)]. Ces méthodes se sont retrouvées confrontées à un choix cornélien :

- les méthodes qui conditionnent facilement aux données, basées sur le remplissage des cellules d'une grille, ont des difficultés à reproduire des corps sédimentaires avec une forme de chenaux ;
- les méthodes qui reproduisent facilement des chenaux, basées sur la définition d'une forme géométrique de chenal, ont des difficultés à conditionner aux données.

Ceci implique que souvent la reproduction des corps sédimentaires et la connectivité sous-jacente sont sacrifiées au profit du conditionnement. Deux interrogations ressortent de ces observations :

- comment analyser la connectivité de simulations stochastiques afin de comparer ces simulations ?
- comment améliorer la reproduction de la connectivité dans ces simulations ?

## **Analyse de la connectivité de simulations stochastiques**

Comme de nombreuses simulations se basent sur la reproduction de statistiques d'un modèle a priori, la comparaison des réalisations se fait souvent d'un point de vue statistique [p. ex. [Boisvert et al., 2010](#), [Tan et al., 2014](#)]. Or cette approche néglige la connectivité, qui est pourtant un aspect clef dans les utilisations des simulations stochastiques. D'autres méthodes se focalisent sur les composantes connexes des réalisations [p. ex. [Deutsch, 1998](#), [De Iaco, 2013](#)]. Une composante connexe est ici un ensemble de cellules, de telle façon que pour deux cellules il existe un chemin de cellules voisines de même faciès reliant l'une à l'autre. Sur chaque composante connexe constituant une réalisation, il est possible de mesurer divers indicateurs, comme leur volume, puis de comparer ces indicateurs entre les réalisations. Cela permet d'avoir une idée de la connectivité des corps sédimentaires.

Nous proposons ici un ensemble d'indicateurs basés sur ces composantes connexes pour aller plus loin dans l'analyse de la connectivité (figure 2). Ces

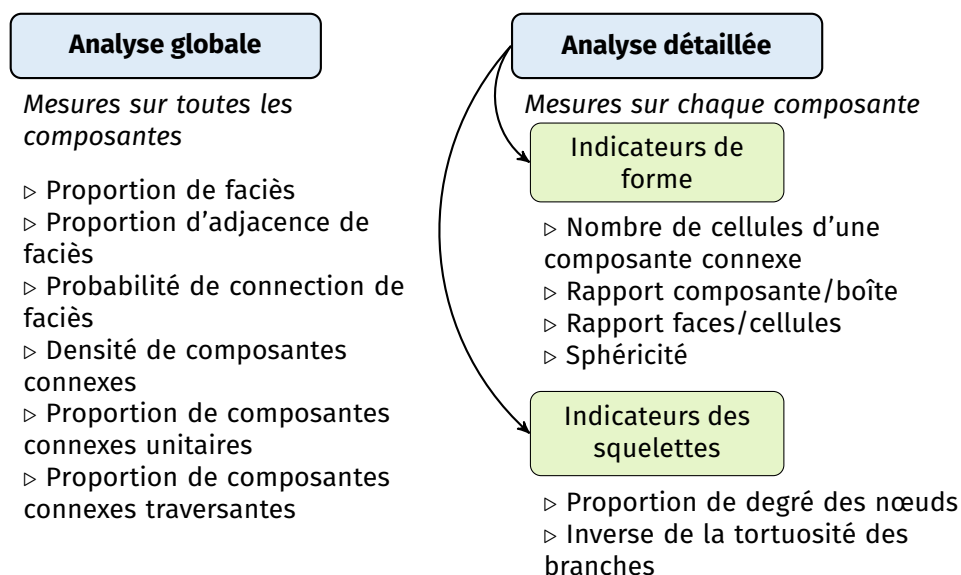


FIGURE 2 Indicateurs utilisés pour la comparaison de réalisations.

indicateurs sont ensuite utilisés pour comparer des réalisations. Cette comparaison est simplifiée par le calcul d'une dissemblance entre les réalisations à l'aide des indicateurs. Cette dissemblance se base sur une combinaison de distance euclidienne et de divergence de Jensen-Shannon. L'analyse des dissemblances s'avère longue et fastidieuse face à plusieurs centaines de réalisations, ce qui est commun en simulation stochastique. Le positionnement multidimensionnel (*MultiDimensional Scaling* ou MDS) [pour une revue de la méthode voir [Cox and Cox, 1994](#)] représente chaque réalisation par un point, avec les distances entre les points les plus proches possible des dissemblances entre les réalisations (figure 3). Le principal avantage de cette méthode est de pouvoir placer les points dans un espace de faible dimension, idéalement deux dimensions pour faciliter l'analyse. Comme la représentation des dissemblances est biaisée par le faible nombre de dimensions, il est indispensable de retourner aux valeurs de dissemblances, sous la forme d'une carte de chaleur, puis aux indicateurs pour valider et parfaire l'analyse.

L'application à un cas synthétique montre que le classement des réalisations diffère de ce qui est attendu suite à une analyse visuelle. L'étude plus précise des indicateurs révèle néanmoins la cohérence des indicateurs, qui s'avèrent rapide à mettre en œuvre et simples à analyser.

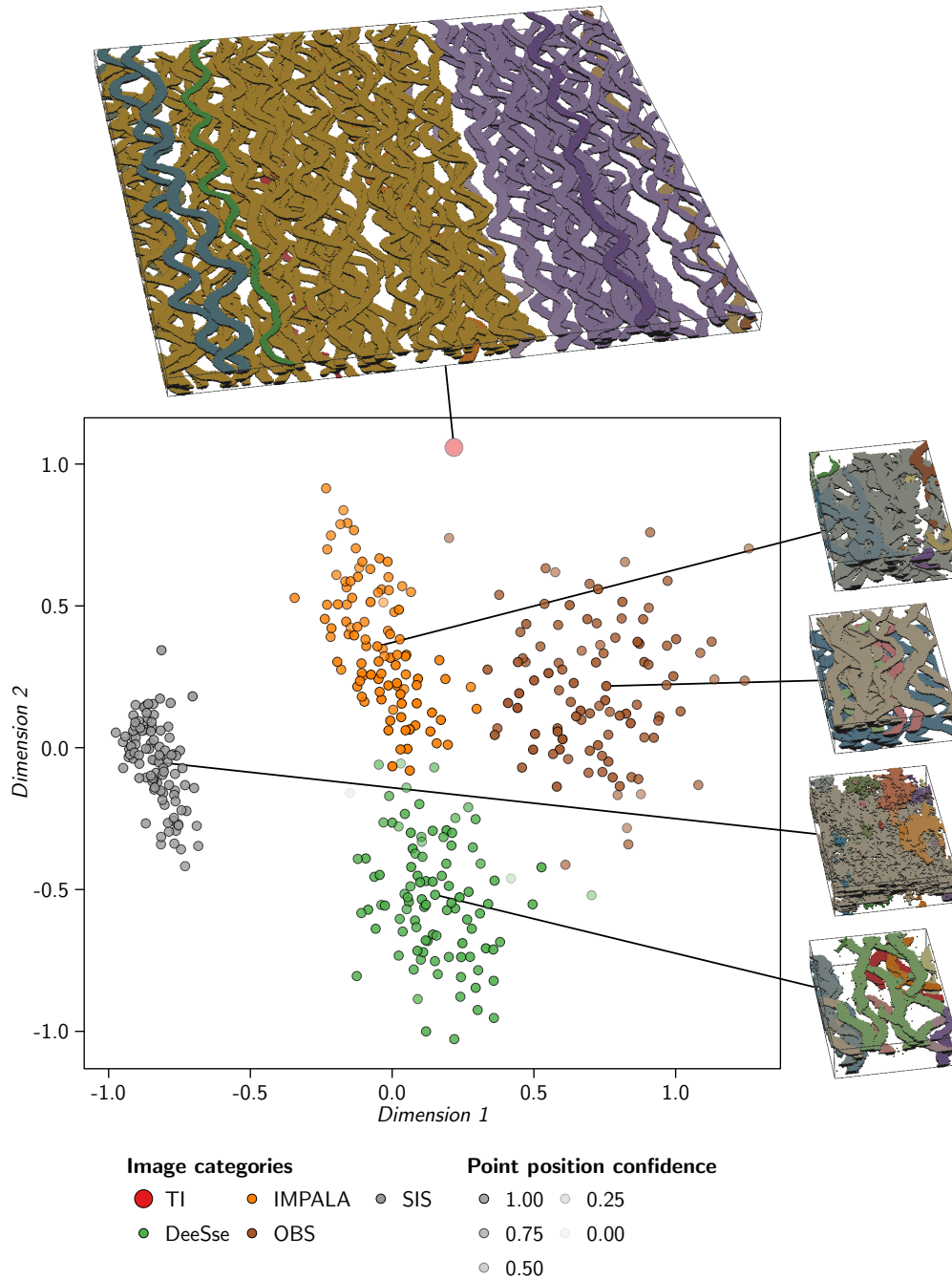


FIGURE 3 Exemple d'application du MDS à un ensemble de réalisations provenant de différentes méthodes (d'après Rongier et al. [2015]). Les réalisations de chacune des méthodes forment des groupes clairement distincts les uns des autres qui sont reliés à des différences de connectivité.



## **Préservation de la morphologie des chenaux dans les simulations stochastiques conditionnées**

Un des éléments ayant un impact significatif sur la connectivité et les simulations d'écoulements est la préservation de la continuité des chenaux. Mais concilier cet élément avec l'ensemble des données disponibles est une tâche délicate. La méthode proposée ici se base sur une grammaire formelle, le système de Lindenmayer ou L-système [Lindenmayer, 1968]. Les L-systèmes sont particulièrement employés en biologie afin de simuler des plantes et des arbres. La simulation d'arbres implique notamment la prise en compte d'informations environnementales pour intégrer par exemple l'effet de la gravité ou la compétition pour la lumière.

Cette approche a été adaptée pour simuler stochastiquement des chenaux conditionnés à des données de puits ou dérivées d'images sismiques. Des règles prédéfinies gèrent la simulation de la morphologie des chenaux, permettant de simuler aussi bien des chenaux rectilignes que sinueux. Au cours de son développement, cette morphologie est influencée par des contraintes attractives ou répulsives. Ces contraintes permettent de prendre en compte divers types de données (figure 4) : interprétation de corps sédimentaires au niveau des puits, connectivité entre les puits, cube de proportion de faciès ou confinement des chenaux.

L'application à plusieurs cas synthétiques intégrant plus ou moins de données illustre la capacité de la méthode à prendre en compte de nombreuses données. Les contraintes induisent une déformation de la morphologie du chenal, même si tout est fait pour garder cette déformation la plus faible possible. En contrepartie, elles permettent d'assurer le conditionnement aux données et la continuité du chenal est toujours préservée. Or cette continuité a plus d'impact sur les écoulements que la sinuosité des chenaux.

## **Prise en compte des relations spatiales entre chenaux dans les simulations stochastiques**

Si les L-systèmes permettent de prendre en compte de nombreuses données, reproduire précisément l'organisation des chenaux reste compliqué, voir impossible. Cette organisation découle des processus d'évolution des chenaux et contrôle l'emboîtement de ces chenaux, donc la connectivité. Dans un système turbiditique, un chenal est dévié au fur et à mesure de son développement de manière plus ou moins abrupte par migration et avulsion. Peu de méthodes s'attachent à reproduire précisément l'organisation des chenaux. Les plus connues

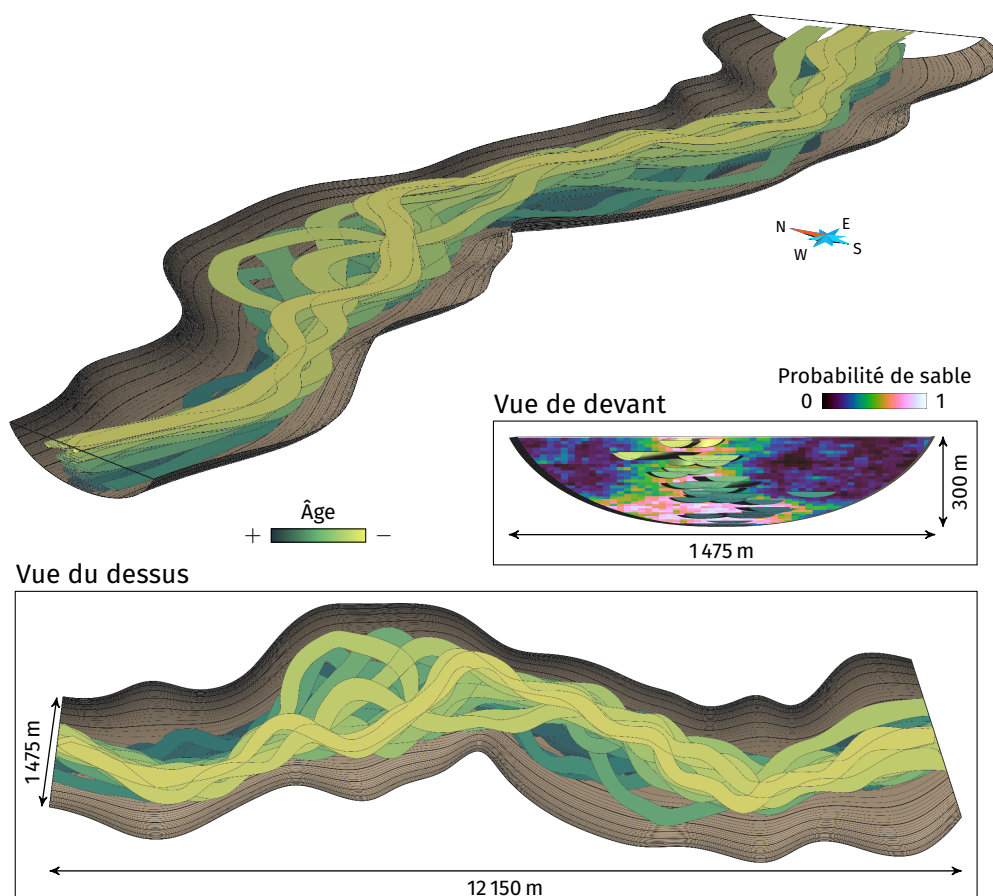
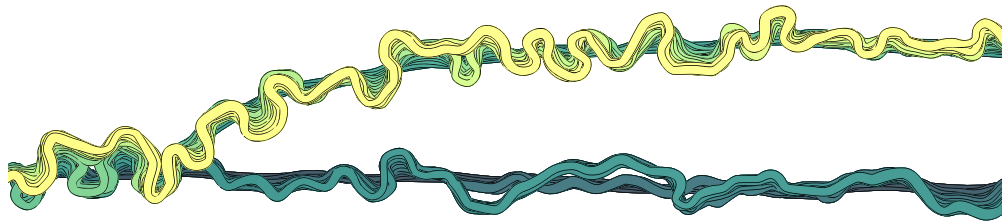


FIGURE 4 Exemple de réalisation de chenaux turbiditiques dans un chenal principal. Les chenaux sont conditionnés à un cube de proportion de sable et par le chenal principal, dont ils ne doivent pas dépasser les bords.

se basent sur des modèles physiques de migration [Lopez, 2003, Pyrcz et al., 2009]. Ces modèles ont comme inconvénients un paramétrage souvent contraignant et une validité loin d'être établie [Camporeale et al., 2007]. Peu de méthodes essaient d'être plus descriptives pour passer outre les limitations des modèles physiques [p. ex. Teles et al., 1998, Viseur, 2001, Labourdette, 2008].

La méthode proposée ici est similaire dans son principe aux méthodes basées sur des modèles physiques. Elle part d'un chenal initial, soit simulé avec un L-système, soit interprété à partir de données sismiques. Puis la migration de ce chenal est simulée soit par simulation gaussienne séquentielle (*Sequential Gaussian Simulation* ou SGS) soit par simulation multipoints (*Multiple-Point*

**Processus normal avec SGS**



**Processus inverse avec SGS**

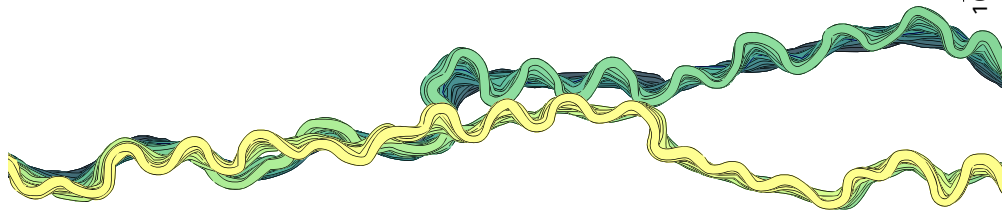


**FIGURE 5** Exemples de réalisations avec une migration basée sur des simulations gaussiennes séquentielles. Le processus normal implique de commencer la simulation de la migration par le plus jeune des chenaux, c-à-d celui en bas de séquence. Le processus inverse implique de commencer la simulation de la migration par le plus vieux des chenaux, c-à-d celui en haut de séquence. Cette dernière se justifie par le fait que ce chenal en haut de séquence est souvent observable sur les données sismiques.

*Simulation* ou MPS) si un modèle d'entraînement est disponible. L'avulsion est gérée aléatoirement : un emplacement est tiré aléatoirement le long du chenal et un nouveau chenal est simulé par L-système à partir de ce point.

L'ensemble permet de simuler les motifs de migrations observés de manière récurrente dans les systèmes turbiditiques anciens comme modernes. De plus, cette méthode permet de simuler la migration soit à partir du premier chenal d'une séquence, selon un processus normal, soit à partir du dernier, selon un processus inverse (figure 5). Dans le processus inverse les chenaux rétro-migrent depuis le dernier jusqu'au premier. Cette méthode est particulièrement pertinente car sur des données sismiques le dernier chenal d'un complexe peut souvent être interprété. Cela permet ainsi d'initier le processus à partir des données.

## **Conclusions**

L'ensemble de ces nouvelles approches permettent de mieux appréhender la connectivité dans les simulations stochastiques. L'analyse de la connectivité est un élément primordial afin d'étudier sa reproduction et les impacts potentiels en ce qui concerne l'estimation des incertitudes et la simulation des écoulements. Mieux représenter les corps sédimentaires liés aux dépôts perméables permet une meilleure estimation de la connectivité. De ce point de vue, être capable de représenter des chenaux conditionnés aux données, comme le font les L-systèmes, puis de reproduire précisément leur organisation, comme le fait la migration, est primordial. Le conditionnement aux données de la migration doit encore être exploré afin de parfaire le processus de simulation.



# Contents

<b>Preface</b>	<b>xxxv</b>
<b>Introduction</b>	<b>xxxvii</b>
1 Motivations . . . . .	.xxxvii
2 Objectives . . . . .	xliv
3 Outline . . . . .	xliv
4 Working context . . . . .	xlvi
<b>1 Channelized systems and connectivity: a review through the example of turbiditic systems</b>	<b>1</b>
1.1 Introduction . . . . .	2
1.2 An example of channelized environment: the turbiditic systems	3
1.2.1 About turbidity currents . . . . .	3
1.2.2 About turbiditic systems . . . . .	4
1.2.3 Constituting elements . . . . .	6
1.3 Connectivity in turbiditic systems and impact on fluid flows .	10
1.3.1 Turbiditic system deposits and reservoir properties . .	10
1.3.2 Connectivity within a channel and between channels .	12
1.3.3 Connectivity influence on the reservoir and its exploitation	13
1.4 Processes controlling channel stacking in turbiditic systems .	14
1.4.1 Turbidity current circulation and secondary flow . . . .	16
1.4.2 Continuous channel migration . . . . .	18
1.4.3 Discrete processes and avulsion . . . . .	22
1.5 Stochastic simulation of channelized bodies and their connectivity . . . . .	26
1.5.1 Methods to stochastically simulate channelized bodies	27
1.5.2 Controlling the connectivity in stochastic simulations of channelized bodies . . . . .	31
1.6 Conclusions . . . . .	35

<b>2 Analyzing stochastic simulations of sedimentary bodies using connected components</b>	<b>37</b>
2.1 Introduction . . . . .	38
2.2 Indicators to measure simulation quality . . . . .	40
2.2.1 Basic element: the connected component . . . . .	40
2.2.2 Global analysis through all the components of a given facies . . . . .	41
2.2.3 Detailed analysis of the connected components . . . . .	44
2.3 Quality analysis considerations . . . . .	49
2.3.1 Influence of different grid dimensions . . . . .	49
2.3.2 Indicator rescaling . . . . .	52
2.3.3 Dissimilarity calculation . . . . .	52
2.3.4 Heat map . . . . .	54
2.3.5 Multidimensional scaling . . . . .	54
2.4 Application of the method and discussion . . . . .	57
2.4.1 Dataset . . . . .	58
2.4.2 Visual inspection of the realizations . . . . .	60
2.4.3 About MDS methods and accuracy . . . . .	62
2.4.4 Analysis of the global dissimilarities . . . . .	65
2.4.5 Analysis of the dissimilarities with the conceptual model . . . . .	71
2.4.6 Indicator behavior . . . . .	75
2.5 Conclusions and perspectives . . . . .	81
<b>3 Stochastic simulation of channelized sedimentary bodies using a constrained L-system</b>	<b>83</b>
3.1 Introduction . . . . .	84
3.2 L-system principles . . . . .	87
3.2.1 Basic L-systems . . . . .	87
3.2.2 Classical alphabet and geometrical interpretation . . . . .	88
3.2.3 Stochastic L-systems . . . . .	90
3.2.4 Context-sensitive L-systems . . . . .	90
3.2.5 Parametric L-systems . . . . .	91
3.2.6 Environmentally-sensitive and open L-systems . . . . .	91
3.2.7 Bracketed L-systems . . . . .	92
3.3 L-system for channel stochastic simulation . . . . .	93
3.3.1 Simulation domain definition . . . . .	93
3.3.2 Channel object parameterization . . . . .	94
3.3.3 Initial turtle state . . . . .	95
3.3.4 Basic considerations and alphabet . . . . .	96
3.3.5 Rule definition . . . . .	97

3.3.6	L-system parameters . . . . .	101
3.3.7	Extending the influence of the global direction . . . . .	103
3.3.8	Simulating the channel width and thickness . . . . .	104
3.4	Adding external constraints . . . . .	104
3.4.1	Formalization . . . . .	105
3.4.2	Sources of constraining elements . . . . .	107
3.4.3	Constraining element selection . . . . .	109
3.4.4	Constraint definition . . . . .	110
3.4.5	Adding the constraints to the L-system . . . . .	112
3.4.6	Constraint setting . . . . .	113
3.5	Illustration of channel simulation on simple cases . . . . .	117
3.5.1	L-system parameter impact . . . . .	117
3.5.2	L-system rule change . . . . .	119
3.5.3	Conditioning impact . . . . .	122
3.6	Application . . . . .	129
3.6.1	Dataset . . . . .	129
3.6.2	Simulation principle . . . . .	131
3.6.3	Unconditional realizations . . . . .	132
3.6.4	Realizations conditioned to the sand probability cube . . . . .	132
3.6.5	Realizations conditioned to the sand probability cube and the well sedimentary data . . . . .	133
3.7	Discussion and perspectives . . . . .	140
3.7.1	About the channel morphology . . . . .	141
3.7.2	About constraints and conditioning . . . . .	145
3.7.3	Post-processing the conditioning . . . . .	147
3.7.4	Better introducing the channel width and thickness in the conditioning . . . . .	147
3.7.5	Conditioning to well sedimentary data . . . . .	148
3.7.6	Conditioning to well connectivity data . . . . .	148
3.7.7	Conditioning to a sand probability cube . . . . .	149
3.7.8	Integrating seismic-interpreted objects . . . . .	149
3.7.9	About the parameterization . . . . .	150
3.7.10	About the use of L-systems . . . . .	151
3.7.11	About the simulation process . . . . .	152
3.7.12	Numerical aspects . . . . .	152
3.8	Conclusions . . . . .	154
<b>4</b>	<b>A geostatistical approach to the simulation of stacked channels</b>	<b>157</b>
4.1	Introduction . . . . .	158
4.2	New channel generation . . . . .	162



## Contents

4.2.1	Channel initiation . . . . .	162
4.2.2	Regional avulsion . . . . .	163
4.3	SGS for forward or backward migration . . . . .	165
4.3.1	Principle . . . . .	165
4.3.2	Parameter set . . . . .	167
4.4	MPS for forward or backward migration . . . . .	170
4.4.1	Principle . . . . .	170
4.4.2	Parameter set . . . . .	174
4.4.3	Size parameters . . . . .	174
4.4.4	Threshold parameters . . . . .	174
4.5	Numerical aspects . . . . .	175
4.5.1	Curvature computation . . . . .	175
4.5.2	Regridding . . . . .	176
4.5.3	Smoothing . . . . .	176
4.5.4	Neck cutoff determination . . . . .	177
4.6	Simple applications . . . . .	177
4.7	Comparison of different channel stacking in terms of connectivity	183
4.7.1	Case study . . . . .	183
4.7.2	Indicator results . . . . .	186
4.8	Discussion and perspectives . . . . .	193
4.8.1	About the migration pattern simulation . . . . .	195
4.8.2	About the discrete process simulation . . . . .	197
4.8.3	About the parameterization . . . . .	198
4.8.4	About small-scale variations and smoothing . . . . .	199
4.8.5	About the usefulness of the migration process . . . . .	200
4.8.6	About the simulation process with migration . . . . .	200
4.8.7	About data conditioning . . . . .	201
4.8.8	Numerical aspects . . . . .	201
4.9	Conclusions . . . . .	202
	<b>Conclusions</b>	<b>203</b>
1	Contributions . . . . .	203
1.1	Indicators and an analysis process to compare stochastic simulations of sedimentary bodies by focusing on the connectivity . . . . .	203
1.2	A method to stochastically simulate channelized bodies using a constrained L-system . . . . .	204
1.3	A method to stochastically simulate stacked channelized bodies using a geostatistical approach . . . . .	205
2	Perspectives . . . . .	206

2.1	Sensitivity tests and application to real data . . . . .	206
2.2	Improvements of the indicators . . . . .	206
2.3	Further use of L-systems . . . . .	207
2.4	Better management of the data . . . . .	207
2.5	Introduction of the channel fill . . . . .	208
2.6	Link with fluvial systems . . . . .	209
<b>Appendix A</b>	<b>Simulation parameters of chapter 2</b>	<b>211</b>
<b>Appendix B</b>	<b>Simulation parameters and L-system rules of chapter 3</b>	<b>213</b>
<b>Appendix C</b>	<b>Simulation parameters of chapter 4</b>	<b>217</b>
<b>Appendix D</b>	<b>Karst network simulation with L-systems</b>	<b>221</b>
<b>Appendix E</b>	<b>Karst conduit simulation with e-ODSIM</b>	<b>239</b>
	<b>Bibliography</b>	<b>253</b>



# List of Figures

1	Effet du remplissage et de l'organisation spatiale de chenaux, plus ou moins emboîtés les uns dans les autres, sur la circulation des fluides. . . . .	xii
2	Indicateurs utilisés pour la comparaison de réalisations. . . . .	xiv
3	Exemple d'application du MDS à un ensemble de réalisations provenant de différentes méthodes (d'après Rongier et al. [2015]).	xv
4	Exemple de réalisation de chenaux turbiditiques dans un chenal principal. . . . .	xvii
5	Exemples de réalisations avec une migration basée sur des simulations gaussiennes séquentielles. . . . .	xviii
6	Example of an outcrop analog of an oil field: the Storvola Mountain, Svalbard, Norway (modified from Johannessen and Steel [2005], Johannessen et al. [2011], Grundvåg et al. [2014]). .	xxxviii
7	Schiehallion field main sand reservoir (modified from Gainski et al. [2010]) . . . . .	xxxix
8	Examples of data used to characterize a reservoir (modified from Hanna et al. [2015]) . . . . .	xli
9	Usual workflow to build a geological model for flow simulation.	xlii
1.1	A modern submarine fan: the Congo (ex-Zaire) fan (modified from Babonneau et al. [2002], Droz et al. [2003] and Anka et al. [2009]). . . . .	5
1.2	Conceptual model showing a turbidity current within a channel (from Shanmugam et al. [1993]). . . . .	7
1.3	Example of hierarchy of turbiditic architectural elements, based on that of Champion et al. [2005] (from Stright et al. [2014]). . .	8
1.4	Conceptual model showing the incision and filling of a master channel (from Deptuck et al. [2003]). . . . .	9

## List of Figures

1.5	Example of lobe architectural element classification (from Prélat et al. [2010]). . . . .	11
1.6	Conceptual models showing two different kinds of channel filling (from McHargue et al. [2011]). . . . .	12
1.7	Impact of the channel fill and stacking on the connectivity. . . . .	15
1.8	Diagram illustrating a secondary flow in a channel bend (from Lajeunesse et al. [2010]). . . . .	16
1.9	Comparison between the vertical velocity profile in subaerial and in submarine flows (modified from Salles [2006]). . . . .	17
1.10	Example of numerical flow simulation results within the bend of a submarine channel (modified from Janocko et al. [2013a]). . . . .	19
1.11	Potential bars that can form within a sinuous turbiditic channel (from Janocko et al. [2013a]). . . . .	20
1.12	Influence of the flow characteristics on the formation of bars (from Janocko et al. [2013a]). . . . .	21
1.13	Example of channel migration patterns in a turbiditic system in West Africa (modified from Labourdette and Bez [2010]). . . . .	22
1.14	Conceptual model of punctuated migration (from Maier et al. [2012]). . . . .	24
1.15	Seismic amplitude map showing an avulsion, Angola, West Africa (from Kolla et al. [2001]). . . . .	25
1.16	Neck cutoffs observed on seismic slices along the Joshua channel, Gulf of Mexico (from Posamentier [2003]) . . . . .	26
1.17	Principle of cell-based methods, with the example of sequential indicator simulation using a variogram [Deutsch and Journel, 1992] and multiple-point simulation, here the method IMPALA [Straubhaar et al., 2011], using a training image. . . . .	28
1.18	Principle of object-based methods, with the example of FLUVSIM for channel object simulation (modified from Deutsch and Tran [2002]). . . . .	30
1.19	Example of realization simulated with a pseudo-process method (from McHargue et al. [2011]). . . . .	33
2.1	Possible neighborhoods for a given central cell in a regular grid (modified from Deutsch [1998]). . . . .	41
2.2	Connected components of a given facies in a two-dimensional structured grid. . . . .	42
2.3	Connected components of figure 2.2 represented with their bounding boxes (image 1). . . . .	45

2.4	Example of skeletons for the connected components of the figure 2.3. . . . .	47
2.5	Training image and examples of realizations for each categories. . . . .	58
2.6	View of all the channel connected components within the reference image and examples of realizations for each categories. . . . .	61
2.7	View of all the skeletons of the connected components for the TI and for a realization of each category. . . . .	62
2.8	MDS representation of the dissimilarities between the images of the case study generated using classical scaling and validation graphs. . . . .	63
2.9	MDS representation of the dissimilarities between the images of the case study generated using SMACOF and validation graphs. . . . .	64
2.10	Simplification of the MDS representation of the dissimilarities between the images of the case study generated using SMACOF. . . . .	66
2.11	Heat map representation of the dissimilarity matrix computed based on the reference image and simulations of the case study. . . . .	67
2.12	MDS representation of the dissimilarities between the TI, some TI analogs and the OBS realizations generated using SMACOF and validation graphs. . . . .	70
2.13	Box-plots comparing the facies proportions and facies connection probability for the TI, some TI analogs and the OBS realizations. . . . .	71
2.14	MDS representation of the dissimilarities between the images of the case study generated using SMACOF and validation graphs. . . . .	72
2.15	Box-plots comparing the realizations of each method with the TI. . . . .	74
2.16	Box-plots comparing the range of indicators computed on the channels for the different methods, except the node degree proportions. . . . .	76
2.17	Box-plots comparing the range of indicators computed on the levees for the different methods, except the node degree proportions. . . . .	77
2.18	Mean node degree proportions of the channel skeletons for each category. . . . .	78
2.19	Mean node degree proportions of the levee skeletons for each category. . . . .	79
3.1	Types of stochastic simulation methods and relationship between geological structure representation and conditioning. . . . .	85
3.2	Workflow for channel simulation based on L-systems with data and parameter sources. . . . .	86
3.3	Example of string and its geometrical interpretation. . . . .	88

## List of Figures

3.4	Example of string and geometrical interpretation (adapted from Prusinkiewicz and Lindenmayer [1996]). . . . .	92
3.5	Example of curvilinear grid and representation of its parametric space (inspired by Mallet [2004]). . . . .	94
3.6	Channel envelope modeled with NURBS surfaces and required parameters for its simulation. . . . .	95
3.7	Principle of channel discretization for L-system simulation. . . . .	96
3.8	Simplified illustration of channel simulation based on a L-system. . . . .	99
3.9	Parameters used to characterize an ideal channel bend. . . . .	101
3.10	Principle of constraint application to a L-system. . . . .	106
3.11	Parameters defining the area which select the constraining elements. . . . .	109
3.12	Parameters defining the magnitude of a relative constraint. . . . .	111
3.13	Variations of bend length and curvature and influence on the channel morphology. . . . .	118
3.14	Variations of half-wavelength and amplitude and influence on the channel morphology. . . . .	119
3.15	Impact of the global direction weight on the simulated channels. . . . .	120
3.16	Non-stationary channels obtained by modifying the L-system rules. . . . .	121
3.17	Examples of unconditional realizations and E-map of 1 000 realizations. . . . .	122
3.18	Examples of realizations conditioned to well sedimentary data and E-map of 1000 realizations . . . . .	123
3.19	Impact of the bandwidth on channels conditioned to well sedimentary data. . . . .	124
3.20	Impact of the L-system weight on channels conditioned to well sedimentary data. . . . .	125
3.21	Examples of realizations conditioned to well sedimentary data and associated E-maps of 1 000 realizations. . . . .	126
3.22	Examples of realizations conditioned to well sedimentary and connectivity data and E-map of 1 000 realizations. . . . .	127
3.23	Examples of realizations conditioned to sand probability map and E-map of 1 000 realizations. . . . .	128
3.24	Example of realization conditioned to a sand probability map and E-map of 1 000 realizations. . . . .	129
3.25	Dataset of the application: a curvilinear grid representing a master channel with a sand probability cube. . . . .	131
3.26	Example of a realization containing 40 channels within a master channel. . . . .	133

3.27	Details on the channel distribution inside the master channel for the realization in figure 3.26 rasterized in the master channel grid.	134
3.28	Channels at the top and at the bottom of the realization in figure 3.26. . . . .	135
3.29	Example of a realization containing 40 channels conditioned to a sand probability cube within a master channel. . . . .	136
3.30	Channel at the top of the realization in figure 3.29. . . . .	137
3.31	Details on the channel trend of the realization in figure 3.29 rasterized in the master channel grid. . . . .	138
3.32	Example of a realization containing channels conditioned to a sand probability cube and well sedimentary data within a master channel. . . . .	139
3.33	Channel at the top of the realization in figure 3.32. . . . .	140
3.34	Example of incompatibility between the data and the L-system path. . . . .	141
3.35	Details on the channel trend of the realization in figure 3.32 rasterized in the master channel grid. . . . .	142
3.36	Details on the well conditioning of the realization in figure 3.32.	143
3.37	Examples of asymmetric bends on a seismic section from Angola, West Africa (modified from Kolla et al. [2001]) and below example of channel simulated with a L-system showing opposite bend asymmetries from the initiation point. . . . .	144
3.38	Examples of realizations conditioned to well sedimentary data using two different conditioning processes and associated E-maps of 1 000 realizations. . . . .	146
4.1	Example of migration patterns on channels interpreted on seismic data from the Benin-major channel-belt, near the Niger Delta (modified from Deptuck et al. [2003]). . . . .	159
4.2	Example of a straight channel (top) and a highly sinuous channel (bottom) simulated with L-system and wrapped with NURBS. . . . .	163
4.3	Principle of global avulsion based on L-system. . . . .	164
4.4	Migration principle: the centerline nodes are moved along a migration vector $\vec{v}_m$ based on the normal $\hat{n}$ to the centerline and a migration factor $\varepsilon_m$ . . . . .	165
4.5	Components of the displacement vector for channel migration. . . . .	166
4.6	Main parameters used for horizontal bend migration with SGS. . . . .	168
4.7	Effect of the variogram range and of the curvature weight on bend migration with SGS. . . . .	169
4.8	Framework for the simulation of the migration factor $\varepsilon_m$ with MPS.	172



List of Figures

4.9 DS simulation principle. . . . .	173
4.10 Effect of the curvature threshold on bend migration with MPS. . .	175
4.11 Application of a forward migration process based on SGS to two channels generated with L-system. . . . .	178
4.12 Enlargements on some areas of the channels on figure 4.11 illustrating different aspect of channel evolution reproduced by the method. . . . .	179
4.13 Application of a backward migration process based on SGS to two channels generated with L-system. . . . .	180
4.14 Enlargements on some areas of the channels on figure 4.13 illustrating different aspect of channel evolution reproduced by the method. . . . .	181
4.15 First and last channel of a forward and backward migration with SGS. . . . .	182
4.16 Application of a forward migration process based on MPS to two channels generated with L-system. . . . .	182
4.17 Dataset of the application: a curvilinear grid representing a master channel with a sand probability cube. . . . .	185
4.18 Example of a realization from the disorganized stacking set. . .	186
4.19 Example of a realization from the conditioned disorganized stacking set. . . . .	187
4.20 Example of a realization from the organized stacking set. . . . .	188
4.21 Multidimensional scaling representation comparing three set of realizations with different methods and parameters. . . . .	189
4.22 Realizations for each set within the two groups separated by the dissimilarities. . . . .	190
4.23 Box-plots comparing the range of indicators – except the node degree proportions – computed on three sets of realizations with different methods and parameters. . . . .	192
4.24 Mean node degree proportions of the levee skeletons for each set and group. . . . .	194
4.25 Two migrating channels with two local abrupt migrations and associated skeletons. . . . .	195
4.26 Skeletons of the channel connected components of the realizations showed in figure 4.22. . . . .	196

# List of Tables

2.1	Set of indicators used for the case study. . . . .	60
2.2	Comparison of dissimilarities and distances between the TI and DeeSse realization 12 and 76 for to MDS methods. . . . .	65
3.1	Basic L-system alphabet and corresponding geometrical interpretation. . . . .	89
3.2	Basic L-system alphabet and corresponding geometrical interpretation for channel axis simulation. . . . .	97
3.3	Input parameters to simulate a channel from L-system and NURBS. . . . .	105
3.4	Constraints defined for channel simulation. . . . .	113
3.5	Parameters to determine a constraint. . . . .	114
3.6	Parameters to define the perception area and to choose the constraining element(s) within that area. . . . .	115
3.7	Parameters to define the constraint direction. . . . .	115
3.8	Parameters to define the constraint magnitude. . . . .	116
3.9	Input parameters for the user. . . . .	116
3.10	Simulation time for a realization containing one channel. . . . .	152
3.11	Simulation time for a realization containing one channel with two different conditioning processes. . . . .	153
3.12	Simulation time for a realization for each set of realizations in the master channel. . . . .	153
4.1	Set of indicators and associated weights used for the case study. . . . .	184
A.1	Parameters used to simulate the channelized environment with DeeSse. . . . .	211
A.2	Parameters used to simulate the channelized environment with IMPALA. . . . .	211
A.3	Parameters used to simulate the channelized environment with the object-based method of Petrel. . . . .	212

List of Tables

A.4	Variogram parameters used to simulate the channelized environment with SIS. . . . .	212
B.1	Parameters used to simulate the non-stationary channels. . . . .	213
B.2	Parameters used to simulate the channels of the figures 3.17, 3.18 and 3.23. . . . .	214
B.3	Parameters used to simulate the channels within the master channel of the synthetic case. . . . .	215
B.4	Rules used to simulate channels with a bend length $l_B$ from a distribution $F_{l_B}$ and a curvature $c$ from a distribution $F_c$ . . . . .	216
C.1	Parameters used to simulate the channels of figure 4.2. . . . .	217
C.2	Parameters used to simulate the SGS-based migrations in the simple cases. . . . .	218
C.3	Parameters used to simulate the MPS-based migrations in the simple cases. . . . .	219
C.4	Parameters used to simulate the organized stacking realizations. . . . .	220

# Preface

## Remerciements

Commençons par une petite citation attribuée à M. Winston Churchill : « Ce n'est que quand il fait nuit que les étoiles brillent. » Peut-être pas la meilleure, mais elle prend un sens tout particulier au moment d'écrire ces lignes. Parce que je suis loin d'avoir été le seul acteur de mon parcours jusqu'à cette thèse. Parce que j'ai eu la chance d'avoir été accompagné par une ribambelle de gens sans qui rien n'aurait été possible. Trop de gens pour pouvoir tous les remercier nommément, même si je n'en pense pas moins. Ainsi ce qui va suivre tiens plus de l'énumération focalisée sur mes années de thèse et n'évoquera pas l'ensemble des possibles, malgré quelques débordements.

Cela va tellement de soi et pourtant... Un incommensurable merci à Pauline pour m'avoir fait confiance durant toutes ces années, comprenant mes années de thèse mais également mes années de master. Suite logique, un immense merci à Philippe pour sa confiance, mais aussi pour tous les agréables moments et discussions associées à Neuchâtel. Un sincère merci à Judith, qui a toujours répondu présente quand j'en avais besoin. Enfin un ample merci à Julien et Sébastien pour des discussions toujours pertinentes durant ces trois ans (et demi).

Un auguste merci à Guillaume pour m'avoir laissé l'opportunité de poursuivre en thèse, ainsi qu'à Fatima puis Sophie pour m'avoir libéré des tâches administratives avec une efficacité sans égale. Merci également à Pierre et Christophe pour avoir fait de même avec les aspects informatiques.

Un colossal merci à tous les thésards dont j'ai croisé la route, aussi bien à Nancy qu'à Neuchâtel. Vous êtes tous pour beaucoup dans le merveilleux souvenir que je conserverai de cette expérience. Une petite mention particulière aux divers membres du bureau F-221 pour leur résistance contre vents et marées face à la disparition du respect. Je ne me lancerai pas plus avant dans une énumération qui serait déjà bien fournie avec les seuls thésards, et qui

## Preface

s'élargirait plus encore en ajoutant les nombreuses autres personnes qui m'ont accompagné de plus ou moins loin dans mon périple.

J'ai bien sûr une pensée pour ma famille, en commençant par la famille proche – en particulier mes sœurs – puis en poursuivant avec le sens le plus large que le mot « famille » puisse prendre : oncles, tantes, cousins, cousines, nourrice, amis et bien d'autres. J'extrait plus particulièrement de cet agrégat mon colloc', avec qui cette aventure fut un monumental plaisir. Malheureusement, toutes les bonnes choses ont une fin.

Naturellement mes parents n'étaient pas directement mentionnés au paragraphe précédent pour leur réserver le mot de la fin : je vous aime.

## Acknowledgements

This work was performed in the frame of the RING project at the Université de Lorraine in co-supervision with the CHYN at the Université de Neuchâtel. I would like to thank the industrial and academic sponsors of the Gocad Research Consortium managed by ASGA for their support and Paradigm for providing the SKUA-GOCAD software and API. I also thank the thesis committee members for assessing this work and for their helpful remarks.

# Introduction

## 1 Motivations

Fluids and their circulation play a fundamental role in geological structure formation, evolution and alteration. This begins at the surface, from mountains to the sea-floor, with the erosion and deposition of sediments due to fluid circulations. These fluids often circulate within channels: the resulting sedimentary deposits are so concentrated in space following given patterns. This affects many different and essential resources. Concentrations of organic matter within the deposits can latter produce coal, oil and/or gas [e.g., [McCabe et al., 1993](#)]. The channels themselves are often filled for a large part with sand. The preserved spaces between the sand particles enable underground fluid circulations. These circulations may lead to the deposition of metals such as gold or uranium with a significant economic interest [e.g., [Buck, 1983](#), [Youngson and Craw, 1999](#)]. Moreover, the fluids contained within the rocks are also interesting for themselves. Channels form reservoirs when they store oil and/or gas after their migration [e.g., [Martin, 1993](#), [Mayall et al., 2006](#), [Pranter and Sommer, 2011](#)]. They can also constitute aquifers, containing potential drinkable water resources or geothermal energy sources [e.g., [Fitterman et al., 1991](#), [Jussel et al., 1994](#), [García-Gil et al., 2015](#)]. And fluid storage within those rocks is more and more investigated for economic or climatic concerns [e.g., [Evans and Chadwick, 2009](#), [Braathen et al., 2012](#)].

In those prospects, the remaining spaces within the rock, i.e., the rock porosity (figure 6), are fundamental. The connections between these spaces, i.e., their connectivity, determine the fluid ability to circulate within the domain of interest. The rock permeability measures this ability. The permeability is then a major property to understand flow circulations, so a major element required for flow simulations. Estimating the permeability calls for an estimation of the connected porosity. And estimating the porosity calls for a representation of the rock type within the domain of interest. As stated previously, sandy fa-

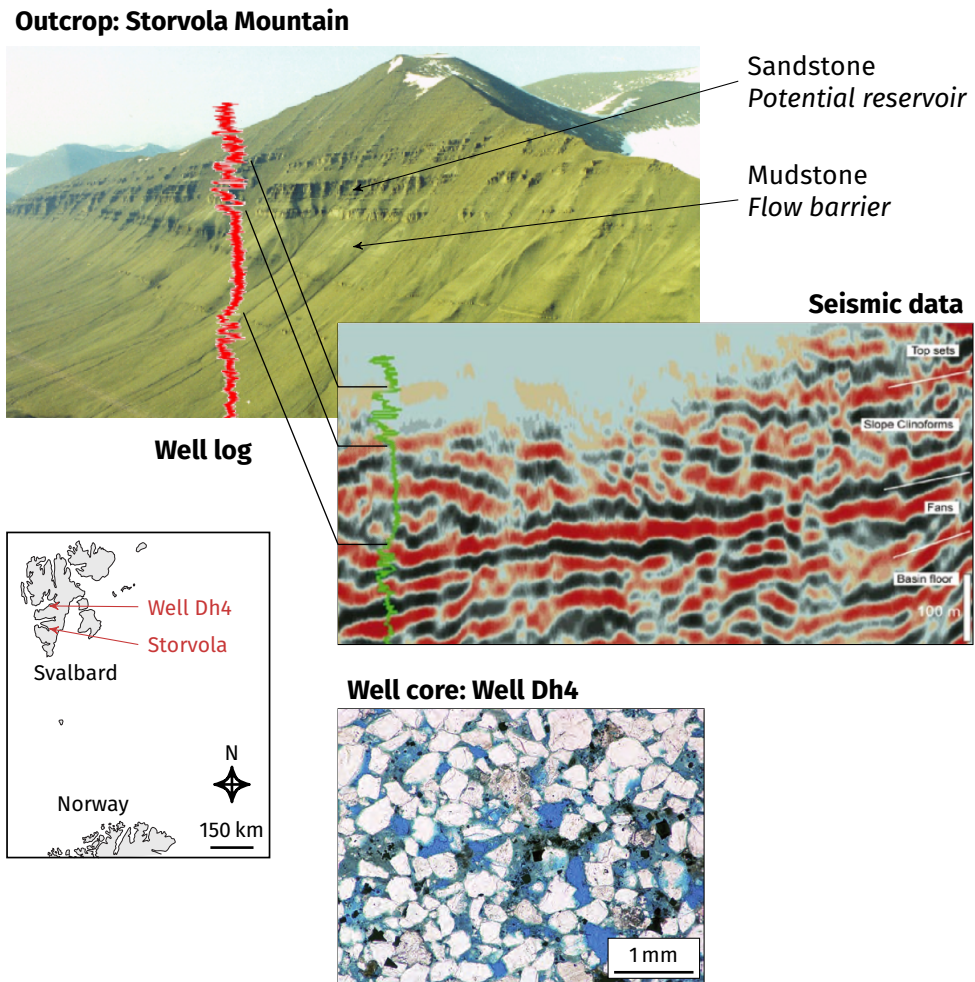


**Figure 6** Example of an outcrop analog of an oil field: the Storvola Mountain, Svalbard, Norway (modified from [Johannessen and Steel \[2005\]](#), [Johannessen et al. \[2011\]](#), [Grundvåg et al. \[2014\]](#)). The Storvola mountain is about 7 km long and 900 m high. The well log is a gamma ray log coming from the Sysselembreen well, drilled north-west of the Storvola mountain. It is 450 m long and is approximately placed along the mountain stratigraphy [[Luthi and Flint, 2014](#)]. The seismic comes from a 2D seismic line passing through the Sysselembreen well. The microscopic image shows a sandstone sampled from the well Dh4 located farthest north in Svalbard (modified from [Braathen et al. \[2012\]](#)). The white grains are quartz and the blue areas are the rock pores. These pores store fluids.

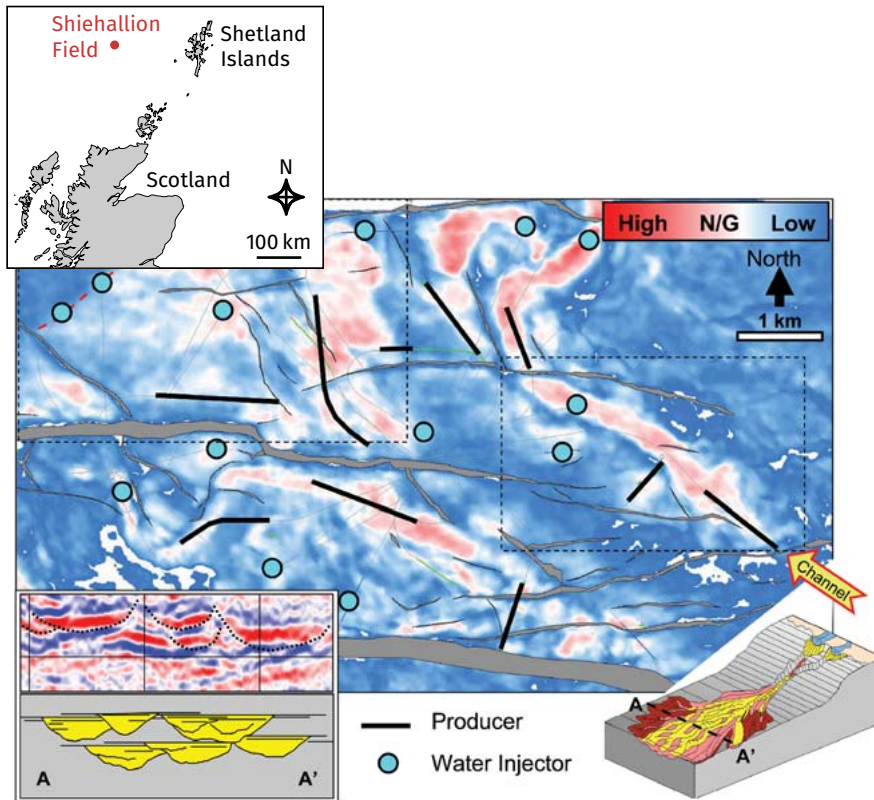


**Figure 7** Shiehallion field main sand reservoir (modified from Gainski et al. [2010]). High net-to-gross (N/G) areas corresponds to submarine channels whose depositional environment is illustrated in the bottom right figure. The grey lines indicate faults.

cies (figure 6) often have a significant connected porosity and form interesting reservoirs. On the other hand shales (figure 6) have a very low permeability: fluids can not circulate in such facies, which can act as flow barriers and may compartmentalize a reservoir.

The Shiehallion field is an interesting case to illustrate those concepts of reservoir and barrier features. It is an oil field located north of Scotland (figure 7), in the North Atlantic Ocean. Its reservoir compartments are composed of sandy rocks deposited by submarine channels with a south to north trend [Gainski et al., 2010]. Figure 7 shows the net-to-gross ratio of the main reservoir part. The net-to-gross ratio represents the ratio between the volume of actual reservoir facies over the total volume of rock within the field. A high ratio, the red areas on the map, means a significant sand content, a low ratio, the blue



areas on the map, a low sand content. Thus, the red areas roughly represent the channels and the related reservoir compartments. Those compartments have a very elongated shape characteristic of the channels.

The field production started in 1998. But soon the reservoir compartments appeared less inter-connected than initially estimated. This came from a wrong estimation of the potential flow barriers. A first and significant type of barriers are large faults that cut the field in a west-east trend. A fault results from a failure within the rock. However, such failure does not necessarily increase the porosity: some faults are sealed and act as flow barriers. This happens to be the case for most of the faults within the field. And their orientation almost perpendicular to the channels reduces even more the connectivity. Another type of barriers was observed: shales at the channel interfaces inducing a loss of connectivity between channels. These sedimentary barriers were too small to appear on the available data, making them difficult to infer.

At the end, the number of wells to maximize the oil recovery had to be more than doubled compared to the development plan. All this led to direct economic consequences, for instance an increase of the exploitation costs or a possible inability to maximize the recovery in some reservoir areas. But more generally it induces a mismanagement of the resource. If some strategies exist to manage those cases at best [e.g., [Gainski et al., 2010](#)], the Shiehallion case illustrates why better assessing the connectivity from the start is essential. Here representing the connectivity calls for representations of reservoir and barrier features. Faults act as barriers. Channels are not just filled with sandy material and can contain flow barriers. The filling defines the intra-connectivity of the channels but also the inter-connectivity between different channels. Delimiting the channels is a first step to help estimate their filling.

This delimitation transfers the notion of connectivity from the voids within the channel filling to the channels themselves. The channel connectivity refers to two aspects:

- Representing the connectivity along a channel. This requires in particular to be able to maintain the continuity of the channelized body.
- Representing the connectivity between the channels. Channels are not just individual objects but result from a temporal and spatial evolution related to flow processes. Thus, their spatial arrangement reflects this history.

Those aspects are fundamental to represent the reservoir parts and barriers within a channel and so to reproduce at best the permeability of the reservoir.

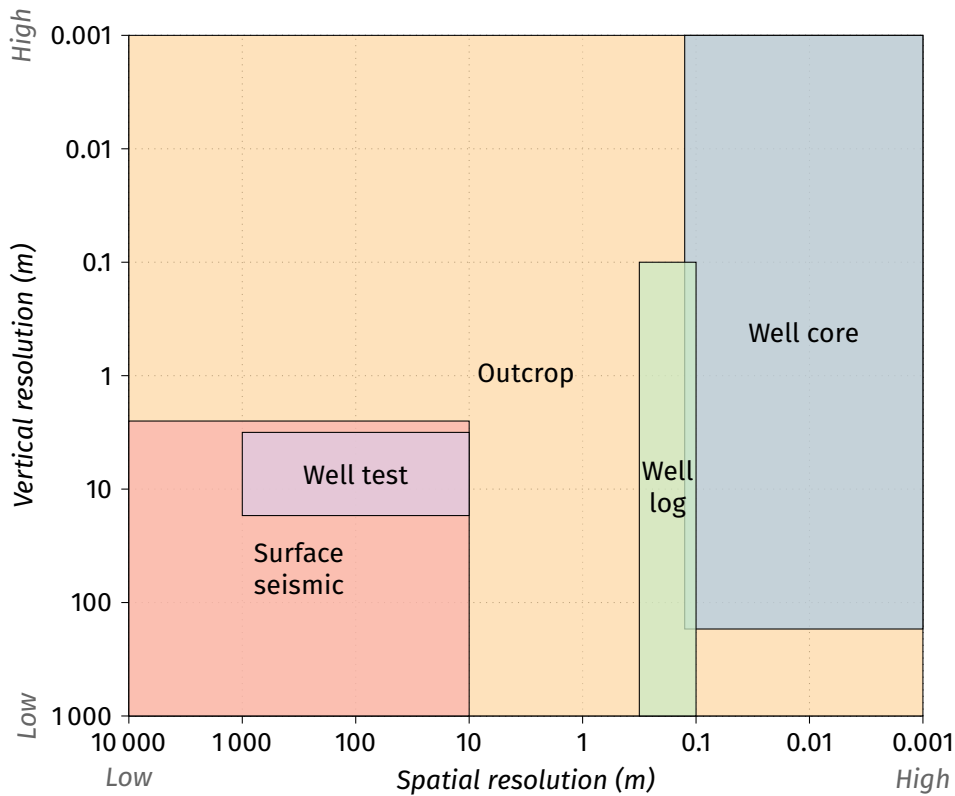


**Figure 8** Examples of data used to characterize a reservoir (modified from Hanna et al. [2015]). The outcrop is a surface analog of a reservoir and helps to better understand potential reservoir characteristics. Figure 6 gives an illustration of these elements.

However, our view of the geological structures in the underground is always partial. The Shiehallion field illustrates also this aspect: the net-to-gross was deduced from seismic data. A seismic image is similar to an ultrasound of the underground. This gives a view of the whole field, but only at a low resolution (figures 6 and 8). Indeed no precise channels are visible on figure 7, and some flow barriers were missed because their size is under the seismic resolution. In the best cases, it remains possible to interpret sedimentary bodies on a seismic if the resolution is high enough. Well data give a preciser view of the rock properties but only at a local scale (figure 8). Tracer tests between wells and well tests can help to identify larger scale information on the structure connectivity. In the Shiehallion field such tracer tests helped to determine more precisely the

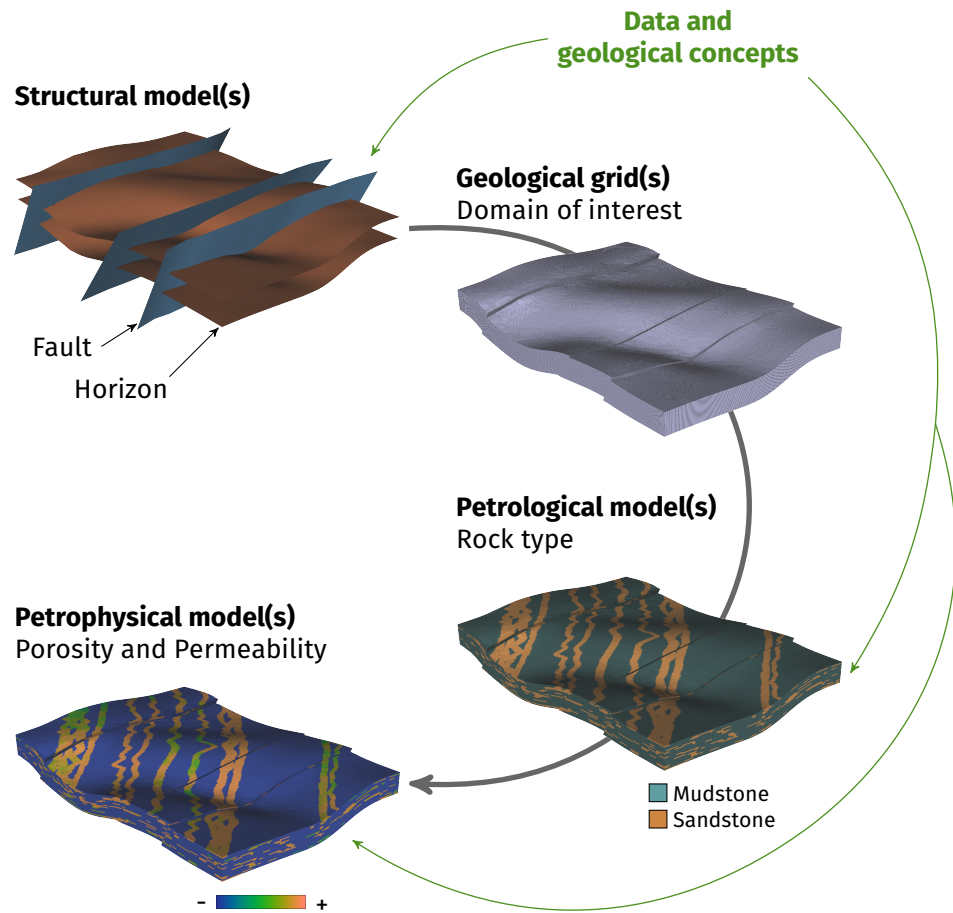


**Figure 9** Usual workflow to build a geological model for flow simulation.

reservoir compartmentalization. For a geological study, all those data provide a precise view of the underground at only some locations. Aside from those locations, they give at best a glimpse of the geological structures. Being able to cross those views requires building a three-dimensional representation of the rock properties.

These representations, called geomodels, integrate as much information as possible from the well and/or seismic data and look at completing the remaining blanks. The usual workflow (figure 9) consists in modeling the horizons delimiting the geological layers and the faults. The resulting model is called a structural model [Caumon et al., 2009]. This structural model serves as a

basis to build a geological grid. The geological grid is populated with properties representing the lithology, then the porosity and finally the permeability. For computational reasons, this grid is usually upscaled to a flow simulation grid. Flow simulations then help to better estimate the flow behavior within the domain of interest.

When building a geomodel, there is a need to complete some blanks due to:

- Some lacks in the data, as illustrated previously. These lacks come from the data resolution and the spatial coverage, and also from potential measurement errors.
- The lack of knowledge about the geological processes that have shaped the domain of interest. This embraces two questions: what are the involved processes? And how do they work?

It is then impossible to completely describe the geology of a given domain of interest. Thus, our vision of that domain is uncertain. A solution is to introduce some interpretation linking the data to geological concepts coming from the regional context or analog cases. This interpretation is often human-driven and subjective, and leads to a single deterministic model. Depending on the interpreter and its experience, the resulting models can be radically different [Bond et al., 2007]. This leads to the necessity of building several geomodels for a given case. However, it requires a significant amount of work. To overcome this, the idea is to simulate several equiprobable models considering all the available data. Those equiprobable models come from some randomness added to the workflow. Several steps, such as the horizon and fault modeling or the rock property simulations, are then stochastic. It gives access to a potentially infinite number of models for a given set of data. And depending on the differences between the models, it gives an idea of the uncertainties attached to the modeling process.

Studying these uncertainties is a prime concern when coming to the petrophysical modeling. Indeed, the related models integrate the smaller-scale geological bodies on which the lack of data is the most striking: well data do not inform much on the body extension and seismic data resolution is often too small to completely identify these bodies. Stochastic models are then essential. Simulating petrophysical models begins with the simulation of the lithology. This step includes in particular the simulation of the channelized bodies, whose connectivity is fundamental. Different approaches exist to simulate such channels [e.g., Deutsch and Journel, 1992, Mariethoz and Caers, 2014, Pyrcz and Deutsch, 2014], with a struggle between data and geological concept integration:

- Some methods easily take into account the data but have trouble reproducing the channel bodies and their connectivity.
- Other methods provide far better representation of the channelized bodies but have trouble taking into account the data.

## 2 Objectives

This work aims at exploring the integration of the connectivity in the stochastic simulation of geological structures, focusing on channelized environments. This is done through two main themes of research.

The first theme is the analysis of the connectivity of realizations. Most of the stochastic simulation methods are based on reproducing statistics and not the connectivity. In that perspective, being able to compare realizations from the viewpoint of the connectivity is essential considering its impact on the flow. The proposed method further explores the use of connected components to analyze realization connectivity and to compare those realizations.

The second theme aims at improving the simulation of channelized sedimentary bodies in terms of connectivity. One difficulty in stochastic simulation is to preserve the significant continuity of channels while conditioning to various data. The proposal here is to rely on a formal grammar, the Lindenmayer system, to simulate the channel morphologies while conditioning to the available data. Then it serves as a basis to stochastically simulate the channel evolution. It improves the connectivity by introducing more concepts derived from geological observations in the simulation process.

## 3 Outline

The thesis is divided in four chapters developing the two previous scopes. If the connectivity is a unifying concern throughout the manuscript, each chapter can be read independently from the other.

Chapter 1 further develops the notion of connectivity in channelized systems and their modeling. In that perspective, it focuses on a particular channelized environment, the turbiditic systems. After describing the system architecture and its impact on the connectivity, the processes controlling this architecture are detailed. The integration of the connectivity within the stochastic simulation of such environments is then discussed.

Chapter 2 looks into the first scope. It first exposes a set of indicators to compare realizations with a focus on the connectivity of the geological structures.

These indicators rely on the connected components of realizations or conceptual models. The computation of dissimilarities with the indicators facilitates the comparison. The application on a synthetic case study highlights the solutions to make the dissimilarity analysis easier.

Chapter 3 is a first look at the second scope: it focuses on the preservation of the connectivity along a channel while assuring data conditioning. It details a method of channel simulation based on a formal grammar system, the Lindenmayer system. The method relates on rules to develop channelized morphologies. Constraints related to data conditioning influence this development by attraction or repulsion. A synthetic case illustrates the modeling possibilities offered by this method.

Chapter 4 further explores the second scope to better preserve the connectivity between channels. As developed in chapter 1, this connectivity results from the channel evolution. The proposed method stochastically simulates channel evolution with a descriptive method based on geostatistical approaches. It introduces more geological concepts within the simulations while keeping a descriptive approach. A synthetic case illustrates the impact of such method on the channel connectivity.

A last chapter summarizes the results and further develops some perspectives.

Some of the parameters used in the application cases of the previous chapters are given in the appendices A, B and C.

This work is completed by appendices describing a parallel work about karsts.

Appendix C summarizes the results of a master project supervised during the doctoral work. It applies the Lindenmayer system to the stochastic simulation of karst networks. The connectivity of the network was a main concern during the method development. It has the ability to simulate both branchwork and anastomotic patterns.

Appendix D is an article published in Geomorphology during the doctoral work. It presents the work initiated during the M.Sc. internship about the stochastic simulation of karst conduits, and thus completes the work presented in appendix A.

## **4 Working context**

This work was funded by the Gocad Research Consortium managed by ASGA. It was performed in the frame of the RING project in the GeoRessources laboratory at Université de Lorraine and of the CHYN at Université de Neuchâtel.

Its development was mostly integrated and put into practice through the

plug-in *ConnectO* of the SKUA-GOCAD software provided by Paradigm. The software environment for statistical computing R was used for the dissimilarity analysis in chapter 3.

It leads to the following contributions:

<sup>(r)</sup> *peer-reviewed article*, <sup>(o)</sup> *oral presentation*, <sup>(p)</sup> *poster*, <sup>(a)</sup> *proceeding article*, \* *presenter*

**Chapter 2** <sup>(r)</sup> **G. Rongier**, P. Collon, P. Renard, J. Straubhaar, J. Sausse *Comparing connected structures in ensemble of random fields*, submitted to *Advances in Water Resources*

<sup>(p, a)</sup> **G. Rongier\***, P. Collon, P. Renard, J. Straubhaar, J. Sausse (2015) *Quality Analysis of Geostatistical Simulations through their Connected Structures*, EAGE Petroleum Geostatistics 2015, Biarritz, France

<sup>(p)</sup> **G. Rongier\***, P. Collon, P. Renard, J. Straubhaar, J. Sausse (2014) *Assessment of multiple point simulation quality focusing on connected geobodies*, GeoEnv 2014 - 10<sup>th</sup> conference on Geostatistics for Environmental Applications, Paris, France

<sup>(p)</sup> **G. Rongier\***, P. Collon, P. Renard, J. Straubhaar, J. Sausse (2014) *Exploring multiple-point realization quality through connected geobodies*, AAPG 2014 Annual Convention & Exhibition, Houston, Texas, USA

<sup>(o, a)</sup> **G. Rongier\***, P. Collon, P. Renard, J. Straubhaar, J. Sausse (2013) *Reproduction assessment of connected geobodies in multiple-point simulation*, 33<sup>rd</sup> Gocad Meeting, Nancy, France

**Chapter 3** <sup>(p, a)</sup> **G. Rongier\***, P. Collon, P. Renard, J. Ruiu (2015) *Channel Simulation Using L-system, Potential Fields and NURBS*, EAGE Petroleum Geostatistics 2015, Biarritz, France

<sup>(o, a)</sup> **G. Rongier\***, P. Collon, P. Renard (2014) *Channel axis simulation based on Lindenmayer systems*, 34<sup>th</sup> Gocad Meeting, Nancy, France

**Chapter 4** <sup>(o, a)</sup> **G. Rongier\***, P. Collon, P. Renard (2015) *A new application of L-systems to model channel system architecture and connectivity*, 35<sup>th</sup> Gocad Meeting, Nancy, France

Other contributions result from parallel works:

<sup>(o, a)</sup> P. Anquez\*, **G. Rongier**, P. Collon (2015) *Stochastic simulations of karst networks with Lindenmayer systems*, 35<sup>th</sup> Gocad Meeting, Nancy, France

<sup>(p, a)</sup> D. Lavandier\*, **G. Rongier**, J. Ruiu, P. Collon (2015) *3D reconstruction of karstic conduit from sparse laser data*, 35<sup>th</sup> Gocad Meeting, Nancy, France

- <sup>(o, a)</sup> M. Parquer\*, J. Ruiu, G. Caumon, P. Collon, **G. Rongier** (2015) *Towards more genetics concepts and data integration in channel simulation*, 35<sup>th</sup> Gocad Meeting, Nancy, France
- <sup>(r)</sup> **G. Rongier**, P. Collon, M. Filipponi (2014) *Simulation of 3D karst conduits with an object-distance based method integrating geological knowledge*, *Geomorphology* 217, 152–164
- <sup>(r)</sup> **G. Rongier**, P. Collon (2014) *Conduits Karstiques en 3D : une méthode de simulation stochastique*, *Karstologia*, 63, 58–60
- <sup>(o, a)</sup> P. Collon\*, **G. Rongier**, M. Le Mesnil, L. Dewaide, V. Hallet (2014) *Modélisation géométrique des systèmes karstiques : des réseaux aux conduits*, 24<sup>e</sup> Réunion des Sciences de la Terre, Pau, France
- <sup>(p, a)</sup> M. Le Mesnil\*, P. Collon, L. Dewaide, P. Mejía-Herrera, **G. Rongier**, V. Hallet (2014) *Karst conduit generation: the Furfooz area case study (Belgium)*, 34<sup>th</sup> Gocad Meeting, Nancy, France
- <sup>(o)</sup> **G. Rongier\***, P. Collon, M. Filipponi (2014) *Incorporation of geomorphological information into the stochastic simulation of karst conduits*, GeoEnv 2014 - 10<sup>th</sup> conference on Geostatistics for Environmental Applications, Paris, France

All this includes the supervision of three master students at the National School of Geology (ENSG) in Nancy: P. Anquez (2014-2015), D. Lavandier (2014-2015) and P. Mourlanette (2015-2016).





## Chapter 1

# Channelized systems and connectivity: a review through the example of turbiditic systems

**Abstract** Channelized systems develop in various environments. Among them turbiditic systems rise a significant interest due to their ability to store fluids, such as oil or gas. Analyzing the sedimentary structures within turbiditic systems reveals a complex and heterogeneous organization. The fundamental architectural element of turbiditic systems, the channel, is often filled by sand-rich deposits, potential reservoir units, often framed by mud-rich deposits that constitute potential flow barriers. The channel stacking impacts the spatial relationship between the sand-rich and the mud-rich deposits. Thus, it has a significant impact on the connectivity of the sand-rich deposits. This stacking comes from a long-term evolution of the channels through migration and avulsion. Reproducing such processes in stochastic simulations helps to get closer to the reservoir connectivity. Object-based simulation methods start to take into account migration and avulsion. Cell-based methods still have some trouble in reproducing such complex architectures. However, they better integrate data than object-based methods. Thus, a better reproduction of the complex architecture within turbiditic systems while conditioning all the available data remains an open topic. It is necessary to obtain a more accurate estimation of the reservoir connectivity.

## 1.1 Introduction

Channelized systems are complexes characterized by the development of channelized sedimentary bodies due to the circulation of fluids. Many environments develop channelized bodies: in fluvial and turbiditic environments, channelized systems lead to the erosion and deposition of sediments from the continents to the abyssal plain under the oceans. They form sand-rich bodies, including channels or lobes.

These sand-rich bodies have raised an increasing interest, especially because of their ability to store and let circulate fluids. Their economic impact is already undeniable as oil and/or gas reservoirs, regardless of their origin, fluvial [e.g., Tyler, 1988, Martin, 1993, Pranter and Sommer, 2011] or turbiditic [e.g., Abreu et al., 2003, Mayall et al., 2006, Snedden, 2013]. Besides, channels can constitute highly interesting aquifers [e.g., Fitterman et al., 1991, Jussel et al., 1994, Mulligan et al., 2007].

Channelized system study is also useful outside their ability to store fluids. Placers and paleoplacers represent economically significant deposits in terms of gold [e.g., Youngson and Craw, 1999], uranium [e.g., Buck, 1983], tin [e.g., Aleva, 1985], platinum-group elements [e.g., Konstantinovskii, 2005] or diamonds [e.g., Bluck et al., 2005]. In other domains, unconsolidated sediments related to channelized systems can have a huge impact on buildings [e.g., Hernández Del Pozo et al., 2005] and these systems can also be implicated in various environmental studies [e.g., Blum and Törnqvist, 2000, Moore et al., 2003].

The growing interest of the oil industry for deep-water reservoirs has further developed the concern about turbiditic systems [e.g., Mayall et al., 2006, Labourdette, 2007, Janocko et al., 2013b]. Turbiditic systems form the largest sediment accumulation on Earth [Talling et al., 2015], with related structures spreading over tens to hundreds of kilometers. These structures and the related heterogeneity have a significant impact on the reservoir connectivity. However, they are thousands of meters under the oceans, making them difficult to study. The processes responsible for their formation remain less well known than in fluvial context.

In such context, the uncertainties due to the lack of knowledge about these processes and the data scarcity make the use of stochastic simulation even more valuable. It implies to be able to simulate channels, structures with a highly elongated shape, that condition to the available data.

This chapter aims at developing the significant impact of channels on the reservoir connectivity, with the particular interest of reservoir modeling. To do so, it relies on the example of the turbiditic environment (section 1.2). The

## 1.2 An example of channelized environment: the turbiditic systems

next sections illustrate the connectivity in such systems (section 1.3) and the processes leading to that connectivity (section 1.4). The last section describes the types of methods that exist to stochastically simulate channels and the options to deal with the connectivity (section 1.5).

### 1.2 An example of channelized environment: the turbiditic systems

Turbiditic systems are transitional systems transporting sediments from the continental margin to the oceanic basin floor. Turbidity currents play a major role in this transport.

#### 1.2.1 About turbidity currents

Turbiditic systems are the results of density current circulations on the sea floor, usually in water depth from 100 m to 4 000 m. A density current is a current denser than its surrounding fluids and kept in motion by gravity in relation to the difference of density. Concerning turbiditic systems, the current is subaqueous and turbid, meaning that it contains suspended sediments. The higher density of the current originates from these sediments. More strictly, turbidity currents are a type of sediment gravity flows with a Newtonian rheology and a turbulent state. The upward component of the flow turbulence mainly supports the sediments [e.g., Middleton and Hampton, 1973, Mulder and Alexander, 2001, Shanmugam, 2002]. However, this definition is not universally accepted [Mulder and Alexander, 2001, Shanmugam, 2002] and some authors use a less strict definition that includes other types of density currents [e.g., Kneller and Buckee, 2000].

Turbidity currents have large dimensions. They can be from several kilometers to more than 200 km wide [e.g., Pirmez and Imran, 2003, Talling, 2014], even if they become thinner as the distance from the current axis increases. They vertically measure from a few meters to hundreds of meters [e.g., Komar, 1969, Stow and Bowen, 1980, Pirmez and Imran, 2003]. Considering the large dimensions of the resulting deposits, turbidity currents can travel over several hundreds of meters to more than 1 000 km [e.g., Salles, 2006, Talling et al., 2007]. Their speed varies from a few kilometers per hour to more than 70 km.h<sup>-1</sup> [e.g., Genesseeaux et al., 1980, Piper et al., 1999, Salles, 2006]. The major currents that build a turbiditic system can happen every year to every thousands of years [e.g., Talling, 2014] and last from a few hours to several days.

## 1.2.2 About turbiditic systems

Turbiditic systems are classified according to two main parameters [[Reading and Richards, 1994](#), [Richards et al., 1998](#)]:

- The number of system feeders and their characteristics.
- The size of the sediment particles, e.g., gravel-rich, sand-rich or mud-rich systems.

The feeders are the current suppliers for the system. They divide in three categories:

- One punctual source, forming submarine fans.
- Multiple punctual sources, forming submarine ramps.
- Multiple linear sources, forming slope aprons.

Submarine fans are the most famous turbiditic systems, and the term “turbiditic system” is often used instead of submarine fan. With submarine ramps, they rely on stable feeder, such as rivers or deltas. The turbidity currents tend to come from hyperpycnal flows, which form when the density of the river flow is higher than the density of the basin water, or from failures due to sediment accumulations at the river mouth, at the prodelta or at the shelf-edge [e.g., [Piper and Normark, 2001](#), [Wynn et al., 2007](#)]. Submarine ramps and fans tend to have an organized architecture. On the contrary, slope aprons come from more ephemeral feeders, such as a slope failure. They do not have a clear organization, which reduces their interest as reservoirs. The following sections tend to focus on submarine fans due to an abundant literature, especially on modern analogs.

Besides the feeder and the sediment type, other features influence the development of a turbiditic system [e.g., [Bouma, 2004](#)]: the tectonic activity, the sea-level variations, the climate, the basin characteristics, the Coriolis force, etc. At the end, the system architecture results from the alternation of erosion and deposition events from the shore to the oceanic basin. Turbidity currents drive these events by transporting the sediments through the system. The system often begins with a canyon, i.e., an entrenchment along the continental slope. After the slope, the canyon ends and the system is far less confined. It is then free to evolve along the oceanic basin (figure 1.1). Channelized structures can develop from the canyon to the basin, but their development is more striking in the basin. Due to the lighter confinement than in the canyon, the channel path can vary a lot. Avulsions lead to the abandonment of a channel and to the

1.2 An example of channelized environment: the turbiditic systems

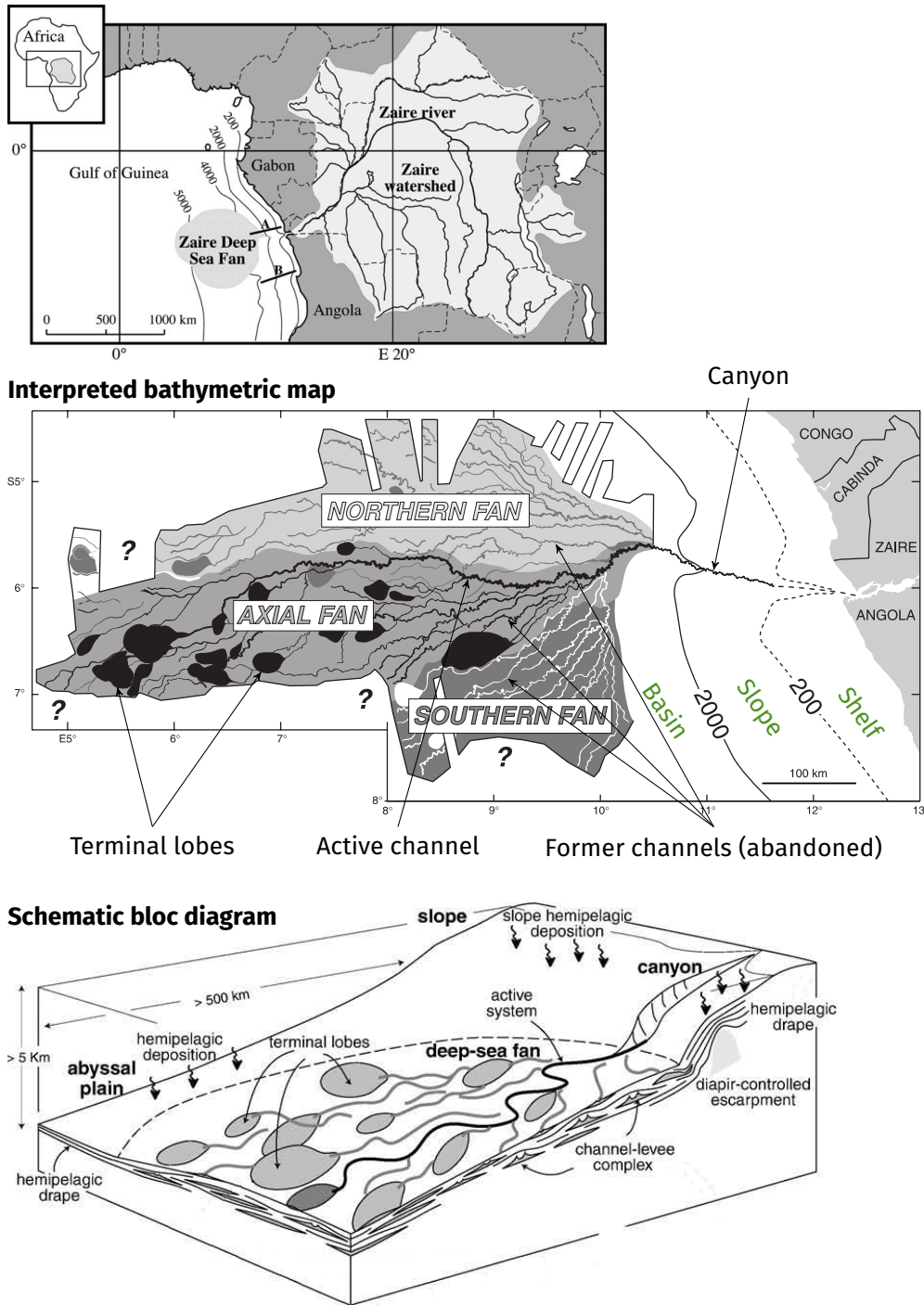


**Figure 1.1** A modern submarine fan: the Congo (ex-Zaire) fan (modified from Babonneau et al. [2002], Droz et al. [2003] and Anka et al. [2009]).

formation of a new channel. It gives a fan architecture to the system. Only one channel path is active at a given time [Wynn et al., 2007]. The other observable channels are abandoned. From the slope to the basin, the channel widths tend to decrease [Flood and Damuth, 1987]. Channels often end with large ellipsoidal structures called terminal lobes.

### 1.2.3 Constituting elements

Turbidity currents usually start to erode the sea floor after their initiation, due to a high speed and a coarser load of sediments. In its advance, the current progressively loses its speed due to a decreasing slope and a loss of energy. Thus, it progressively moves from an erosive regime to a depositional regime. This depositional regime leads to the formation of several types of sedimentary bodies [e.g., Mutti and Normark, 1991, Normark et al., 1993].

#### Channel-levee systems

The main structures resulting from this erosion/deposition alternating are channels. Channels are highly elongated structures that are U or V-shaped in cross-sections. Turbidity currents initiate these structures during their erosive phase. Then the channels drive the currents and are progressively filled when the currents get into a depositional regime.

Due to the low difference of density between the turbidity current and the surrounding water, the current often overflows from the channel margins (figure 1.2). Such overflowing currents often have a mudier content than the current remaining in the channel axis. The deposition of their sediments form margin deposits called levees or overbanks.

Channels in turbiditic systems often develop in a nested structure: channel-like shapes can be identified within other channel-like shapes. Sometimes the limit between a channel and a confining structure is hard to determine [Wynn et al., 2007].

#### Architectural element hierarchy within channel-levee systems

Several classifications have been proposed to define relevant and recurring architectural elements related to turbiditic channels [e.g., Sprague, et al., 2002, Mayall et al., 2006, McHargue et al., 2011] (figure 1.3). The classifications differ in terms of approach and element denominations, but their characteristics are relatively similar.

The principal architectural element is the channel element of McHargue et al. [2011] or the individual channel of Mayall et al. [2006]. A channel comprises

## 1.2 An example of channelized environment: the turbiditic systems

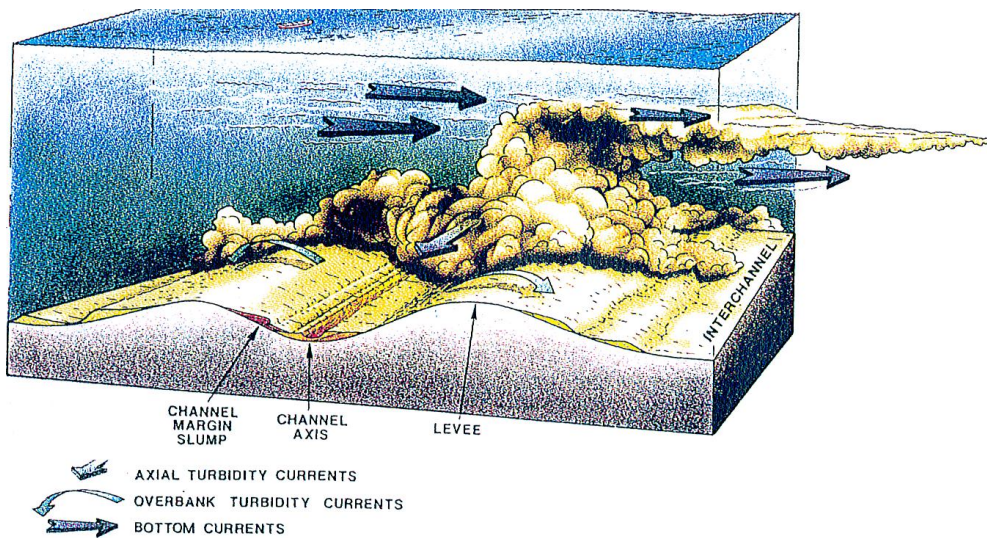


**Figure 1.2** Conceptual model showing a turbidity current within a channel (from Shanmugam et al. [1993]). The channel constrains more or less the current. Thus some components of the current leave the axial current and form overbank currents.

a bounding surface and all the sediments filling it. It is usually tens of meters thick and hundreds of meters wide. A channel contains several subchannel elements called stories [Sprague, et al., 2002, McHargue et al., 2011]. These elements have a channel-like shape and are composed of beds. Beds are the smallest architectural elements, with dimensions from the millimeter to the meter. They correspond to the deposits formed by a single turbiditic event [Macauley and Hubbard, 2013, Stright et al., 2014]. These deposits include divisions from the Bouma et al. [1962] and Lowe [1982] sequences. Along the channel margins, levees are formed in a depositional context. Terraces can appear in a more erosional context.

Channels usually stack to form larger-scale architectural elements, e.g., complexes and complex-sets [McHargue et al., 2011] or channel belt and channel belt complexes [Janocko et al., 2013b]. The stacking pattern and the genetic relationship between the channels define these larger-scale elements. Their boundaries may be difficult to determine on the field. It leads to some difficulty in interpreting the complete hierarchy, with the use of the same denomination to characterize different elements at different scales [e.g., Wynn et al., 2007].

In any case, channels often form within a larger-scale confinement. Along the continental slope, the canyon is a first confinement. It is mainly an erosional structure, into which sediments circulate to the basin. On the basin, the erosive



## 1 Channelized systems and connectivity: a review

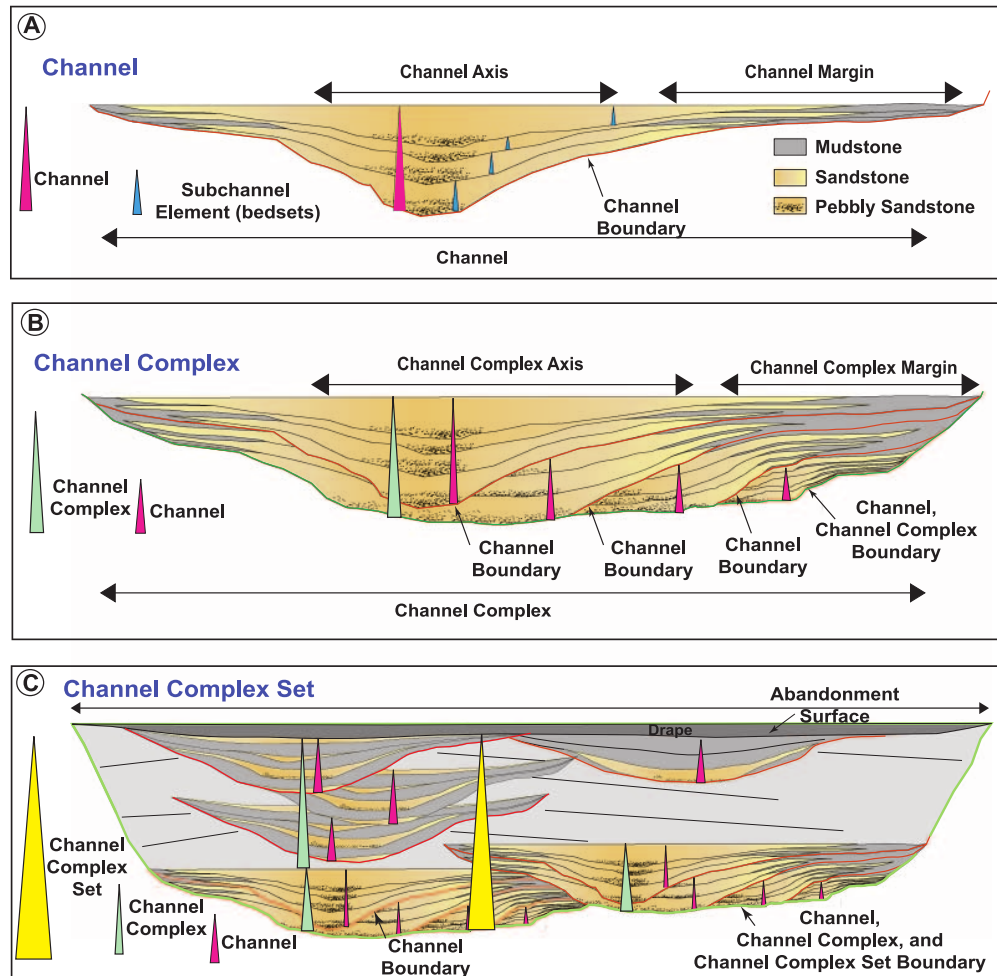


**Figure 1.3** Example of hierarchy of turbiditic architectural elements, based on that of [Campion et al. \[2005\]](#) (from [Stright et al. \[2014\]](#)).

early phase of the turbidity events can create a new confinement. The resulting element has a channel-like shape (figure 1.4). It is usually hundreds of meters thick and several kilometers wide. This element corresponds to the channel as introduced by [Mayall et al. \[2006\]](#): a large erosionally based channel delimited by a third order stratigraphic sequence boundary. It has various names, e.g., master channel [[Kolla, 2007](#)], submarine incised valley [[Janocko et al., 2013b](#)], erosional fairway [[Deptuck et al., 2003](#)]. The upper part of the currents may also overspill from the master channel margins. This leads to the deposition of sediments over the channel banks. These sediments form overbanks or levees.

## 1.2 An example of channelized environment: the turbiditic systems

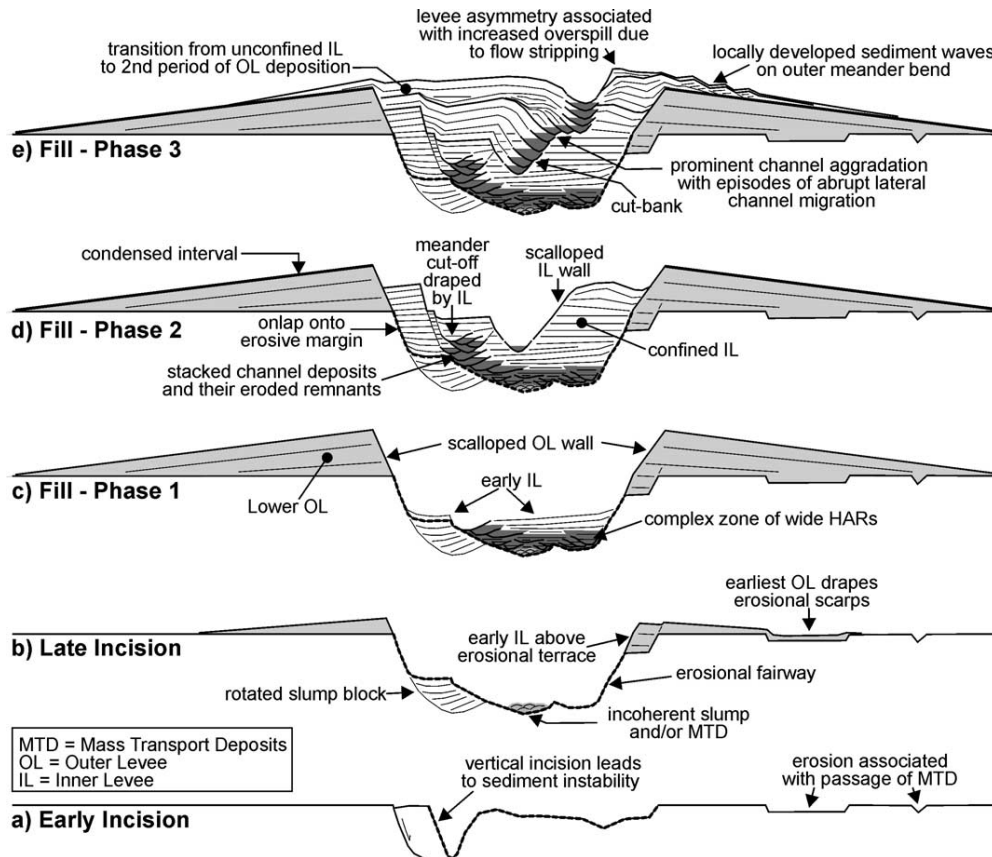


**Figure 1.4** Conceptual model showing the incision and filling of a master channel (from Deptuck et al. [2003]). Channel initiation and filling are responsible for the filling of the master channel.

Thus, overbanks form at two scales [Kolla, 2007] (figure 1.4):

- Along the channel margins. They are called inner/secondary overbanks/levees.
- Along the master channel margins. They are called outer/master overbanks/levees.

When the outer overbanks are high enough, they confine the channel development. The overbank height depends on the mud content of the currents. A high mud-content increases the levee cohesion, leading to higher levees with a larger confining capacity [e.g., Galloway, 1998].

## Lobes

Channelized structures act as transitional conduits for the sediments from the continental margin to the sea floor. Lobes result from the accumulation of sediments at a channel way out. During their circulation through the channels, the sediments are more or less sorted. The characteristics of the terminal lobes depend on the nature of the sediment input, e.g., mud-rich or sand-rich, and on the sorting power of the channels [Mulder and Etienne, 2010]. Terminal lobes are the most distal element of a turbiditic system. A distinction can be made between terminal lobes at the end of a channel and avulsion lobes. Avulsion lobes occur when an overbank breaches. It is a first step before the formation of a new channel path [e.g., Droz et al., 2007, Kolla et al., 2007] (for more details about avulsion, see section 1.4.3).

Globally a lobe has an ellipsoidal and convex-up morphology. The horizontal shape is more or less elongated depending on the confinement. It is usually several meters thick and tens of kilometers wide [e.g., Shanmugam and Moiola, 1988, Mulder and Etienne, 2010]. Internally, the lobe starts by a channeled part, corresponding to the continuation of the channels [Mulder and Etienne, 2010]. Overbanks can develop, but with a high sand content. Thus, avulsions are frequent, with the formation of new channel paths. The external parts of a lobe are composed of sheet-like structures. The first structure is deposited right after the channel mouth and contains the coarser sediments. The second structure contains the finer sediments. Similarly to channels, hierarchical models exist for lobes, which gather for instance into complexes (figure 1.5) [Prélat et al., 2009].

## 1.3 Connectivity in turbiditic systems and impact on fluid flows

Turbiditic systems contain various structures with complex internal facies heterogeneities. The main question is then the impact of such heterogeneities on the flow.

### 1.3.1 Turbiditic system deposits and reservoir properties

The facies deposited by a turbiditic system can be roughly separated in two categories:

- The sand-rich deposits have a high sand content, so coarse-grained sediments, and a low mud content. The grain size lets plenty of space after

### 1.3 Connectivity in turbiditic systems and impact on fluid flows

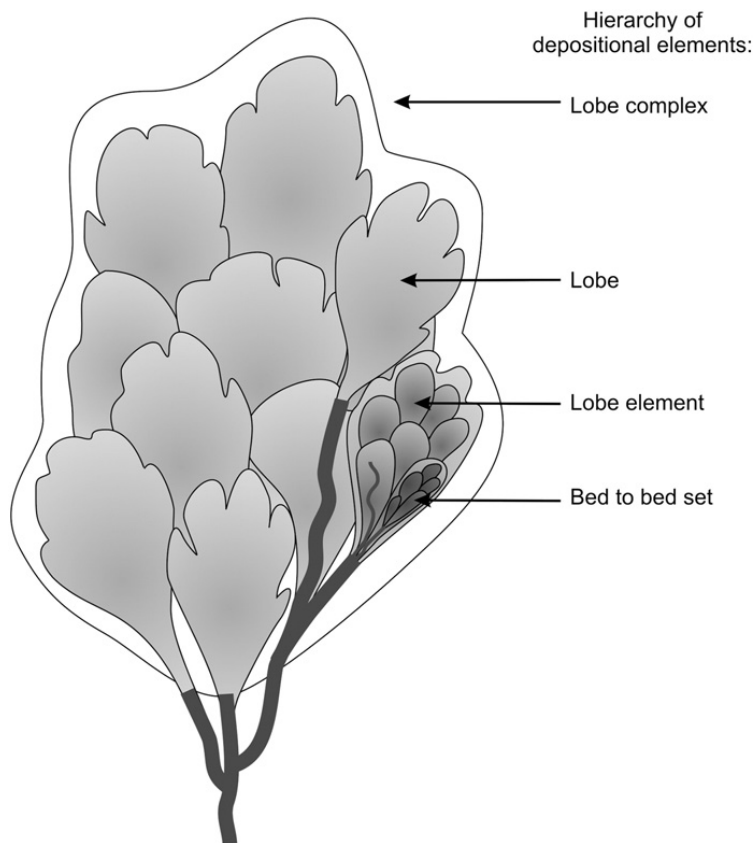


**Figure 1.5** Example of lobe architectural element classification (from Pr lat et al. [2010]). The feeder channel is at the bottom, in dark gray.

deposition. Thus, such deposits often have a significant permeability and interesting reservoir properties.

- The mud-rich deposits have a high mud content, so fine-grained sediments. Such deposits have a far lower permeability than sand-rich deposits and can constitute flow barriers.

Among the architectural elements previously defined, channels and lobes are known to form interesting reservoirs due to their high sand-content [e.g., Shanmugam and Muiola, 1988, Mayall et al., 2006]. Overbanks can also form potential reservoirs depending on their sand content [Mayall and O'Byrne, 2002, Beaubouef, 2004]. The main questions concern the fluid circulation ability within and between all these structures. For instance fluid circulation within the overbanks may be difficult considering their heterogeneity and the poor

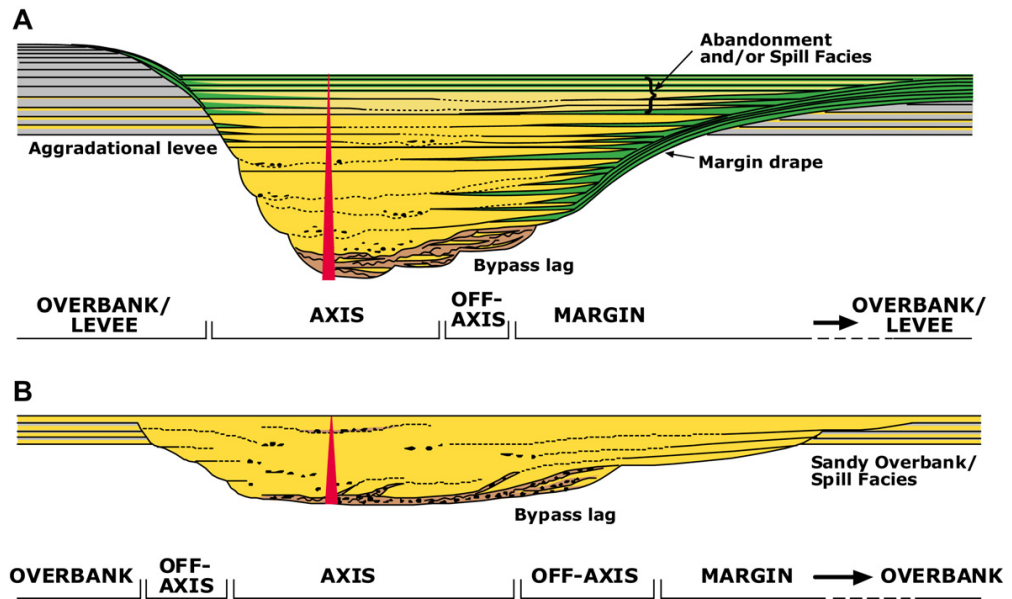


**Figure 1.6** Conceptual models showing two different kinds of channel filling (from McHargue et al. [2011]). Model A is an under-filled channel with a moderate to high rate of overbank development. It contains several mud-rich deposits (in green, gray and brown), potential flow barriers. Model B is filled channel with a low rate of overbank development. Mud drapes are rare and the sand-content (in yellow) is important, with even potential sand deposits on the overbanks.

lateral continuity of the thicker sand-rich beds. This question is even more complex because a channel and a levee can be spatially adjacent without a genetic relationship [Cronin et al., 2000]. The following sections illustrate the potential connectivity issues by focusing on the channels, as they are a fundamental structuring feature of turbiditic systems and have a significant reservoir potential.

### 1.3.2 Connectivity within a channel and between channels

A key aspect in a reservoir perspective is the connectivity between the sand-rich deposits. Channels are filled with such deposits, hence their reservoir potential. But the channel fill is usually not homogeneous: it depends on the characteristics of the turbiditic system, such as the mud-content of the sediment supply. The resulting architecture can be quite complex with combinations of sand-rich beds and mud-rich beds (figure 1.6) [e.g., Labourdet, 2007, McHargue et al., 2011, Alpak et al., 2013].

### 1.3 Connectivity in turbiditic systems and impact on fluid flows

The first deposits result from the end of the erosive phase. They are composed of poorly sorted particles with mud clasts. This basal lag has a low permeability and constitutes a potential barrier for the flow. The channel axis is then filled with alternating sequences of coarse-grained sand to fine-grained sand. These sequences have usually a significant permeability and concentrate the essential part of the reservoir potential. The channel margins may contain mud drapes along the margins and mud-rich beds intercalated with sand-rich beds. These muddy elements have a low permeability, with two consequences:

- The fluid circulation between the channel axis and margins can be perturbed. Some fluids are then bypassed and remains in the margin
- The fluid circulations between the channels can be impossible.

The channel margins and the related overbanks can also collapse before and/or during the channel filling. It forms slumps with a significant mud content, so a poor permeability. The upper part of the channel may be filled with abandonment deposits. Such deposits are mud-rich and constitute another potential flow barrier.

To summarize, margin drapes, margin collapse deposits, basal lags and abandonment deposits can all form flow barriers all around the channel. But they do not necessarily compartmentalize the reservoir. Indeed, the relative positioning of channels has a huge impact on the barrier influence [Labourdettes et al., 2006, Labourdettes, 2007]. Following their genetic relationships, channels are more or less stacked. The stacking can be described by a lateral and a vertical offset between two successive channels. The offset is not constant between two channels and can even vary significantly over short distances [Mayall et al., 2006, Deptuck et al., 2007]. It impacts the spatial relationships between the reservoir deposits and the flow barriers. The stacking also influences the preservation of the potential flow barrier by limiting their erosion [Labourdettes, 2007]. Depending on the stacking, a mud-rich deposit prevents the flow circulation between two channels or not.

#### **1.3.3 Connectivity influence on the reservoir and its exploitation**

Two elements are essential to characterize the reservoir compartmentalization: the channel fill and the channel stacking. The channel fill determines the spatial distribution of the flow barriers and the channel stacking controls the impact of such barriers on the compartmentalization. Thus, their effect on the reservoir connectivity is significant [e.g., Labourdettes et al., 2006, Larue and Hovadik, 2008, Alpak et al., 2013]. Moreover, while the channel stacking may be interpretable on seismic data, the channel fill is often subseismic, what complicates

the estimation of the reservoir connectivity. It has been well illustrated by the Shiehallion field case [e.g., [Gainski et al., 2010](#)]: the reservoir compartments are less inter-connected than initially estimated. The first overestimation of the connectivity partly comes from unobserved margin collapses and drapes due to their subseismic scale. In practice, it led to double the well number to maximize the oil recovery.

Thus channel fill and stacking have a significant impact on the exploitation strategy, in particular concerning the well positioning [[Mayall and O'Byrne, 2002](#)]. Figure 1.7 illustrates this aspect: an injector was drilled and a location for a producer has to be chosen. The most permeable units are within the channels, and the inter-channel area is composed of mud-rich overbank deposits. Thus, the permeability is far higher along the channel direction than perpendicularly. The flow starts from the injector and reaches the producer 1 at first. Then it goes in the second channel and reaches the producer 2. From this point of view, the producer 1 risks a rapid water breakthrough and less oil recovery. The producer 2 seems far more interesting. However, this approach does not take into account the potential barriers between the channels. Basal barriers, such as basal lags, may let the flow circulate. Lateral barriers, such as margin drapes, may not, especially if the stacking is lateral. A vertical stacking at this location may let the flow circulate. Thus, the connectivity between the wells has to be carefully estimated, or the producer 2 will be useless due to the lack of connectivity between the two channels.

Channel fill and stacking also influence the well trajectory [[Mayall and O'Byrne, 2002](#), [Mayall et al., 2006](#)]. A strategy when drilling a well is to go through as many barriers as possible. This allows bypassing the potential compartmentalization. The well geometry must be adapted to the channel stacking to cross as many channels as possible: vertical if the stacking is mostly vertical, horizontal if the stacking is mostly lateral. Thus, the channel stacking is a fundamental aspect to study because of its relationship with the flow barriers and the related impact on the connectivity.

### **1.4 Processes controlling channel stacking in turbiditic systems**

The channel stacking comes from the lateral and vertical evolution of channels. This evolution depends on the turbidity current circulation within the channels and on the channel confinement, e.g., the presence of a master channel and overbanks.

#### 1.4 Processes controlling channel stacking in turbiditic systems

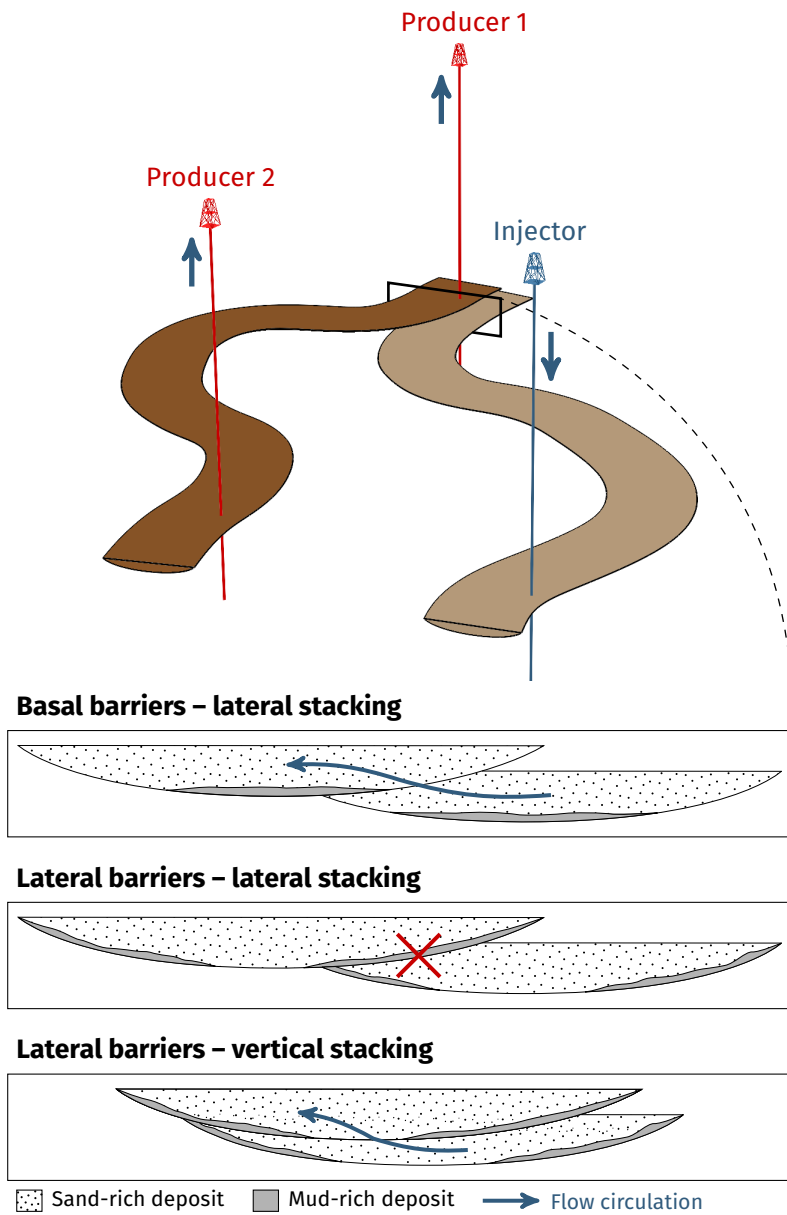


**Figure 1.7** Impact of the channel fill and stacking on the connectivity. This impact has significant implications on the well locations (see the text for details).



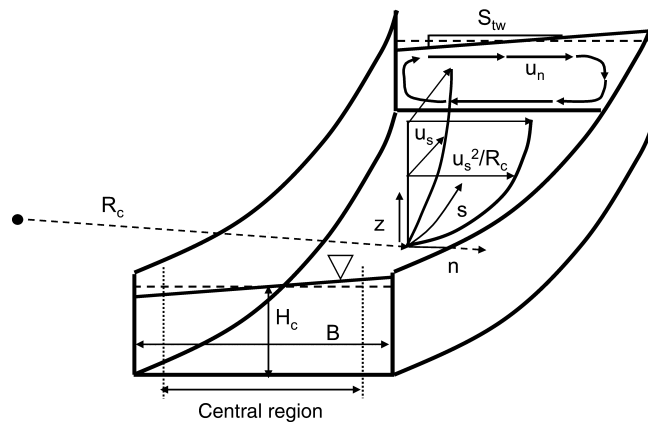


**Figure 1.8** Diagram illustrating a secondary flow in a channel bend (from Lajeunesse et al. [2010]).  $u_s$  is the primary flow velocity,  $u_n$  is the secondary flow velocity and  $u_s^2/R_c$  represents the centrifugal force. As a result, the flow is super-elevated along the outer bend (on the right).

### 1.4.1 Turbidity current circulation and secondary flow

Within a channel, a current follows a primary flow oriented along the channel direction. Perpendicularly to the channel orientation, the flow varies following the channel morphology, especially its curvature [e.g., Einstein, 1926, Rozovskiĭ, 1957, Imran et al., 1999]. The centrifugal force pushes the current toward the outer bank of the bend, elevating the current at the outer bend compared with the inner bend. This induces a pressure gradient in the opposite direction, so a force toward the inner bank of the channel. Contrary to the pressure force, the centrifugal force depends on the current velocity. And that velocity is not uniform. Vertically, the velocity is lower along the channel floor due to frictions (figure 1.8). Thus, the centrifugal force overcomes the pressure force at the top of the channel, and at the bottom, the pressure force overcomes the centrifugal force. This induces a rotational secondary flow. Combined with the primary flow, it gives a helical structure to the current. Besides the curvature, other features influence the development of a secondary flow, such as the channel topography or the current turbulence.

Secondary flows have been highly studied in the subaerial currents of rivers [e.g., Rozovskiĭ, 1957, Ikeda et al., 1981, Johannesson and Parker, 1989]. In such currents, the secondary flow goes from the outer bank to the inner bank along the bottom of the bend apex. It is directed inward, with the helix rising against the inner bend (figure 1.9). However, the direction of rotation of the secondary flow is more controversial in submarine currents. Both laboratory

## 1.4 Processes controlling channel stacking in turbiditic systems

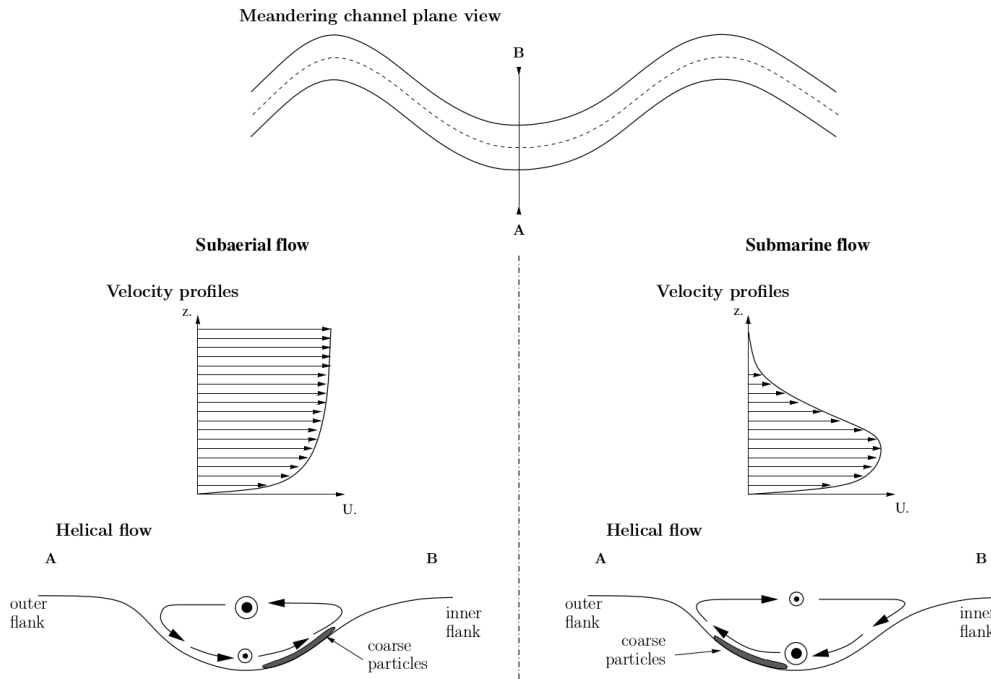


**Figure 1.9** Comparison between the vertical velocity profile in subaerial and in submarine flows (modified from Salles [2006]). The location of the maximum velocity along the profile can give rise to a different direction of rotation of the resulting helical flow.

experiments and numerical simulations have shown inward-directed secondary flows in submarine channels, i.e., with the same direction than in rivers [e.g., Imran et al., 2007, Islam et al., 2008, Imran et al., 2008]. But other laboratory experiments and numerical simulations show a reverse direction of rotation [e.g., Corney et al., 2006, Keevil et al., 2006, Corney et al., 2008]. The secondary flow then goes from the apex inner bank to the apex outer bank along the bend bottom (figure 1.9). It is directed outward, with the helix rising against the outer bank.

Such reversed secondary flow comes from the particular velocity profile of submarine flow. In subaerial flow, the difference of density between the current, i.e., the water in the river, and the surrounding fluid, i.e., the air, is such that the current does not mix with the surrounding fluid. Thus, the elevation of the current is limited and the maximum speed is at the top of the current. In submarine conditions, the difference of density between the current and the surrounding fluids is low. This enables a far higher current elevation, with

the current going far more easily outside the channel. It induces a different velocity profile, with a maximum velocity in the lower part of the current. The maximum velocity can be closer to the channel bottom, with lower velocities at the channel top. Then the direction of rotation is the opposite of that in subaerial flow.

Recently, some authors point out that the direction of rotation of the secondary flow within submarine channel may not be uniform [Abad et al., 2011, Giorgio Serchi et al., 2011, Janocko et al., 2013a]. Indeed, the direction of rotation depends on the velocity profile, and especially on the elevation of the maximum velocity of the current. If that elevation is close to the channel floor, the secondary flow is directed outward. If that elevation is close to the channel top, the secondary flow is directed inward. Thus, the channel morphology and the current characteristics both influence the rotation direction.

Under the action of the centrifugal, pressure and friction forces, the velocity profile of the current is non-uniform. Variations of the velocity profile appear vertically, but also transversally to the channel orientation (figure 1.10). The velocity is lower along the bank on which the helix is rising, and higher along the opposite bank. These velocity differences induce sediment deposition along the bank on which the helix is rising and erosion along the opposite bank. Such processes rule the channel evolution.

#### **1.4.2 Continuous channel migration**

Channel evolution often refers to channel migration. Erosion and deposition processes along the two banks of the channel influence the migration, which is called continuous or gradual migration [e.g., Abreu et al., 2003, Kolla, 2007]. While one bank is eroded, the other is stretched by sediment deposition, leading to channel migration.

The migration deeply relies on the sediment deposition through the location of the depocentres, also called bars or accretion packages, within the channel (figure 1.11) [e.g., Abreu et al., 2003, Janocko et al., 2013a]. Three main types of bars are observable:

- Point-bars, also called lateral accretion packages (LAP), develop along the inner bank of a bend.
- Transition bars develop between the inner- to outer- or outer- to inner-bank transition.
- Outer-bank bars (OBB) develop along the outer bank of a bend.

#### 1.4 Processes controlling channel stacking in turbiditic systems

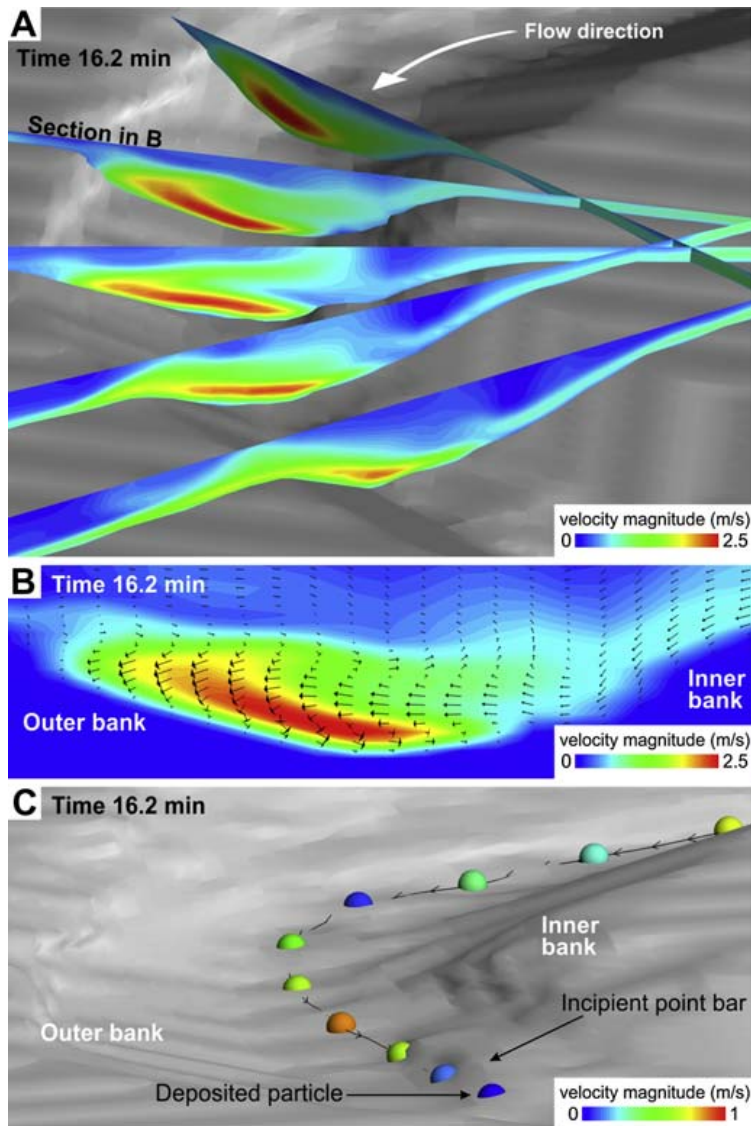


**Figure 1.10** Example of numerical flow simulation results within the bend of a submarine channel (modified from Janocko et al. [2013a]): A. Velocity field of the current along the channel. The maximum velocity concentrates along the outer bank of the bend. B. Profile along the bend with the velocity field and the associated helix. C. Simulation of the transport of a particle. This particle is deposited along the inner bank due to the lower velocities.

## 1 Channelized systems and connectivity: a review

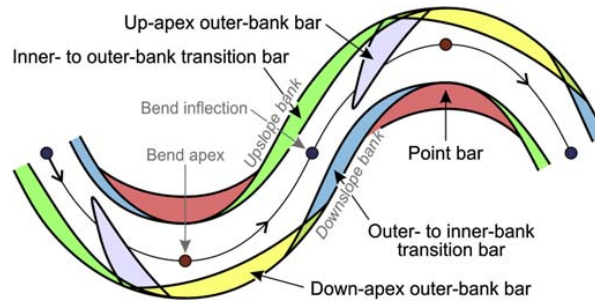


**Figure 1.11** Potential bars that can form within a sinuous turbiditic channel (from Janocko et al. [2013a]).

Bars often have a significant sand content, with more or less muddy interbeds that can perturb the connectivity [Abreu et al., 2003]. Inner overbanks cover them. All these depocentres are associated to different trends in the development of the channel. Their deposition relates on the flow characteristics.

The factors controlling the flow circulation within channels are still subject to controversy [e.g., Dorrell et al., 2013, Sumner et al., 2014]. According to Janocko et al. [2013a], four key factors control the channel development:

- The deviation of the conduit profile from the equilibrium profile: for a flow with given characteristics, it is possible to define an equilibrium profile along which the aggradation and the erosion are minimal. Thus, the channel-floor gradient tends to approximate the equilibrium profile. If so, the flow is in a slope-equilibrium state. If not, the flow tends to aggrade or to erode the channel.
- The deviation of the helix curvature from the channel curvature: the flow helix depends on the channel morphology. It also depends on the flow discharge, which impacts in particular the planform amplitude and wavelength of the helix. When these parameters evolve similarly to the amplitude and wavelength of the channel bends, the flow is “in phase” with the channel geometry. If the discharge changes abruptly, the consistency between the flow and the channel geometry can be lost. In such cases, the direction of secondary flow rotation in the bends can be reversed.
- The deviation of the current elevation from the channel elevation: the ratio of the flow elevation over the channel elevation determines the flow confinement. When this ratio is low, the flow is “under-sized” to “in-size” with the channel. When this ratio is high, the flow is “over-sized” compared to the channel. In such case, the current is poorly confined. The

## 1.4 Processes controlling channel stacking in turbiditic systems

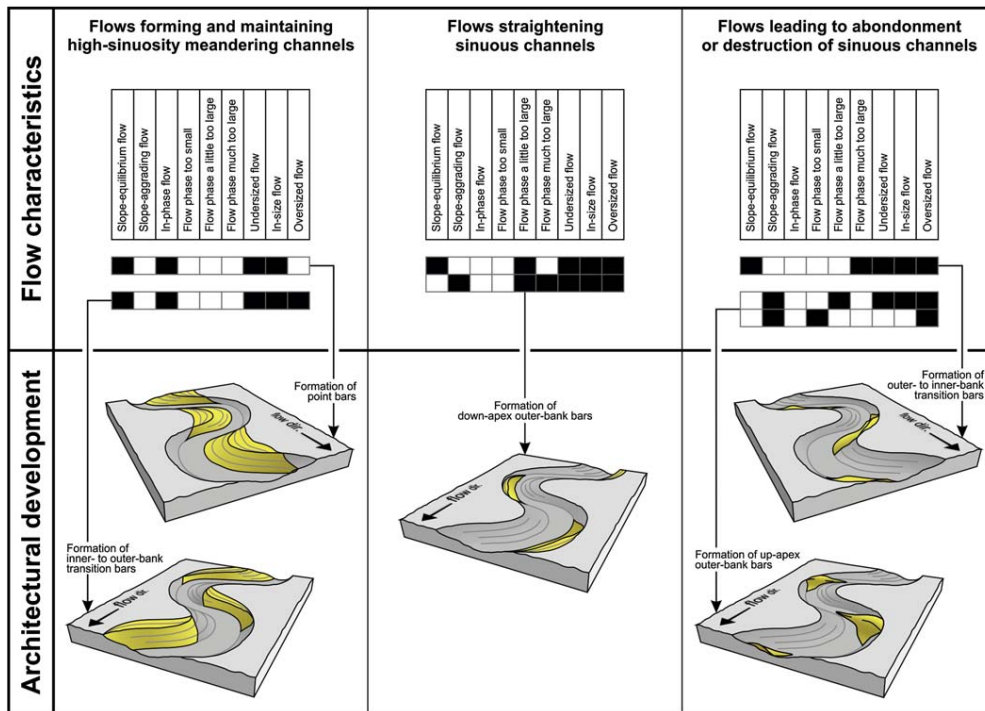


**Figure 1.12** Influence of the flow characteristics on the formation of bars (from Janocko et al. [2013a]). The black squares indicate the development condition of the related bars.

centrifugal force dominates and leads preferentially to the deposition of sediments at the outer bank. This classification concerns the flow entering the channel, independently of the downstream degree of flow overspill.

- The relationship between the flow power and the bank strength: it is fundamental for channel migration. If the flow power is too high and/or the bank strength too weak, the flow tends to leave the channel, either in an avulsion or in a braided pattern. If the flow power is too weak and/or the bank strength too high, the flow can not erode the bank and the channel do not migrate.

All these combined factors influence the sediment deposition and the erosion (figure 1.12). This gives rise to four major migration patterns:

- Lateral migration of the channel bends, also called swing, possibly associated to expansion, relies on point bar formation. The channel tends

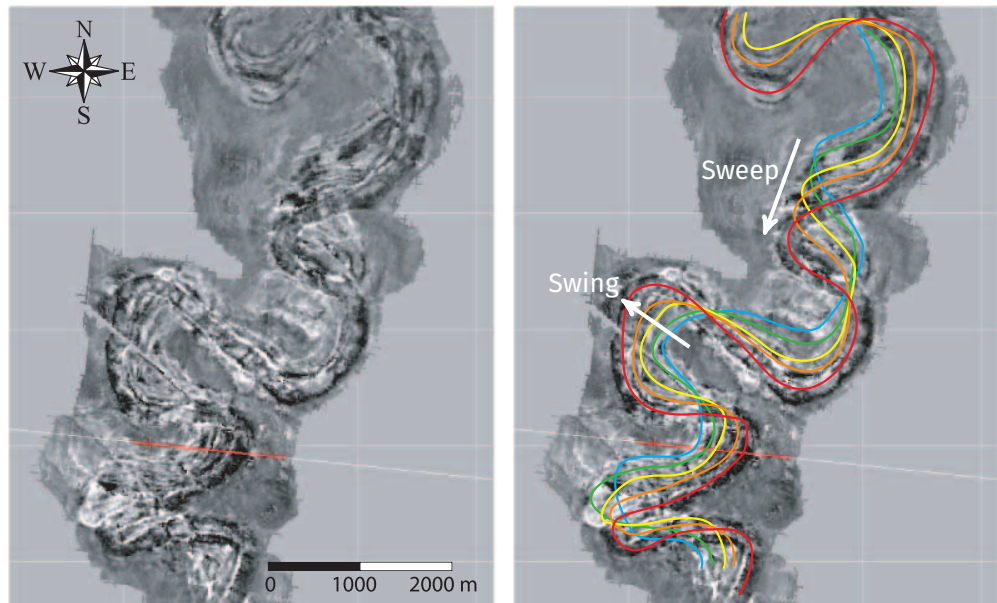


**Figure 1.13** Example of channel migration patterns in a turbiditic system in West Africa (modified from [Labourdette and Bez \[2010\]](#)).

to migrate perpendicularly to the flow direction [[Peakall et al., 2000](#), [Posamentier, 2003](#)] (figure 1.13), increasing the channel sinuosity.

- Downsystem migration or sweep relies on the development of inner- to outer-bank bars. The channel tends to migrate along the flow direction [[Peakall et al., 2000](#), [Posamentier, 2003](#)] (figure 1.13).
- Retro-migration relies on the development of outer-bank bars. The migration is perpendicular to the flow direction, but with a straightening of the channel [[Nakajima et al., 2009](#)].
- Aggradation corresponds to the vertical migration of the channel. It is highly significant in turbiditic systems, with channels aggrading over hundreds of meters [[Peakall et al., 2000](#)].

All these patterns can combine depending on the flow properties.

### 1.4.3 Discrete processes and avulsion

The flow deviation from the channel elevation and the bank strength are also influenced by the overbank deposits. These deposits increase the margin height

#### 1.4 Processes controlling channel stacking in turbiditic systems

and participate to the flow confinement. The development of the overbanks depends on the sand-content of the flow [e.g., [McHargue et al., 2011](#)], so on the sediment supply and on the energy of the flow. When the flow is sand-rich, the aggradation is low due to the low cohesion of the sand deposits. Thus, the overbanks are poorly developed, what significantly limits the confinement. When a new flow event begins, the previous channel has less influence on the development of the new channel, which can follow more or less different paths. The channel stacking is then disorganized.

When the flow is muddier, the cohesiveness of the deposits increases, and so does the aggradation. The overbanks are then more developed, with a better ability to confine the flow. The previous channel have then much more influence on the new one. The channel stacking is organized. The channel sinuosity also influences the stacking organization: when the sinuosity is high, the flow tends to have difficulty in following the channel geometry due to abrupt changes in the channel orientation. Thus, the new channel less likely follows the previous one, leading to a disorganized stacking.

The development of overbanks favors the flow confinement, leading to a less lateral or downsystem continuous migration. It is often associated with a significant aggradation. Less developed overbanks induces a disorganized stacking between the channels. This process relies on local changes of the channel path with the incision of a new channel. It does not relate on the deposition of bars combined with erosion, but still induces channel migration (figure 1.14). This process is called discrete, abrupt or punctuated migration [[Abreu et al., 2003](#), [Deptuck et al., 2003](#), [Kolla, 2007](#), [Maier et al., 2012](#)]. In continuous migrations, the bars form along the channel margins, which influence the bar organization. In discrete migration, the previous channel is filled and then eroded. This influences the spatial relationship between the heterogeneities of the channel fill. The resulting impact on the connectivity is then different than with a continuous migration process. Otherwise, the same migration patterns can be found with continuous and discrete migration [[Kolla, 2007](#)]. Continuous and discrete migrations do not seem exclusive, and both can occur within a single channel [[Abreu et al., 2003](#)].

Discrete migrations correspond to a local abandonment of the channel path, i.e., a local avulsion. The avulsion can be regional and leads to the complete abandonment of the channel path. Upstream to the avulsion location, the flow continues to circulate within the channel. Downstream to the avulsion location, a new channel initiates (figure 1.15). The process forms a new channel and possibly a new master channel. The conditions and development phases of an avulsion remain poorly known. As with discrete migration, the overbank confinement ability plays a significant role. Less developed overbanks



## 1 Channelized systems and connectivity: a review

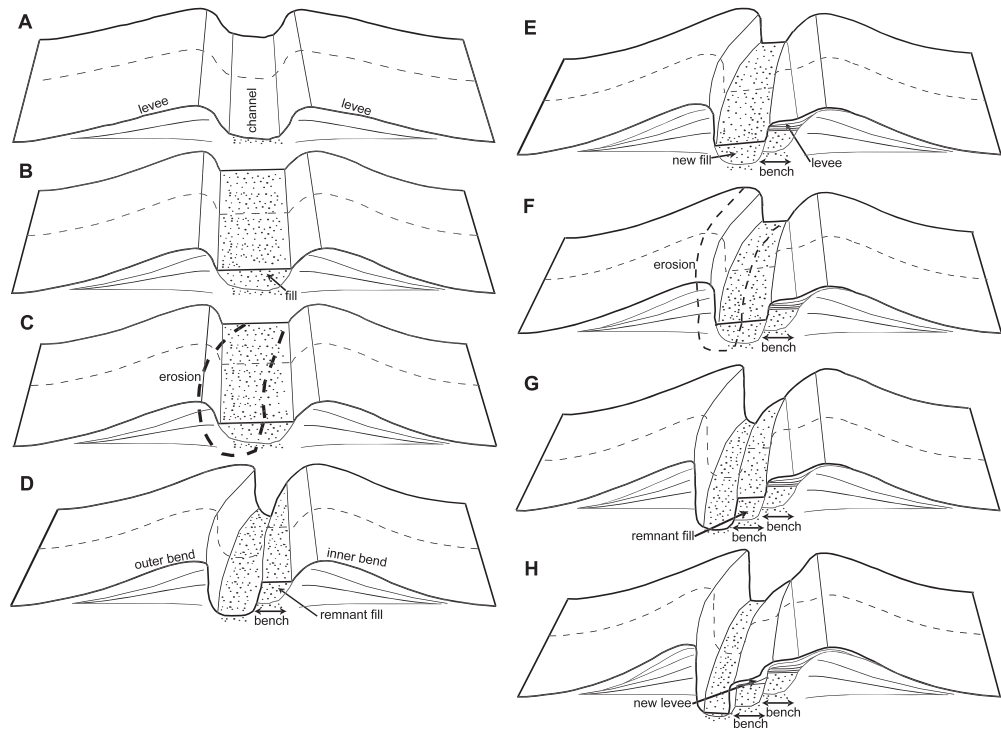


**Figure 1.14** Conceptual model of punctuated migration (from Maier et al. [2012]). A channel forms (A, D, G) and is partially filled (B, E). A new channel is incised, with a lateral and eventually a negative vertical shift (C; F). The remaining part of the previous channel has a terrace-shape on which overbanks develop (E; H).

favor avulsion. The progressive channel fill can also decrease the overbank confinement and favors avulsion [Armitage et al., 2012]. The avulsion initiation usually requires a levee breaching. Thus, the flow velocity plays a major role in the process [Kolla et al., 2007]. The channel sinuosity also influences the avulsion initiation: a higher sinuosity favors the possibility of an avulsion. Avulsion tends to occur most likely at the end of the canyon mouth, where the confinement is less significant [Armitage et al., 2012]. Once the overbank is breached, a lobe forms outside the channel. If the flow continues to go through the breach, it feeds the lobe, until the development of small channels and associated overbanks [Droz et al., 2007]. This last phase continues until one channel stabilizes and becomes the new channel.

Neck cutoffs are another kind of discrete process [Peakall et al., 2000, Posamentier, 2003]. Such structures come from the lateral migration. When a bend migrates with expansion, its extremities tend to get closer. This evolution

#### 1.4 Processes controlling channel stacking in turbiditic systems

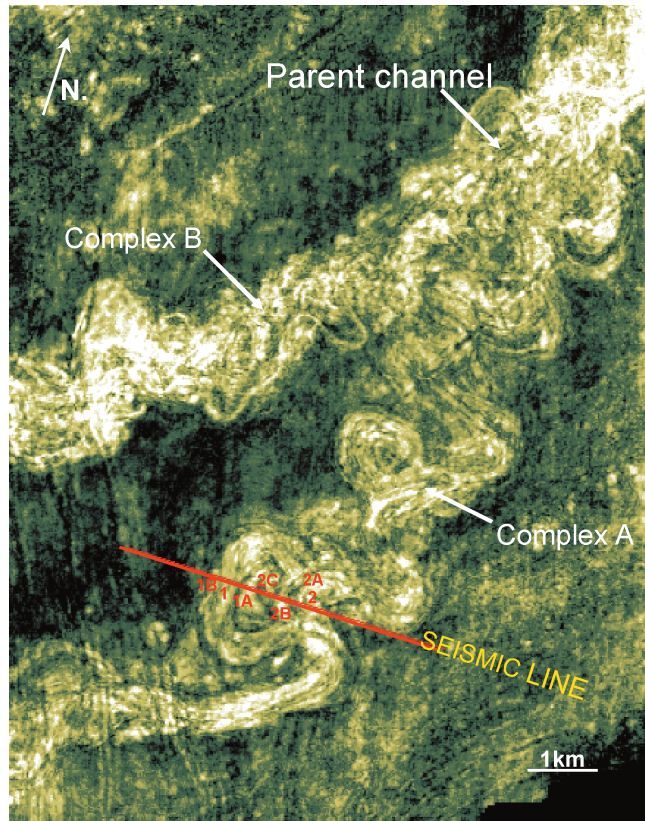


**Figure 1.15** Seismic amplitude map showing an avulsion, Angola, West Africa (from [Kolla et al. \[2001\]](#)). This system started with the migration of a channel from the parent channel to the complex A. Then an avulsion occurred, leading to the abandonment of the complex A. A new channel formed and has migrated to the current course, going from the parent channel to the complex B.

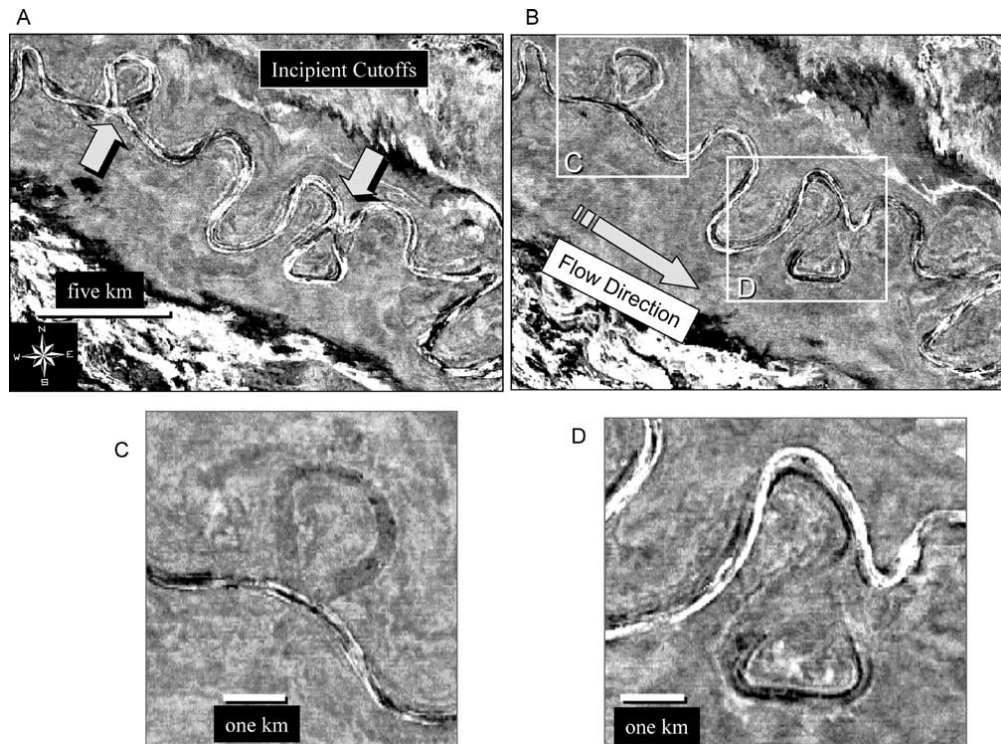


**Figure 1.16** Neck cutoffs observed on seismic slices along the Joshua channel, Gulf of Mexico (from [Posamentier \[2003\]](#))

comes with an increasing curvature along the bend. When the bend extremities are close enough, the high curvature makes it easier for the flow to bypass the bend. The bend is then abandoned and the flow circulates directly between the former bend extremities, along a straighter path (figure 1.16). Such process tend to limit the spatial expansion of the channels due to the migration. The abandoned bend is then filled by mud-rich sediments overspilling from the channel. This sedimentary body constitutes a potential flow barrier.

## 1.5 Stochastic simulation of channelized bodies and their connectivity

Turbiditic systems can form reservoirs either before or after the sediment consolidation. Before consolidation [e.g., [Ostermeier, 2001](#)], the system is close to its deposition state, thus potentially under thousands of meters of water. After consolidation [e.g., [Braathen et al., 2012](#)], the system is altered due to further

geological processes, such as diagenesis, folding or faulting. Thus, the uncertainties about the reservoir structure and connectivity are often significant when facing a potential reservoir. Stochastic geomodeling is then especially useful to limit the biases in the interpretation.

### 1.5.1 Methods to stochastically simulate channelized bodies

Stochastic simulation methods can be divided following several criteria. A classical criterion is the support of the simulation results, i.e., a property within a grid or vectorial objects. In both cases, the methods simulate sedimentary bodies, such as channels, overbanks or lobes.

#### Cell-based methods

Cell-based methods regroup all the methods that simulate realizations by giving a value to each cell of a grid. The grid is a discretized representation of the domain of interest. The value gotten by each grid cell can be a sedimentary body type, for instance channel or levee (figure 1.17). These methods are mostly based on geostatistics. Their purpose is to reproduce in the whole grid the statistics obtained from a prior model. The model comes from the data or from a conceptual model. The data are most often punctual well data, interpreted in terms of sedimentary bodies. The conceptual model is a complete representation of the sedimentary objects of interest. Cell-based methods reproduce directly the result of the geological processes. Thus, they can also be qualified as structure-imitating methods.

Sequential indicator simulation (SIS) [Deutsch and Journel, 1992] is a well-known method for the simulation of discrete properties. The prior model comes from the data. Two elements compose this prior:

- The sedimentary object proportions, which indicate the importance of each sedimentary body.
- The variogram, which measures the correlation between two points depending on the distance between these points. For instance a channel leads to a high correlation along the channel direction and a lower correlation along the transversal direction (figure 1.17). The variogram captures the elongated shape of channel.

SIS relies on a sequential simulation process, i.e., the previously simulated values influence the next simulation steps, performed following a random path. At each simulation step, a value is simulated on the basis of a kriging system using the variogram. Such process ensures the conditioning to punctual data, as

## 1 Channelized systems and connectivity: a review

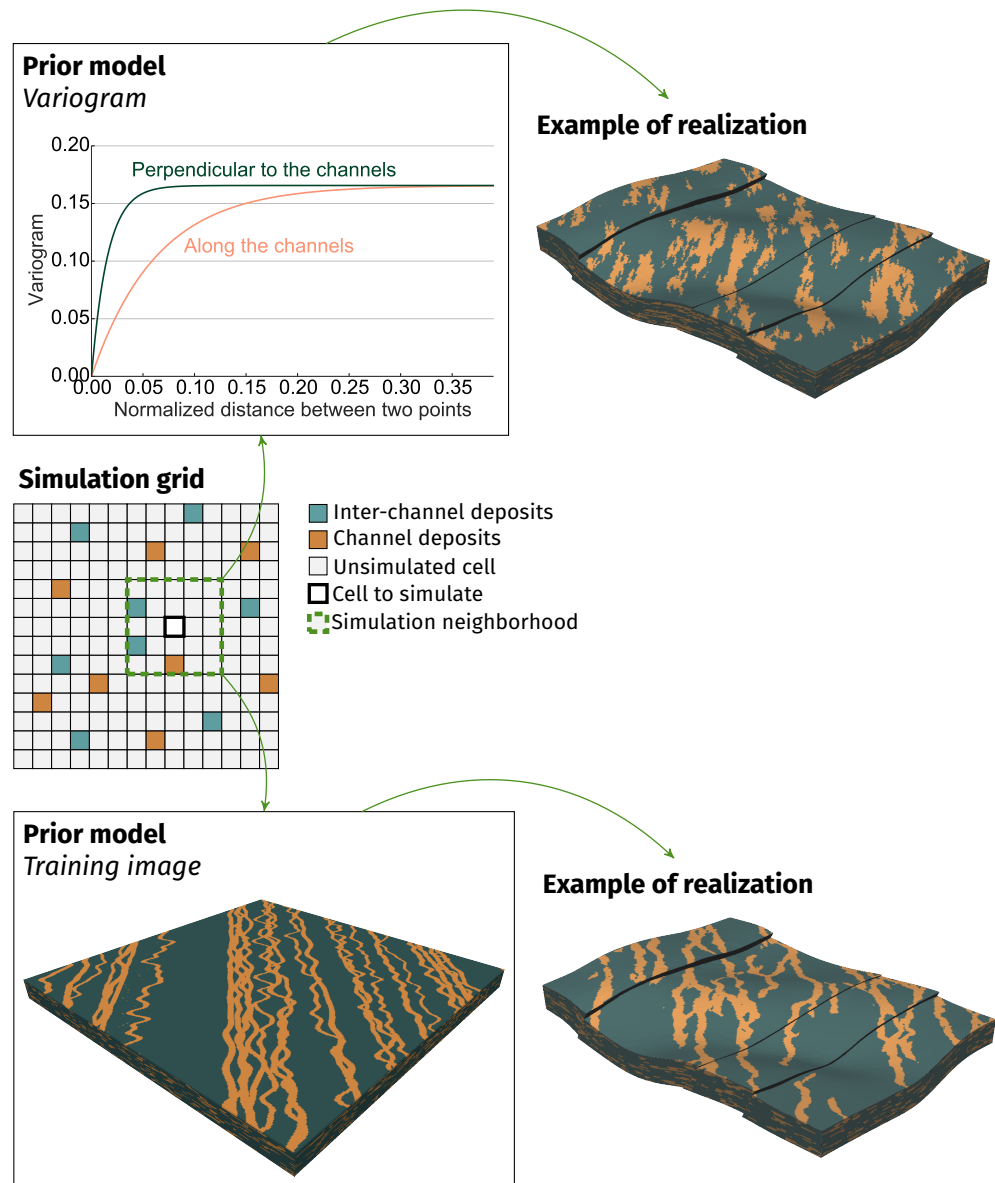


**Figure 1.17** Principle of cell-based methods, with the example of sequential indicator simulation using a variogram [Deutsch and Journel, 1992] and multiple-point simulation, here the method IMPALA [Straubhaar et al., 2011], using a training image. The simulated values come from a prior model based on the known cell configuration in the neighborhood of the cell to simulate.

the data are attributed to cells at the beginning of the process. The plurigaussian simulation (PGS) [Galli et al., 1994] introduces a facies transition map to the prior. This map governs the relationships between the different sedimentary bodies, for instance if two bodies are in contact or not.

With multiple-point simulations (MPS), the prior no longer comes from the data. The principle is to borrow the higher-order statistics from a conceptual representation of the sedimentary objects to simulate [Guardiano and Srivastava, 1993]. This representation is called a training image and is the prior model (figure 1.17). The simulation process remains sequential. The purpose is to look at the configuration of cells with a known value around the cell to simulate. The training image is scanned to find the cells with the same neighboring configuration. This gives the probabilities of the possible discrete values considering the configuration of the neighborhood. The main issue with the original method is its computation time, as the training image is completely scanned for each cell to simulate. Two strategies were developed to improve the computation time:

- Scanning the training image once and for all before the simulation process [Strebelle, 2002, Straubhaar et al., 2011]. At the end of the scan, a data structure storage, either a tree or lists, conserves the probabilities of the possible discrete values considering the configuration of the neighborhood.
- Scanning the training image at each simulation step to compute a distance between neighborhood configurations [Mariethoz et al., 2010]. A distance threshold determines when the configuration with the lowest distance value is reached. The central cell of this configuration provides the simulated value. Thus, the scanning the whole training image is not always necessary.

### Object-based methods

Object-based methods rely on the definition of geometric forms representing the sedimentary bodies of interest (figure 1.18). Each geometric form comes with its set of parameters. For instance, a radius and a thickness are enough to define a puck. It is a vectorial approach to the modeling of sedimentary objects. Thus, object-based methods do not necessarily require a grid in the simulation process, contrary to cell-based methods.

The classical approach for object-based modeling starts with the definition of a domain of interest. The objects are then randomly placed within the domain. The object parameters are drawn from statistical laws given in input.

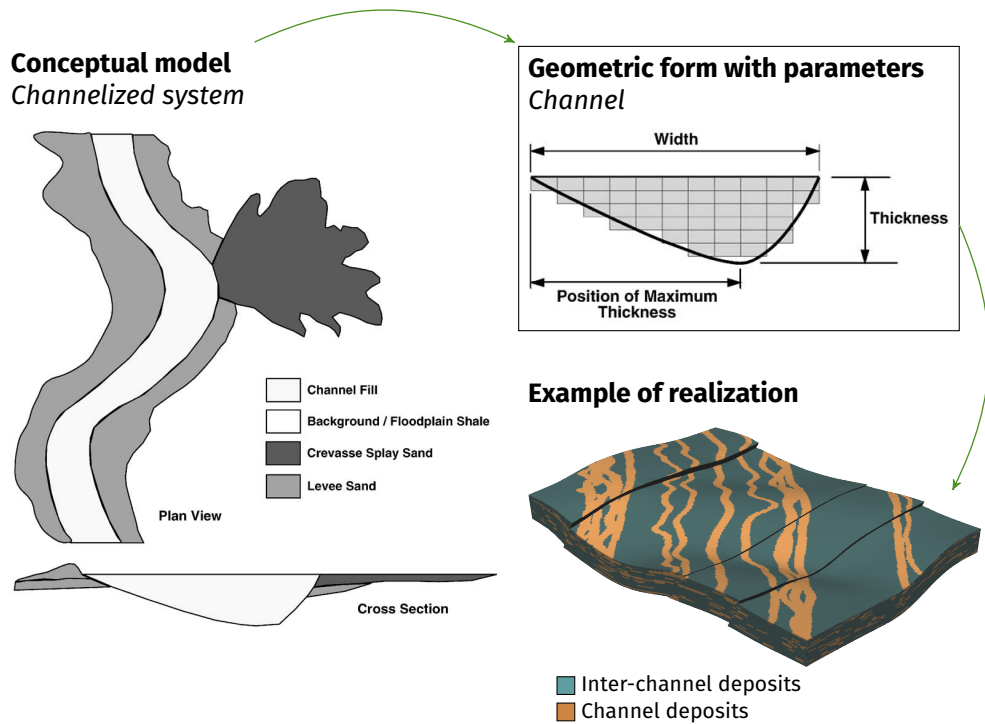


**Figure 1.18** Principle of object-based methods, with the example of FLUVSIM for channel object simulation (modified from Deutsch and Tran [2002]).

The simulation of channels was at first introduced for a fluvial context [Deutsch and Wang, 1996]. But the similar morphologies between fluvial and turbiditic channels [e.g., Kolla, 2007] explain the use of the same object geometry in turbiditic context. The classical parameterization of a channel relies on the channel centerline, also called backbone [e.g., Wietzerbin, 1994, Viseur, 2001, Deutsch and Tran, 2002]. The centerline defines the channel orientation and sinuosity. Then three parameters build the channel section (figure 1.18):

- The width at the top of the channel.
- The maximal channel thickness.
- The position of the channel maximal thickness along the section.

Other geometric definitions exist for levees, lobes and point bars [e.g., Viseur, 2001, Deutsch and Tran, 2002, Hassanpour et al., 2013, Ruiu et al., 2015b]. Some methods even rely on the simulation of point bars rather than on the simulation of a sinuous channel object [Hassanpour et al., 2013].

### **1.5.2 Controlling the connectivity in stochastic simulations of channelized bodies**

The connectivity of the turbiditic deposits relies on the representation of channels, with their stacking and their fill. Possible strategies to integrate the connectivity within stochastic simulations are (i) better representing the channels and their stacking and (ii) conditioning to as much data as possible. In practice, this representation is in conflict with data conditioning in both cell-based and object-based methods. The data, especially well data, are yet the only information about the reservoir to have a low uncertainty. Thus their conditioning is essential.

#### **Reproducing the channelized bodies while conditioning to the sedimentary data**

Sedimentary data inform about the location of the channelized bodies. They come from punctual interpreted well data or from channel parts directly interpreted on seismic data if the resolution is high enough. These data are called hard data due to their low uncertainty.

Cell-based methods ensure hard data conditioning by filling the grid one cell at a time. However, they have difficulty in reproducing sedimentary objects. This aspect is well known with SIS. The variogram looks at the two-points statistics. So it ignores all the higher-order statistics and miss some information [Journal and Zhang, 2006]. Despite a better control on the object relationships, PGS faces the same issue. Higher-order statistics are necessary to build more consistent models. But they are difficult, if not impossible, to infer from the data. This explains the development of MPS.

MPS better reproduce sedimentary objects than SIS or PGS. Nevertheless, highly continuous structures like channels or small-scale and thin features like margin drapes are still far from being precisely reproduced. The preservation of their continuity is a major source of concern. It has given rise to many improvements [e.g., Liu and Journel, 2004, Strebelle and Remy, 2005] and many new methods, such as simulating all the cells within a neighborhood at once from the training image instead of a single cell [e.g., Arpat and Caers, 2004, Chatterjee and Dimitrakopoulos, 2012, Tahmasebi et al., 2012]. But this introduces conditioning difficulties.

On the other hand, the reproduction of sedimentary bodies by object-based simulations is far more satisfying from a geometrical point of view. The only requirement is to have a sedimentary body sufficiently known and described to define a parameterization. Another interesting aspect is the possibility to build



curvilinear grids within the objects [e.g., [Deutsch and Wang, 1996](#), [Shtuka et al., 1996](#), [Ruiu et al., 2015a](#)]. This facilitates the modeling of the channel fill and its heterogeneities, such as basal lags or margin drapes.

However, data conditioning of predefined objects is uneasy. The most straightforward approach is the rejection sampling: a simulated channel is kept if it fits some data [e.g., [Deutsch and Wang, 1996](#)]. Such method is highly inefficient when the number of data increases or with seismic-interpreted bodies. Other methods simulate a channel centerline conditioned to the data with a sequential Gaussian simulation [e.g., [Shmaryan and Deutsch, 1999](#)]. The simulation of high-sinuosity channels is not directly possible with such approach. [Oliver \[2002\]](#) proposes an iterative process to fit a whole channel centerline simulated with any method to well data. Other methods have a more local approach, either by deforming the channel [e.g., [Viseur, 2001](#)] or locally re-simulating the channel [[Mariethoz et al., 2014](#)]. However, all these methods tackle the well data conditioning and not the conditioning of seismic-derived data such as sand probability cube. MPS can also be considered as a way to condition object-based methods. This is at the cost of the sedimentary object reproduction, so at the cost of their connectivity.

### **Reproducing the relationships between the channelized bodies**

Simulating the relationship between sedimentary objects, in particular the channel stacking, is rather difficult with cell-based methods. Again, MPS are better able to handle the channel stacking than SIS or even PGS thanks to the training image. Similarly to the channelized body morphology, the stacking is yet poorly reproduced. Object-based methods *sensu stricto* randomly place the objects. While the placement of the previous objects can influence that of a new object, the resulting organization is far from the precise channel organization due to migration and avulsion.

Thus, event-based methods, also called pseudo-genetic or pseudo-process methods, manage to introduce genetic concepts in object-based methods [e.g., [Pyrz et al., 2012](#)]. They intend to be process-imitating and not just structure-imitating. Pseudo-process-based methods were introduced for fluvial modeling. They rely on the work done on 2D physical simulation of river migration. 3D simulation of the flow circulating in a channel is highly time and resource consuming. 2D methods rely on a depth-averaged simulation and are more efficient. They link the migration to the asymmetry in the flow field induced by the channel curvature and responsible for the erosion/deposition processes leading to the migration [[Ikeda et al., 1981](#)]. The simulation starts from an initial centerline which migrates during the process. These methods are used

### 1.5 Stochastic simulation of channelized bodies and their connectivity

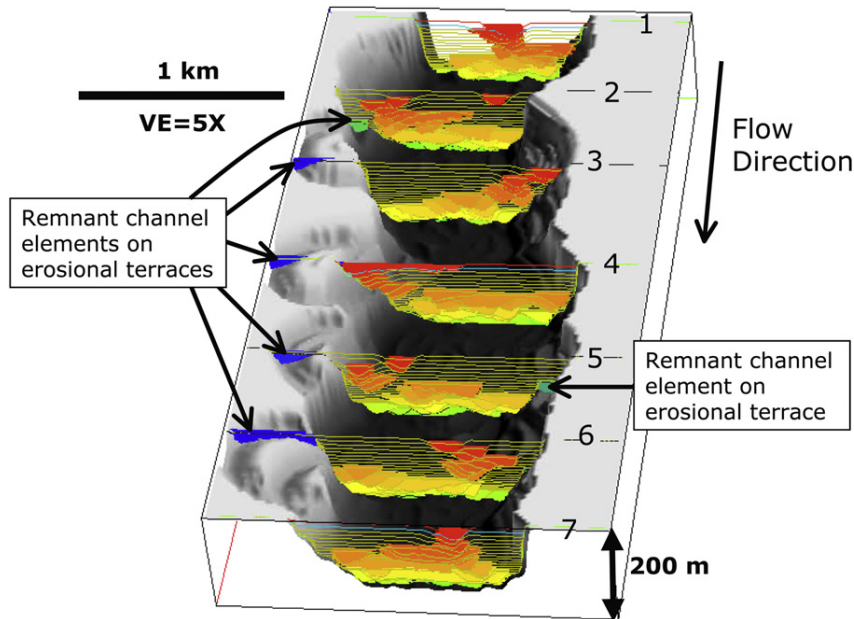


**Figure 1.19** Example of realization simulated with a pseudo-process method (from [McHargue et al. \[2011\]](#)). The channels at the bottom of the master channel have a disorganized stacking, while the channel at the top have an organized stacking.

in a stochastic simulation process by [Lopez \[2003\]](#) and [Pyrzcz et al. \[2009\]](#). The channel parameterization remains the same as in object-based methods, with a centerline, a width, a thickness and a position of the thickness maximum. Each channel is related to the previous one through the centerline evolution.

Data conditioning is more problematic as the consistency between the channels has to be ensured. However, these methods significantly improve the possibility to simulate realistic-looking channel complexes (figure 1.19). They are primary designed for a fluvial context, but [Imran et al. \[1999\]](#) adapted the 2D genetic simulation of migration to turbiditic channels. [Pyrzcz et al. \[2009\]](#) method was also directly applied to illustrate the development of turbiditic channels by [McHargue et al. \[2011\]](#). However, the physical processes behind submarine channels are controversial [e.g., [Corney et al., 2006](#), [Imran et al., 2008](#), [Corney et al., 2008](#)]. Lately, [Dorrell et al. \[2013\]](#) argue that two-dimensional physical models are not accurate enough to capture the full three-dimensional structure of the flow field. This influences the possible migration patterns, so the channel stacking and the connectivity. Three-dimensional simulations are then required, but their validity remains controversial [e.g., [Sumner et al., 2014](#)] and they are computationally demanding. Their utility is then doubtful

in a stochastic framework.

### **Conditioning to connectivity data**

Seismic data are a first source of information about the connectivity. If the resolution is high enough, some channels can be directly interpreted and provide hard data. The channel stacking is then often observable [e.g., [Mayall et al., 2006](#), [Deptuck et al., 2007](#)]. However, the channel fill is usually under the seismic resolution [e.g., [Labourdette et al., 2006](#), [Gainski et al., 2010](#)]. If the seismic resolution is too low, some information can be extracted to condition the simulation, such as a facies proportion or probability cube [e.g., [Strebelle et al., 2003](#)]. Thanks to their spatial coverage, such data can help to constraint the simulation at a large scale. They are called soft data.

The wells give a more precise information about the location of the reservoir compartments and the flow barriers. However, this information is only punctual. The wells can only give large-scale connectivity data in terms of flow circulation. Tracer tests help to determine if two wells are connected. A tracer is introduced in an injector well. If the tracer is recovered on a producer well, the two wells are connected. Other information, such as the rate of recovery or the travel time, gives a first insight on the circulation path between the two wells. Production data also help to better characterize the flow behavior within the reservoir. Putting together these deductions with other data such as seismic data facilitates the understanding of the reservoir dynamic.

These data can also be introduced within the realizations. The usual approach consists in finding the model parameters such as the reservoir behavior of the resulting models matches that observed on the wells. This process, called history matching, is done through an inverse problem [e.g., [Aanonsen et al., 2009](#), [Oliver and Chen, 2010](#)]. In a forward process, a model is simulated with given parameter values to predict the flow behavior. In an inverse process, the flow behavior observed on the wells is used to determine the possible model parameters. History matching relies on an optimization scheme to find the model parameters [[Oliver and Chen, 2010](#)], and is often computationally demanding.

Only few methods have been developed to constrain directly the realizations during their simulation. The principle consists in taking into account if two or several wells are connected, i.e., if a path of channel deposits link one well to the other(s). The productivity data themselves are not taken into account. [Allard and Group \[1993\]](#) constrain a cell-based simulation to both the spatial structure of the prior and connectivity data. This approach simulates an initial field honoring the connectivity data and applies a Gibbs sampler to reproduce the spatial structure. [Renard et al. \[2011\]](#) constrain MPS realizations by extracting

a continuous path between the wells from the training image and by using it as conditioning data. Thus, it can be used with all the MPS methods. This approach enables to condition object-based methods to connectivity data, by using the object-based realizations as training images for the MPS.

## 1.6 Conclusions

The interest for channelized system is due to the ability of their deposits to store fluids. From this point of view the connectivity between the reservoir facies, i.e., the sand-rich deposits, is fundamental. Turbiditic systems transport large quantities of sediments from the continental margin to the oceanic basin. These sediments circulate within channels through turbidity currents. The channels have nested structures, with channel evolving within master channels. Considering channels, the main features influencing the connectivity are their fill and their stacking. Channel fill is often heterogeneous, with mud-rich flow barriers. The channel stacking comes from channel migration and avulsion. These processes give rise to various genetic and spatial relationships between the channels, with a significant impact on the connectivity.

Such stacking is difficult to take into account in stochastic simulations. This is especially due to the difficulty to combine advanced geological representations with data conditioning. A better representation of the channel stacking is fundamental to ensure a correct connectivity estimation. It must be done jointly to a better integration of the available data, including the connectivity data. The study of the connectivity through channel heterogeneities and the related modeling aspects are here presented through turbiditic systems. Similar principles remains valid to reservoir/aquifer from fluvial systems.



## Chapter 2

# Analyzing stochastic simulations of sedimentary bodies using connected components

**Abstract** Many stochastic simulation methods are available to model sedimentary bodies. But realizations obtained with different methods and parameter values seem to differ visually. A major concern is the impact of those differences on the connectivity and then on fluid flow. The impartial analysis of the differences between realizations is so of prime interest. Here we propose to emphasize that analysis on the connectivity. The process relates on indicators computed from the connected components of the realizations. Some describe their spatial distribution, others their global shape or their topology. To analyze the realization differences, we compute dissimilarities between the images from the indicators. Heat maps and multidimensional scaling then facilitate the dissimilarity analysis. The application of this method to a synthetic case leads to some practical considerations. The multidimensional scaling is a powerful visualization tool, but it induces dissimilarity misrepresentations. The heat map displays the real dissimilarities and is more appropriate for a detailed analysis. The comparison with a multiple-point histogram method shows differences in the realization ranking. In any case, the indicators highlight differences between the realizations, whose connectivity actually varies. Further studying the indicator behavior could be beneficial to a better analysis of the connectivity within stochastic simulations.

## 2.1 Introduction

Connectivity is a key aspect of a geological study for its influence on fluid circulations. From a reservoir engineering perspective, it especially relates to sedimentary bodies with high and low permeabilities. It also relates to the spatial organization of these bodies and the resulting inter-connections. An incorrect body connection can bias the results of the flow simulations [Journal and Alabert, 1990, Gómez-Hernández and Wen, 1998, Labourdette et al., 2006]. Reproducing these sedimentary bodies together with their relations is so of prime importance [e.g., Deutsch and Hewett, 1996, King and Mark, 1999].

Stochastic simulations aim at generating possible representations of the sedimentary objects with respect to the available data. Several methods exist, with an usual separation in two main categories:

- Pixel-based methods simulate one cell at a time, based on a prior model describing the objects of interest. In sequential indicator simulation (SIS) [Deutsch and Journel, 1992], the prior is a variogram built upon the two-point statistics of the data. Hard data conditioning with such method is easy. But the simulated bodies do not look like geological objects. This is especially true for objects with curvilinear geometries such as channels, whose continuity is badly preserved. The plurigaussian simulation (PGS) [Galli et al., 1994] limits this difficulty by accounting for the facies relationships. Multiple-point simulations (MPS) go a step further by borrowing multiple-point statistics not from the data but from an external representation of the expected geology, the training image (TI) [Guardiano and Srivastava, 1993].
- Object-based methods rely on the definition of geometric forms and their associated parameters. Each form represents a particular sedimentary body [e.g., Viseur, 2001, Deutsch and Tran, 2002]. The objects are then randomly placed in the domain of interest with parameters drawn in statistical laws. More recent approaches introduce some genetic aspects to improve the object organization [e.g., Lopez, 2003, Pyrcz et al., 2009]. They provide more geologically consistent results. For instance channel continuity and relationships are better preserved than with pixel-based methods. But this is at the detriment of the ease of parametrization. And all those approaches have difficulty to condition the objects to data.

All those methods have advantages and drawbacks. This will influence the choice of a method and its parameters when dealing with a case study.

However few work aims at systematically analyzing the quality of a set of realizations. The quality control often consists in comparing the histogram and

variogram of several realizations with those of the data, or of the training image if any [e.g., [Strebelle, 2002](#), [Mariethoz et al., 2010](#), [Tahmasebi et al., 2012](#)]. It is completed by a visual evaluation of the global structures, which is subjective and limited to a few realizations, often in two-dimensions [e.g., [Tahmasebi et al., 2012](#), [Yin et al., 2009](#)].

Some authors provide some objective measures of the realization quality. [Boisvert et al. \[2010\]](#) and [Tan et al. \[2014\]](#) propose to analyze the multiple-point histogram. [De Iaco and Maggio \[2011\]](#) and [De Iaco \[2013\]](#) also explore the multiple-point statistics with high-order cumulants. Other authors focus on the further use of the realizations, often related to fluid circulations, and not on the imposed prior model. For instance [Meerschman et al. \[2012\]](#) use the connectivity function with the histogram and variogram to analyze the simulation parameter impact for the Direct Sampling MPS method [[Mariethoz et al., 2010](#)]. [Deutsch \[1998\]](#) uses directly the connected components determined from lithofacies, porosity and permeability models. He computes indicators such as the number of connected components or their sizes to rank the realizations. [De Iaco and Maggio \[2011\]](#) and [De Iaco \[2013\]](#) also use some statistics related to the connected components, such as their number or their mean surface and volume. These indicators on connected components have the advantage of being easy to compute and figure out. [Comunian et al. \[2012\]](#) rely on some of the previous indicators to analyze the quality of three-dimensional structures simulated from two-dimensional training-images. They also consider the equivalent hydraulic conductivity tensor as an indicator. However, this requires to have an idea of the hydraulic conductivities for the simulated facies.

In parallel, an important question is how to visualize the results. To compare the realizations authors often look at each quality indicator one by one. [Scheidt and Caers \[2009\]](#) and [Tan et al. \[2014\]](#) both rely on the computation of dissimilarity values between the realizations. Those dissimilarities are computed based on the quality indicators measured on each realization. They are then visualized based on a MultiDimensional Scaling (MDS) [e.g., [Torgerson, 1952](#), [Shepard, 1962a,b](#)]. MDS represents the realizations as points, with the distance between the points as close as possible to the dissimilarities. The global analysis of the realization dissimilarities is so easier.

The present work aims at analyzing and discussing a set of statistical indicators to quantify the quality of stochastic simulations. This method performs on categorical three-dimensional images representing the facies constituting the sedimentary bodies of interest. It can be applied on realizations from one or several stochastic simulation methods and/or parameter values. Conceptual images representing ideally the bodies to simulate can also be considered. Here the simulation quality is seen through the reproduction of the sedimen-



tary body connectivity. The chosen set of indicators (section 2.2) relies on quantitative measurements on connected components and their skeletons. The indicators are used in dissimilarity computations to analyze the quality more directly (section 2.3). Several realizations obtained with different simulation methods (section 2.4.1) are then used to test the methodology (section 2.4). A comparison is made with the multiple-point histogram used as indicator.

### 2.2 Indicators to measure simulation quality

The indicators studied in this paper are based on the notion of connected components. Thus, they focus on the connectivity inside the three-dimensional image of the sedimentary bodies of interest. They are all quite simple and each one only gives a partial information about the connectivity and its structure. But their combination provides a more detailed characterization.

The indicators work with both regular and irregular structured grids. Thus the indicators based on volumes or surfaces are rather computed using number of cells and number of faces. This avoids biases related to different grid geometries, which give different indicator values even if the objects are the same when transferred in the same grid. The idea is to compare the components in the parametric space of the grids [e.g., [Shtuka et al., 1996](#)], as simulation methods often model geological objects in that space. The following sections describe the various indicators retained for this study. They can be separated in two groups: the first one contains global indicators related to the set of all connected components of a given facies, the second one contains indicators characterizing the connected components individually.

#### 2.2.1 Basic element: the connected component

A simulation of geological objects is often done into a grid composed of cells. It is so a discretized representation of the sedimentary bodies of interest. Those cells are linked one to another by their faces, their edges and/or their corners [[Renard et al., 2011](#)]. In the case of the structured grids used for this work, one cell has three possible neighborhoods (figure 2.1):

1. One neighborhood composed of six face-connected cells.
2. One neighborhood composed of eighteen face- and edge-connected cells.
3. One neighborhood composed of twenty-six face-, edge- and corner-connected cells.

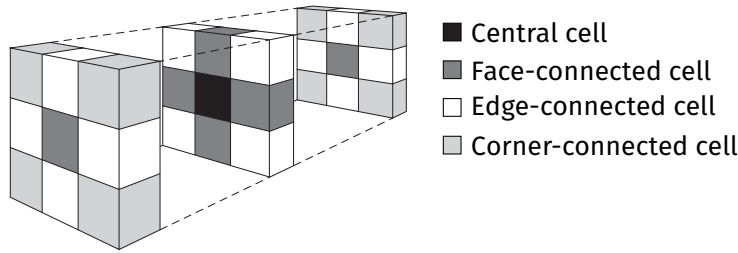


**Figure 2.1** Possible neighborhoods for a given central cell in a regular grid (modified from Deutsch [1998]).

The connected components are defined using those neighborhoods: two cells belonging to the same facies are connected if a path of neighboring cells remaining within the same facies exists (figure 2.2).

This definition leads to a distinction between the sedimentary objects, such as a channel or a crevasse splay, and the connected components. Indeed, the sedimentary objects often tend to cross each others, giving one connected body where there is in fact several sedimentary bodies (figure 2.2). The range of possible shapes is larger for the connected components than for the individual object. This aspect complicates the comparison between images. But determining the connected components is far easier than trying to retrieve the geological objects. This is also close to the functioning of pixel-based methods, which do not try to reproduce geological objects but groups of cells, and therefore connected components.

### 2.2.2 Global analysis through all the components of a given facies

The global analysis gathers the indicators that do not characterize a particular connected component but an ensemble of connected components. They provide one value per facies.

#### Facies proportion

The facies proportion is of major importance in reservoir modeling considering its influence on porosity and permeability simulation. The proportion  $p$  of a facies  $f$  is defined as:

$$p_f = \frac{n_f}{n_t} \quad (2.1)$$

with  $n_f$  the number of cells of facies  $f$  and  $n_t$  the total number of cells.

## 2 Analyzing stochastic simulations of sedimentary bodies

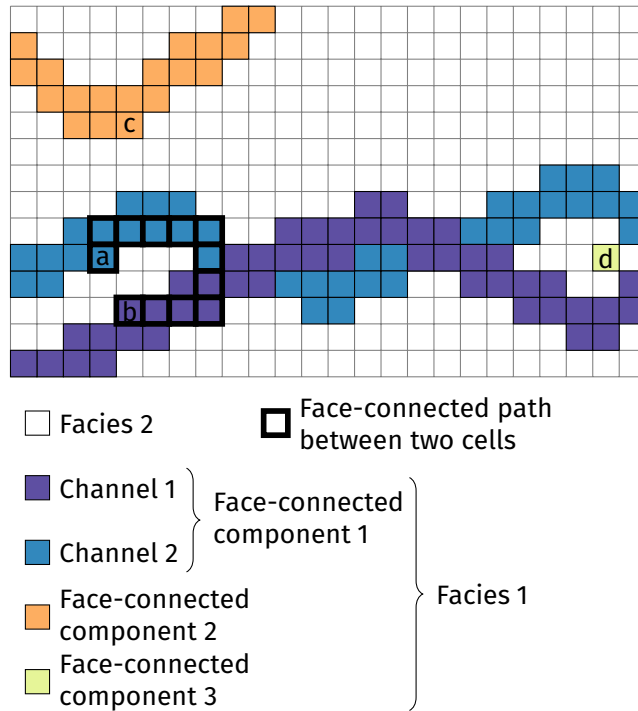


**Figure 2.2** Connected components of a given facies in a two-dimensional structured grid. The cells *a* and *b* are connected and belong to the same connected body. There is no possible connected path between those cells and *c*, which belongs to another connected body. The cell *d* constitutes a third connected body in the case of a face-connected neighborhood. In the case of an edge- or corner-connected neighborhood, *d* belongs to the connected body 1.

### Facies adjacency proportion

The adjacency proportion between the facies quantifies the spatial relationships between those facies. The proportion  $p^a$  of a facies  $f$  adjacent to a facies  $j$  is defined as:

$$p_{f,j}^a = \frac{n_{f,j}}{n_{f,t}} \quad (2.2)$$

with  $n_{f,j}$  the number of cells of facies  $f$  adjacent to the facies  $j$  and  $n_{f,t}$  the total number of cells of  $f$  adjacent to a facies different from  $f$ .

### Facies connection probability

The connection probability  $\Gamma$  quantifies the global connectivity of a given facies  $f$ . It is calculated as the proportion of pairs of connected cells among all the pairs of cells of the considered facies [Renard et al., 2011]:

$$\Gamma_f = \frac{1}{n_f^2} \sum_{i=1}^{N_f} (n_f^i)^2 \quad (2.3)$$

with  $n_f$  the total number of cells of facies  $f$ ,  $N_f$  the number of connected components of the facies  $f$  and  $n_f^i$  the number of cells of the connected component  $i$  associated to facies  $f$ .

### Connected component density

The density  $\epsilon$  of connected components for a facies  $f$  expresses the number of components per image cells:

$$\epsilon_f = \frac{N_f}{n_t} \quad (2.4)$$

with  $N_f$  the number of connected components of the facies  $f$  and  $n_t$  the total number of cells.

### Unit connected component proportion

The unit connected component proportion quantifies the number of connected components constituted by only one cell. The creation of such bodies may correspond to some erroneous and unwanted small scale noise. In that case, it is better to avoid them for the shape indicator computation (see section 2.2.3). The proportion  $p^u$  of unit volume connected components of a facies  $f$  is:

$$p_f^u = \frac{N_f^u}{N_f} \quad (2.5)$$

with  $N_f^u$  the number of unit volume connected components of the facies  $f$  and  $N_f$  the number of connected components for the same facies.

### Traversing connected component proportion

Connected components can have various behaviors against the grid: they can be in the middle of the grid without contact with a border (figure 2.2, connected component 3), along one border, along two adjacent borders (figure

2.2, connected component 2) or traversing the grid completely from one border to the opposite border (figure 2.2, connected component 1). These last components having a main impact on the flow, their reproduction is of prime importance. The proportion  $p^c$  of traversing connected components of facies  $f$  is defined as the proportion of connected components that connect one border to the opposite one:

$$p_f^c = \frac{N_f^c}{N_f - N_f^u} \quad (2.6)$$

with  $N_f^c$  the number of traversing components for the facies  $f$ ,  $N_f$  the total number of components for the facies  $f$  and  $N_f^u$  the number of unit components for the facies  $f$ .

### 2.2.3 Detailed analysis of the connected components

The following indicators are proposed to characterize any particular connected component. The values for different components are gathered to obtain one value per facies and make the indicator comparison easier.

#### Shape indicators

Global measures such as facies proportions are not sufficient to characterize precisely the impact of the related facies on the flow [e.g., Western et al., 2001, Mariethoz, 2009]. In particular, Oriani and Renard [2014] showed the influence of the connected component geometry – i.e., their shape – on the equivalent hydraulic conductivity, and therefore on the flow behavior. The following shape indicators characterize the connected component shape through simple surface and volumetric measures. They all give one value per component. The arithmetic mean of those values provides a value of the indicator for a given facies.

**Number of connected component cells** The number of cells  $n_f^g$  within a connected component  $g$  of a facies  $f$  represents the size of a connected component.

**Box ratio** The box ratio is based on the axis-aligned bounding boxes of the components (figure 2.3). It is related to the tortuosity of a component and to its orientation relative to the grid axis. The box ratio  $\beta$  of the connected component  $g$  of the facies  $f$  is expressed between 0 and 1 using the following formula:

$$\beta_f^g = \frac{n_f^g}{n_f^b} \quad (2.7)$$

## 2.2 Indicators to measure simulation quality

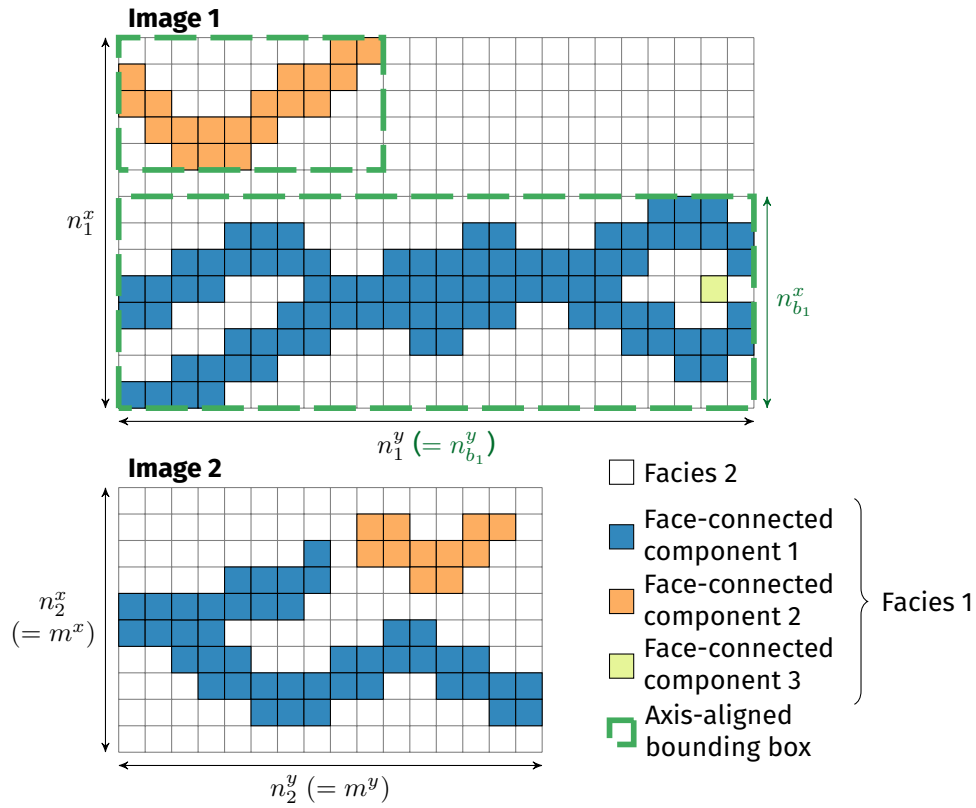


**Figure 2.3** Connected components of figure 2.2 represented with their bounding boxes (image 1). Image 2 is another image in a different grid. The two grids have different dimensions along the  $x$  axis, which can influence both the number of connected components and the number of grid cells. But they also have different dimensions along the  $y$  axis, along which the channels are oriented. Changes along the  $y$  axis influence the number of grid cells, but not the number of channels. In that case, the comparison of the density of the two images is biased. The same principle stands for the number of cells of each components. Differences between the number of cells for the component 1 of each image mainly come from the difference in grid dimension along  $y$ , not from real differences of connectivity.  $n_1^x$  and  $n_1^y$  represent the number of cells along the axis  $x$  and  $y$  for image 1,  $n_2^x$  and  $n_2^y$  the number of cells along the axis  $x$  and  $y$  for image 2 and  $n_{b_1}^x$  and  $n_{b_1}^y$  the number of cells along the axis  $x$  and  $y$  for the axis-aligned bounding box  $b$  of the connected component 1.  $m^x$  and  $m^y$  are the lower sizes between the two grids for the axis  $x$  and  $y$  (see section 2.3.1 for more details).

## 2 Analyzing stochastic simulations of sedimentary bodies

with  $n_f^g$  the number of cells of the connected component  $g$  of the facies  $f$  and  $n_f^b$  the number of cells occupied by its axis-aligned bounding box.

**Faces/cells ratio** The faces/cells ratio is equivalent to the surface/volume ratio, which compares the surface area of a component with its volume. Deutsch [1998] uses it as a measure of the tortuosity of the components, but it is also affected by their roughness. The faces/cells ratio  $\zeta$  of the connected component  $g$  of the facies  $f$  is expressed as:

$$\zeta_f^g = \frac{m_f^g}{n_f^g} \quad (2.8)$$

with  $m_f^g$  the number of faces along the surface of the connected component  $g$  of the facies  $f$  and  $n_f^g$  its number of cells.

**Sphericity** The sphericity  $\phi$  compares the shape of a connected component  $g$  for a facies  $f$  with a sphere [Wadell, 1935]. It ranges between 0 and 1, where 1 corresponds to a sphere, and is expressed as:

$$\phi_f^g = 36\pi \frac{(n_f^g)^2}{(m_f^g)^3} \quad (2.9)$$

with  $n_f^g$  the number of cells of the connected component  $g$  of the facies  $f$  and  $m_f^g$  its number of faces along its surface.

### Skeleton indicators

The skeletons are one-dimensional representations of the connected components. They are particularly used to assess the reproduction of the component topology.

**Basic element: the skeleton** A curve-skeleton is a thin one-dimensional representation of a three-dimensional shape. It is composed of nodes linked together by one or more segments (figure 2.4). The degree of a node is the number of segments connected to that node. Skeletons are often used to study some geometrical and topological features of a shape (figure 2.4).

There are several ways to compute skeletons [e.g., Serra, 1983, Jain, 1989, Brandt and Algazi, 1992]. Two methods have been considered for this work:

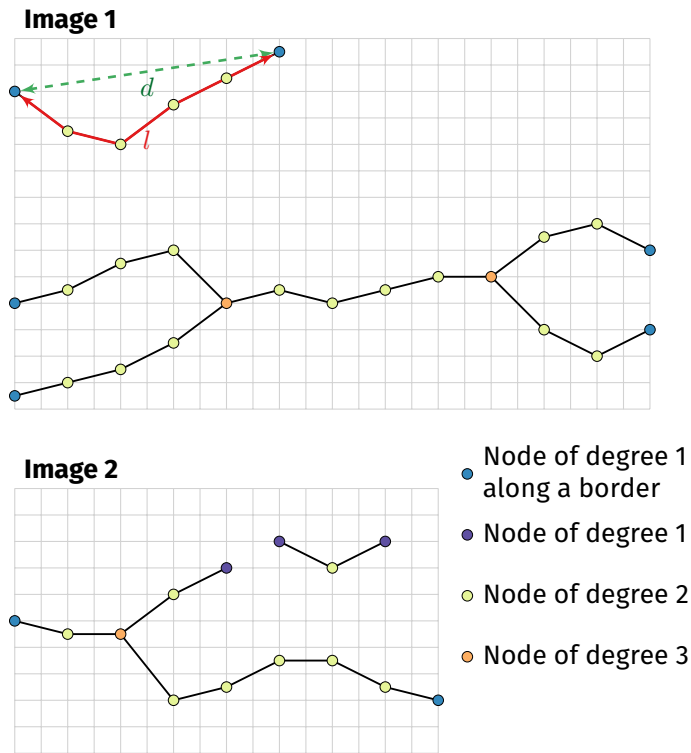


**Figure 2.4** Example of skeletons for the connected components of the figure 2.3. If image 2 has no connection with a degree higher than 3, such as image 1, it displays some dead-ends highlighted by nodes with a degree one in the middle of the grid. This difference emphasize mis-reproductions of the channel connectivity. In image 1,  $l$  represents the curvilinear length of the branch and  $d$  the distance between its extremities. These measures are used to compute the tortuosity, which can also differ between the images.

- The thinning-based method is distinguished by [Cornea et al. \[2007\]](#) as the methods with the best control on the skeleton connectivity. The algorithm retained here was defined by [Lee et al. \[1994\]](#) and implemented in Gocad by [Barthélemy and Collon-Drouaillet \[2013\]](#).
- A second method is based on slicing the grid along a given axis. The grid is subdivided into parallel slices of a given thickness. On each slice the connected components are computed and one node is assigned to each component. The nodes are then linked by computing the connected components over two adjacent slices. If two components from two slices form one connected component when the slices are combined, their nodes



are linked. If they form several components, their nodes are not linked.

The thinning-based method appears to perform better in two dimensions than the slicing-based method. But in three dimensions it tends to generate many small-scale loops which perturb both the topology and the geometry. This gives indicator behaviors that are hard to predict or explain. The slicing does not necessarily capture those small-scale elements depending on the slice size. While the geometry of the components is less well reproduced, the topology is better captured. It may not skeletonize the components smaller than the slice thickness, but this is compensated in some way by the other indicators, such as the number of component cells or the unit component proportion, which notice the presence of such small components. The thinning tends to generate skeletons with many nodes, which are heavy to manipulate. The slicing-based method has the same issues but far more limited when using quite high slice thicknesses. This aspect can be essential when dealing with several hundreds of images. Only the slicing method has been kept for this work, due to its ability to better capture the topology and to limit the skeleton size.

**Node degree proportion** The node degree proportion is based on the number of segments connected to a given node (figure 2.4). It is related to the topology of the skeleton and gives access to a deeper study of the connectivity of the sedimentary bodies of interest. The proportion  $p^n$  of nodes of degree  $n$  over all the skeletons for a given facies  $f$  is expressed as:

$$p_f^n = \frac{o_f^n}{o_f} \quad (2.10)$$

with  $o_f^n$  the number of nodes of degree  $n$  for all the skeletons of the connected components of the facies  $f$  and  $o_f$  the total number of nodes of the skeletons of the connected components for the facies  $f$ . Here we separate into two different classes the nodes of degree one along a border of an image and those in the middle of the image. The first ones relate to component terminations due to the limited size of the image. The other ones may relate to a bad body reproduction, for instance with channels that should be continuous and without dead-ends. The proportions for the different degrees give a histogram of node degrees.

**Branch inverse tortuosity** A branch is a part of a skeleton defined as an ensemble of segments that link nodes of degree 2 and delimited by two nodes of degree different from 2 (figure 2.4). The inverse tortuosity  $t$  quantifies how twisted a branch  $b$  is, with values ranged between 0 and 1. This measure is

related to the geometry of the skeleton. It is expressed for a branch  $b$  belonging to a skeleton  $s$  of a component of a given facies as:

$$t_s^b = \frac{d_s^b}{l_s^b} \quad (2.11)$$

with  $l_s^b$  the curvilinear length of the branch  $b$  of the skeleton  $s$  and  $d_s^b$  the Euclidean distance between the two extremity nodes of the same branch. The values for all the branches of all the skeletons related to an image are averaged to obtain one indicator value for that image.

## 2.3 Quality analysis considerations

The final purpose of this work is to compare the quality of realizations. The indicators are thus computed on the realizations, which may come from different methods and/or parameters. Then dissimilarity values based on the indicators help to compare the realizations.

### 2.3.1 Influence of different grid dimensions

It is common to compare realizations having different grid dimensions. For instance in MPS, the training image is often chosen larger than the simulation grid to maximize pattern repeatability. Consequently, the grid dimensions influence the size of the traversing connected components. Channels are a perfect example of such continuous bodies traversing the grid completely. This impacts some indicators, such as the density and the number of component cells. A direct use of those indicators may be detrimental to the quality analysis and a workaround is required.

#### Correction for the connected component density

When some connected components of a facies are traversing (see section 2.2.2), reducing the grid dimension along the component traversing extension can change the component size but not necessarily their number. For instance changing the grid size along the channel orientation does not change the number of channels. But it changes the grid volume and so does the density. Comparing two images of different sizes can affect the density whereas there is nothing wrong about the quality.

To overcome this aspect, the connected component density (formula 2.4) is replaced by:

$$\epsilon_f = \frac{N_f}{\vartheta_t} \quad (2.12)$$

## 2 Analyzing stochastic simulations of sedimentary bodies

with  $N_f$  the number of connected components of the facies  $f$  and  $\vartheta_t$  is a corrected number of grid cells corresponding to a mix between the dimensions of each compared images:

$$\vartheta_t = \vartheta^x \times \vartheta^y \times \vartheta^z \quad (2.13)$$

with  $\vartheta^x$ ,  $\vartheta^y$  and  $\vartheta^z$  respectively the corrected number of cells along the axis  $x$ ,  $y$  or  $z$ . These corrected numbers of cells are chosen depending on the smallest axis size among all the compared images and the size of the connected components. For an ensemble  $S$  of images to be compared, we note  $m^i$  the minimal size along the axis  $i$  over the images in  $S$ :

$$m^i = \min_{s \in S} (n_s^i) \quad i \in \{x, y, z\} \quad (2.14)$$

with  $n_s^i$  the number of cells along the axis  $i$  for the image  $s$ . Determining the corrected numbers of axis cells for a given image  $r$  of  $S$  depends on the size of its connected components:

$$\vartheta^i = \begin{cases} m^i & \text{if } \exists g \in r, n_g^i \geq m^i \\ n_r^i & \text{otherwise} \end{cases} \quad i \in \{x, y, z\} \quad (2.15)$$

with  $g$  a connected component of  $r$ ,  $n_r^i$  the number of cells along the axis  $i$  for the image  $r$  and  $n_g^i$  the number of cells along the axis  $i$  for the component  $g$ .

For instance in (figure 2.3), the component 1 of image 1 is larger than image 2 along the  $y$  axis. On the other hand, no component of that facies is larger than image 2 along the other axes. The corrected volumes for the image 1  $\vartheta_{t,1}$  and for the image 2  $\vartheta_{t,2}$  are so:

$$\begin{aligned} \vartheta_{t,1} &= n_1^x \times n_2^y \times n_1^z \\ \vartheta_{t,2} &= n_2^x \times n_2^y \times n_2^z \end{aligned} \quad (2.16)$$

with  $n_1^x$ ,  $n_1^y$  and  $n_1^z$  the number of cells along the axis  $x$ ,  $y$  and  $z$  for image 1 and  $n_2^x$ ,  $n_2^y$  and  $n_2^z$  the number of cells along the axis  $x$ ,  $y$  and  $z$  for image 2. Image 1 is so considered as truncated to limit the effect of the traversing bodies on the density.

### Correction of the number of connected component cells

The objects are expected to have roughly the same range of sizes in all the images. But this expectation is no longer relevant in the case of traversing bodies (see section 2.2.2), whose dimensions must vary following the size of the supporting grid. As for the connected geobody density, the possible

### 2.3 Quality analysis considerations

difference of image sizes imposes to rescale the number of cells of a connected component.

The rescaling is based on the estimation of the component bounding box size if this component was transferred within the grid of the smallest size. This bounding box size can be defined following a number of cells  $\vartheta_b$ :

$$\vartheta_b = \vartheta^x \times \vartheta^y \times \vartheta^z \quad (2.17)$$

with  $\vartheta^x$ ,  $\vartheta^y$  and  $\vartheta^z$  respectively the corrected numbers of cells of the bounding box along the axis  $x$ ,  $y$  or  $z$ . These corrected numbers of cells are following the same principles as to find the corrected number of cells for the density. Determining the corrected numbers of axis cells requires the same parameter  $m^i$  (formula 2.14):

$$\vartheta^i = \begin{cases} m^i & \text{if } n_b^i \geq m^i \\ n_b^i & \text{otherwise} \end{cases} \quad i \in \{x, y, z\} \quad (2.18)$$

with  $n_b^i$  the number of cells along the axis  $i$  for the bounding box of the component. Finally the corrected number of cells  $\vartheta_f^g$  for the component  $g$  of the facies  $f$  is proportional to the ratio between the number of cells of its corrected bounding box  $\vartheta_b$  and the number of cells of its actual bounding box  $n_b$ :

$$\vartheta_f^g = n_f^g \times \frac{\vartheta_b}{n_b} \quad (2.19)$$

For instance the component 1 on image 1 of figure 2.3 has a corrected number of cells  $\vartheta_1$  of:

$$\vartheta_1 = n_1 \times \frac{n_{b_1}^x \times n_2^y \times n_{b_1}^z}{n_{b_1}^x \times n_{b_1}^y \times n_{b_1}^z} = n_1 \times \frac{n_2^y}{n_{b_1}^y} \quad (2.20)$$

with  $n_1$  the number of cells of component 1,  $n_{b_1}^x$ ,  $n_{b_1}^y$  and  $n_{b_1}^z$  the numbers of cells of its axis-aligned bounding box along the axis  $x$ ,  $y$  or  $z$  and  $n_2^x$ ,  $n_2^y$  and  $n_2^z$  the numbers of cells of image 2 along the axis  $x$ ,  $y$  or  $z$ . This reflects the impossibility to make that component fit into image 2. Its size needs so to be rescaled to be compared with objects of image 2.

The image dimensions has less impact on the other shape indicators. For instance when the size of a traversing object increases, so does its bounding box and the box ratio does not necessarily vary. Thus the corrected number of component cells is not used in the other shape indicator computation.

### 2.3.2 Indicator rescaling

The rescaling ensures that the differences between the ranges of indicator values will not affect the comparison. The histogram-based indicators – facies proportion, facies adjacency proportion and node-degree proportion – are not rescaled, to preserve their histogram behavior for the dissimilarity computation (section 2.3.3). Two methods can be used for rescaling: normalization and standardization.

The normalization method consists in rescaling linearly the indicators values between 0 and 1. The indicator  $I_i$  is the  $i^{\text{th}}$  indicator of the set previously defined. When computed for the facies  $f$  of the realization  $r$ , we will denote the computed indicator  $I_{if}^r$ . The normalization is then obtained by rescaling it between its minimum and maximum values:

$$\text{norm}(I_{if}^r) = \frac{I_{if}^r - m_{if}}{M_{if} - m_{if}} \quad (2.21)$$

with  $M_{if}$  the maximum value for the same indicator and facies among all the images and  $m_{if}$  the minimal value for the same indicator and facies among all the images.

The standardization method consists in using reduced-centered indicator values. For an indicator  $i$  the standardized value for a facies  $f$  of a realization  $r$  is obtained using the following formula:

$$\text{stand}(I_{if}^r) = \frac{I_{if}^r - \mu_{if}}{\sigma_{if}} \quad (2.22)$$

with  $\mu_{if}$  the mean for the same indicator and facies among all the images and  $\sigma_{if}$  the standard deviation for the same indicator and facies among all the images. The indicator normalization has been kept in this work to maximize the indicator variations between the images.

### 2.3.3 Dissimilarity calculation

The principle of comparing two images is to determine how dissimilar these images are. The indicators can be seen as coordinates of the compared images. But these indicators are heterogeneous: they are either based on histograms or on continuous values. The computation of a dissimilarity value between two images requires a heterogeneous metric.

Following the example of [Wilson and Martinez \[1997\]](#), two different metrics are combined into a heterogeneous Euclidean/Jensen-Shannon metric. It uses the Jensen-Shannon distance, square root of the Jensen-Shannon divergence

[Rao, 1987, Lin, 1991], for the histogram-based indicators – facies proportion, facies adjacency proportion and node-degree proportion – and the Euclidean distance for all the other indicators. The distance between two images  $r$  and  $s$  for a given indicator  $i$  of a given facies  $f$  is given by:

$$d(I_{if}^r, I_{if}^s) = \begin{cases} d_{JS}(I_{if}^r, I_{if}^s) & \text{if } I_{if}^r \text{ and } I_{if}^s \text{ are histograms} \\ d_E(I_{if}^r, I_{if}^s) & \text{if } I_{if}^r \text{ and } I_{if}^s \text{ are continuous values} \end{cases} \quad (2.23)$$

with  $I$  the indicator values.  $d_{JS}$  represents the Jensen-Shannon distance:

$$d_{JS}(H_i^r, H_i^s) = \sqrt{\frac{1}{2} \sum_{j=1}^n \left[ H_{ij}^r \log \left( \frac{H_{ij}^r}{\frac{1}{2}(H_{ij}^r + H_{ij}^s)} \right) + H_{ij}^s \log \left( \frac{H_{ij}^s}{\frac{1}{2}(H_{ij}^r + H_{ij}^s)} \right) \right]} \quad (2.24)$$

with  $H_i^r$  and  $H_i^s$  the histograms of the indicator  $i$  for respectively the images  $r$  and  $s$ ,  $n$  the number of classes for each histogram,  $H_{ij}^r$  and  $H_{ij}^s$  the proportions for the class  $j$  in the corresponding histograms.  $d_E$  represents the Euclidean distance used with rescaled indicators:

$$d_E(I_{if}^r, I_{if}^s) = \sqrt{(\text{resc}(I_{if}^r) - \text{resc}(I_{if}^s))^2} \quad (2.25)$$

with  $I_{if}^r$  and  $I_{if}^s$  the values of the indicator  $i$  for the facies  $f$  of respectively the images  $r$  and  $s$  and  $\text{resc}$  either *norm* (formula 2.21) or *stand* (formula 2.22). The final dissimilarity  $\delta$  between two images  $r$  and  $s$  given their respective sets of indicators  $I^r$  and  $I^s$  is:

$$\delta(I^r, I^s, \omega, \nu) = \sqrt{\omega_1 d_{JS}(I_1^r, I_1^s, \nu)^2 + \sum_{i=2}^{12} \sum_{f=1}^n \omega_i \nu_f d(I_{if}^r, I_{if}^s)^2} \quad (2.26)$$

with  $I_1^r$  and  $I_1^s$  the facies proportion histogram for the two images,  $I_{if}^r$  and  $I_{if}^s$  all the other indicator values depending on the indicator and the facies and  $n$  the number of facies.  $\omega$  represents the set of weights  $\omega_i$  that control the impact of each indicator.  $\nu$  represents the set of weights  $\nu_f$  that control the impact of each facies. Note that the facies proportion histograms are the only indicators with one result for all the facies. Thus the facies proportions are treated differently from all the other indicators. The Jensen-Shannon distance used in that case is

## 2 Analyzing stochastic simulations of sedimentary bodies

slightly modified:

$$d_{JS}(H_i^r, H_i^s, \nu) = \sqrt{\frac{1}{2} \sum_{f=1}^n \nu_f \left[ H_{if}^r \log \left( \frac{H_{if}^r}{\frac{1}{2}(H_{if}^r + H_{if}^s)} \right) + H_{if}^s \log \left( \frac{H_{if}^s}{\frac{1}{2}(H_{if}^r + H_{if}^s)} \right) \right]} \quad (2.27)$$

The dissimilarity values computed by 2.26 between all the images constitute a non-negative symmetric matrix. This matrix has a zero diagonal corresponding to the dissimilarity between an image and itself. The dissimilarity matrix can be directly visualized with a heat map or treated by multidimensional scaling to get a more practical visualization.

### 2.3.4 Heat map

The heat map is a simple graphical representation of a matrix where the matrix values correspond to colors. In our case, the heat map is a two-dimensional representation. This colored representation highlights patterns in the dissimilarity matrix, either between realizations or between simulation methods. The main advantage of the heat map is to show the real dissimilarity values, contrary to the multidimensional scaling described in the next subsection.

The heat map also enables to classify the images and/or to apply clustering methods on it. A simple yet informative classification is the ranking according to the dissimilarities of the images toward one particular image. When using more advanced clustering methods, the matrix rows and columns are permuted to gather close values into the same cluster.

### 2.3.5 Multidimensional scaling

Multidimensional scaling (MDS) [e.g., [Torgerson, 1952, 1958](#), see [Cox and Cox, 1994](#) for a review] is a set of data visualization methods to explore dissimilarities between objects – represented by a dissimilarity matrix – through a dimensionality reduction: it aims at producing a configuration of the objects as optimal as possible in a lower dimensional representation.

#### Principle and methods

Finding the configuration of the images in a  $k$  dimensional representation consists in locating a set of points representing the objects in a  $k$ -dimensional

Euclidean space – with  $k$  being at most equal to the number of images minus one. The point localization is done so that the Euclidean distance  $d$  (2.28) between two points matches as closely as possible the dissimilarities between the images.

$$d_{r,s} = \sqrt{\sum_{i=1}^k (x_{ri} - x_{si})^2} \quad (2.28)$$

with  $r$  and  $s$  two images,  $k$  the dimension number of the Euclidean space,  $x_{ri}$  and  $x_{si}$  the coordinates of respectively  $r$  and  $s$  in the  $i$ -th dimension. Dissimilarities can be determined from data gathered on the objects.

Several multidimensional scaling methods have been proposed, depending on the type of dissimilarities and on the way to match the dissimilarities with the distances. Here, two metric multidimensional scaling methods are used: the classical scaling and the Scaling by MAjorizing a COMplicated Function (SMACOF).

**Classical scaling** Classical scaling [Torgerson, 1952, 1958, Gower, 1966] is a metric MDS method that considers the dissimilarities to be already Euclidean distances. The coordinates of the points corresponding to the images are so directly retrieved from that matrix. As the Euclidean assumption is very strict, it may be relaxed to a metric assumption. In that case, the dissimilarities must be distances. This is consistent with our dissimilarity based on a heterogeneous metric. To overcome the relaxation effects – in particular possible negative eigenvalues during the calculation of the point coordinates – two solutions can be considered [Cox and Cox, 1994]:

- Either choose the number of dimensions without taking into account those linked to negative eigenvalues.
- Either add a constant term to all the dissimilarity values except those between the same image. The purpose is to make the dissimilarities equal to Euclidean distances.

Those eigenvalues can also be used to assess the choice of the number of dimensions. The proportion of variation  $p^v$  of the  $k$  first eigenvalues – corresponding to the  $k$  chosen dimensions – compared with all the eigenvalues is given by [Cox and Cox, 1994]:

$$p^v = \frac{\sum_{i=1}^k \lambda_i}{\sum_{i=1}^n |\lambda_i|} \quad (2.29)$$



## 2 Analyzing stochastic simulations of sedimentary bodies

with  $\lambda_i$  the eigenvalues and  $n$  the total number of eigenvalues. It represents the weight of the  $k$  first dimensions on the distance values. The closest from 1  $p^v$  is, the better is the chosen dimension number  $k$ . In the case of the metric assumption without using a constant term, the negative values may not be taken into account for the calculation of  $p^v$ .

**Scaling by majorizing a complicated function (SMACOF)** The SMACOF [De Leeuw, 1977, De Leeuw and Heiser, 1977, 1980] is also a metric MDS method, but it only considers that the dissimilarity matrix is metric and not Euclidean. Its goal is to get distances as close as possible from the dissimilarities using a majorization, i.e., the optimization of a given objective function called stress, through an iterative process.

Following the same principle as the impact of the eigenvalues with classical scaling, the final stress value helps to assess the choice of the number of dimensions: the lower the stress is, the better is that choice.

### Validation of the number of dimensions

Following the chosen number of dimensions for the representation, the point configuration matches more or less the dissimilarity values. Verifying that the dimension number is enough for a good match between the dissimilarities and the distances is so of prime importance. Two approaches allow testing the chosen dimension number:

**The scree plot:** It represents the stress of the SMACOF against the dimension number. An equivalent representation for the classical scaling is the eigenvalue against the dimension number, besides looking at the proportion of variation. The stress and the eigenvalues both follow globally convex decreasing functions that tend toward 0 when the dimension number increases. A stress or an eigenvalue close or equal to zero means that the higher dimensions are unnecessary to represent the dissimilarities. The best number of dimensions is between the point with the highest flexion of the curve and the beginning of the sill at zero. The dimension value right after the point with the highest flexion is generally enough for a decent representation.

**The Shepard diagram:** It represents the distances against the dissimilarities. The better the correlation, the better the choice of dimension number.

The dimension number  $k$  generally used is 2 or 3 for practical visualization purpose. Both MDS methods have been used on the following case study to

analyze how good is the match between the distances and the dissimilarities for a two-dimensional representation and what is the impact of the MDS method on the resulting representation.

### Estimation of the point position confidence

The point position confidence is another way to assess the MDS ability to represent the dissimilarities. For each point  $r$ , an error  $e$  highlights the mismatch between the dissimilarities  $\delta$  and the distances  $d$  with all the other points  $s$ :

$$e_r = \sum_s |(a\delta_{r,s} + b) - d_{r,s}| \quad (2.30)$$

with  $a$  and  $b$  the linear regression coefficients found on the Shepard diagram. This measure gives a more local representation of the miss-representation than the scree plot or the Shepard diagram.

For visualization purpose, that error is then normalized, giving the confidence  $c$  for a given image  $r$ :

$$c_r = 1 - \frac{e_r - e_{min}}{e_{max} - e_{min}} \quad (2.31)$$

with  $e_{max}$  and  $e_{min}$  respectively the greatest and the lowest error values amongst the errors of all the images. This confidence can then be attributed to its corresponding point in the MDS representation through the point transparency: the less transparent the point is, the best the dissimilarities related to this point with all the other points are represented.

## 2.4 Application of the method and discussion

The method, as described in the previous sections, consists of three steps:

1. Indicator computation.
2. Dissimilarity computation in a matrix.
3. Dissimilarity visualization and analysis, especially with MDS.

The first two steps have been implemented in a C++ plugin for the SKUA-GOCAD geomodeling software [Paradigm, 2015]. The last step has been realized using the software environment for statistical computing R [R Core Team, 2012] with the addition of the R packages SMACOF [De Leeuw and Mair, 2009], NMF [Gaujoux and Seoighe, 2010] and ggplot2 [Wickham, 2009].

## 2 Analyzing stochastic simulations of sedimentary bodies

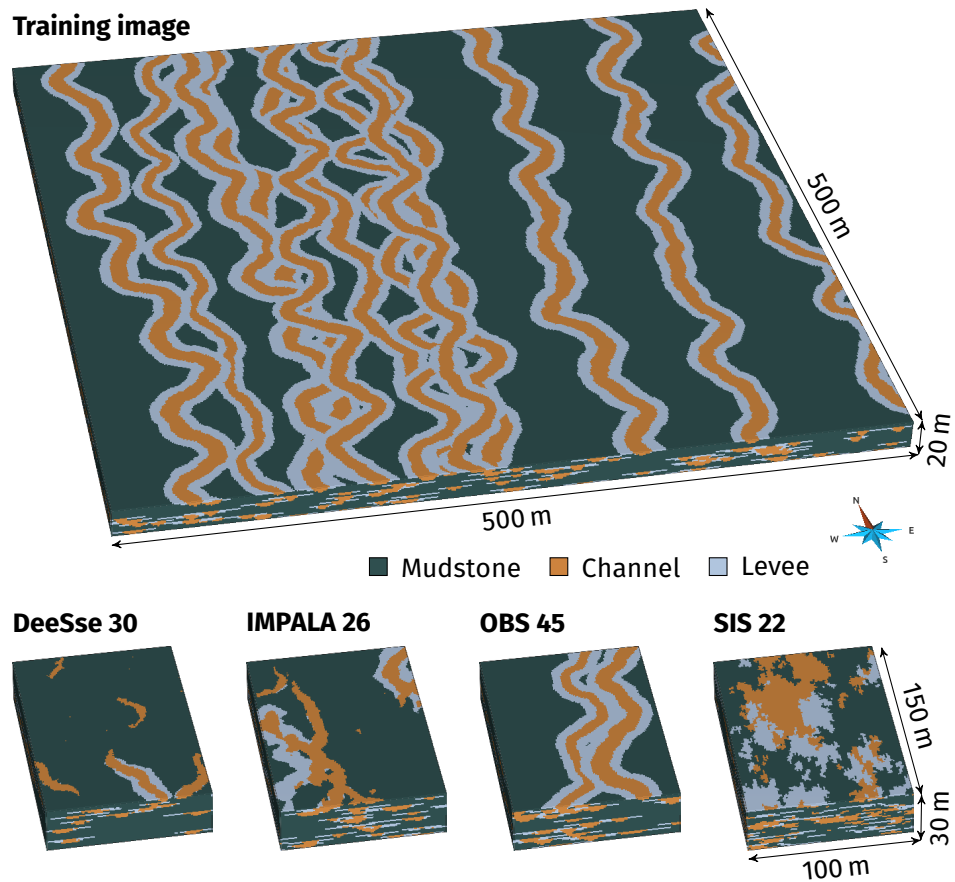


**Figure 2.5** Training image and examples of realizations for each categories. These realizations are the closest to their category mean points in the MDS representation (figure 2.10).

### 2.4.1 Dataset

The whole analysis process is applied to a synthetic dataset related to a channelized system. This case study aims to highlight some practical aspects of the method application. It uses some particular simulation methods but no general conclusion should be drawn on the simulation methods themselves based on this case.

The channelized system is composed of sandy channels with levees into a mudstone environment. This case falls within the scope of a MPS study: a training image (TI) (figure 2.5) is generated using the object-based method of the software Petrel [Schlumberger, 2015] (see A, table A.3, for the simula-

tion parameters), and several simulation methods are used to try to reproduce the sedimentary bodies observed in the TI. The huge difference of grid size comes from the need of enough pattern repeatability for the MPS methods. The following realizations are simulated:

**DeeSse:** 100 MPS realizations generated with the DeeSse implementation [Straubhaar, 2011] of the direct sampling method [Mariethoz et al., 2010]. Contrary to more traditional MPS methods, the direct sampling bypasses the conditional probability computation and resamples randomly the training image. It relies on the compatibility – measured with a distance – between the conditioning data and the patterns scanned in the training image. The resampling step selects the first pattern with a distance lower than a given threshold. The training image is the TI and the set of parameters is given in table A.1) in the appendix A.

**IMPALA:** 100 MPS realizations generated with the method IMPALA [Straubhaar et al., 2011]. Contrary to the DeeSse, IMPALA still computes the conditional probabilities during the simulation. To improve the efficiency of this computation, the method stores the training image patterns in a list. The training image is scanned once at the beginning and the list is used instead during the simulation. The training image is the TI and the set of parameters is given in table A.2) in the appendix A.

**OBS:** 100 object-based realizations generated with the same method and parameters used to generate the TI (A, table A.3).

**SIS:** 100 sequential indicator simulation realizations generated using variograms based on the facies in the TI (A, table A.4).

The purpose here is to compare the realizations with the TI. It should lead to retain the method and associated parameters that reproduce at best the connectivity of the TI for the studied case. The indicators used in this case study (table 2.1) are all equally considered ( $\omega_i = 1$  for all  $i$  in formula 2.26). This avoids any subjective bias that could arise from favoring a given indicator. The mudstone environment is the resultant of the channels and levees placement. It has so no precise shape by itself and may blur the analysis. It gets a weight of 0 while channels and levees both get each a weight of 1 ( $\nu_{mudstone} = 0$ ,  $\nu_{channel} = 1$  and  $\nu_{levee} = 1$ ). Channels and levees are considered equally important to reproduce, but this aspect is related to the case study and could be further discussed. Slices of 17 cells along the grid axis with the same orientation than the channels are used for the skeletonization. The unit volume connected components (see section 2.2.2) give little information on the shape of the most

## 2 Analyzing stochastic simulations of sedimentary bodies

**Table 2.1** Set of indicators used for the case study. The indicator descriptions are in section 2.2.

Set	Subset	Indicator	Symbol	Weight
Global analysis (measures on all the components)		Facies proportion	$p$	1
		Facies adjacency proportions	$p^a$	1
		Facies connection probability	$\Gamma$	1
		Corrected connected component density	$\epsilon$	1
		Unit connected component proportion	$p^u$	1
		Traversing connected component proportion	$p^c$	1
Detailed analysis (measures on each component)	Shape indicators	Corrected number of connected component cells	$n$	1
		Box ratio	$\beta$	1
		Faces/cells ratio	$\zeta$	1
		Sphericity	$\phi$	1
	Skeleton indicators	Node degree proportions	$p^n$	1
	Branch inverse tortuosity	$t$	1	

important connected bodies considering flow circulation: the channels. But they can have a significant influence on the averaged shape indicators (section 2.2.3). They are so ignored during the computation of those shape indicators.

### 2.4.2 Visual inspection of the realizations

Looking at the connected components (figure 2.6) highlights some expectations for the dissimilarity analysis. Two aspects must be analyzed: the reproduction of the channel shapes and the reproduction of the connectivity between the channels. In the studied case, the reproduction of the shape is pretty easy to analyze visually. The SIS realizations do not display any objects similar to channel/levee system and are so far dissimilar from the TI. The OBS realizations look similar to the TI, which is what is expected considering that they come from the same method and parameters. DeeSse realizations have objects similar to channels, even if some continuity issues appear. They also seem to have an insufficient number of channels. IMPALA realizations have quite linear objects but which poorly reproduce channel and levee shapes.

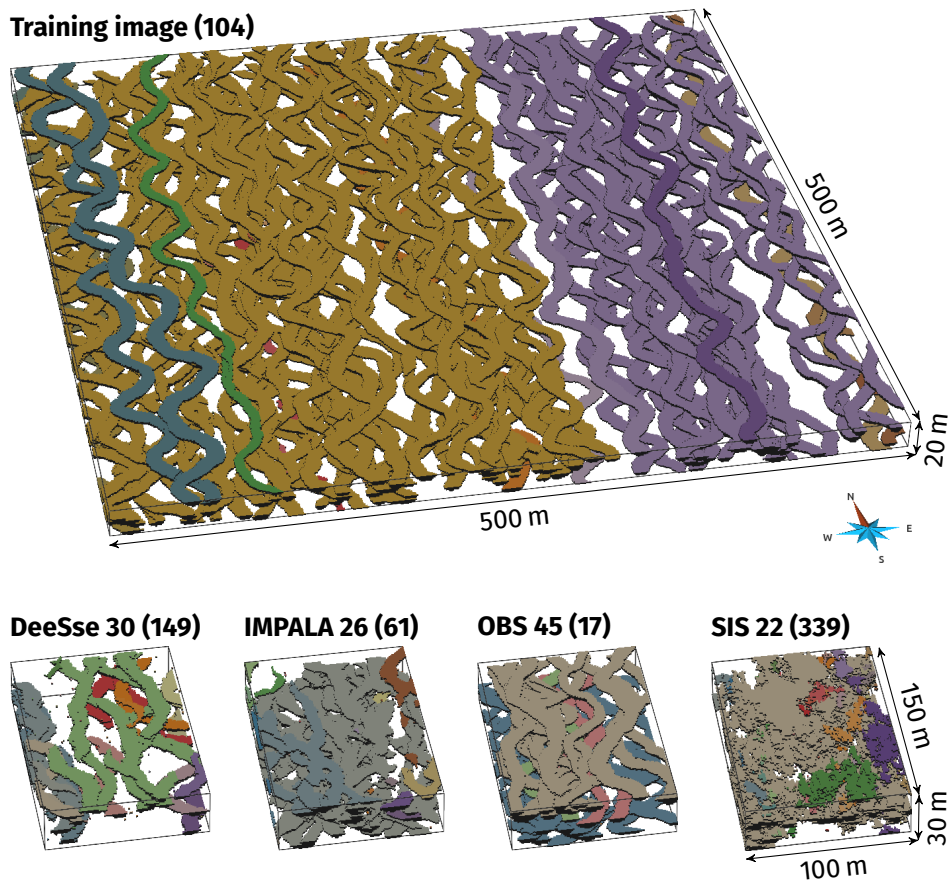


**Figure 2.6** View of all the channel connected components within the reference image and examples of realizations for each categories. The number in parentheses are the number of connected components of each image.

Estimating the connectivity of the objects in three-dimensional images is more difficult. The TI channels seem highly connected. The objects in the SIS realizations do not locally intersect like channels do and are far too connected. DeeSse realizations contain less objects and seem under-connected compared to the TI. The distinction between OBS and IMPALA realizations is difficult concerning the connectivity. Looking at the skeletons of the connected components (figure 2.7) corroborates those observations. DeeSse realizations are clearly under-connected compared with the other categories. SIS ones are over-connected. IMPALA realizations seem a bit more connected than OBS ones. The connectivity within the training image is clearly non-stationary.

## 2 Analyzing stochastic simulations of sedimentary bodies

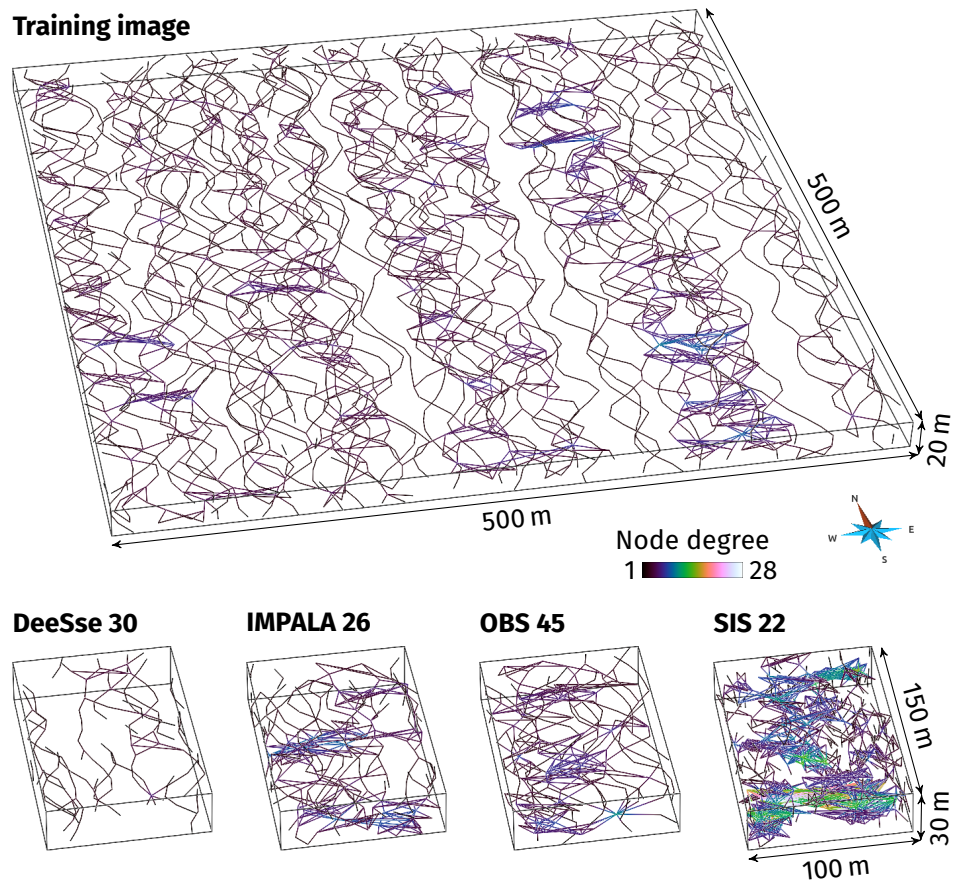


**Figure 2.7** View of all the skeletons of the connected components for the TI and for a realization of each category.

### 2.4.3 About MDS methods and accuracy

Two MDS methods are tested with this case study: the classical scaling (figure 2.8) and the SMACOF (figure 2.9). The representations of each methods seem similar at first glance: the TI position is the only significant difference. But the point positions can vary significantly between the two representations. This is especially noticeable on the Shepard diagrams associated with both representations: if the correlation coefficients are rather good, the distances are sometimes far from being at least proportional to the dissimilarities. This can also lead to some misrepresentations of the dissimilarities. For instance, the realization DeeSse 76 should be closer to the TI than the realization DeeSse 12

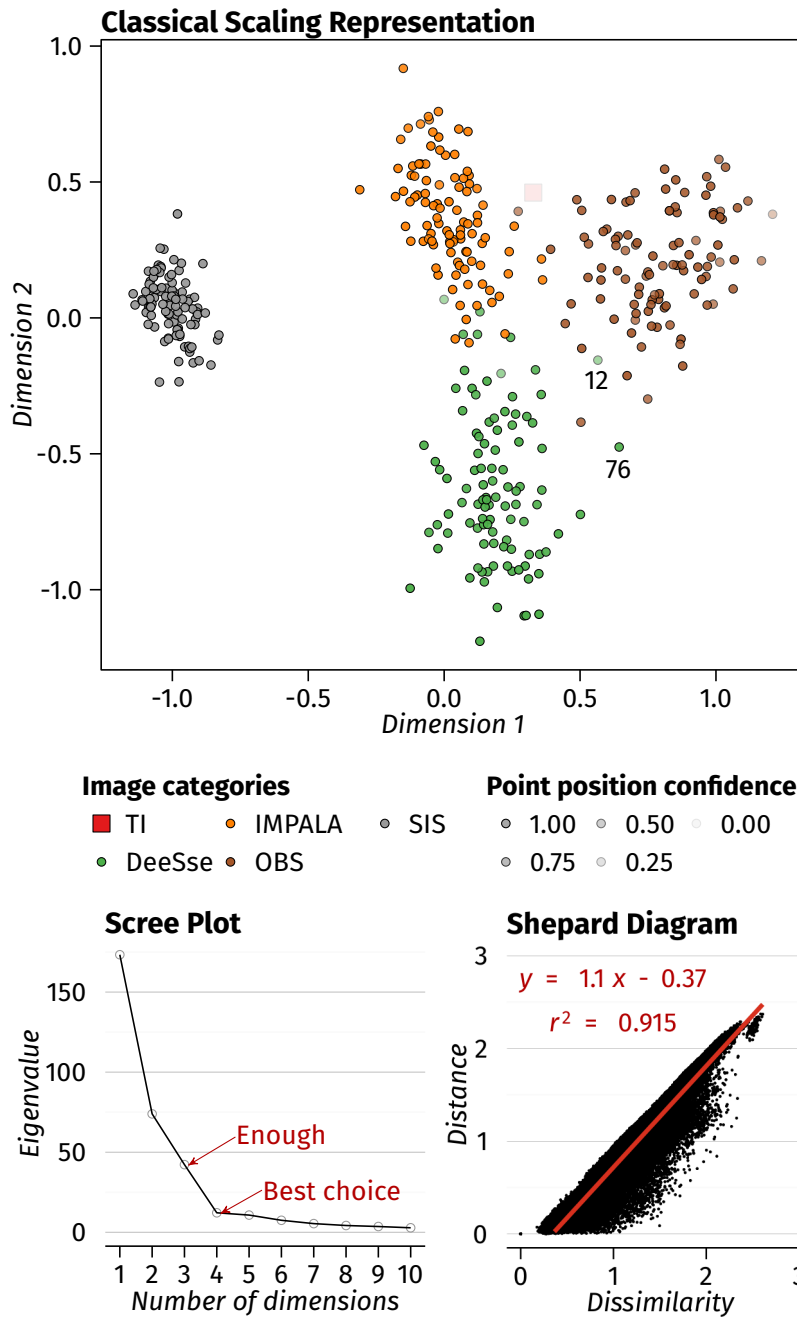


**Figure 2.8** MDS representation of the dissimilarities between the images of the case study generated using classical scaling and validation graphs. The scree plot only displays the eigenvalues up to 10 dimensions on 400 possible.



2 Analyzing stochastic simulations of sedimentary bodies

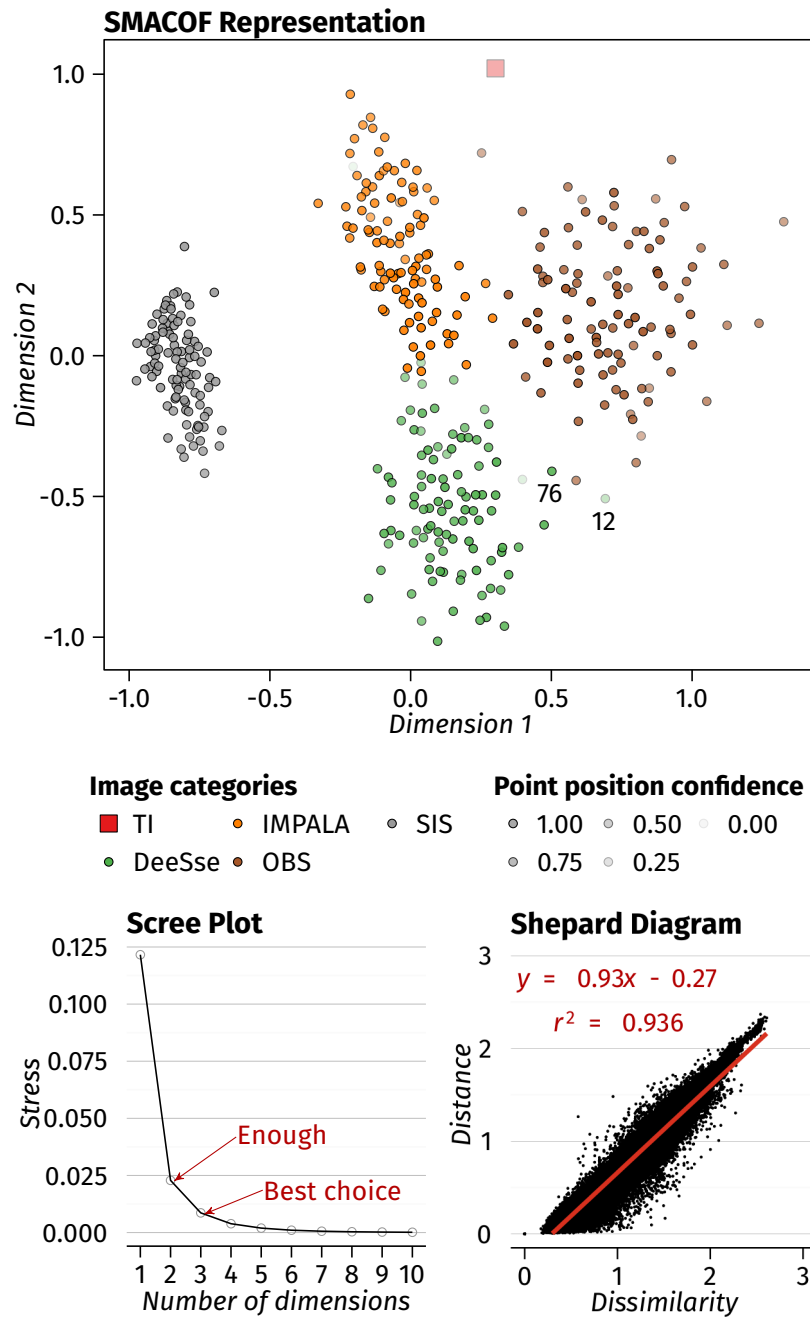


**Figure 2.9** MDS representation of the dissimilarities between the images of the case study generated using SMACOF and validation graphs. The scree plot only displays the stress values up to 10 dimensions on 400 possible.

**Table 2.2** Comparison of dissimilarities and distances between the TI and DeeSse realization 12 and 76 for to MDS methods. CS stands for classical scaling.

Compared images	Dissimilarity	CS distance	SMACOF distance
TI - DeeSse 12	1.773	0.661	1.577
TI - DeeSse 76	1.590	0.988	1.445
DeeSse 12 - DeeSse 76	0.962	0.329	0.213

(table 2.2). These two realizations are also more similar all together than with the TI. These dissimilarities are better reproduced by the SMACOF representation. The classical scaling even places the DeeSse realization 12 closer to the TI than the DeeSse realization 76. In this case using the classical scaling could lead to misleading interpretations.

The SMACOF method leads to a better representation as shown by the coefficient of determination  $r^2$  of the Shepard diagram. This coefficient represents the goodness of fit of the linear regression. It measures so the correlation between the dissimilarities and the distances. The scree plot of the classical scaling also shows that a two-dimensional representation is not sufficient: a three-dimensional representation would perform better, and a four-dimensional representation would have been the best choice. For the SMACOF, a two dimensional representation seems enough. A three-dimensional one would have been better, but at the detriment of visibility. For visualization purpose a two-dimensional representation should always be favored. Several MDS methods exist and they are not all equivalent for a given dissimilarity matrix. Testing different MDS methods could help to avoid using greater number of dimensions. In this case study, the two-dimensional representation given by the classical scaling is not sufficient. The SMACOF one is more precise, even if it does not represent perfectly the dissimilarities.

#### 2.4.4 Analysis of the global dissimilarities

The first step of the dissimilarity analysis consists in looking at the global relationships between the realizations and the related methods. The MDS representation is ideal due to its clarity and ease of reading. But as highlighted in the previous section, caution should be exercised in its interpretation.

## 2 Analyzing stochastic simulations of sedimentary bodies

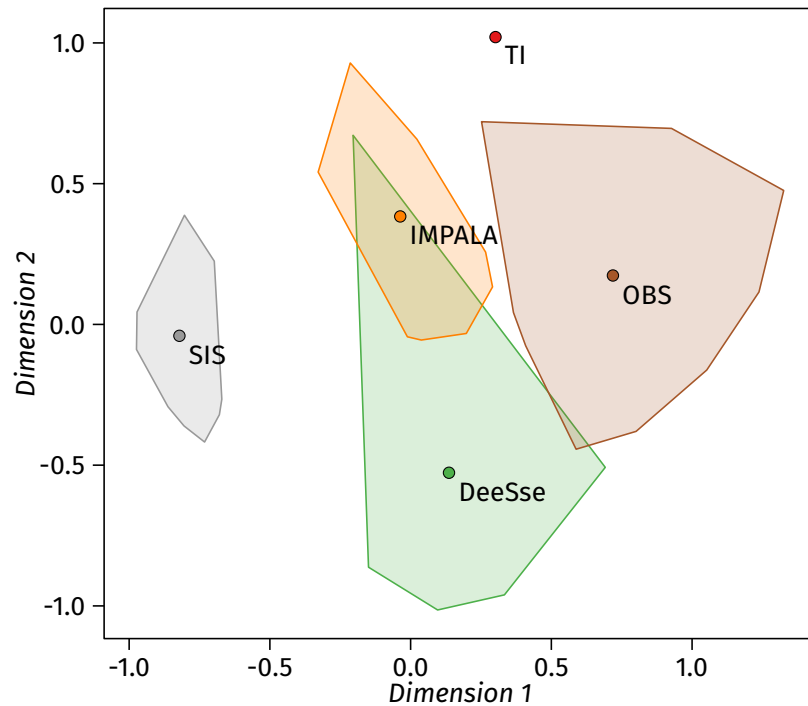


**Figure 2.10** Simplification of the MDS representation of the dissimilarities between the images of the case study generated using SMACOF. The points are defined using the mean coordinates of all the MDS points of each category. The extension of each category is represented by the convex hull of all the MDS points of each category.

### Inter-category dissimilarities

The MDS representation reveals a clear distinction between the different methods. The TI is quite far from the different categories, but seems closer to the IMPALA and OBS realizations. The SIS realizations are completely separated from the other categories.

A simplification of the MDS representation can also make the inter-category analysis clearer (figure 2.10). In that case, each category is represented by the point of mean coordinates and the convex hull of all its points. The proximity of the mean points and the eventual intersection of the convex hulls make the global analysis easier. Here the SIS realizations appear more clearly separated. DeeSse, IMPALA and OBS realizations are quite close. The overlapping between DeeSse and IMPALA seems significant, but it is mainly due to one realization. The IMPALA realizations are globally the closest from the TI, but some OBS realizations are closer. As the TI and the OBS realizations come from the

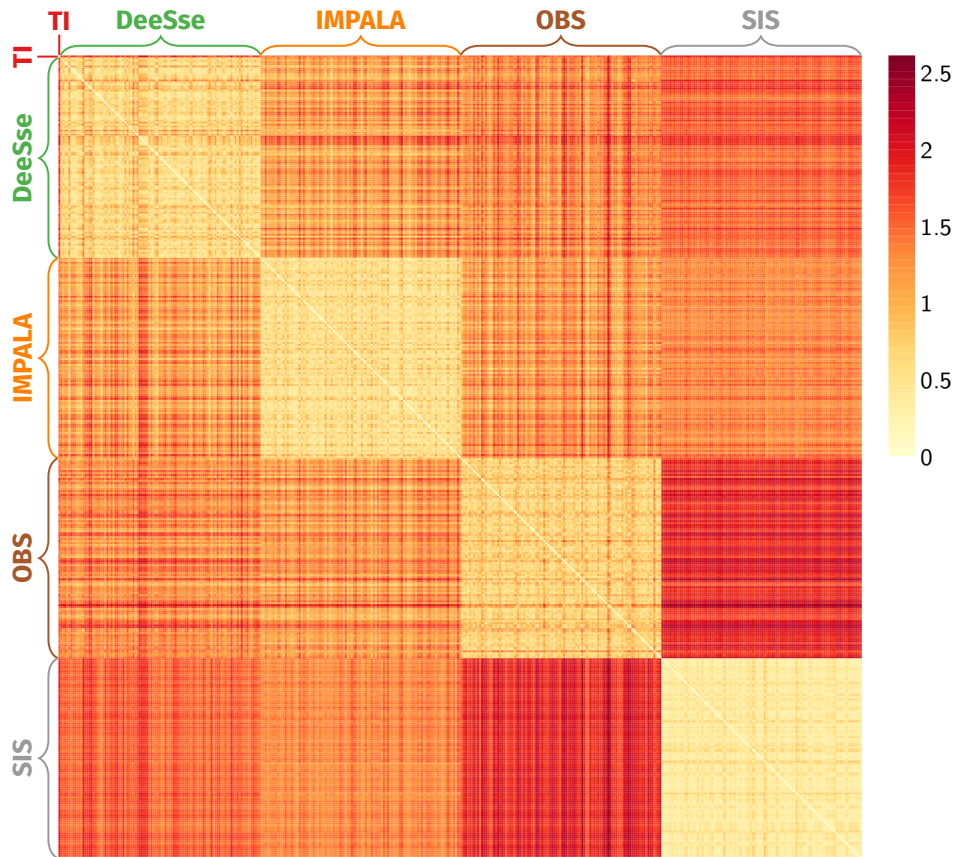


**Figure 2.11** Heat map representation of the dissimilarity matrix computed based on the reference image and simulations of the case study. The color scale represents the dissimilarity values.

same method and parameters, having the IMPALA realizations closer is quite surprising. This calls for a deeper analysis, especially considering the possible mismatches caused by the MDS.

Analyzing the heat map (figure 2.11) allows verifying the interpretations done on the MDS. The heat map is a more elegant way of analysis than examining a dissimilarity matrix which may contain several hundreds of values. It appears to be more difficult to read than a MDS representation. But the same conclusions can be made. The main point is to look at the squares formed by comparing two categories of images. When those squares are red, the categories are dissimilar. Each category is identifiable through the squares that appear on the colored matrix. The SIS realizations are clearly dissimilar to the

other categories, especially the OBS category. The OBS realizations are also distinguishable from the DeeSse and IMPALA realizations.

### **Intra-category dissimilarities**

The same principles can be applied to compare the realizations within a category, so the realizations of a given method and a given set of parameters. Looking at the convex hull size provides a representation of how dissimilar the realizations of the category are, so how variable are the results of a given method. The realizations with less variability are the SIS ones, which all seem to have similar connectivity patterns. This is consistent with the great visual similarity of the SIS realizations. And the globular aspect of the SIS connected components enhances this similarity. Then come the IMPALA realizations, with a bit more of variability. The DeeSse and OBS categories have even larger convex hulls, so a larger variability.

The same observations can be done on the heat map when looking at the color whiteness and uniformity of the squares along the diagonal. The SIS realizations appear highly similar all together and the IMPALA realizations more variable. The DeeSse and OBS realizations have again a greater variability, with quite high dissimilarity values.

### **About the difference in grid dimensions**

One surprising aspect is the clear difference in the dissimilarities between the TI and the OBS realizations. All these images come yet from the same simulation method with the same parameter values, only the grid changes: the grid of the TI – the training grid – is larger than that of the OBS realizations – the simulation grid. The different grid dimensions could be an explanation for that clear difference:

- The TI displays a non-stationary connectivity pattern: some areas contain only one connected component as the channels are all connected, whereas other areas contain more connected bodies. This implies huge differences in terms of connectivity depending on the areas of the TI. When restrained to a smaller grid, this could give different results.
- The indicators most sensitive to variations of image size have already been adapted to take this aspect into account. However, this adaptation is rather an approximation and a bias may still exist in the comparison.

To check that the difference in the dissimilarities really comes from the difference of grid size, several TI analogs have been simulated. These analogs

are realizations from the same method, parameter values (see [A](#), table [A.3](#)) and grid than the TI. The application of the method highlights a significant difference between the realizations from different grids: the TI and analogs on one side, the OBS realizations on the other side (figure [2.12](#)). Thus, the TI is not a realization with a particular connectivity pattern.

A closer look at the indicators is part of the answer. The TI, the analogs and the OBS realizations have all similar channel and levee proportions (figure [2.13](#)). The channels and levees occupy the same volume inside the two grids. The facies connection probabilities for both channels and levees give a clearer difference between the realizations in the two grids (figure [2.13](#)). The probability that two cells of the same facies belong to the same connected component is higher in the training grid than in the simulation grid. This is consistent with the difference of grid dimensions. When the grid dimension along the channel direction increases, the probability that two channels cross each other to form a single connected component increases too, especially here with sinuous channels. In such case, the characteristics of the connected components are impacted by the grid size.

### Comparison with multiple-point histograms

Multiple-point histograms have made their way as indicators of a realization quality with MPS methods [e.g., [Boisvert et al., 2010](#), [Tan et al., 2014](#)]. We propose here to compare the results obtained with those histograms to the previous results. The histograms are based on a  $3 \times 3 \times 3$  pattern and are computed on three levels of multi-grid [[Tran, 1994](#)], giving three histograms per image. The comparison between the images is based on the dissimilarity calculation presented in section [2.3.3](#). To compare two images, the Jensen-Shannon distance [2.24](#) is used between the histograms of each multi-grid levels. Then the Jensen-Shannon distances are assembled with a Euclidean norm, similarly to [2.26](#).

The SMACOF representation (figure [2.14](#)) shows some similarities with the previous one (figure [2.9](#)). The methods are all separated one from the other. The SIS realizations are all far from the other categories, even if their dissimilarities do not seem well represented. The OBS realizations do not mix much with the DeeSse and IMPALA realizations. Similarly, DeeSse and IMPALA realizations are quite close but do not really merge much.

Some differences appear in terms of variability. The SIS realizations seem far more variable and so does the IMPALA ones. But the most significant difference comes from the dissimilarity with the TI. The TI is inside the convex hull of the OBS realizations. These OBS realizations are so the closest to the TI. It is then

2 Analyzing stochastic simulations of sedimentary bodies

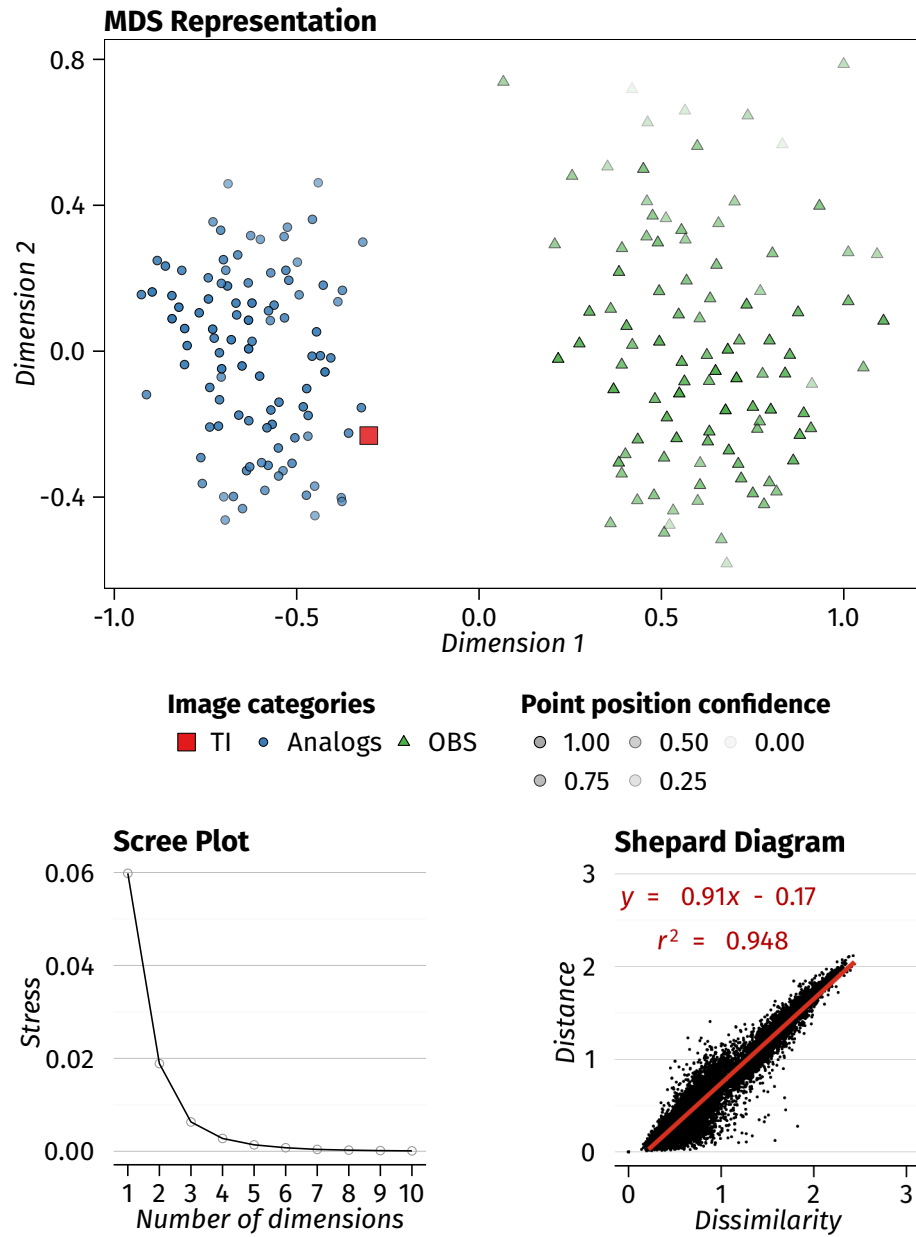


**Figure 2.12** MDS representation of the dissimilarities between the TI, some TI analogs and the OBS realizations generated using SMACOF and validation graphs. The scree plot only displays the stress values up to 10 dimensions on 200 possible.

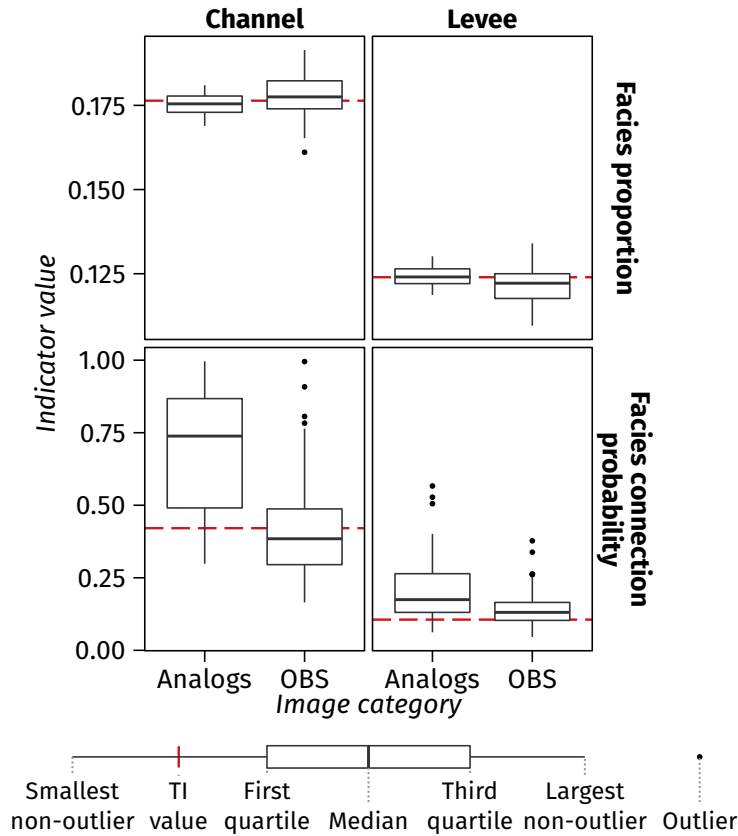


**Figure 2.13** Box-plots comparing the facies proportions and facies connection probability for the TI, some TI analogs and the OBS realizations.

hard to say which one of the DeeSse or IMPALA category is the closest.

All this highlights first differences between indicators. The indicator choice, if any, is not insignificant. It has an influence on the realization ranking. Further study of the indicator behavior is important to better characterize their measures.

### 2.4.5 Analysis of the dissimilarities with the conceptual model

Using MPS calls for a conceptual model of the bodies to simulate. The realizations have to reproduce these bodies and their characteristics, as the connectivity. This makes the quality analysis easier. Indeed, the analysis comes down to a single row of the dissimilarity matrix (or column due to the matrix symmetry). A MDS representation is not necessary any more and all the process can rest on



2 Analyzing stochastic simulations of sedimentary bodies

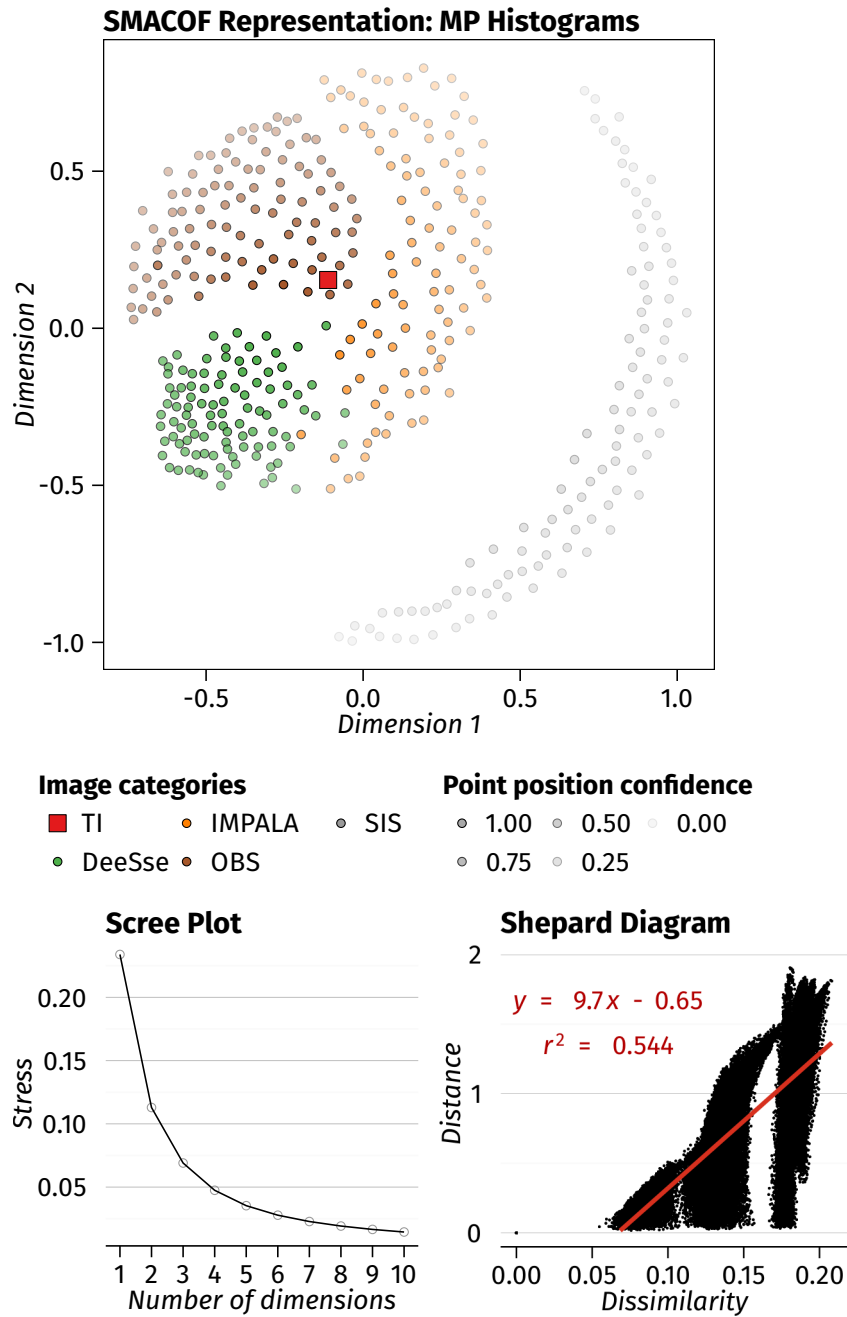


**Figure 2.14** MDS representation of the dissimilarities between the images of the case study generated using SMACOF and validation graphs. The dissimilarities are based on the multiple-point (MP) histograms of the images. The scree plot only displays the stress values up to 10 dimensions on 400 possible.

the real dissimilarity values.

Here only the first row of the dissimilarity matrix is kept. It corresponds to the dissimilarities with the TI (figure 2.15, All the indicators). The IMPALA realizations are globally the closest to the TI; then come the OBS realizations that have a large dissimilarity range; follow the DeeSse realizations and finally the SIS realizations. This differs from the visual inspection of the component shapes: the OBS realizations should be the closest, followed by the MPS methods (DeeSse and IMPALA) and then by SIS realizations. When considering also connections between the objects in the visual inspection, having the DeeSse and SIS realizations as the furthest seems more consistent. This is coherent with the analysis previously done on the MDS representation. But a more detailed analysis is needed to understand the ranking.

The main advantage of such box-plot representation is to compare the ranking based on different indicators. The global (figure 2.15, Global indicators) and shape indicators (figure 2.15, Shape indicators) both have a ranking close to all the indicators. But the global indicators place the DeeSse realizations a bit closer to the TI than the OBS realizations. And the shape indicators place the SIS realizations closer to the TI than the DeeSse realizations. All those indicators measure globally the connected component distribution and shapes. On the other side, the node degree proportions (figure 2.15, Node degree proportions) have a ranking identical to the multiple-point histograms (figure 2.15, MP histograms): OBS realizations are the closest to the TI, followed by the DeeSse and the IMPALA realizations. The SIS realizations are the farthest and remain completely separated from the other categories. This ranking is more consistent with what can be observed visually. And those indicators are different from the other ones as they have a closer view at the connected components. The shape indicators analyze the components at a larger scale and do not see the shape variations in detail, contrary to the multiple-point histograms. On the other side the multiple-point histograms have no clear information on the connections between the patterns, so on the connectivity. The node degree proportions only look at the connectivity, not the shape. Their ranking is consistent with the one of the multiple-point histograms. But they separate more clearly the realizations than the multiple-point histograms.

The choice of the indicators and their combination have therefore a major influence on the analysis. Each indicator has its own way of seeing the sedimentary bodies in the realizations. Understanding the impact of various body organization on them is thus of prime importance, to see the kind of information they can provide, how they behave combined with other indicators and if this information and combinations are clearly relevant to analyze sedimentary bodies and their connectivity.

## 2 Analyzing stochastic simulations of sedimentary bodies

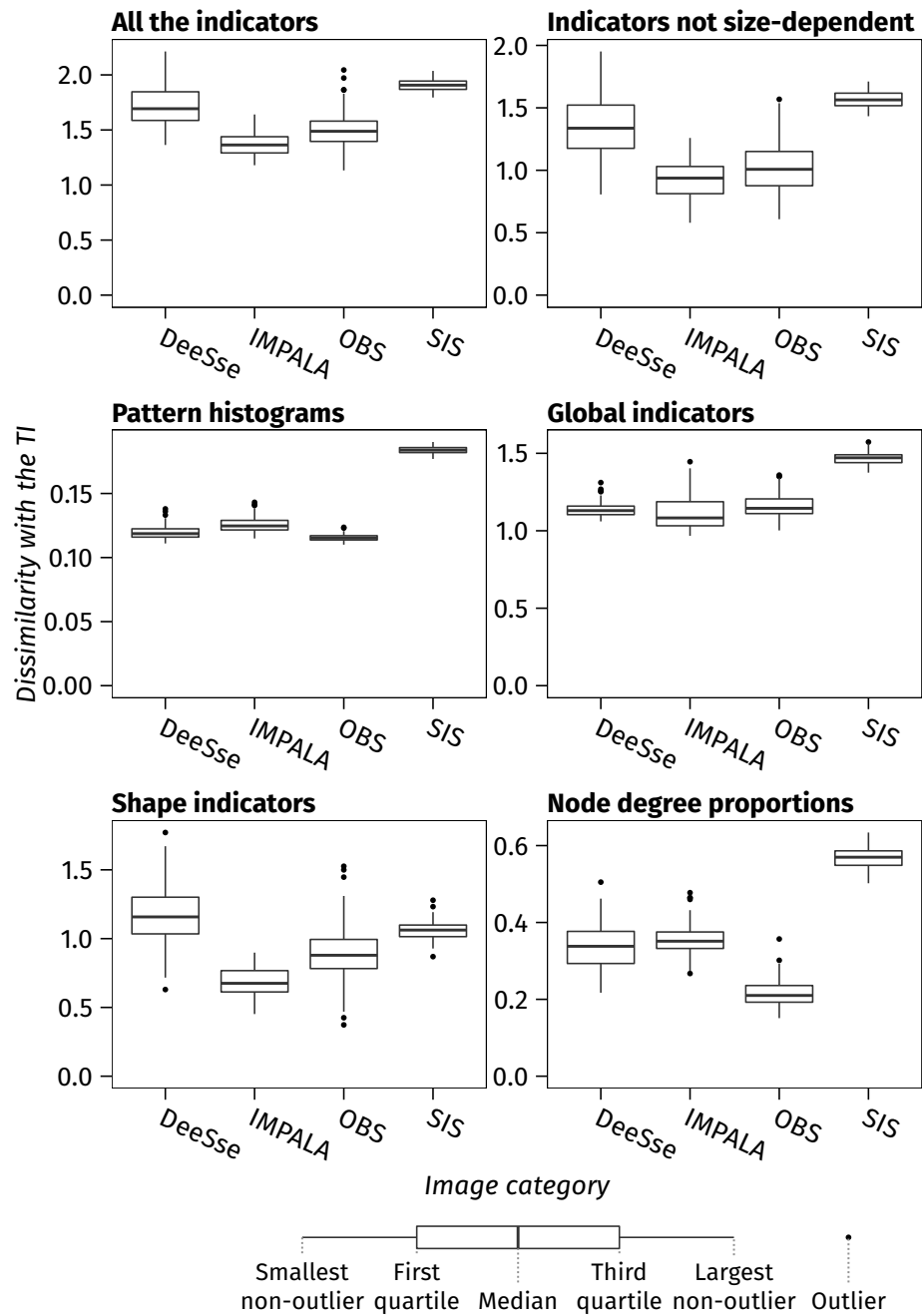


**Figure 2.15** Box-plots comparing the realizations of each method with the TI. The dissimilarities depend on different indicators in each box-plot. The indicators not size-dependent are all the indicators except the component density (section 2.2.2) and the numbers of cells (section 2.2.3).

### 2.4.6 Indicator behavior

Indicators computed for the different methods are given in figures 2.16, 2.18 for the channels and in figures 2.17, 2.19 for the levees. For both channels and levees, the facies proportions and the facies adjacency proportions of IMPALA and OBS are closer to the TI than the other methods, with globally better results with the object-based method. OBS realizations are also interesting in terms of facies connection probability. Globally the connection probability is consistent with the visual observations on the realizations and their skeletons: DeeSse realization components are clearly less connected than OBS ones, this is related to the poor reproduction of the channel proportion, and IMPALA and SIS realization components tend to be over-connected compared to the TI.

The other indicators related to the connected components display much contrasted behaviors. The corrected component density behavior differs following the facies. For the levees, all the methods are quite close all together but far from the TI. For the channels, the SIS realizations have a high density compared with the other categories. DeeSse realizations follow them and OBS realizations have the smallest density. IMPALA realizations are the closest from the TI. This behavior can be linked with the number of component cells: the OBS realizations have the largest components, so at similar proportions a low density is consistent. SIS corrected number of component cells is quite low and their density is high, meaning that those realizations contain many small components. The high connection probability indicates in that case the presence of one huge component. This corresponds to the observations on the realizations. The same observation can be made with IMPALA, but with a less clear behavior. The tendency of SIS and IMPALA realizations to generate small components also appears through the traversing component proportion: it is lower than for the other methods, so fewer components connecting two opposite borders of the image. OBS realizations are less dense, so fewer components relative to the occupied volume, and have relatively bigger components than the TI, with many traversing ones. Expecting a higher connection probability would be reasonable, but as said before the connection probability of OBS realizations is roughly similar to the TI value. This behavior can be related to the difference of image size in two ways:

- The density and the number of component cells for the TI are not the ones measured on the image: they are modified to take into account the difference of image size. This process is essential to be able to compare the indicators. However, it does not remove all the errors due to the difference of grid size. The indicator correction may be improved to lower the errors. But there will always be a doubt on the indicator accuracy.

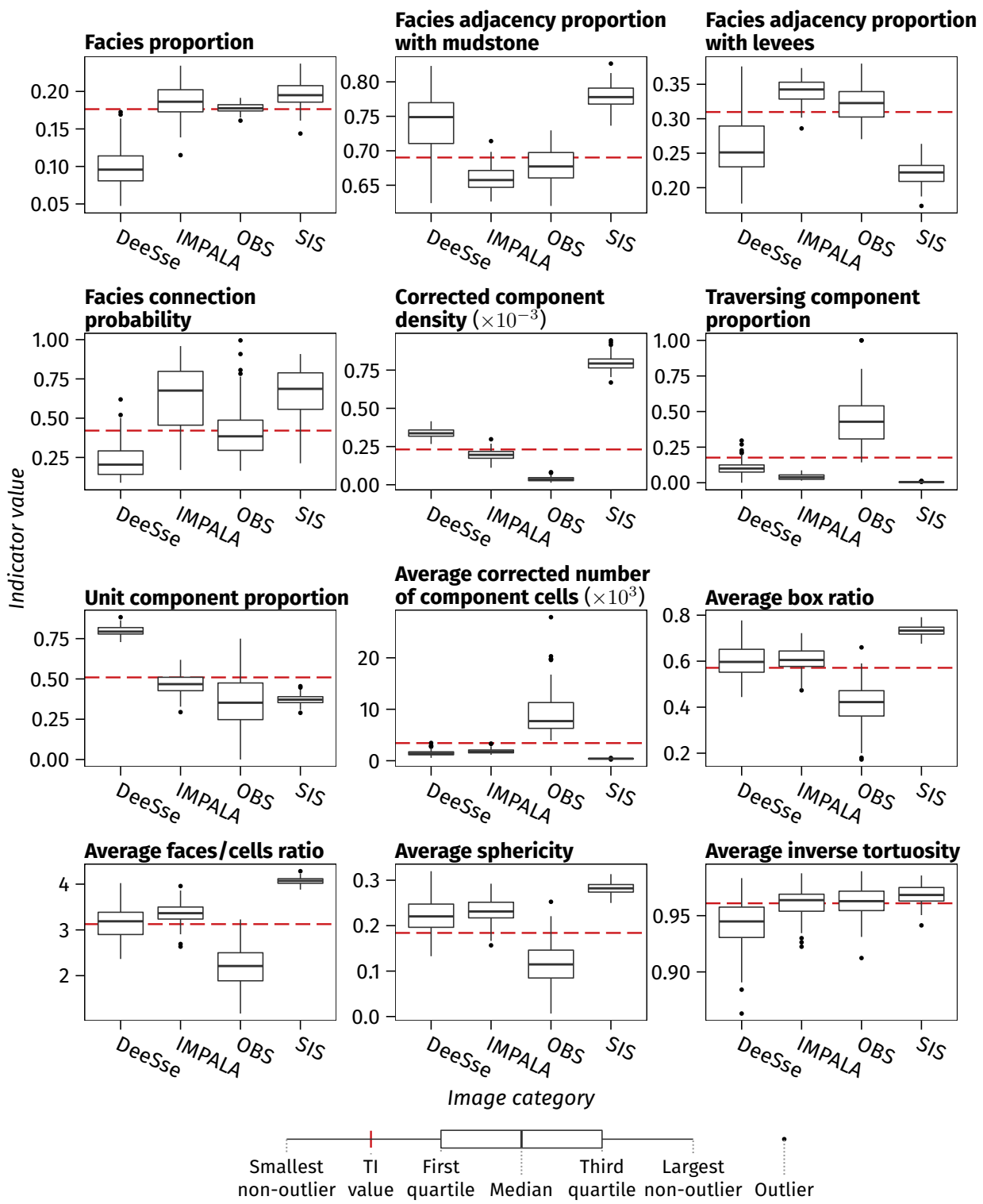


**Figure 2.16** Box-plots comparing the range of indicators computed on the channels for the different methods, except the node degree proportions.

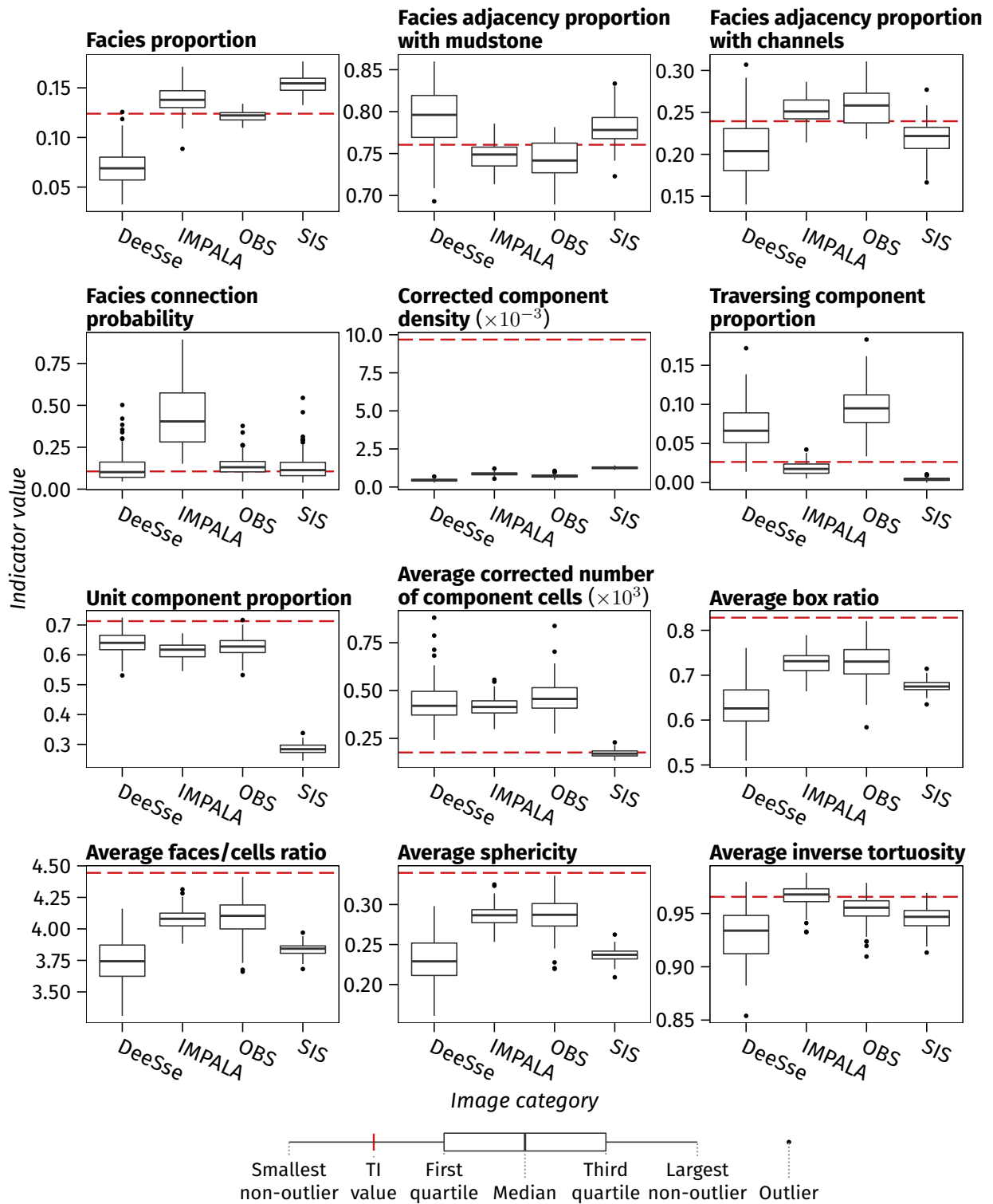


**Figure 2.17** Box-plots comparing the range of indicators computed on the levees for the different methods, except the node degree proportions.

## 2 Analyzing stochastic simulations of sedimentary bodies

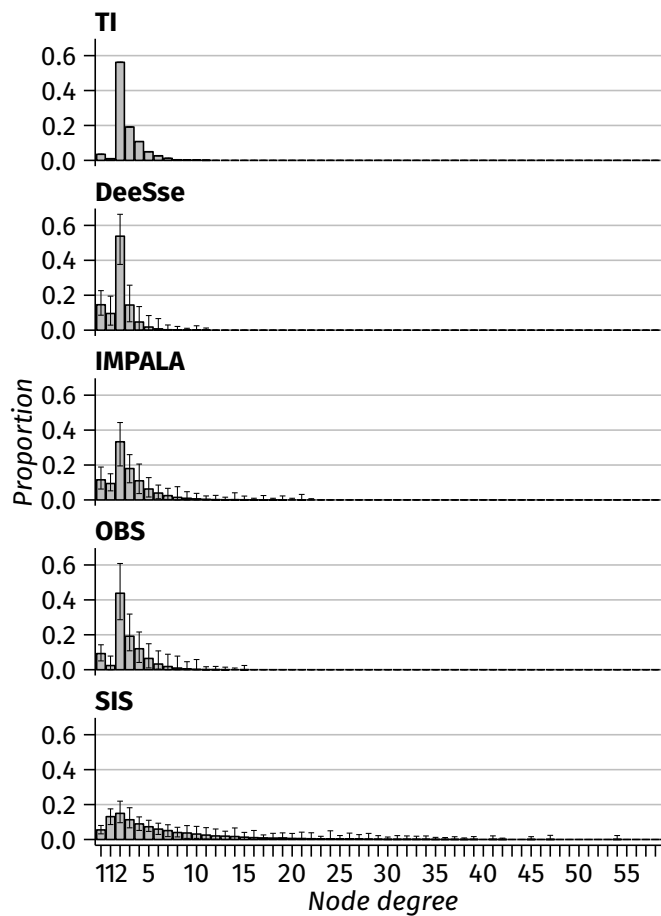


**Figure 2.18** Mean node degree proportions of the channel skeletons for each category. The error bars display the minimum and maximum proportions. The first node degree 1 corresponds to the nodes of degree one along a grid border. The second node degree 1 corresponds to the nodes of degree one inside the grid.

- When the image size following the channel direction is increased, the probability to have channels hitting each other also increases, especially here with sinuous channels. The channels tend to form one connected component at the image scale, whereas at a smaller scale they can form different components. This aspect can be seen in the box ratio and in the sphericity. These two indicators are far less influenced by different grid dimensions than the density or the number of component cells. They are so not based on corrected values. However, they are smaller for the OBS realizations than for the TI. The sphericity highlights the more

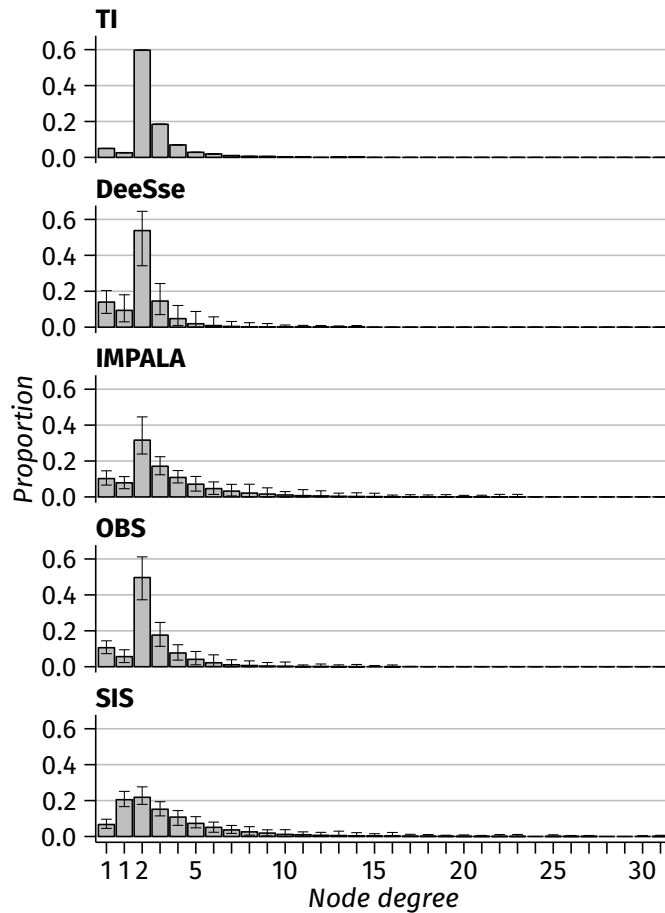


**Figure 2.19** Mean node degree proportions of the levee skeletons for each category. The error bars display the minimum and maximum proportions. The first 1 node degree corresponds to the nodes of degree one along a grid border. The second 1 node degree corresponds to the nodes of degree one inside the grid.

linear aspect of the OBS components, which are gathering fewer channels. The difference in box ratio must come from the fact that gathering two channels does not necessarily increase the bounding box compared to the channels taken individually. This tends to increase the box ratio, what explains the behavior of the TI compared to the OBS realizations.

One solution to limit the impact of different image size could be to extract one or several sub-images of the same size from each image. The comparison would then be made between the sub-images. However, it should be noticed that in this particular case the global ranking to the TI do not change much when



not using the corrected density and numbers of component cells (figure 2.15, Indicators not size-dependent).

The unit component proportion for the channels appears to be high for all the methods. The only clear distinction is from the DeeSse realizations, which have much more unit components than the other images. This is even clearer for the levees, with high proportions for all the categories except the SIS. It is useful to take into account that parameter in the calculation of the other indicators considering its potential influence. But it does not seem highly informative of an image quality. Using it as an indicator could be questioned considering the influence of such component on the fluid flow.

When choosing the skeletonization method and its parameters, we privileged the topology over the geometry. This means avoiding small-scale loops which perturb the node degree proportions. This choice has a direct impact on the inverse tortuosity values: if some variations appear between the categories, those variations are very low with values between 0.9 and 1. As 1 is a straight line, it appears that the skeleton branches are not very tortuous. This comes from the rather large slice thickness used to generate skeletons without small-scale loops. Using thinner slices could help to get more valuable information from the inverse tortuosity. But it could be at the detriment of the node degree proportions. Further work has to be done to improve the feature extraction by the skeletons.

Nevertheless, skeletons seem interesting objects to study the connectivity. Both facies have similar distributions of node degree proportions for all the categories (figure 2.18 and 2.19). SIS realizations have more connections than the other realizations, with far higher node degrees. In return this lowers the proportions of the smaller node degrees, especially the nodes of degree 2. The other categories have more similar distributions. The training image has numerous nodes of degree 2. DeeSse realizations have fewer connections than the TI, with less node of high degrees and more nodes of degree 1. IMPALA realizations have more connections, with fewer nodes of degree 2 and more high degree nodes. OBS realizations have the most similar distributions compared with the TI, as stated by the dissimilarity analysis (figure 2.15, Node degree proportions). This confirms the visual observations on the skeletons (figure 2.7). All the categories have fewer nodes of degree 2 than the TI and more nodes of degree one. The numbers of higher degree nodes vary following the category. At the end the connectivity seems indeed different from the TI for all the categories.

Compared to the previous indicators, the multiple-point histograms provide a more detailed analysis of the different object shapes in an image. Integrating it to the other indicators is so interesting. It would bring their ability to analyze

object shape with more details than the shape indicators currently used and with less impact of different image sizes, at least from what can be seen on this example. Node degree proportions could perfectly complete them to deeply analyze the connectivity and the reproduction at large-scale. Considering that, further studies are needed to understand the relationship between those histograms and the previous indicators, and in particular the shape indicators. This illustrates the difficulties to objectively analyze realization quality.

## 2.5 Conclusions and perspectives

This work develops an analysis process to compare several categorical images in terms of connectivity. The process relies on the computation of dissimilarities from a given set of indicators. These indicators are based on connected components. They cover various aspect of the realizations, from their facies proportions to the size of their components. Their analysis in the presented case highlights their ability to distinguish between realizations simulated with different methods.

The multidimensional scaling summarizes all this information through two-dimensional representations of the dissimilarities. It is a powerful and practical visualization tool to get a first idea of the relationships between the images. But it should be kept in mind that MDS representations provide only a partial view of the dissimilarities. Moreover, the representation and its quality are method-dependent. The MDS representation should so always be interpreted cautiously. Analyzing the dissimilarity matrix shall always be favored rather than analyzing the MDS representations. The heat map helps to have an easier check on the MDS interpretation. Then an analysis should be done on particular rows or column of the matrix depending on the studied cases. This gives access to simple but powerful visualization tools that work on the real dissimilarities.

The realization ranking when gathering the indicators is not what could be expected. But a detailed analysis shows the consistency of the indicator behaviors. Indicators of the connected component shape are interesting for their simplicity. But their sensitivity to the grid size is a real issue. A correction is proposed here, but it does not remove completely the error. It could be interesting to perform the analysis not on the images but on sub-images with the same dimensions. Multiple-point histograms also seem a valid option to analyze more locally the component shape. Skeleton-based indicators appear to be quite promising. The node degree proportions provide a simple way to compare connectivity structures. Further work should be done on the skeletons to better characterize both the connected component topology and geometry.

## 2 Analyzing stochastic simulations of sedimentary bodies

Thus, the present work shows that analyzing the behavior of various indicators needs to be continued. More case studies should be considered. Channels are known to have a heterogeneous filling, with shale acting as a flow barrier. It could be interesting to model and work on the component formed by the reservoir facies rather than by the sedimentary objects they belong to. Starting with real data would also be beneficial.

## Chapter 3

# Stochastic simulation of channelized sedimentary bodies using a constrained L-system

**Abstract** Stochastically simulating realistic sedimentary bodies while conditioning all the available data is an important topic of research. In the particular case of channelized systems, that task is even more difficult due to the highly elongated shape of the channels. The classical dilemma is either simulating channel objects with a poor conditioning ability or simulating within a grid with a poor reproduction of the channel objects. We propose to focus the simulation of channel objects on data conditioning rather than reproducing perfectly their sinuosity. We rely on a formal grammar system, the Lindenmayer system or L-system, to stochastically simulate the channel morphologies resulting of the deposition processes. The L-system puts together channel segments based on user-defined rules and parameters, such as the element size or the angle between two consecutive elements. The succession of segments is then interpreted to generate non-rational uniform B-splines (NURBS) representing straight to highly meandering channels. Data are taken into account during the channel development using constraints. The constraints attract or repulse the channel from the data. They enable to condition various types of data, from well data to probability cubes or a confinement. The application to various synthetic cases highlights its ability to manage various data while preserving at best the channel morphology. Some improvements are still required to better condition the data at small-scale.

### 3.1 Introduction

Stochastic simulation methods rely on two main objectives: representing the geology as precisely as possible and honoring all the available data. Precisely representing the geological structures is essential to pursue the study of a reservoir. These structures may contain fluids or act as flow barriers. From this point of view their connectivity and its reproduction are fundamental. Channelized systems are a specific case of such structures. Their main constituting elements are highly continuous channelized sedimentary bodies – up to several hundreds of kilometers in turbiditic systems – often filled with sand. These channels are so potential reservoirs.

Representing channels causes several problems to stochastic simulation methods. Cell-based methods [e.g., [Deutsch and Journel, 1992](#), [Galli et al., 1994](#), [Strebelle, 2002](#)] attribute a category to each cell within a discretized domain, based on a prior model. Conditioning to well data is easy with such process, but most of the time the channel continuity is not preserved. This leads to a connectivity different from the prior model or from object-based methods (figure 3.1). These object-based methods [e.g., [Viseur, 2001](#), [Deutsch and Tran, 2002](#), [Pyrz et al., 2009](#)] rely on defining a geometrical representation of the channels, with parameters such as their width or their wavelength. They preserve the channel continuity. However, data conditioning is difficult, contrary to cell-based methods. This is partly due to the highly elongated shape of channels and the poor flexibility of their representations.

Simulating channels requires a balance between some geological concepts, such as the channel elongated shape, and data conditioning (figure 3.2). Wells are a first and prime source of data. They help to locate the channels and may give some indication about the connectivity between the wells. Seismic data are less precise than well data, but they give an information at larger scales. They can provide sand probability cubes for instance. If the resolution is good enough, some objects can be directly interpreted on seismic data.

In numerical biology, tree and root simulation methods rely also on object-based approaches [e.g., [Prusinkiewicz and Lindenmayer, 1996](#), [Palubicki et al., 2009](#), [Leitner et al., 2010](#)]. One of their interesting developments is the consideration of the environment influence to improve the simulation realism: influence of gravity, influence of the sun light distribution or influence of the presence of other trees, etc. [e.g., [Mvech and Prusinkiewicz, 1996](#), [Streit et al., 2005](#), [Taylor-Hell, 2005](#)]. These methods are based on a formal grammar, the Lindenmayer system or L-system. It was first proposed as a formal description of the development of filamentous organisms [[Lindenmayer, 1968](#)]. Despite their ability to integrate various data, very few works relate on formal gram-

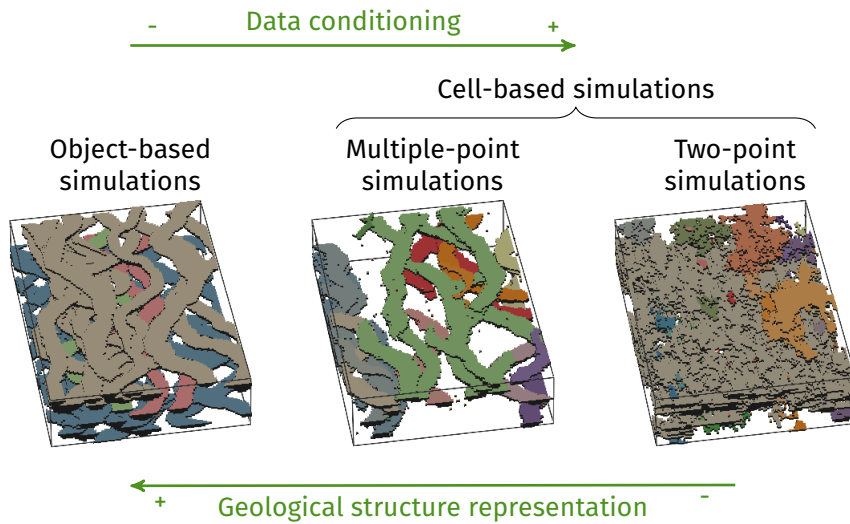


**Figure 3.1** Types of stochastic simulation methods and relationship between geological structure representation and conditioning. The figures show the channels in realizations from different simulation methods, with the colors highlighting the connected components of the channels. These simulation methods have to model the same structures with priors from the same source. The resulting realizations differ significantly, in particular in term of connectivity.

mars to simulate channels. Hill and Griffiths [2009] use an analog model to define some rules for a formal grammar system. These rules are the basis for stochastic simulation, in a process similar to multiple-point simulation. However data conditioning remains limited to sparse hard data, i.e., well data or channel segment interpreted from seismic data.

The present work aims at applying the principles of L-systems (section 3.2) to object-based approaches. The main idea is to simulate the morphology resulting from the flow processes forming channels. L-system rules simulate the channel morphology (figure 3.2), from straight to highly sinuous channels (section 3.3). During the application of the L-system rules, constraints influence the channel growth to condition to various data (section 3.4). The purpose of this research is to facilitate data conditioning as compared to other object-based approaches while keeping the main added-value of these approaches: the preservation of the channel shape. An illustration of the parameter impact and the addition of constraints to the system is based on simple cases (section 3.5). A more complete synthetic case study considers the simulation of turbiditic channels within a submarine canyon. It leads to a discussion on the integration of data

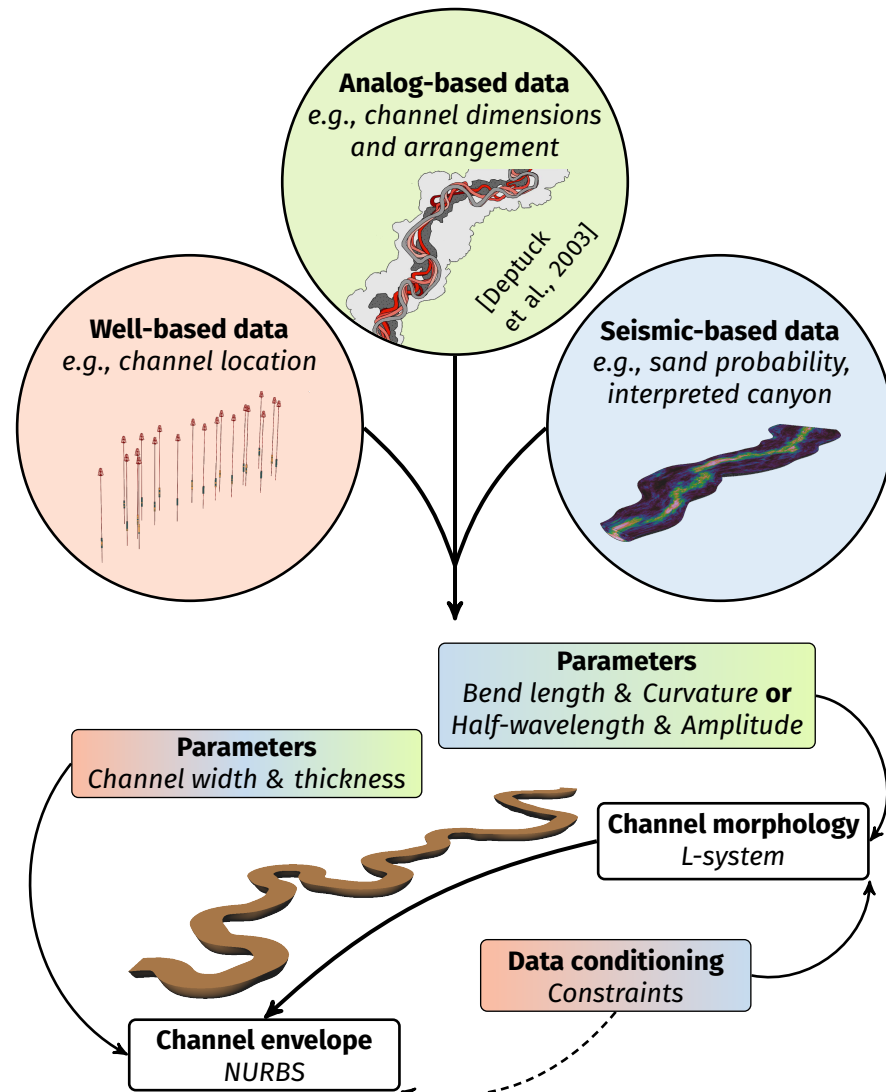


**Figure 3.2** Workflow for channel simulation based on L-systems with data and parameter sources.

of different types, such as well sedimentary data or facies probability cubes, in the simulation of turbiditic channels within a submarine canyon (section 3.6).

The whole method was implemented in C++ within the Gocad plug-in ConnectO. The channel envelopes with NURBS were implemented by J r my Ruiu within the Gocad plug-in GoNURBS [Ruiu et al., 2015b].

## 3.2 L-system principles

As formal grammar systems, L-systems rely on string rewriting. Letters from an alphabet are tied together by production rules to form and change strings. For an exhaustive review about L-systems, see [Prusinkiewicz and Lindenmayer \[1996\]](#).

### 3.2.1 Basic L-systems

A L-system starts with an initial string called the axiom ( $\omega$ ). A set of rules, called production rules ( $p_i, i \in [1, n]$ ,  $n$  being the number of rules), controls the rewriting. The rules are first applied on the axiom and then on its substitutes, following a certain number of iterations, the order. In the most simple type of L-system, the rules are made of a predecessor and a successor:

$$\text{predecessor} \longrightarrow \text{successor}$$

The principle is to scan the axiom or its substitute. Each time a predecessor is found, its corresponding successor replaces it. For instance with the following system:

$$\begin{aligned} \omega & : b \\ p_1 & : a \longrightarrow ab \\ p_2 & : b \longrightarrow a \end{aligned}$$

The evolution of the system for an order of five is:

$$\begin{aligned} 0 & : b \\ 1 & : a \\ 2 & : ab \\ 3 & : aba \\ 4 & : abaab \\ 5 & : abaababa \end{aligned}$$

In the previous system, both rules are applied at each iteration until the order is reached. Another possibility is to express directly which rule can be used at which iteration, giving here:

$$\begin{aligned} \omega & : b_0 \\ p_1 & : a_i \longrightarrow a_{i+1}b_{i+1} \quad 0 \leq i \leq 4 \\ p_2 & : b_i \longrightarrow a_{i+1} \quad 0 \leq i \leq 4 \end{aligned}$$



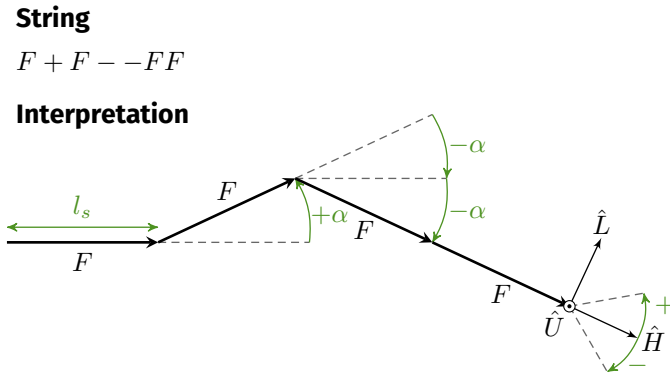


**Figure 3.3** Example of string and its geometrical interpretation.  $l_s$  is a segment length and  $\alpha$  the angle between to successive segments. The letter interpretations are given in table 3.1. The vectors  $\hat{H}$ ,  $\hat{L}$  and  $\hat{U}$  are represented at the current turtle position  $\vec{P}$ . They control the further displacement of the turtle.

Compared to other formal grammar systems, the L-system is parallel and not sequential: at a given iteration, the rules are applied simultaneously on all the letters.

### 3.2.2 Classical alphabet and geometrical interpretation

The purpose of the geometrical interpretation is to graphically represent the string resulting from the rewriting. At each letter of the alphabet corresponds an action that drives the string representation. Several interpretation methods exist, the most famous being the turtle interpretation [Prusinkiewicz, 1986].

The turtle is represented by a position vector  $\vec{P}$  and an orthonormal coordinate system centered on the turtle position (figure 3.3). Three orientation vectors compose that system:

- $\hat{H}$  is the direction along which the turtle moves forward.
- $\hat{L}$  is the direction to the left for the turtle.
- $\hat{U}$  is the up direction for the turtle.

The position and the three vectors of the turtle's coordinate system form the turtle's state.

Two operations change the turtle's state:

- Moving forward of a given length  $l_s$ .

**Table 3.1** Basic L-system alphabet and corresponding geometrical interpretation.

Letters	Interpretation
$F$	Move forward of a length $l_s$ and draw a segment between the new position and the former one
$f$	Move forward of a length $l_s$ without drawing a segment
$+$	Turn left by an angle $\alpha$ based on the rotation matrix $R(\hat{U}, \alpha)$
$-$	Turn right by an angle $\alpha$ based on the rotation matrix $R(\hat{U}, -\alpha)$

- Rotating of a given angle  $\alpha$  following a given axis represented by  $\hat{H}$ ,  $\hat{L}$  or  $\hat{U}$ .

The rotation is based on the following update of the vectors:

$$\begin{bmatrix} \hat{H}' & \hat{L}' & \hat{U}' \end{bmatrix} = \begin{bmatrix} \hat{H} & \hat{L} & \hat{U} \end{bmatrix} R(\hat{V}, \alpha) \quad (3.1)$$

where  $\hat{H}$ ,  $\hat{L}$  and  $\hat{U}$  are the current vectors,  $\hat{H}'$ ,  $\hat{L}'$  and  $\hat{U}'$  are the updated vectors,  $\hat{V}$  is  $\hat{H}$ ,  $\hat{L}$  or  $\hat{U}$  depending on the wanted rotation axis,  $\alpha$  is the rotation angle in radian and  $R$  is the rotation matrix:

$$R(\hat{V}, \alpha) = \begin{pmatrix} \cos \alpha + V_x^2(1 - \cos \alpha) & & & & & & \\ V_y V_x(1 - \cos \alpha) + V_z \sin \alpha & & & & & & \\ V_z V_x(1 - \cos \alpha) - V_y \sin \alpha & & & & & & \\ & V_x V_y(1 - \cos \alpha) - V_z \sin \alpha & & & & & \\ & \cos \alpha + V_y^2(1 - \cos \alpha) & & & & & \\ & V_z V_y(1 - \cos \alpha) + V_x \sin \alpha & & & & & \\ & & V_x V_z(1 - \cos \alpha) + V_y \sin \alpha & & & & \\ & & V_y V_z(1 - \cos \alpha) - V_x \sin \alpha & & & & \\ & & \cos \alpha + V_z^2(1 - \cos \alpha) & & & & \end{pmatrix} \quad (3.2)$$

with  $\hat{V} = (V_x, V_y, V_z)$ . Then, the turtle position  $\vec{P}$  is updated to its new position  $\vec{P}'$  by taking into account the wanted length  $l_s$ :

$$\vec{P}' = \vec{P} + l_s \hat{H}' \quad (3.3)$$

A letter of the alphabet can then change the turtle's state based on those two operations, i.e., moving forward and rotating. It is also possible to give a

tangible form to the interpretation by generating an object segment (figure 3.3). The main symbols of the classical L-system alphabet and their interpretation are given in table 3.1. Other symbols exist for pitching based on a rotation around  $\hat{L}$  and rolling based on a rotation around  $\hat{H}$ .

### 3.2.3 Stochastic L-systems

Basic L-systems produce deterministic systems. There are two ways of adding stochasticity to obtain different strings and interpretation from one system:

- Randomizing the L-system parameters, especially those of the geometric interpretation, i.e., the angle  $\alpha$  and the length  $l_s$ .
- Randomizing the production rule selection:

$$predecessor \xrightarrow{p} successor$$

with  $p \in [0, 1]$  the rule probability for the rule drawing.

Whereas the first way affects only the geometry of the system, the second one can affect both the geometry and the topology. In the following example, the rules  $p_1$  and  $p_2$  are not both applied at each iteration. Only one of them is chosen each time following a random draw based on the given probabilities:

$$\begin{aligned} \omega & : b \\ p_1 & : a \xrightarrow{0.75} ab \\ p_2 & : a \xrightarrow{0.25} bbb \\ p_3 & : b \longrightarrow a \end{aligned}$$

### 3.2.4 Context-sensitive L-systems

Context-sensitive L-systems give the possibility to look at the context of the predecessor. When looking at a rule application, the string has not only to match the predecessor, but also its context. This context is separated in two parts: the left context corresponds to the letters that should be just before the predecessor and the right context to the letters that should be just after:

$$left\ context < predecessor > right\ context \longrightarrow successor$$

The context can be one-sided if needed, i.e., with only a left context or only a right context. For instance, the rule  $p_1$  can only be applied if the predecessor

$a$  is followed by  $b$  and the rule  $p_2$  can only be applied if the predecessor  $b$  is preceded by  $aa$ :

$$\begin{aligned} \omega & : b \\ p_1 & : a > b \longrightarrow ab \\ p_2 & : aa < b \longrightarrow a \end{aligned}$$

### 3.2.5 Parametric L-systems

Parametric L-systems were defined to improve the numerical power of L-systems and their ability to deal with continuous phenomena. One or several parameters can be assigned at each letter of the alphabet. They can be updated when rewriting a predecessor into its successor:

$$\text{predecessor}(\text{parameters}) : \text{conditions} \longrightarrow \text{successor}(\text{parameters}')$$

The use of parameters also enables the definition of conditions. The use of the rules is then subject to the condition validation. In this case, a string has not only to match the predecessor letters, but the number of parameters for each letters has also to be the same and the conditions, if any, have to be validated. Here, the letter  $b$  is associated to one parameter  $h$  that can represent anything from a branch length to a concentration of a certain element. The rule  $p_2$  can only be applied to a letter  $b$  with one parameter and as long as that parameter is less than 1:

$$\begin{aligned} h & = 0 \\ \omega & : b(h) \\ p_1 & : a \longrightarrow ab(h + 0.1) \\ p_2 & : b(h) : h \leq 1 \longrightarrow a \end{aligned}$$

$h$  is global for the whole system and is not reset at the end of each iteration.

### 3.2.6 Environmentally-sensitive and open L-systems

In the previous L-system types, the turtle interpretation is a post-processing step to associate a geometry to a string. It has no effect on the string rewriting, which can be limiting in many applications. For instance the growth of a plant is influenced by its environment, such as the light exposure. In these cases the rewriting and the interpretation must take into account the influence of the environment.

In environmentally-sensitive L-systems, the turtle interpretation is done after each rewriting step [Prusinkiewicz et al., 1994]. Query modules enable

**String**

$ABC - [+DE][SG[+HI[-JK] + L]MNO]$

**Interpretation**

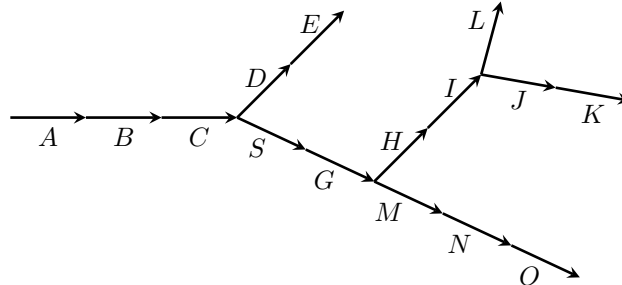


**Figure 3.4** Example of string and geometrical interpretation (adapted from Prusinkiewicz and Lindenmayer [1996]). Letters *A* to *O* are different to facilitate the reading, but have all the same effect as a *F* from table 3.1.

to get some information from the interpretation and its relationship with its environment. For instance the rewriting process can get the current turtle state to influence the next rewriting steps.

Open L-systems generalize environmentally-sensitive L-systems [Mvech and Prusinkiewicz, 1996]. They have the same ability to receive information from the environment, but with the additional ability to update that environment following the system growth. For instance the growth of a root is influenced by the water repartition within the ground. Along its development, the root uses that water and so modify its distribution in the soil. In this case the root growth has also an impact on the environment, which then affects the root growth.

### 3.2.7 Bracketed L-systems

Trees are based on a branching structure. To simulate trees, L-systems have to be able to generate branches. Square brackets are used to handle branches: the opening bracket [ records the current turtle state while the closing bracket returns to the saved state ]. Between the brackets are mentioned the letters corresponding to the branch (figure 3.4).

The introduction of brackets is simple for all the previous L-system types, except the context-sensitive L-systems. When searching a left context and meeting a closing bracket, the branch has to be ignored and the search has to start again after the corresponding opening bracket.

All those systems can be combined together, giving the possibility to take into

account various natural phenomena, for instance the propagation of a signal in a branch through auxin transport, and to generate various objects, from trees to fractals (for more details see [Prusinkiewicz and Lindenmayer \[1996\]](#)).

## 3.3 L-system for channel stochastic simulation

Depending on their depositional environment, channels can display various morphologies, from straight to highly sinuous channels. In this work, we use L-system to simulate the channel morphology. The idea is to represent the channelized bodies resulting from the flow processes and not the flow processes themselves.

### 3.3.1 Simulation domain definition

Channelized systems that raise interest as reservoirs are not necessary in their depositional state. They have been affected by various geological events, possibly implying folding and faulting. It is difficult if not impossible to introduce all these events in the L-system.

The structural modeling workflow leads to the generation of a geological grid based on the horizons and the faults within the domain of interest (figure 9, introduction). This geological grid is often hexahedral and conformable to those horizons and faults. Its parametric space  $(u, v, t)$  can so be interpreted as a depositional space, with  $(u, v)$  the geographical coordinates and  $t$  the time (figure 3.5) [[Mallet, 2004](#)].

The channel simulation does not necessarily need to be applied in the Euclidean  $(x, y, z)$  space representing the current geological space. Any space can be used if a transformation exists to represent the system in the Euclidean space at the end. Using the parametric space of a grid representing the domain of interest circumvents the issue of taking into account the evolution of the domain after the channel deposition. It implies that the grid is conformable to the horizons delimiting the formations associated with channelized systems.

In some cases the parametric space of a grid has some drawbacks, such as unwanted deformations of the grid cells. A more complex approach such as the Geo-Chronological model (GeoChron) [[Mallet, 2004](#)] can be used to parameterize a depositional space. GeoChron relies on a mathematical formulation of time-stratigraphy concepts defined by [Wheeler \[1958\]](#). It provides a new space in which the horizons are flat and the faults have disappeared, similarly to the deposition space. From a simulation point of view the principle remains the same: simulating the channels in the depositional space and then transferring the resulting models into the Euclidean space.

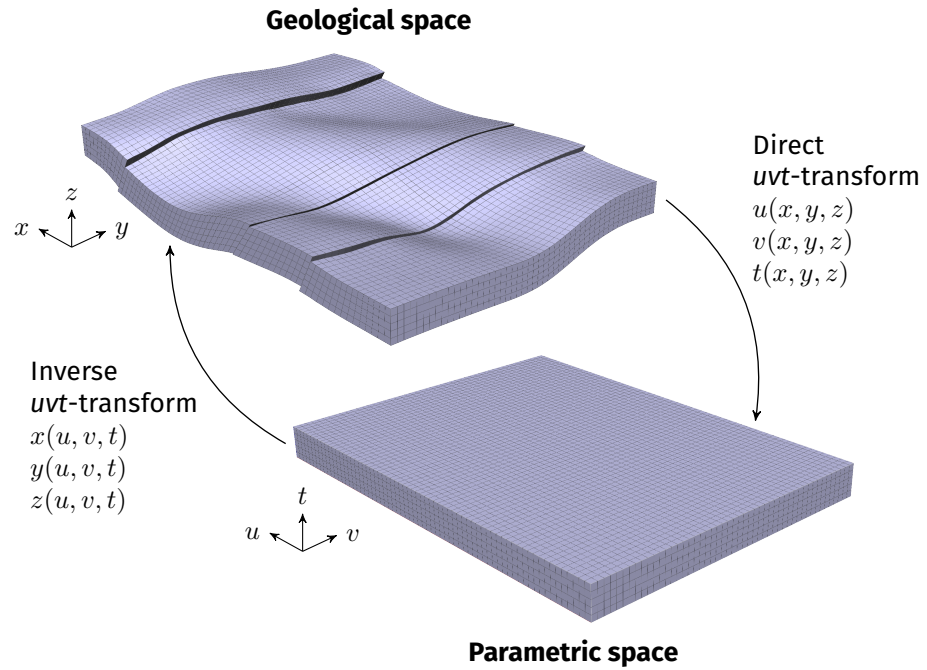


**Figure 3.5** Example of curvilinear grid and representation of its parametric space (inspired by Mallet [2004]).

### 3.3.2 Channel object parameterization

The channel object is based on the channel boundary model defined by Ruiu et al. [2015b]. It relies on Non-Uniform Rational B-Splines (NURBS), a generalization of the Bézier curves [Piegl and Tiller, 1995]. NURBS present the advantage of being easy to deform, which can be useful for data conditioning. Five NURBS surfaces are gathered to form a channel: one flat surface represents the top of the channel, two curved surfaces joining at the channel maximal depth represent the sides and bottom of the channel and two flat surfaces represent the channel extremities. Four parameters are necessary to build the NURBS model (figure 3.6):

- A discretized channel centerline, also called backbone [e.g., Wietzerbin, 1994, Viseur, 2001, Pyrcz et al., 2009]. This centerline is at the channel top and informs about the channel sinuosity.
- A set of channel widths along the centerline.
- A set of channel thicknesses along the centerline.

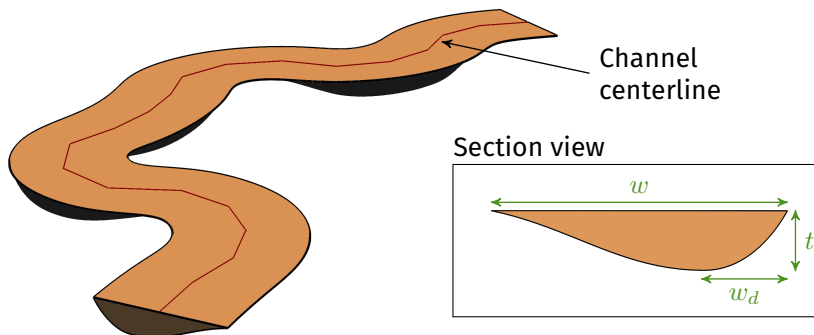


**Figure 3.6** Channel envelope modeled with NURBS surfaces and required parameters for its simulation.  $w$  is the channel width and  $t$  is the channel thickness.  $w_d$  is the length between the outer border of the channel and the maximum depth. The asymmetry aspect ratio is equal to  $w_d/w$ .

- An asymmetry aspect ratio.

The process simulates at first the L-system string, which contains all the parameter values required to generate the channel object. Thus, the channel representation is only created at the end of the simulation process.

### 3.3.3 Initial turtle state

The initial position of the system can come from different sources:

- Directly given by the user.
- Randomly drawn among the not yet conditioned well channel data. In this case, a data is first drawn, and the position is randomly perturbed both horizontally and vertically depending on the channel minimal width and minimal thickness. At the end, the channel still fits the data but at different locations at each simulation.
- Randomly drawn within the domain of interest.
- Randomly drawn within the domain of interest with the influence of a sand probability cube, if one is defined within the domain.

A channel global direction comes from an input azimuth and defines the turtle's initial coordinate system, with the turtle's head directly oriented along this direction. The global direction can be the same for the whole channel, or it can come from a property defined within the domain of interest. In this case, the direction is given by the property at the initial position of the channel.



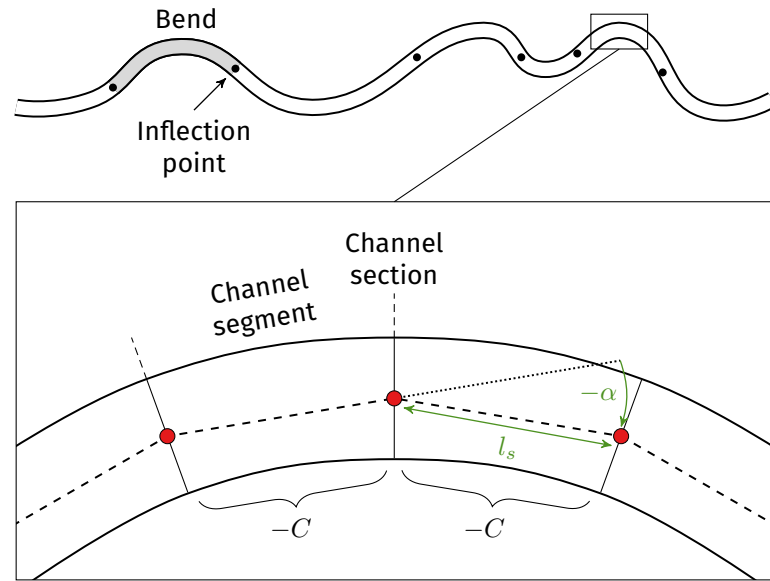


**Figure 3.7** Principle of channel discretization for L-system simulation. The red dots correspond to the position of the channel sections, obtained from the turtle interpretation.  $l_s$  is both a channel element length and the distance between two successive sections.  $\alpha$  is the angle between two successive sections, i.e., the change of orientation between two successive channel segments.

### 3.3.4 Basic considerations and alphabet

After the parameterization, a channel can be seen as a discretized object composed of channel segments separated by transversal channel sections (figure 3.7). A section is at the end of its respective segment. Each section is aligned on the bisector between its segment and the next segment, as in the NURBS model [Ruiu et al., 2015b]. An orientation and a distance from the previous section characterize a given section. The L-system rewriting process determines the location of each section, which then gets a channel width and thickness at this location. Thus, each section knows all the parameters to build the channel object (see section 3.3.2) at that position. The geometrical interpretation consists in building the NURBS representation.

Five letters constitute the alphabet to model the succession of sections:  $+$ ,  $-$ ,  $C$ ,  $T$  and  $I$  (table 3.2). The letters  $+$  and  $-$  modify the orientation of the system just as in the classical L-system. They have a main impact on the channel morphology. The letter  $C$  is comparable in its effect to the letter  $F$  defined in table 3.1. A channel section is symbolized by a  $\pm C$  pair.

**Table 3.2** Basic L-system alphabet and corresponding geometrical interpretation for channel axis simulation.

Letters(parameters)	Interpretation
$I$	First letter of a L-system string giving the initial position
$T$	Do nothing
$C(l_s)$	Move forward of a length $l_s$ and draw a channel section between the new position and the former one
$+(\alpha)$	Turn left by an angle $\alpha$ based on the rotation matrix $R(\hat{U}, \alpha)$
$-(\alpha)$	Turn right by an angle $\alpha$ based on the rotation matrix $R(\hat{U}, -\alpha)$

The letter  $I$  has no influence in the string rewriting process. It is only used during the geometrical interpretation to state the initial position of the channel. The letter  $T$  has no influence on the geometrical interpretation. It is only used during the string rewriting to assure the channel growth, as detailed in the next section.

### 3.3.5 Rule definition

A channel is decomposed into several bends separated by inflection points (figure 3.7). A bend is a succession of channel segments whose orientations change along the same direction. Thus, it is a succession of  $\pm C$  letters, with  $\pm$  being  $+$  or  $-$  but remaining the same along the bend. The number of channel segments within each bend is here an essential parameter. The L-system process for channel simulation calls for four parameters:

- A default segment length  $l_d$ .
- An angle between two successive segments  $\alpha$ .
- A bend length  $l_B$ , i.e., the curvilinear distance between two inflection points.
- A channel length  $l_C$ , which is not necessary with a simulation domain.

The L-system rules are separated in three steps: the initiation, the development and the closure. In each rule,  $l_B$  and  $l_d$  determine the number  $n_s$  of segments of a bend by:

$$n_s = \lceil l_B/l_d \rceil \quad (3.4)$$

### 3 Stochastic simulation of channelized sedimentary bodies

where  $\lceil x \rceil$  rounds  $x$  upward. The actual segment length  $l_s$  is recomputed as follows:

$$l_s = l_B / n_s \quad (3.5)$$

#### Initiation and development rules

The initial position of the channel does not need to be an extremity of the channel. Indeed, the initial position can be drawn in the middle of the simulation domain and not necessary on its border. Thus, a channel is divided into two branches: the first branch grows in one direction and the second branch in the opposite direction. The initiation rules start this branching structure (figure 3.8). It is symbolized by the brackets, with in between the letters corresponding to the first branch. The initiation rules simulate a single bend separated into two parts, one for each branch. The numbers of segments for each part,  $n_{s_1}$  and  $n_{s_2}$ , are computed by:

$$\begin{aligned} n_{s_1} &\sim \mathcal{U}(1, n_s - 1) \\ n_{s_2} &= n_s - n_{s_1} \end{aligned} \quad (3.6)$$

where  $n_s$  is the total number of segments for the bend and  $\mathcal{U}$  is a uniform discrete distribution with its minimal and maximal values as parameters.  $n_{s_1}$  is randomly drawn from that distribution. This random draw implies:  $n_s \geq 2$ , so  $l_B > l_d$  based on equation 3.4. The initiation rules are stochastic: they simulate a bend in one direction or the other depending on an equal probability of occurrence.

The channel must be oriented along the global direction, which defines the initial turtle's state. The initial turtle's state influences the orientation of the first segment of each branch. The angle of these segments must be modified, otherwise they would follow the global direction whereas the channel could follow a different direction. The angles  $\alpha$  of these segments become:

$$\begin{aligned} \alpha_1 &= \alpha \times \left( \frac{n_s}{2} - n_{s_1} + 1 \right) \\ \alpha_2 &= \alpha \times \left( \frac{n_s}{2} - n_{s_2} \right) \end{aligned} \quad (3.7)$$

A letter  $T$  is placed at each branch extremity to continue the growth.

This growth is assured by the development rules. Their purpose is to assure the channel growth by tying channel bends one after the other. These rules simply replace a  $T$  by a new bend, with a letter  $T$  at the end to pursue the channel development. They are context-sensitive. This enables to change the bend orientation from one bend to the other.

### 3.3 L-system for channel stochastic simulation

**Axiom**  $IT$

**Initiation**

**Rules**

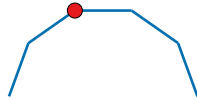
$$T \xrightarrow{0.5} \left[ +(\alpha_1)C(l_s)\{+(\alpha)C(l_s)\}^{n_{s1}-1} T \right] + (180) - (\alpha_2)C(l_s)\{-(\alpha)C(l_s)\}^{n_{s2}} T$$

$$T \xrightarrow{0.5} \left[ -(\alpha_1)C(l_s)\{-(\alpha)C(l_s)\}^{n_{s1}-1} T \right] + (180) + (\alpha_2)C(l_s)\{+(\alpha)C(l_s)\}^{n_{s2}} T$$

**Final string** *Iteration 1*

$I[-C-C-C-T] + (180)+C+C T$

**Interpretation**



**Development**

**Rules**

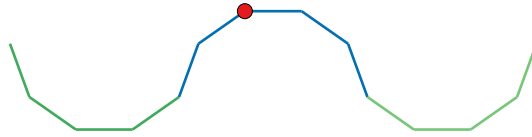
$$-(\alpha)C(l_s) < T \rightarrow \{+(\alpha)C(l_s)\}^{n_s} T$$

$$+(\alpha)C(l_s) < T \rightarrow \{-(\alpha)C(l_s)\}^{n_s} T$$

**Final string** *Iteration 2*

$I[-C-C-C+C+C+C+C T] + (180)+C+C-C-C-C-C T$

**Interpretation**



**Final string** *Iteration 3*

$I[-C-C-C+C+C+C+C-C-C-C-C T] + (180)+C+C-C-C-C-C+C+C+C+C T$

**Interpretation**

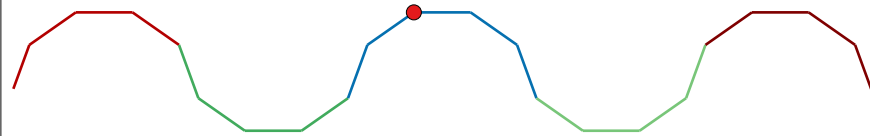


**Figure 3.8** Simplified illustration of channel simulation based on a L-system. The red point is the initiation point for the interpretation. The first iteration initiates the channel structure, divided in two branches, based on stochastic rules. The following iterations handle channel growth depending on the context.

### Stopping criteria and closure rules

For channel simulation the stopping criterion of the rewriting is not an order. When the L-system process occurs within a simulation domain, the process can stop as soon as the two branches go outside the grid. A second possibility is to stop the process as soon as a target channel length  $l_C$  is reached. A parameter  $l_c$  keeps track of the channel length during the growth. When that length is equal or larger than the target channel length  $l_C$ , the rewriting process stops.

Obtaining channels of a precise length is possible through closure rules. In this case, the development rules are called only if the new channel length does not exceed the target channel length:

$$l_c + l_B \leq l_C \quad (3.8)$$

The closing rules redefine the bend length as:

$$l_B = l_C - l_c \quad (3.9)$$

They are called only two times, one per branch, and are expressed as:

$$\begin{aligned} -(\alpha)C(l_s) < T &\longrightarrow \{+(\alpha)C(l_s)\}^{n_{s_n}} \\ +(\alpha)C(l_s) < T &\longrightarrow \{-(\alpha)C(l_s)\}^{n_{s_n}} \end{aligned} \quad (3.10)$$

The number  $n_{s_n}$  of segments in those rules is defined as:

$$n_{s_n} \sim \mathcal{U}(0, n_s) \times i + n_{s_o} \quad (3.11)$$

where  $\mathcal{U}$  is a uniform discrete distribution with its minimal and maximal values as parameters. At the very beginning of the rewriting process,  $i$  is set to 1 and  $n_{s_o}$  to 0. Once a closure rule is called,  $i$  is set to 0 and  $n_{s_o}$  becomes:

$$n_{s_o} = n_s - n_{s_n} \quad (3.12)$$

At the second call, the number of segments of the bend becomes the  $n_{s_o}$  of the first call. This operation gives to the channel the target length  $l_C$ .

In the whole process, two parameters are drawn from some statistical distributions to add more stochasticity to the system:

- The channel length is drawn before the start of the rewriting process.
- A bend length is drawn each time a rule is called, so for each new bend.

The default segment length remains the same for all the segments. The angle between each segment varies for each segment. But this parameter is not directly asked in input, as detailed in the following section.

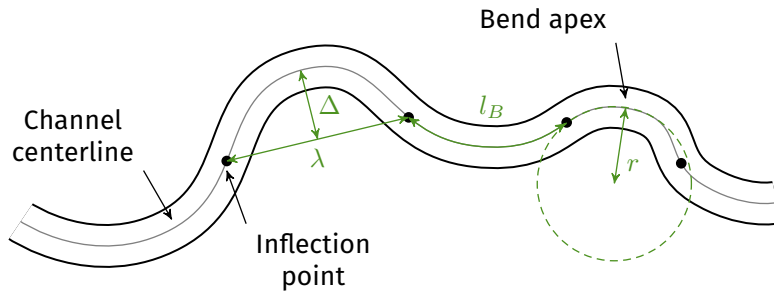


**Figure 3.9** Parameters used to characterize an ideal channel bend.  $l_B$  is the bend length,  $\lambda$  is the bend half-wavelength,  $\Delta$  is the bend amplitude and  $r = 1/c$  is the radius of curvature, with  $c$  the curvature.

### 3.3.6 L-system parameters

The rules for channel simulation call for four parameters: the channel length, the bend length, the default segment length and the angle between two successive segments. Among those parameters, the bend length and the angle define the morphology of the bends and of the channel. From a user point of view, an angle is not a parameter easy to infer. Thus, it could be useful to replace it by other parameters more classically used in the geomorphological description of channel bends. The L-system rules are then modified to handle the conversion between the user input parameters and the L-system parameters. Two sets of exclusive parameters are proposed here: a bend length and a curvature or a bend amplitude and a bend half-wavelength (figure 3.9).

#### Bend length and curvature

The first set of parameters keeps the bend length and only changes the angle between successive channel segments. The idea is to rely on the radius of curvature of a bend, which is the inverse of the curvature. This radius corresponds to the radius of a circle fitted to the apex of the bend (figure 3.9).

For a section  $i$ ,  $\alpha$  is then expressed as:

$$\alpha_i = \frac{c(l_{s,i-1} + l_{s,i})}{2} \quad (3.13)$$

with  $c$  the curvature,  $l_{s,i-1}$  and  $l_{s,i}$  the distances to the previous and next sections, or equivalently the length of the current channel segment and the length of the next segment element.  $\alpha$  is in radian. The curvature does not need to be signed. The sign is defined by the L-system itself by means of the + and –

letters. From a user point of view, a curvature is more independent from the segment length than an angle.

While the draw of a bend length is done from a statistical distribution for each rule, the curvature is drawn from a statistical distribution for each segment. This leads to more various bend morphologies without introducing more parameters. Indeed, using a single radius of curvature for a whole bend is not enough to characterize the variety of bend shapes [Howard and Hemberger, 1991].

From a process perspective, both curvature or radius of curvature could be used. The radius of curvature is a length, so it may be a simpler parameter from a user perspective than a curvature. From a geomorphological point of view, a single value of radius of curvature is often used to characterize a given bend. Here the radius of curvature changes along a bend. So we choose to keep the curvature, which could be less misinterpreted.

Table B.4 of appendix B gathers the complete L-system rules for channel simulation with a bend length and a curvature.

### **Bend half-wavelength and bend amplitude**

The second set of parameters is a simplification of the first one. Indeed, both a curvature and a radius of curvature may be difficult to infer on a bend. This set relies on the bend half-wavelength, i.e., the Euclidean distance between two successive inflection points, and the bend amplitude, i.e., the maximal distance between the half-wavelength line and the bend centerline (figure 3.9).

Without stochasticity in the geometrical parameters, the L-system generates bends with the shape of a circular arc. It is thus possible to link both the bend length  $l_B$  and the curvature  $c$  to a half-wavelength  $\lambda$  and an amplitude  $\Delta$  thanks to the intersecting chord and the law of cosines. The curvature  $c$  is expressed as:

$$c = \frac{8\Delta}{4\Delta^2 + \lambda^2} \quad (3.14)$$

And the bend length  $l_B$  becomes:

$$l_B = \frac{2 \arccos(1 - \Delta c)}{c} \quad (3.15)$$

During the simulation, a half-wavelength and an amplitude are drawn for each bend. They can not be drawn for each segment, as the bend length would then vary for each segment. Thus, the curvature is always the same for each segment of a bend. This may limit the stochasticity of the system and limit the

variety of bend morphologies. A deviation angle  $\delta$  is added to the angle  $\alpha$  to compensate that effect and to add some variability:

$$\alpha_i = \frac{c(l_{s,i-1} + l_{s,i})}{2} + \delta \frac{\pi}{180} \quad (3.16)$$

where  $\alpha$  is in radian and  $\delta$  is in degree.

### 3.3.7 Extending the influence of the global direction

The global direction is one of the input parameters. It is the direction along which the channel should develop. Only the initial turtle's state takes it into account. It does not influence the further developments of the system.

When the L-system parameter values have few variations from bend to bend, the channel continues to follow roughly the channel direction. When the L-system alternates straight and sinuous bends, the resulting channels often self-intersect. These self-intersections are an inconsistency. They result from the L-system interpretation principle: a new segment only knows its previous neighbor and ignores all about the previous segments and their locations.

Extending the influence of the global direction to the whole system helps to better control the channel orientation and limit self-intersections. The global direction  $\hat{D}$  directly influences the turtle's head  $\hat{H}$ :

$$\begin{aligned} \hat{H}' &= \frac{\vec{K}}{\|\vec{K}\|} \\ \vec{K} &= \epsilon_h \hat{H} + \epsilon_d \hat{D} \end{aligned} \quad (3.17)$$

where  $\hat{H}'$  is the new turtle's head,  $\epsilon_h$  is a weight on the L-system,  $\epsilon_d$  is a weight on the global direction.  $\epsilon_h$  and  $\epsilon_d$  are user-defined and allow controlling the influence of the L-system and of the global direction. This process is done by the letters that define the change of orientation between the channel sections, i.e., + and -. It applies after the orientation change done by the L-system.

The input global direction comes from two possible sources:

- A direction directly defined for the whole system.
- A property cube defined over the whole domain of interest. In this case, the direction is updated when simulating a new section depending on the cell in which is the current section.



### 3.3.8 Simulating the channel width and thickness

The L-system in itself simulates the channel centerline required by the channel object. The channel width and thickness are simulated for each section at the end of the L-system rewriting and interpretation. Then, building the channel object means interpolating the channel sections based on their widths and thicknesses and interpolating the channel shape between the sections. The channel width and thickness are simulated at each channel section using a Sequential Gaussian Simulation (SGS).

To simplify the use, several SGS parameters are kept constant, with the idea of having smooth variations between the sections:

- The variogram nugget effect is set to 0.
- The variogram sill is set to 1, as the SGS calls for a normal score transform.
- The variogram model is defined as Gaussian.

Two additional parameters are let to the user: distributions of width or thickness values and variogram ranges for the width and thickness. The ranges define the scale of oscillation of the width and thickness. Both the width and the thickness may vary following the channel curvature. Thus, this curvature is used as a secondary variable of the SGS. This adds another parameter: the curvature weight. When the weight is equal to one, the spatial structure of the width or the thickness strictly follows the spatial structure of the curvature. When the weight is equal to zero, the width or the thickness are completely independent from the curvature.

Table 3.3 resumes all the parameters required to simulate a channel object. It contains the parameters related to the L-system and the parameters defining the section of the channel. The L-system rules do not appear in this list: as they are predefined, they are not strictly an input, but nothing prevents from modifying them.

## 3.4 Adding external constraints

In biology, constraining the development of L-systems manages the interaction between trees and their environment [e.g., [Taylor-Hell, 2005](#), [Longay et al., 2012](#)]. External constraints are added to the L-system through an environmentally-sensitive process. After each rewriting step, an interpretation allows gathering some information about the channel and its environment, such as the channel position relative to a well data. Such information helps to

**Table 3.3** Input parameters to simulate a channel from L-system and NURBS. Only the L-system and envelope parameters are essential. An asterisk symbolizes a parameter not necessarily required with a simulation domain. The parameters in italic call for statistical distributions.

Simulation input	
<b>Domain</b>	Grid representing the domain of interest
	* Initial position
	L-system weight
	<i>Azimuth defining the global direction</i> (in °)
<b>L-system</b>	Global direction weight
	Default segment length (in m)
	* <i>Channel length</i> (in m)
	<i>Bend length</i> (in m) } or { <i>Bend half-wavelength</i> (in m)
	<i>Curvature</i> (in m <sup>-1</sup> ) } or { <i>Bend amplitudes</i> (in m)
	} or { <i>Deviation angles</i> (in °)
	<i>Channel width</i> (in m)
	<i>Channel width range</i> (in m)
<b>Channel section</b>	Curvature weight for the width
	<i>Channel thickness</i> (in m)
	<i>Channel thickness range</i> (in m)
	Curvature weight for the thickness
	Asymmetry aspect ratio

build constraints that influence the further development of the system. The following sections provide a general definition of the constraints, before detailing the constraints predefined for channel simulation.

### 3.4.1 Formalization

A vector materializes a constraint and indicates where the system should preferentially go under the constraint influence. This vector decomposes in three elements:

- $\hat{\Lambda}$  is a normalized vector indicating the constraint direction.
- $\rho$  is the vector magnitude which determines the force of the constraint.
- $\epsilon$  is a user defined weight to adjust the relative importance of each constraint.

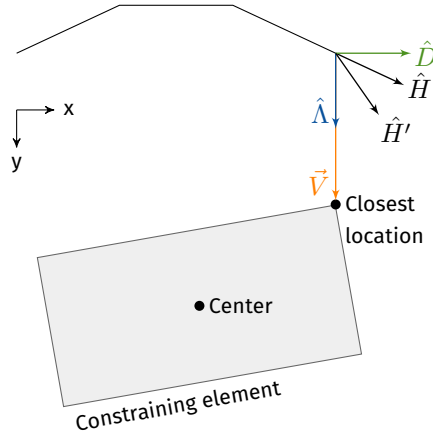
### 3 Stochastic simulation of channelized sedimentary bodies

#### String

$-C - C - C$

#### Interpretation

Attractive constraint



Repulsive constraint

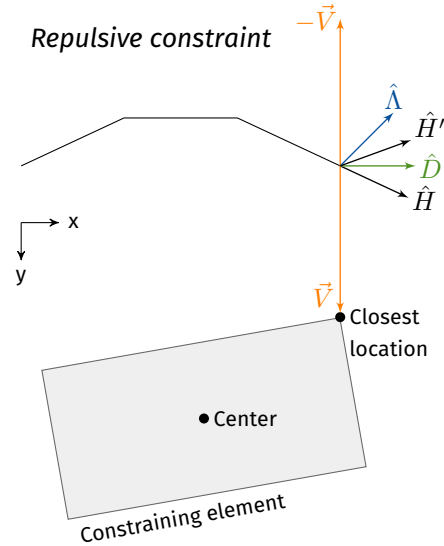


**Figure 3.10** Principle of constraint application to a L-system.  $\hat{H}$  is the current turtle's head and  $\hat{H}'$  the new turtle's head that takes into account the constraint.  $\hat{D}$  is the global direction of the channel.  $\hat{A}$  is the constraint direction, deduced from  $\vec{V}$ .  $\vec{V}$  is the vector between the turtle's head and a point on the constraining element, either its center or the closest location to the turtle's head. The next sections give further details about constraint application.

Either the vector materializing a constraint is directly given as input, or it is defined from a vector between the turtle's head and a given constraining element. In the second case, determining a constraint means choosing a constraining element and determining the constraint vector (figure 3.10).

The constraints are separated into two categories:

- Relative constraints have their magnitude that depends on the distance to their constraining element. Thus, they are only defined relatively to a constraining element, for instance a well or a seismic-interpreted object.
- Global constraints have a magnitude independent from the distance to their constraining element. Thus, they do not necessarily require a constraining element. In this case, the constraint vector is given in input and is constant over the whole system. The channel global direction is

equivalent to a global constraint without constraining element. A probability cube is another example of global constraint, with the constraining element depending on the local maximum probability value.

In addition, a constraint can be (figure 3.10):

- Attractive, i.e., it attracts the system toward the constraining element.
- Repulsive, i.e., it repulses the system from the constraining element.

### 3.4.2 Sources of constraining elements

In channel simulation, adding external constraints has two goals:

- Controlling the relationship between simulated channels and between different parts of a channel.
- Conditioning the channel to data. The two main sources of data are the wells and the seismic cubes.

The previous channels, channel parts, well or seismic data provide potential constraining elements for the system.

#### Previous channel sections

When simulating several channels, some can develop at the same depth and intersect each other. If required, this configuration is preventable by adding repulsion constraints between the previously simulated channels and the new channels. Such repulsive constraints are also useful to further prevent channel self-intersections when the channel sinuosity becomes locally too important. Indeed, the global direction is not always sufficient to prevent self-intersections.

#### Well sedimentary data

Wells are classical data in geology. They provide a local and often precise information about the facies and the associated sedimentary bodies. The simulation process supposes that the sedimentary objects are already interpreted along the wells.

We consider separately two main types of data:

- Channel data comes from channelized bodies, whatever their mud content. The simulated channels have to condition such data, i.e., each channel data must end up in at least one channel for all the realizations. Constraints create an attraction to the data to ensure the conditioning. But all the data should not attract a single channel at the same time.

### 3 Stochastic simulation of channelized sedimentary bodies

- Inter-channel data correspond to all the other sedimentary bodies around channels, such as overbanks. They are often deposited alongside a channel and eroded by the younger channels. A channel should not condition such data, i.e., no inter-channel data must end up in a channel for all the realizations.

#### **Well connectivity data**

When studying or exploiting a reservoir, connectivity data between wells are sometimes available. If so, they can inform about the connection or disconnection of two wells. This forms sets of connected data, which knows their non-connected counterparts. When a channel conditions a data from such set, it has to condition the other connected data. It has also to avoid the entire non-connected data set.

#### **Probability cube**

Seismic data provide an overview of the underground in three-dimensions. Unfortunately their resolution is not always sufficient to identify geological structures. However, some information can still be extracted, such as the sand probability within the domain of interest [e.g., [Strebelle et al., 2003](#)]. As channels often have a sandy filling, those data influence the channel locations: a high channel probability is considered to be positively correlated to a high sand probability. A probability cube first helps to determine the channel initial position (see section [3.3.3](#)) and then influences the channel development. The mean of many realizations, i.e., the E-map, should be as close as possible to the sand probability cube, without forgetting that simulating channels is not simulating sand distributions.

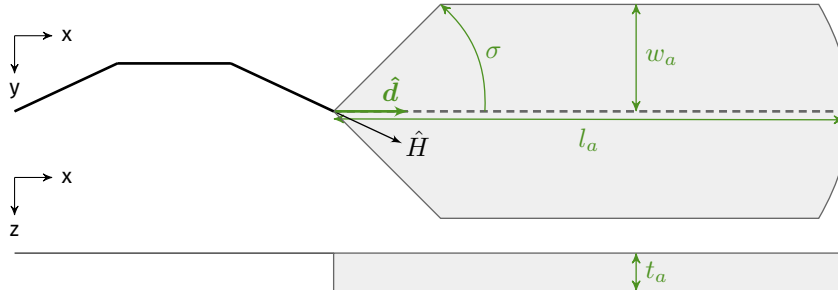
#### **Seismic-interpreted objects**

Sometimes seismic data have a sufficient quality for object interpretation. This interpretation is most of the time done manually. [Ruiu et al. \[2015a\]](#) developed such semi-automated approach with NURBS. The interpreter must digitize the channel centerline. A deformation process automatically fits the NURBS surfaces to the channel observed on the seismic data. The simulation process should take into account such interpreted sedimentary objects.

In turbiditic environments, channels often develop within a confining master channel. This confinement is a major source of uncertainty [[Larue and Hovadik, 2008](#)] and is one of the first features to determine in a reservoir study. When observable on seismic data, the confinement must be interpreted to influence

**String**

$-C - C - C$

**Interpretation**

**Figure 3.11** Parameters defining the area which select the constraining elements.  $\hat{H}$  is the turtle's head.  $\hat{d}$  is the direction of the area,  $\sigma$  is the direction tolerance,  $w_a$  is the maximal half-width of the area,  $l_a$  is the area length and  $t_a$  is the area thickness.

the simulated channels. During the simulation within the confinement, constraints prevent the channels from going out of the master channel: its margins repulse the channel.

### 3.4.3 Constraining element selection

A constraining element influences the system development depending on two factors. The first factor is a perception area from the turtle's head: the constraining elements falling into that area may influence the system. The other elements that fall outside the area are ignored.

This perception area is a band starting from the current position of the system. Four parameters define it (figure 3.11):

- $\hat{d}$  is the center direction of the band.
- $\sigma$  is the direction tolerance, defined as an angle from the center direction.
- $w_a$  is the bandwidth, i.e., the maximal half-width of the area.
- $l_a$  is the area length.
- $t_a$  is the area thickness, defined below the channel segments because they are at the top of a channel.

$w_a$  and  $l_a$  are used to reduce the perception area and limit the number of constraints.

### 3 Stochastic simulation of channelized sedimentary bodies

The second factor is a selection criterion, which defines if a constraining element within the perception area induces a constraint or not. There are three possibilities:

- All the elements within the perception area influence the system.
- Only the closest element to the turtle's head influences the system.
- Only the element with the highest value of a given property influences the system.

Usually those factors are applied for each section during the interpretation. Thus the constraining elements may change between two successive sections: a section has no memory about the constraining elements of the previous sections. For some constraints, especially relative attractive constraints, the system can memorize the constraining elements until the conditioning, even if that element is not in the perception area any more.

#### 3.4.4 Constraint definition

A vector characterizes a constraint through three components: a direction, a magnitude and a weight. The weight is a constant scalar value. The other two elements have more complex definition.

##### Constraint direction

The direction  $\hat{\Lambda}$  of constraint application defines if a constraint is attractive or repulsive:

$$\hat{\Lambda} = \begin{cases} \frac{\vec{V}}{\|\vec{V}\|} & \text{if the constraint is attractive} \\ \frac{\hat{D}-\vec{V}}{\|\hat{D}-\vec{V}\|} & \text{if the constraint is repulsive} \end{cases} \quad (3.18)$$

where  $\hat{D}$  is the global channel direction. Adding the global direction to repulsive constraints helps to limit abrupt direction changes due to a high repulsion.

$\vec{V}$  is the vector between the turtle's head and a particular point on the constraining element. This point can be:

- The center of the constraining element. The vertical component of  $\vec{V}$  is set to zero to avoid any vertical perturbation of the channel centerline.
- The closest location along the element border at the same vertical coordinate.

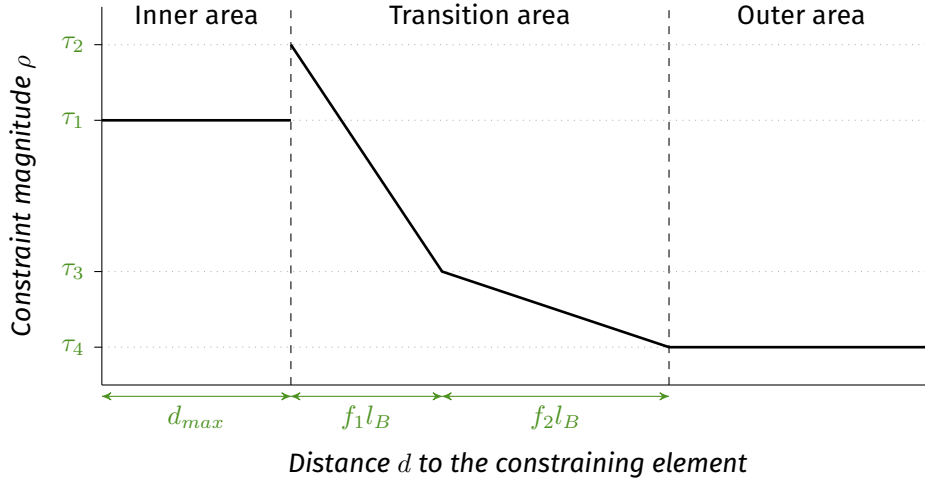


Figure 3.12 Parameters defining the magnitude of a relative constraint.

### Constraint magnitude

The constraint magnitude  $\rho$  varies between 0 and 1 and depends on the constraint type. For a global constraint, the magnitude is expressed as:

$$\rho = 1 \quad (3.19)$$

By definition, the magnitude of a relative constraint varies following the distance  $d$  between the turtle's head and the constraining element:

$$\rho = \begin{cases} \tau_1 & \text{if } d < d_{max} \\ \tau_2 + (\tau_3 - \tau_2) \frac{d - d_{max}}{f_1 l_B} & \text{if } d_{max} \leq d \leq d_{max} + f_1 l_B \\ \tau_3 + (\tau_4 - \tau_3) \frac{d - d_{max} - f_1 l_B}{f_2 l_B} & \text{if } d_{max} + f_1 l_B < d \leq d_{max} + (f_1 + f_2) l_B \\ \tau_4 & \text{if } d > d_{max} + (f_1 + f_2) l_B \end{cases} \quad (3.20)$$

with  $0 \leq \tau_1, \tau_2, \tau_3, \tau_4 \leq 1$ .

Adding a constraint induces a deformation of the L-system. The purpose with a relative constraint is to disrupt as little as possible the morphology generated by the L-system. Thus the magnitude evolves following three areas (figure 3.12).

The inner area is defined by a distance  $d_{max}$  and a magnitude  $\tau_1$ . This is the conditioning area toward which the channel evolves in case of an attractive constraint or the absolutely forbidden area for a repulsive constraint. For channels,  $d_{max}$  is equal to half the channel width.



The outer area is when the turtle's head is far away from the data. The magnitude value in this area  $\tau_4$  must be as low as possible to perturb at least the channel morphology.

In between, the magnitude evolves following the bend length  $l_B$ , because a larger bend length requires more anticipation to attract or repulse. This transition area gradually adjust the magnitude from the outer to the inner area. It has two parts:

- The first part is adjacent to the inner area and its length is controlled by the bend length and a factor  $f_1$ . It is the core part of the constraint influence, which ensures the conditioning.
- The second part is near the outer area and its length is controlled by the bend length and a factor  $f_2$ . Its magnitude variation is less abrupt than in the first part. Thus the constraint effect can begin early without deforming too much the channel morphology.

The magnitude goes from  $\tau_4$ , the magnitude in the outer area, to  $\tau_3$  and then  $\tau_2$ , the highest magnitude value of the constraint.

Representing the magnitude with a piecewise function requires many parameters, but this function is easier to define than a single function with similar variations. Moreover, adding other parameters that could influence the magnitude is far easier with this representation than with a single continuous function.

### 3.4.5 Adding the constraints to the L-system

Once defined, the constraints are added to the turtle head  $\hat{H}$  by modifying the formula 3.17:

$$\begin{aligned}\hat{H}' &= \frac{\vec{K}}{\|\vec{K}\|} \\ \vec{K} &= \epsilon_h \rho_r \hat{H} + \epsilon_d \rho_r \hat{D} + \sum_{j=1}^{n_g} \epsilon_{g,j} \rho_r \hat{\Lambda}_j + \sum_{i=1}^{n_r} \epsilon_{r,i} \rho_i \hat{\Lambda}_i \\ \rho_r &= \prod_{i=1}^{n_r} (1 - \epsilon_{r,i} \rho_i)\end{aligned}\quad (3.21)$$

with  $\hat{H}'$  the new turtle head,  $n_g$  the number of global constraints and  $n_r$  the number of relative constraints.  $\epsilon_{g,j}$  is a user-defined weight for each global constraint  $j$ .  $\epsilon_{r,i}$  is a user-defined weight for each relative constraint  $i$ .  $\epsilon_h$  and  $\epsilon_d$  are the user-defined weights for the L-system and the global direction.  $\rho_i$  is the magnitude of the constraint  $i$  and  $\hat{\Lambda}_i$  the constraint direction. The magnitude  $\rho_r$

**Table 3.4** Constraints defined for channel simulation.

Constraint	Constraint type	Constraining element
Channel self-repulsion	Relative & repulsive	Channel section
Well channel data	Relative & attractive	Well point
Well inter-channel data	Relative & repulsive	Well point
Well connected channel data	Relative & attractive	Well point
Well non-connected channel data	Relative & repulsive	Well point
Probability cube	Global & attractive	Grid cell
Confinement	Relative & repulsive	Grid border

decreases the turtle's head magnitude, the global direction magnitude and the global constraint magnitudes when a relative constraint has a high magnitude. This improves the conditioning by limiting the influence of the other constraints when getting close the considered data.

### 3.4.6 Constraint setting

From all the sources of constraining elements defined in section 3.4.2, some have been retained for their interest in the stochastic simulation of channelized systems:

- Channel self-repulsion helps to prevent self-intersections when simulating highly sinuous channels, which are inconsistencies.
- Wells are classical data and the only data with a low uncertainty. Thus, their conditioning is essential. A well is here considered as a set of aligned points.
- A probability cube derived from seismic data, e.g., a sand probability cube, can give previous information about the sedimentary body continuity and spatial organization.
- The confinement, for instance a canyon or a master channel, is highly important due to its influence on the channel location. Its impact on the uncertainties of the models is significant [Larue and Hovadik, 2008]. Here the confining structure is defined as a hexahedral grid. The channels are simulated within the parametric space of that grid. The two opposite borders parallel to the channel global direction are the constraining elements.

### 3 Stochastic simulation of channelized sedimentary bodies

**Table 3.5** Parameters to determine a constraint.

Feature	Sub-feature	Type	Symbol	Definition
Weight		All	$\epsilon$	Weight to control the relative strengths of the constraints
Constraining element selection	Perception area	All	$\hat{d}$	Center direction
			$\sigma$	Direction tolerance
			$w_a$	Bandwidth
			$l_a$	Length
			$t_a$	Thickness
	Selection	All	$C$	Selection criterion within the perception area
	Memory	All	$M$	Keep the constraining element over the next sections
Direction		All	$L$	Location on the constraining element from which comes the constraint
			$\hat{\Lambda}$	Constraint direction
Magnitude		Relative	$\tau_1, \tau_2, \tau_3, \tau_4$	Magnitude values delimiting the inner, transition and outer areas
			$d_{max}$	Size of the inner area
			$f_1, f_2$	Factors controlling the transition area
		Global		Always 1

All those elements define different constraints (table 3.4).

A relative constraint requires seventeen parameters. A global constraint requires ten parameters, as the magnitude is always one (table 3.5). Such a number of parameters is rather constraining from a user point of view. For the sources introduced previously, it is possible to define default values (tables 3.6, 3.7 and 3.8). These values come from different tests of the method. For most cases, they should be sufficient to ensure the conditioning. If not, the user can still adjust the values.

Among all the parameters, ten parameters remain required in input. Five of them are the weights  $\epsilon$  associated to each constraint. They allow the user to adjust the relative importance of each constraints. Some weights are the

### 3.4 Adding external constraints

**Table 3.6** Parameters to define the perception area and to choose the constraining element(s) within that area.  $\hat{H}$  is the turtle's head,  $\hat{U}$  is the turtle's up direction,  $R$  is the rotation matrix from 3.2,  $\hat{D}$  is the global direction of the channel,  $l_s$  is the channel segment length,  $w_{a,CD}$  is the perception area bandwidth for the well channel data and  $t_{min}$  is the minimal channel thickness. The user input parameters are in bold.

	$\hat{d}$	$\sigma$	$w_a$	$l_a$	$t_a$	$C$	$M$
<b>Channel self-repulsion</b>	$\hat{H}$	$90^\circ$	$+\infty$	$+\infty$	$t_{min}$	Closest	–
<b>Well channel data</b>	$\hat{H} + \hat{D}$	$90^\circ$	$w_{a,CD}$	$+\infty$	$t_{min}$	Closest	No
<b>Well inter-channel data</b>	$\hat{H}$	$125^\circ$	$+\infty$	$+\infty$	$t_{min}$	All	–
<b>Well connected data</b>	$\hat{H} + \hat{D}$	$90^\circ$	$+\infty$	$+\infty$	$t_{min}$	Closest	Yes
<b>Well non-connected data</b>	$\hat{H}$	$125^\circ$	$+\infty$	$+\infty$	$t_{min}$	All	–
<b>Probability cube</b>	$\hat{H} + \hat{D}$	$45^\circ$	$+\infty$	$5l_s$	$t_{min}$	Max value	–
<b>Confinement (border 1)</b>	$\hat{D} + R(\hat{U}, \frac{\pi}{2})$	$0^\circ$	$+\infty$	$+\infty$	$0$	Closest	–
<b>Confinement (border 2)</b>	$\hat{D} + R(\hat{U}, -\frac{\pi}{2})$	$0^\circ$	$+\infty$	$+\infty$	$0$	Closest	–

**Table 3.7** Parameters to define the constraint direction.  $\vec{V}$  is a vector between the turtle's head and the constraining element location and  $\hat{D}$  is the global direction of the channel. The user input parameters are in bold.

	$L$	$\hat{\Lambda}$
<b>Channel self-repulsion</b>	Section position	$\frac{\hat{D} - \vec{V}}{\ \hat{D} - \vec{V}\ }$
<b>Well channel data</b>	Well point	$\frac{\vec{V}}{\ \vec{V}\ }$
<b>Well inter-channel data</b>	Well point	$\frac{\hat{D} - \vec{V}}{\ \hat{D} - \vec{V}\ }$
<b>Well connected data</b>	Well point	$\frac{\vec{V}}{\ \vec{V}\ }$
<b>Well non-connected data</b>	Well point	$\frac{\hat{D} - \vec{V}}{\ \hat{D} - \vec{V}\ }$
<b>Probability cube</b>	Cell center	$\frac{\vec{V}}{\ \vec{V}\ }$
<b>Confinement (border 1)</b>	Border closest location	$\frac{\hat{D} - \vec{V}}{\ \hat{D} - \vec{V}\ }$
<b>Confinement (border 2)</b>	Border closest location	$\frac{\hat{D} - \vec{V}}{\ \hat{D} - \vec{V}\ }$

### 3 Stochastic simulation of channelized sedimentary bodies

**Table 3.8** Parameters to define the constraint magnitude.  $w_{min}$  and  $w_{max}$  are the minimal and maximal channel widths. The user input parameters are in bold.

	$\rho$	$\tau_1$	$\tau_2$	$\tau_3$	$\tau_4$	$d_{max}$	$f_1$	$f_2$
<b>Channel self-repulsion</b>	–	1	1	0.15	0	<b><math>w_{max}</math></b>	0.25	0.25
<b>Well channel data</b>	–	0	1	0.15	0.15	<b><math>w_{min}</math></b>	1	0
<b>Well inter-channel data</b>	–	1	1	0.15	0	<b><math>w_{max}</math></b>	0.25	0.25
<b>Well connected channel data</b>	–	0	1	0.25	0.25	<b><math>w_{min}</math></b>	1	0
<b>Well non-connected channel data</b>	–	1	1	0.15	0	<b><math>w_{max}</math></b>	0.25	0.25
<b>Probability cube</b>	1	–	–	–	–	–	–	–
<b>Confinement (border 1)</b>	–	1	1	0.15	0	<b><math>w_{max}</math></b>	0.25	0.25
<b>Confinement (border 2)</b>	–	1	1	0.15	0	<b><math>w_{max}</math></b>	0.25	0.25

**Table 3.9** Input parameters for the user.  $\epsilon_i$  are constraints weights,  $t_{min}$  is the minimal channel thickness,  $\hat{D}$  is the global direction of the channel,  $w_{a,CD}$  is the perception area bandwidth for the well channel data and  $w_{min}$  and  $w_{max}$  are the minimal and maximal channel widths.

	<b>Input parameters</b>				
<b>Channel self-repulsion</b>	$\epsilon_{SR}$	$\hat{D}$	–	$w_{max}$	$t_{min}$
<b>Well channel data</b>	$\epsilon_{CD}$	$\hat{D}$	$w_{a,CD}$	$w_{min}$	$t_{min}$
<b>Well inter-channel data</b>	$\epsilon_{ICD}$	$\hat{D}$	–	$w_{max}$	$t_{min}$
<b>Well connected channel data</b>	$\epsilon_{CD}$	$\hat{D}$	–	$w_{min}$	$t_{min}$
<b>Well non-connected channel data</b>	$\epsilon_{ICD}$	$\hat{D}$	–	$w_{max}$	$t_{min}$
<b>Probability cube</b>	$\epsilon_{PC}$	$\hat{D}$	–	–	$t_{min}$
<b>Confinement (border 1)</b>	$\epsilon_C$	$\hat{D}$	–	$w_{max}$	–
<b>Confinement (border 2)</b>	$\epsilon_C$	$\hat{D}$	–	$w_{max}$	–

same for different constraints, for instance within the different types of well data. The channel global direction is already required by the L-system. The channel minimal and maximal width and minimal thickness come from the channel width and thickness distributions, which are also required as input by the L-system. The bandwidth for the well channel data is the only parameter with the constraint weights that is not shared with the L-system. It controls on the lateral extension of the perception area, so it determines which data a channel can condition. Hence, this parameter influences the well correlation by the channels.

## 3.5 Illustration of channel simulation on simple cases

The following sections delve into some aspects of the channel simulation with L-systems. The main purpose is to illustrate the impact of the L-system parameters, of the L-system rules and of the constraints on the simulated channels.

### 3.5.1 L-system parameter impact

Among the L-system parameters, some are pretty straightforward, such as the initial position or the global direction. The default segment length determines the length of the channel segments. It influences bend shape: the larger the segment length, the rougher the bend representation. It also influences the simulation time: for a given channel length, using smaller segments calls for more segments.

Two sets of parameters define the channel morphology: the bend length and the curvature or the bend half-wavelength, the bend amplitude and the deviation angle. They are all given as statistical distributions.

The bend length defines the curvilinear distance along a single bend (figure 3.13). The curvature defines the channel sinuosity. Using different distribution types have less impact than changing the distribution parameters. All the channels of figure 3.13 have a uniform distribution defining the curvature, except the blue channel at the bottom, which has a triangular distribution. The distribution for the bend length remains uniform. The channel behind the blue channel is its equivalent with a uniform distribution for the curvature, so  $\mathcal{U}(2 \times 10^{-3}, 4 \times 10^{-3})$  for the curvature and  $\mathcal{U}(600, 1\ 000)$  for the bend length. The triangular distribution leads to fewer variations of the curvature, as the extremums are less likely to be drawn, but it is quite subtle.

The second set of parameters has a mixed influence on the morphology (figure 3.14). Both the bend half-wavelength and amplitude influence the bend length and the sinuosity. The higher the half-wavelength is, the longer are

### 3 Stochastic simulation of channelized sedimentary bodies

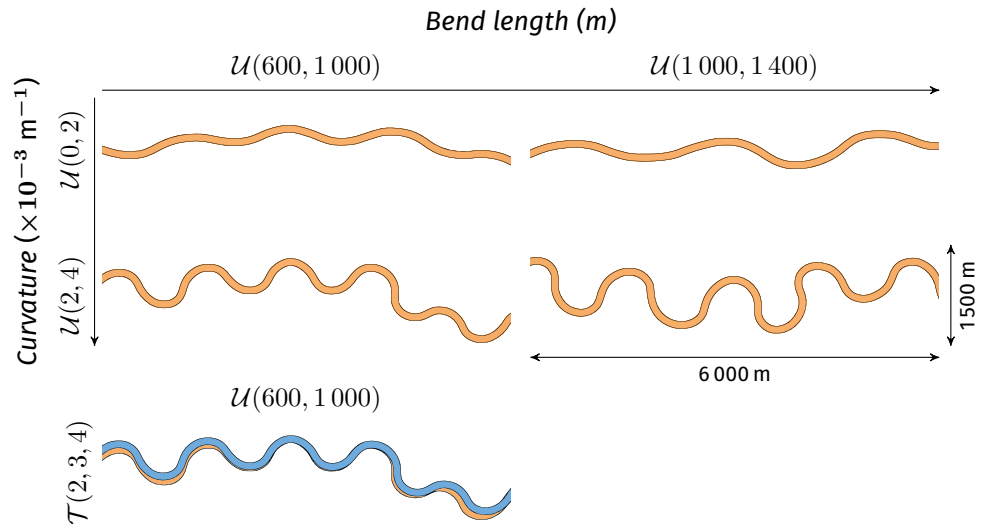


**Figure 3.13** Variations of bend length and curvature and influence on the channel morphology.  $\mathcal{U}$  is a uniform distribution with a minimum and a maximum value as parameters.  $\mathcal{T}$  is a triangular distribution with a minimum, a mode and a maximum as parameters. See the text for more details.

the bends, the lower is the sinuosity. The higher the amplitude is, the longer are the bends, the higher is the sinuosity. The deviation angle perturbs the resulting morphology. All the channels of figure 3.14 have a uniform distribution defining the deviation angle, with a minimal value of 0 and a maximal value of 0.057. The perturbation remains small. Only the blue channel at the bottom comes from a different uniform distribution, with a minimal value of -11.45 and a maximal value of 11.45. The channel behind the blue channel is its equivalent with the deviation angle distribution  $\mathcal{U}(0, 0.057)$ . The deviation angle principally perturbs both the bend half-wavelengths and amplitudes. It also perturbs the bend at a lower scale, with more sharp angles between some segments and more various bend shapes.

The global direction has a direct influence on the channel morphology. When its weight increases, the channel tends to follow more strictly the global direction and to be straighter (figure 3.15). The weight should be adjusted depending on how much the channel has to follow the global direction.

### 3.5 Illustration of channel simulation on simple cases

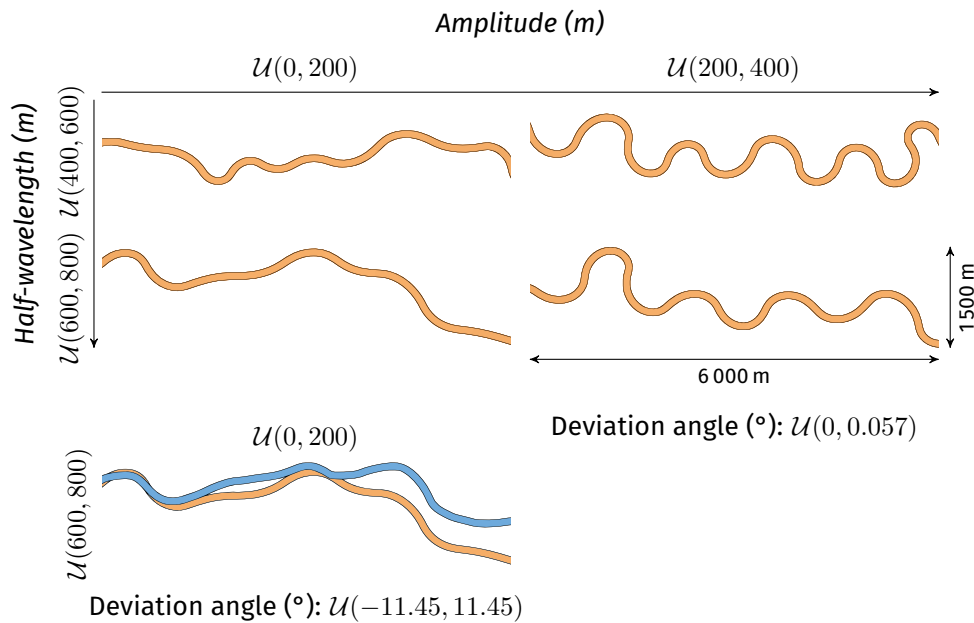


**Figure 3.14** Variations of half-wavelength and amplitude and influence on the channel morphology.  $\mathcal{U}$  is a uniform distribution with a minimum and a maximum value as parameters. See the text for more details.

#### 3.5.2 L-system rule change

The process of channel simulation with a L-system integrates predefined L-system rules. Predefined rules have two main advantages:

- The method is more easily applied.
- The set of rules gives an example of how to simulate channels and facilitates the design of different rules if required.

This second point is especially important: in a L-system framework, the user is free to modify the pre-existing rules or even to choose its own rules. It gives the opportunity to adapt the simulation to particular cases.

This aspect is further illustrated with two examples of non-stationary channels. The first example relies on channels in submarine fans, whose sinuosity tends to decrease from the start of the fan to the abyssal plain [Babonneau et al., 2010]. This can be integrated in the rules by adding a multiplying factor



### 3 Stochastic simulation of channelized sedimentary bodies

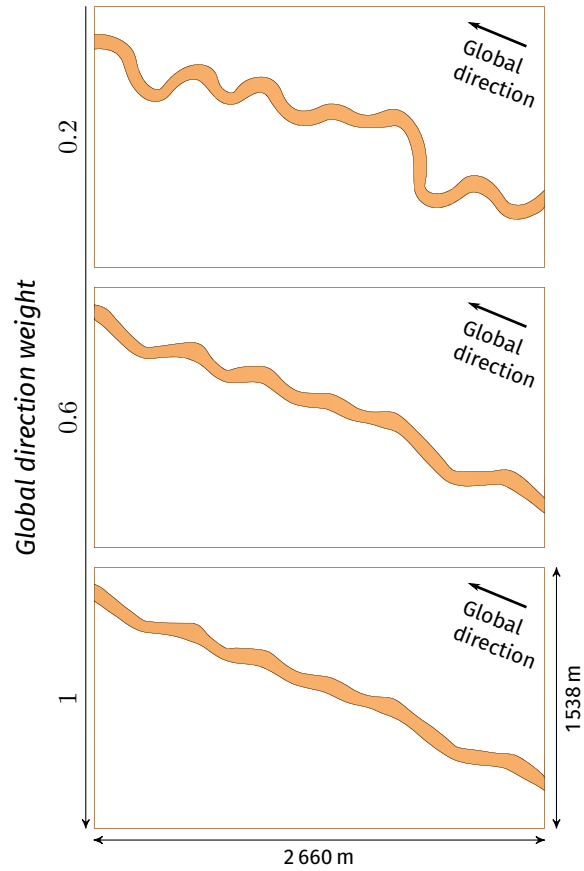


**Figure 3.15** Impact of the global direction weight on the simulated channels. The L-system weight is set to one in each case.

to the curvature. It calls for a modification of the initiation rules:

$$p_0 : \quad \begin{array}{l} T \xrightarrow{0.5} [+C\{+C\}^{n_{s1}-1} T] + (180) - C\{-C\}^{n_{s2}} D \\ T \xrightarrow{0.5} [-C\{-C\}^{n_{s1}-1} T] + (180) + C\{+C\}^{n_{s2}} D \end{array}$$

The developments of each branch are independent by means of a letter  $D$  in addition to the letter  $T$ . Thus, the development rules are doubled: one set for the  $T$  growth, one set for the  $D$ . Each branch gets a different multiplication factor for the curvature. The factors introduced here are purely illustrative and do not come from any empirical law. In the branch with the  $T$ , the curvature  $c$  becomes:

$$c' = c \frac{l_c + 0.5l_C}{2 - 0.5l_C} \quad (3.22)$$

### 3.5 Illustration of channel simulation on simple cases

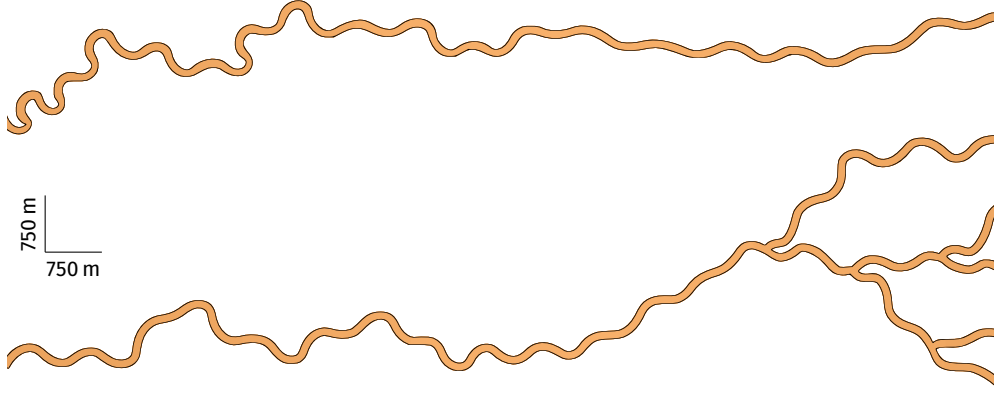


**Figure 3.16** Non-stationary channels obtained by modifying the L-system rules. The input parameters are given in table B.1, appendix B.

with  $c'$  the new curvature value,  $l_c$  the current channel length and  $l_C$  the wanted channel length. Thus, the curvature decreases as the channel grows. In the branch with the  $D$ , the curvature  $c$  becomes:

$$c' = c \frac{2 - 0.5l_C}{l_c + 0.5l_C} \quad (3.23)$$

Thus the curvature increases as the channel grows. This way the channel development is non-stationary (figure 3.16, top channel).

The second example uses the same principle to simulate bifurcations along a channel. The initiation rules are modified as previously. The development rules of the  $T$  branch becomes:

$$\begin{aligned} p_1 : \quad -C < T &\xrightarrow{0.95} \{+C\}^{n_s} T \\ -C < T &\xrightarrow{0.05} \{+C\}^{n_{s_1}} [+C T] \{+C\}^{n_{s_2}} T \\ +C < T &\xrightarrow{0.95} \{-C\}^{n_s} T \\ +C < T &\xrightarrow{0.05} \{-C\}^{n_{s_1}} [-C T] \{-C\}^{n_{s_2}} T \end{aligned}$$

with  $n_s$  the total number of segments for the bend and:

$$\begin{aligned} n_{s_1} &\sim \mathcal{U}(1, n_s - 1) \\ n_{s_2} &= n_s - n_{s_1} \end{aligned} \quad (3.24)$$

with  $\mathcal{U}$  a uniform discrete distribution with its minimal and maximal values as parameters and  $n_s \geq 2$ . This introduces bifurcations in the downstream part

### 3 Stochastic simulation of channelized sedimentary bodies

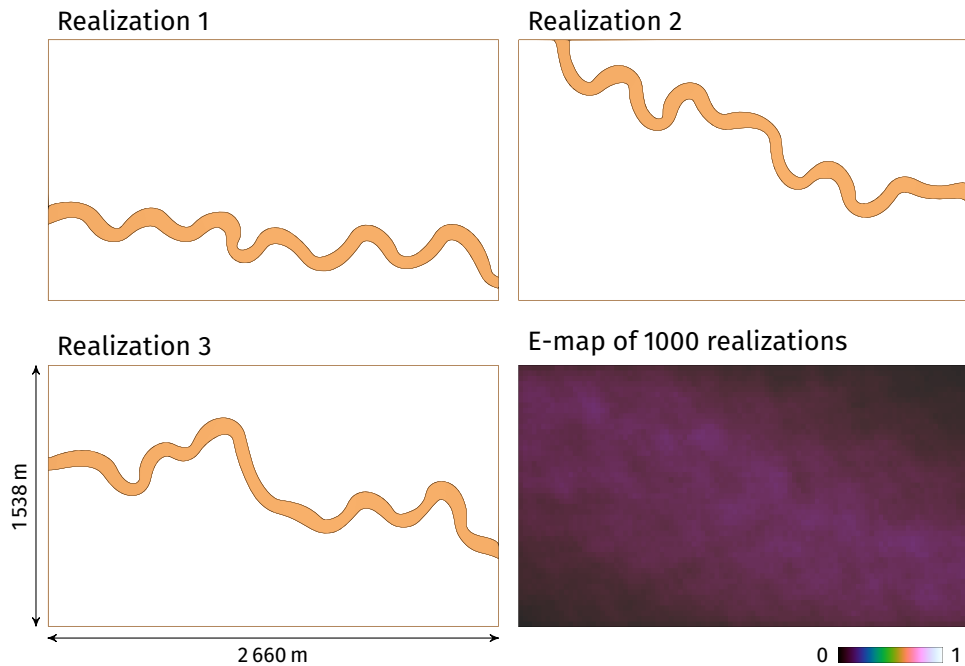


**Figure 3.17** Examples of unconditional realizations and E-map of 1 000 realizations. L-system weight: 1; global direction weight: 0.2

of the channel (figure 3.16, bottom channel). The channel self-repulsion limits intersections between the branches. However, when the number of branches becomes higher than four, intersections are difficult to avoid.

#### 3.5.3 Conditioning impact

This section illustrates the impact of conditioning on the L-system and the channel morphology through several synthetic cases. In each of the following cases, the data contain only one channel within the domain. Thus, only one channel constitutes each realization which must condition to all the data. The channel development stops as soon as the two channel branches are outside the grid. The input parameters for the different cases are given in table B.2, appendix B.

Figure 3.17 presents some channels without data conditioning. The bottom right image is the channel count within each cell of a grid. Without particular data, the channels are distributed inside the whole grid.

### 3.5 Illustration of channel simulation on simple cases

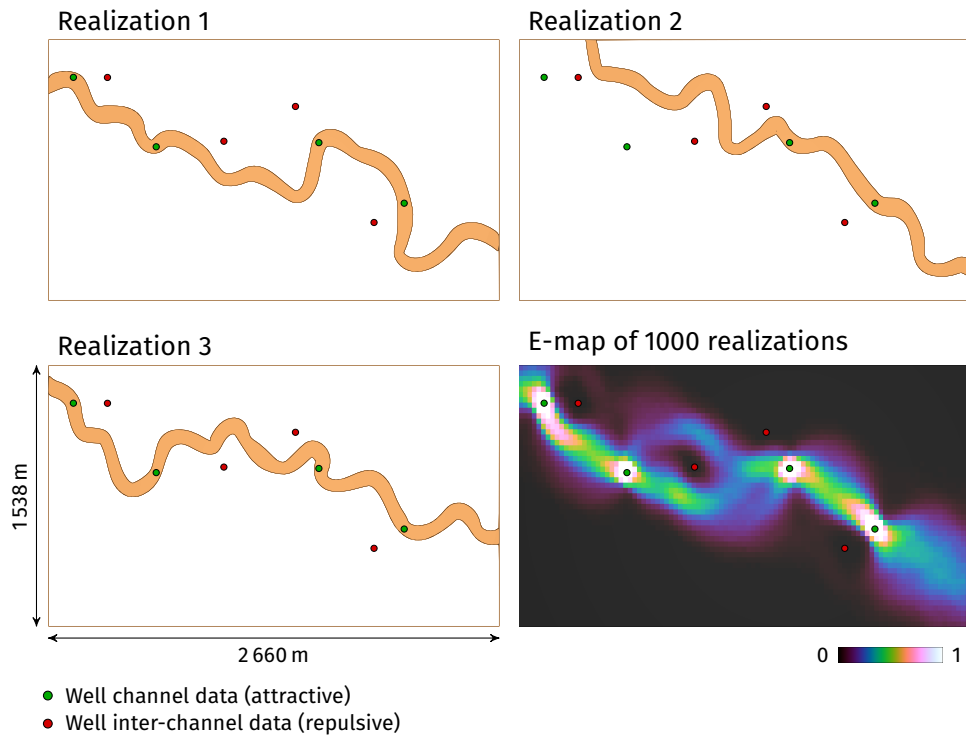


**Figure 3.18** Examples of realizations conditioned to well sedimentary data and E-map of 1000 realizations. L-system weight: 1; global direction weight: 0.2; channel data weight: 1; inter-channel data weight: 1.

#### Well sedimentary data

Figure 3.18 illustrates well sedimentary data conditioning. The channel distribution is not homogeneous any more: the data constraints concentrate the channels along one diagonal of the grid. The conditioning strategy implies a deformation of the channels. These channels tend to be straighter than those without data due to the channel data attraction. The perception area bandwidth is large enough so that this parameter has no influence any more. It favors the conditioning of all the data by a single channel. Figure 3.19 illustrates the influence of the bandwidth: when the bandwidth is small, the L-system has less conditioning possibilities. This gives a control on the well correlation.

Not a single channel conditions a well inter-channel data (figure 3.18). The repulsion effect appears clearly on the E-map. The channels have even some difficulty in coming close to inter-channel data. The constraint magnitude has to be set high enough to ensure that all the channels avoid inter-channel data.

### 3 Stochastic simulation of channelized sedimentary bodies

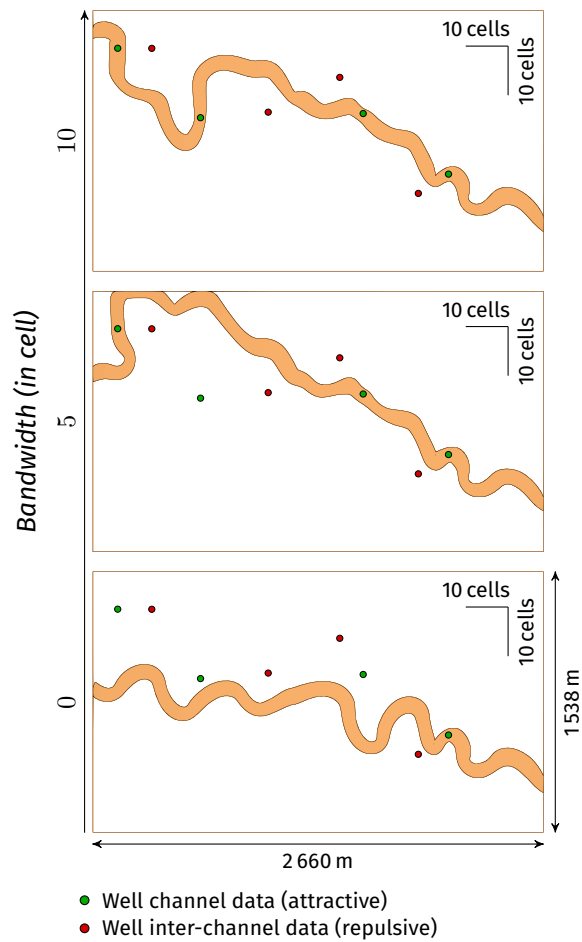


**Figure 3.19** Impact of the bandwidth on channels conditioned to well sedimentary data. Global direction weight: 0.2; channel data weight: 1; inter-channel data weight: 1.

In return, this introduces a bias in the conditioning process.

The well channel data are not conditioned by all 1 000 channels (figure 3.18), but by 925 channels at least and 985 channels at best. This reflects the incompatibility that may occur between the channel development and the data location. Indeed, the channel data to condition may change between two successive channel sections, when the data goes outside the perception area of the second section. It reflects the stochastic well correlation done by the process: all the wells should not necessarily be conditioned by a single channel, and between two realizations the well correlation should be able to change. Depending on

### 3.5 Illustration of channel simulation on simple cases

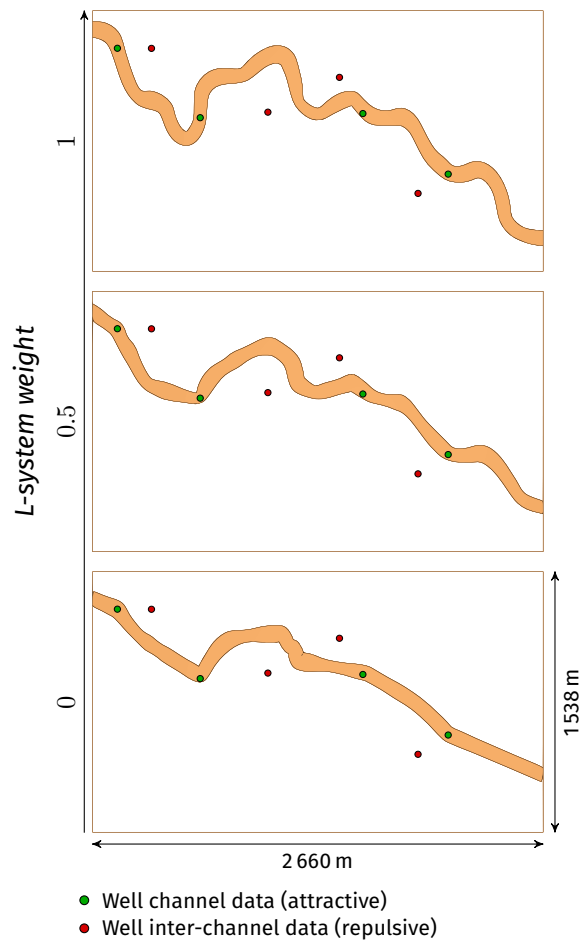


**Figure 3.20** Impact of the L-system weight on channels conditioned to well sedimentary data. Global direction weight: 0.2; channel data weight: 1; inter-channel data weight: 1.

their location, inter-channel data can also prevent channel data conditioning (for instance realization 2 on figure 3.18).

The relative force of the L-system weight compared to the channel data weight also influences both the conditioning and the channel morphology. With a high weight for the data and a low weight for the L-system, the channel goes more directly to the data (figure 3.20). It impacts significantly the channel morphology, but it further ensures the conditioning.

The system is able to condition many well channel data (figure 3.21). Progressively decreasing the L-system weight as the number of data increases ensures the con-

### 3 Stochastic simulation of channelized sedimentary bodies

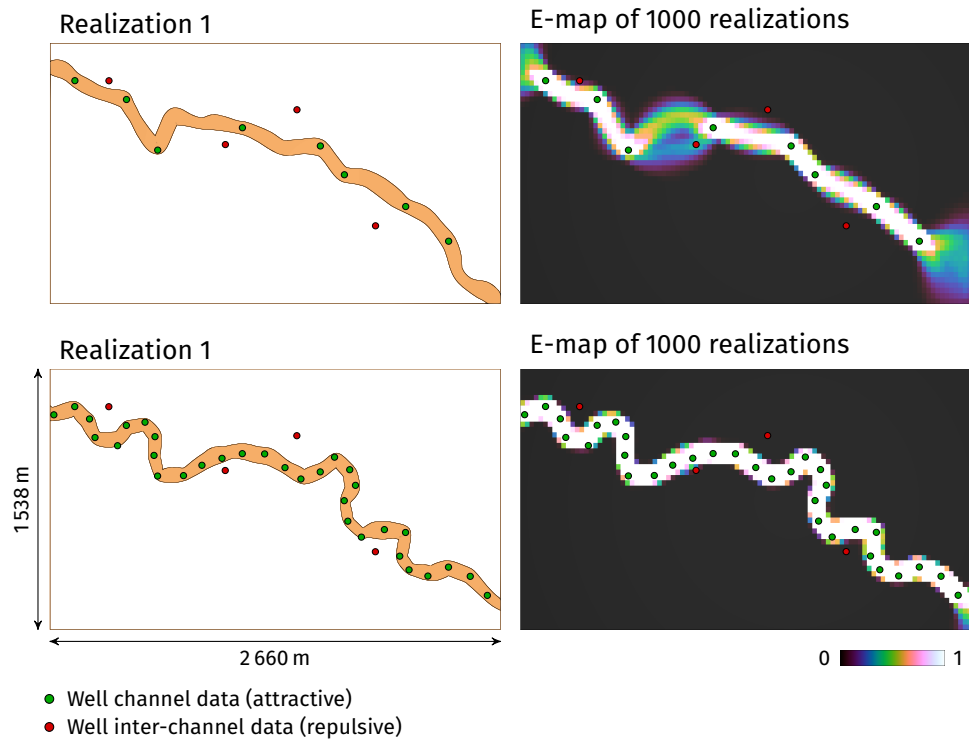


**Figure 3.21** Examples of realizations conditioned to well sedimentary data and associated E-maps of 1 000 realizations. L-system weight: 0.4; global direction weight: 0.1; channel data weight: 1; inter-channel data weight: 0.15 (Top). L-system weight: 0.01; global direction weight: 0.002; channel data weight: 1; inter-channel data weight: 0.25 (Bottom).

ditioning of all the data. Similarly, the weight associated to well inter-channel data is more or less decreased to ensure the channel data conditioning. In return, some channels condition some inter-channel data.

#### Well connectivity data

Figure 3.22 illustrates well connectivity data conditioning with a L-system. The data set is the same as that of the previous section. Among the four channel data, two have to be connected and one should not be connected to those two data. The last channel data does not have any connectivity information: the channels are free to condition it or not. Again, the perception area bandwidth is set large enough to favor the conditioning of all the data by the channels. The channel initial position is fixed near the most right green square for practical

### 3.5 Illustration of channel simulation on simple cases

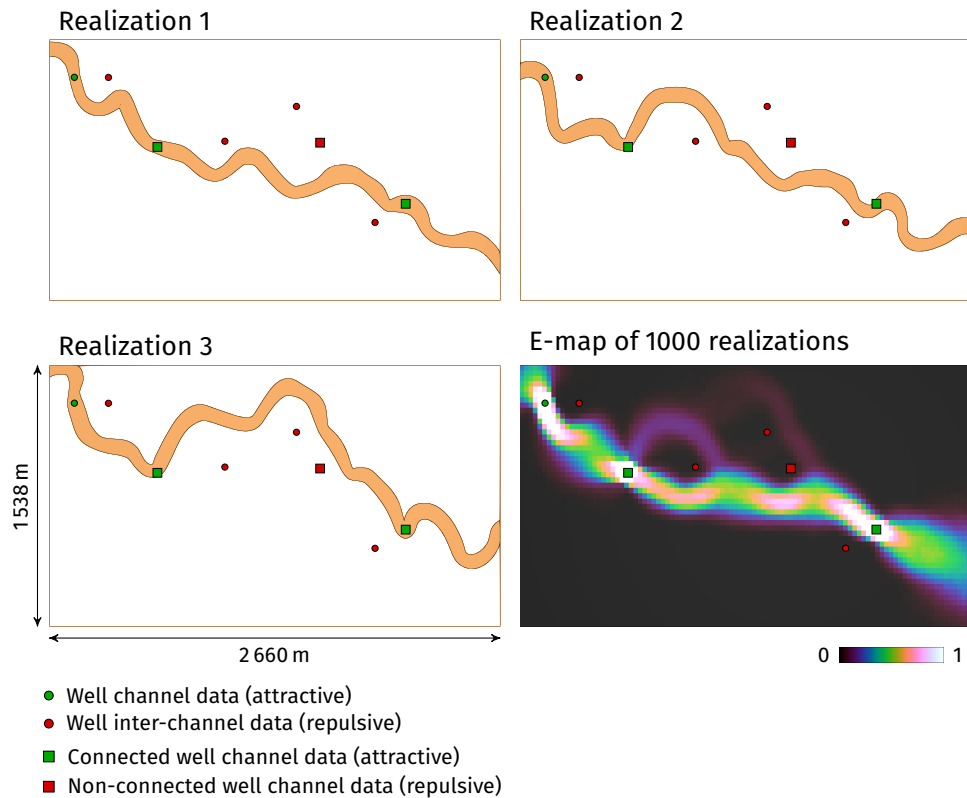


**Figure 3.22** Examples of realizations conditioned to well sedimentary and connectivity data and E-map of 1000 realizations. L-system weight: 1; global direction weight: 0.2; channel data weight: 1; inter-channel data weight: 1.

reasons: all the channels start from the connected set and not from the non-connected data.

Contrary to without connectivity data, the two channel data to be connected are always connected, with the 1000 channels that condition them. The channel morphology tends to be straighter between those data due to the higher constraint magnitude. The non-connected channel data is never connected to the two previous data. The last channel data is conditioned by 999 channels over 1000. Configuration such as in realization 2 on figure 3.18 do not occur much because the two green-square data are already conditioned. It facilitates the conditioning of the last data as the inter-channel are less bothering. The channels still do not condition the inter-channel data.



### 3 Stochastic simulation of channelized sedimentary bodies

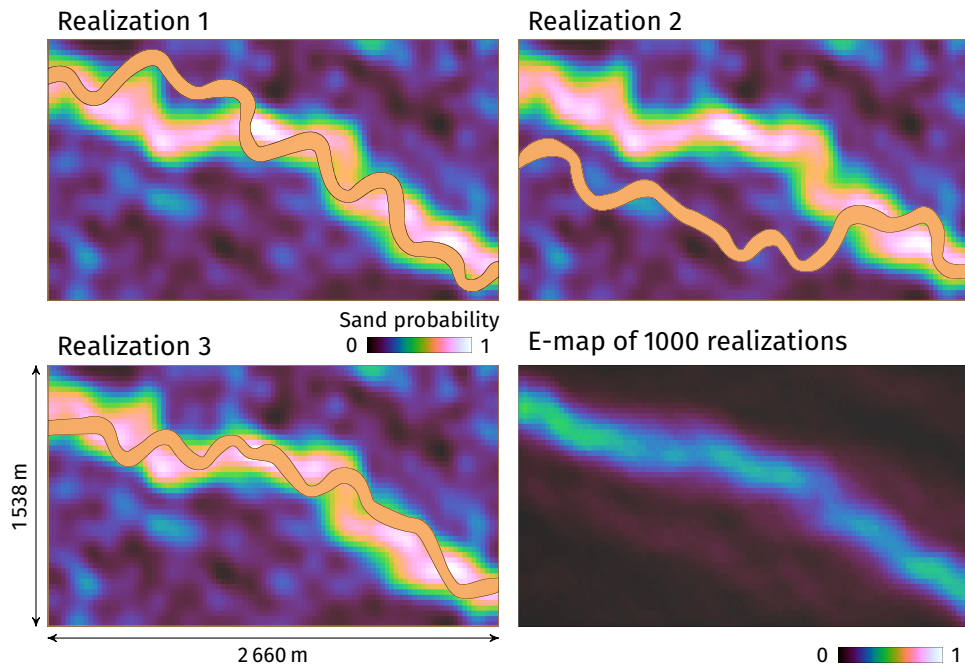


**Figure 3.23** Examples of realizations conditioned to sand probability map and E-map of 1 000 realizations. L-system weight: 1; global direction weight: 0.2; probability cube weight: 0.2.

#### **Sand probability cube**

The sand probability cube is a property defined on each cell of a grid. This cube derives from seismic data for instance. Each grid cell is associated to the probability of having sand-rich deposits in it. Here sand-rich deposits are considered to be associated to a channel. Thus, the sand probability is used to influence the channel development.

The highest probability areas influence the initial position draw and attract the channels during their development. When simulating a high number of realizations, the resulting E-map should be similar to the sand probability: the purpose is to reproduce the probability cube.

Here the channels tend to follow the diagonal of high probabilities (figure 3.23). It appears clearly on the E-map, with a similar diagonal that concentrates more channels than the rest of the domain. However a significant difference remains between the probability values and the E-map values.

Similarly to well channel data, lowering the L-system weight compared to the probability cube weight lets the channels get closer to the high probability

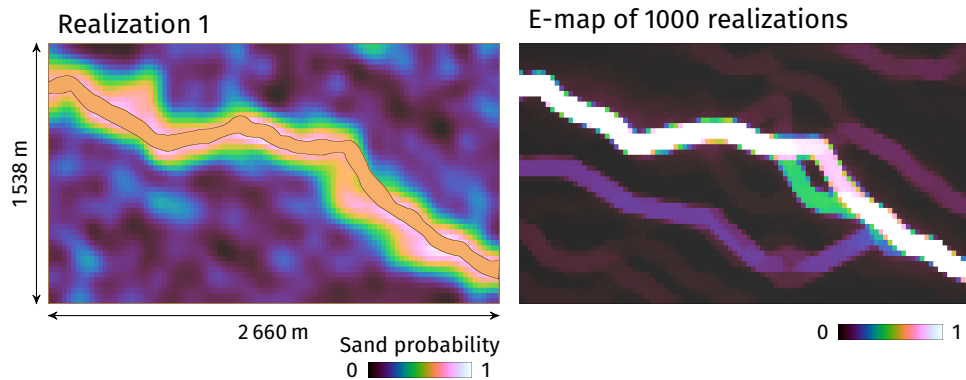


**Figure 3.24** Example of realization conditioned to a sand probability map and E-map of 1 000 realizations. L-system weight: 0.2; global direction weight: 0.2; probability cube weight: 1.

values (figure 3.24). This is still at the cost of the channel morphology. The resulting E-map is less different to the probability cube. Some differences are due to the discontinuity of the high probability areas, whereas the channels are necessarily continuous. It highlights a difference between a sand probability, which can vary within a channel, and a channel probability. When the probability cube weight is high relatively to the L-system weight, the influence of the global direction is fundamental. It ensures that the channels continue their development without going backward. Indeed, the highest sand probability areas are circular and can sometimes re-attract the channel after its first passage.

## 3.6 Application

In this section, a synthetic test case with several data of different types illustrates the application of the method. It requires the combination of several constraints within a three-dimensional environment.

### 3.6.1 Dataset

This synthetic case is inspired by turbiditic systems. In such environment, channels evolve within a master channel. Continuous and discrete migrations control channel evolution. Channel evolution tends to depend on the energy of a turbiditic event [McHargue et al., 2011]. At the beginning of an event, the high energy mostly leads to erosion. As the energy decreases, deposition of sediment starts. Channels mostly migrate laterally, with very few aggradation

### 3 Stochastic simulation of channelized sedimentary bodies

and a stacking between channels that tend to be disorganized due to discrete migrations. When the energy is low enough, the sediment content of the turbidity currents become muddier. This muddier content favors the development of large overbanks. The flow is then more confined, with less lateral migrations. Aggradation dominates this phase, with a significant vertical migration. The purpose is to reproduce that evolution in two successive channel development trends, one horizontal at the bottom of the master channel and one vertical at the top, in the channel realizations.

The master channel is simulated using the channel simulation process. A L-system defines its morphology and NURBS surfaces represent its boundaries. The NURBS surfaces help to build a hexahedral grid aligned with the master channel margins [Ruiu et al., 2015b] (figure 3.25). This grid materializes the master channel and corresponds to the simulation domain. The channels are simulated within the parametric space of the grid. Having the grid aligned with the master channel margins helps the channels to follow the master channel orientation.

The information about the channel evolution comes from a sand probability cube:

- In the lower part of the master channel, the high sand probabilities occupy almost the whole master channel width due to the significant lateral migration.
- In the upper part, the high sand probabilities occupy only a small part of the master channel width due to the significant aggradation.

In a real case, the master channel could come from a seismic interpretation and the sand probability cube could derive from the seismic amplitude.

Three sets of channel realizations are simulated within the master channel:

- The first set does not have other constraint than the repulsion from the confinement, i.e., the master channel.
- The second set must also condition the sand probability cube.
- The last set must condition the confinement, the sand probability cube and the well data. The well data are extracted from a realization of the second set along 20 well paths (figure 3.25). Among these data, well channel data attract the channels and well inter-channel data repulse the channels.

The input parameters for the different sets are given in table B.3, appendix B.

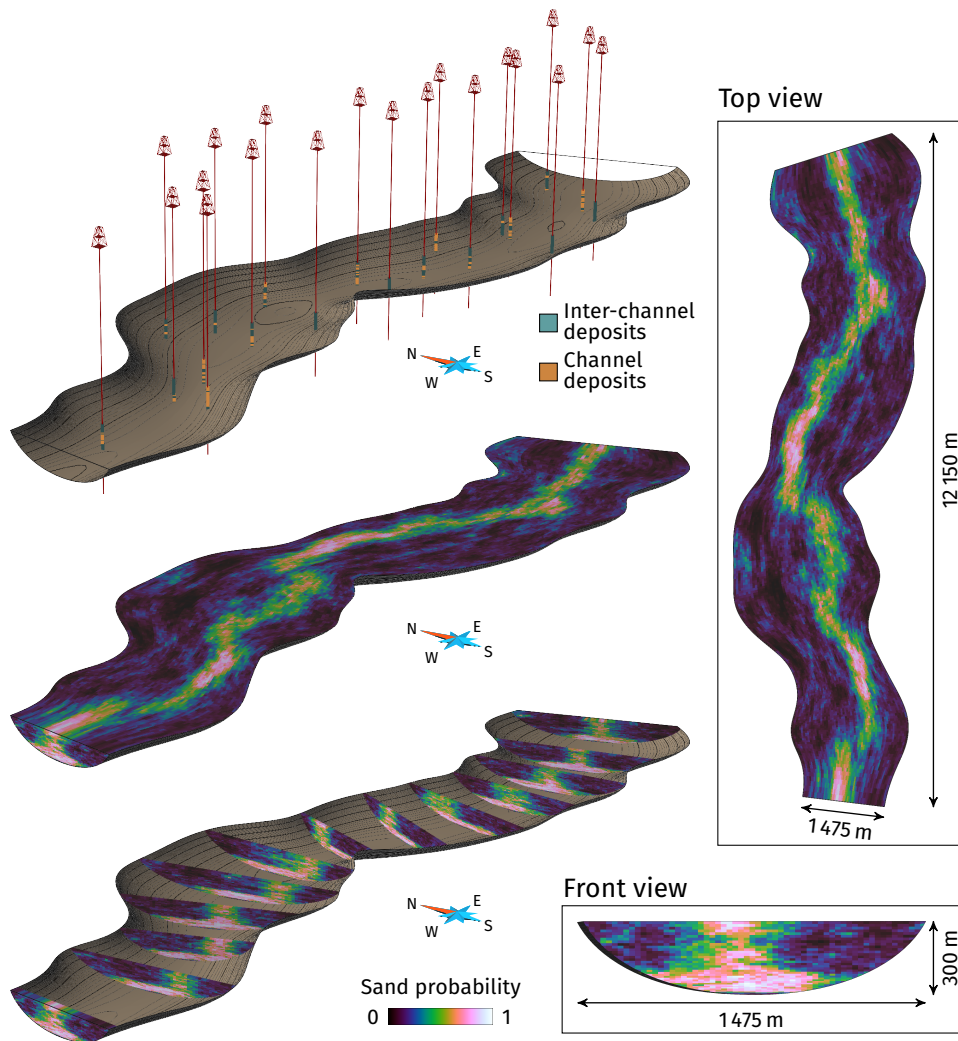


**Figure 3.25** Dataset of the application: a curvilinear grid representing a master channel with a sand probability cube. Twenty wells are positioned along the canyon. Well data are extracted along each well from one simulation.

### 3.6.2 Simulation principle

The principle of the simulation process is simple: channels are simulated until a given number of channels is reached. Without data the channel initial position is randomly drawn inside the grid. The only constraint is that the channels can not go outside the master channel margins. This implies that the initial

position can not be drawn at less than half a channel width from a canyon side. When adding the probability cube, the initial position is influenced by the sand probabilities.

When adding well data, the process is a bit different. It still calls for a number of channels. As long as there are non-conditioned channel data, channels are simulated. The initial position of those channels are drawn close to channel data, and they are then attracted or repulsed by the other data. Once all the well channel data are conditioned and if the channel number is lower than the target channel number, new channels are simulated until this target is reached.

#### **3.6.3 Unconditional realizations**

Some unconditional realizations have been simulated within the grid (figure 3.26). The only constraints are the two repulsive constraints from the master channel margins. The resulting channel distribution is quite uniform in the middle of the grid, but the probability to have a channel is lower close to the master channel margins (figure 3.27). However, the channels can still occupy the whole width of the master channel. And the channel morphology remains sinuous, without any large orientation change between two successive segments. It is only at the master channel bottom that the margin influence is such that the channels are straighter (figure 3.28).

The constraints influence the channel section position. Here the efficiency of the repulsive constraints of the margins is such that no channel location ever goes outside those margins. All channels go through the whole master channel.

#### **3.6.4 Realizations conditioned to the sand probability cube**

Adding the sand probability cube as a constraint limits the horizontal dispersion of the channels (figure 3.29). The influence of the cube is significant in the upper part of the master channel (figure 3.30 and 3.31). The channels tend to gather along a more or less similar path along the high probability areas. The channels in the upper part locally tend to move apart from the vertical high probability trend and to get close to the master channel margins. These shifts are often related to lower probability areas. In the lower part, the influence of the margins is such that the channels are often straighter, with less lateral variations. These aspects tend to blur the transition from a significant lateral development to a more vertical evolution (figure 3.31).

The duality of the channel evolution introduced in the probability cube is more or less clear depending on the realization and the location within the master channel. On average, the vertical trend seems to have a too huge

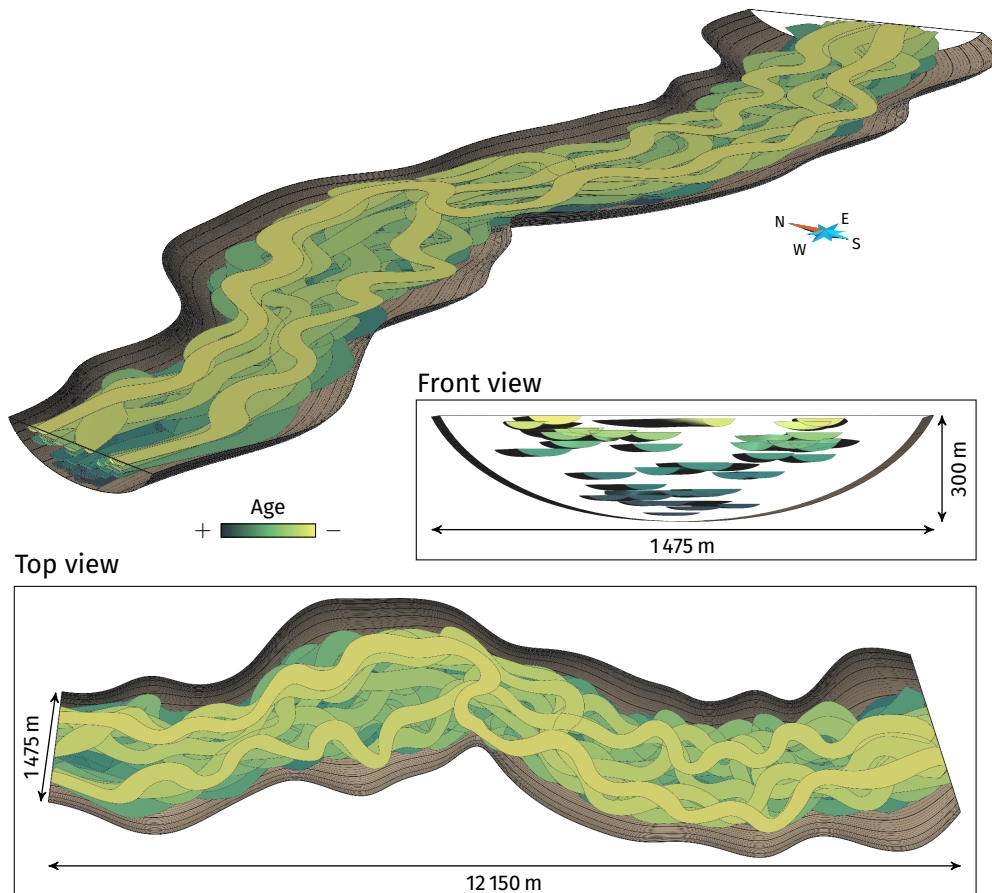


**Figure 3.26** Example of a realization containing 40 channels within a master channel.

influence on the channels (figure 3.31).

### 3.6.5 Realizations conditioned to the sand probability cube and the well sedimentary data

The last set of realizations takes into account the sand probability cube but also the well sedimentary data (figure 3.32). The well data are distributed along 20 wells and form a set of 625 points. The point spacing along a well depends on the master channel grid cells, with one point per cell. The channel and inter-channel data come from the realization presented in section 3.6.4. 234 points are channel data and 391 points are inter-channel data. The channels are free to evolve within the whole master channel and to condition channel

### 3 Stochastic simulation of channelized sedimentary bodies

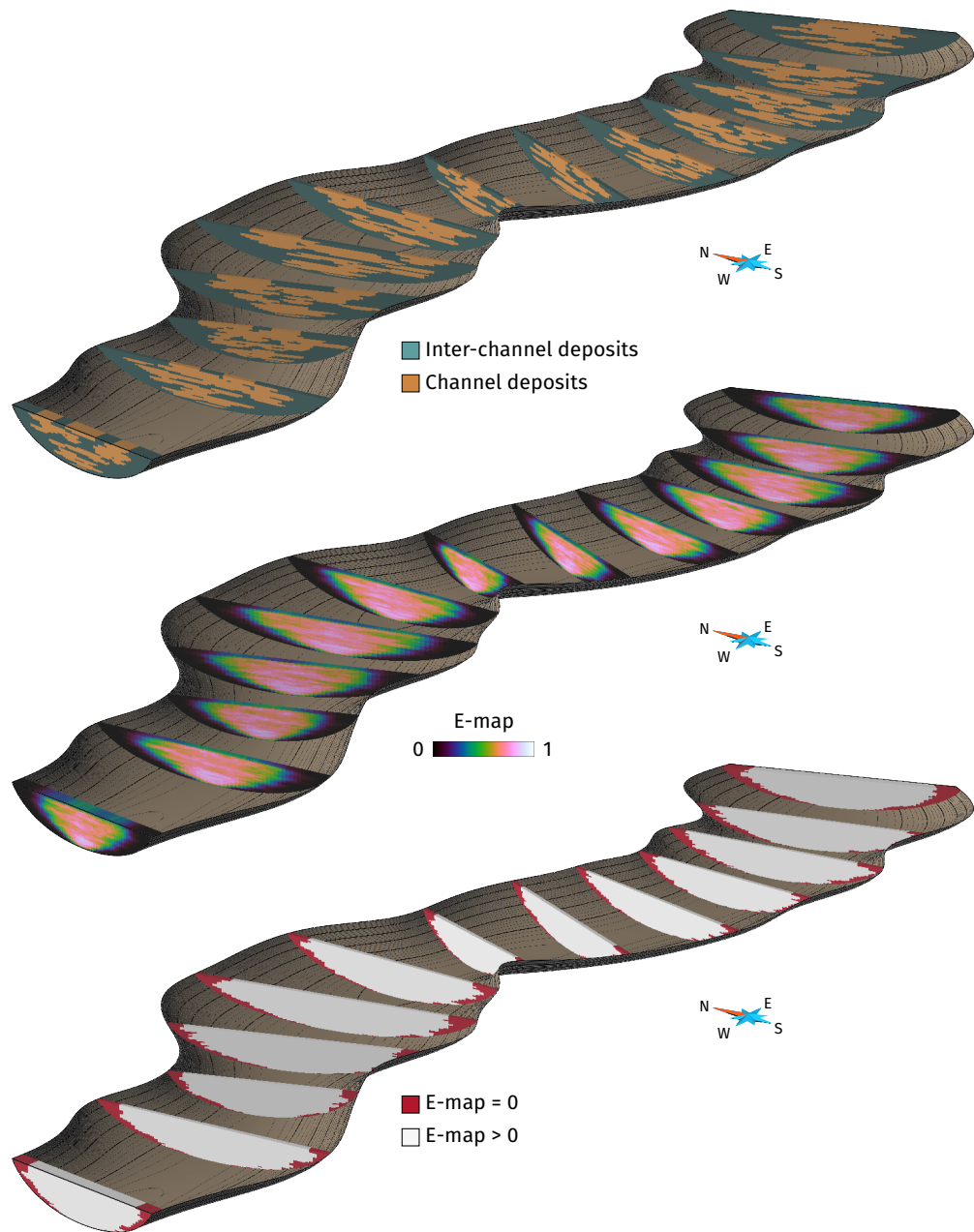
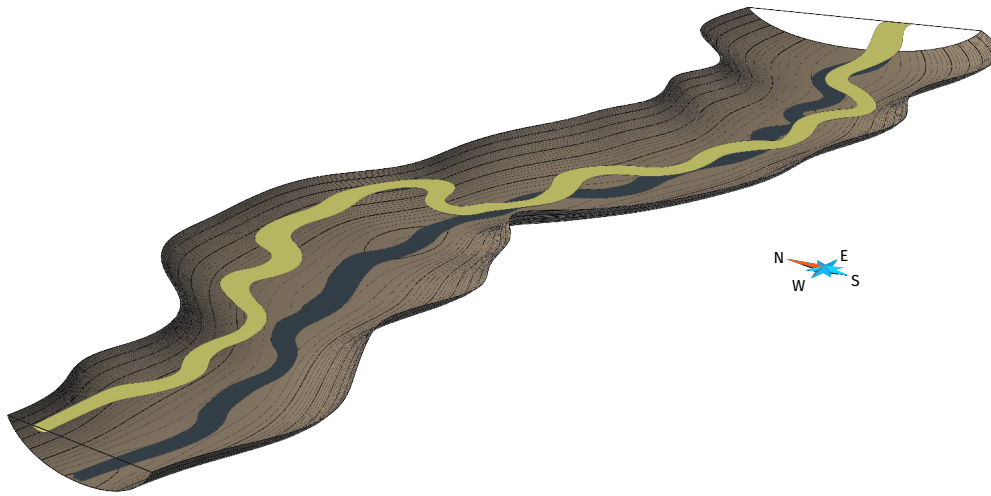


**Figure 3.27** Details on the channel distribution inside the master channel for the realization in figure 3.26 rasterized in the master channel grid. The E-map illustrates the mean channel distribution over the 100 unconditional realizations.



Top view

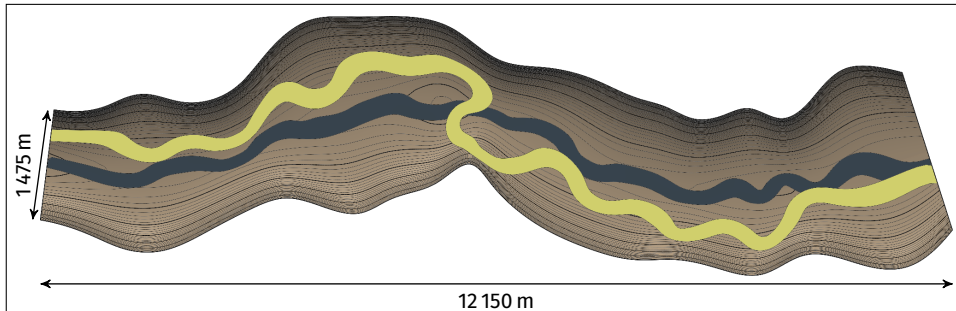


**Figure 3.28** Channels at the top and at the bottom of the realization in figure 3.26.

data along the whole master channel width. Thus the channel data bandwidth for the perception area is set to half the master channel grid width.

This case introduces many constraints:

- The two repulsive constraints from the two master channel margins.
- The attractive constraint from the sand probability cube.
- Possibly one attractive constraint from a channel data, depending on the channel development and the perception area.
- Possibly several repulsive constraints from the inter-channel data, depending on the channel development and the perception area.



### 3 Stochastic simulation of channelized sedimentary bodies

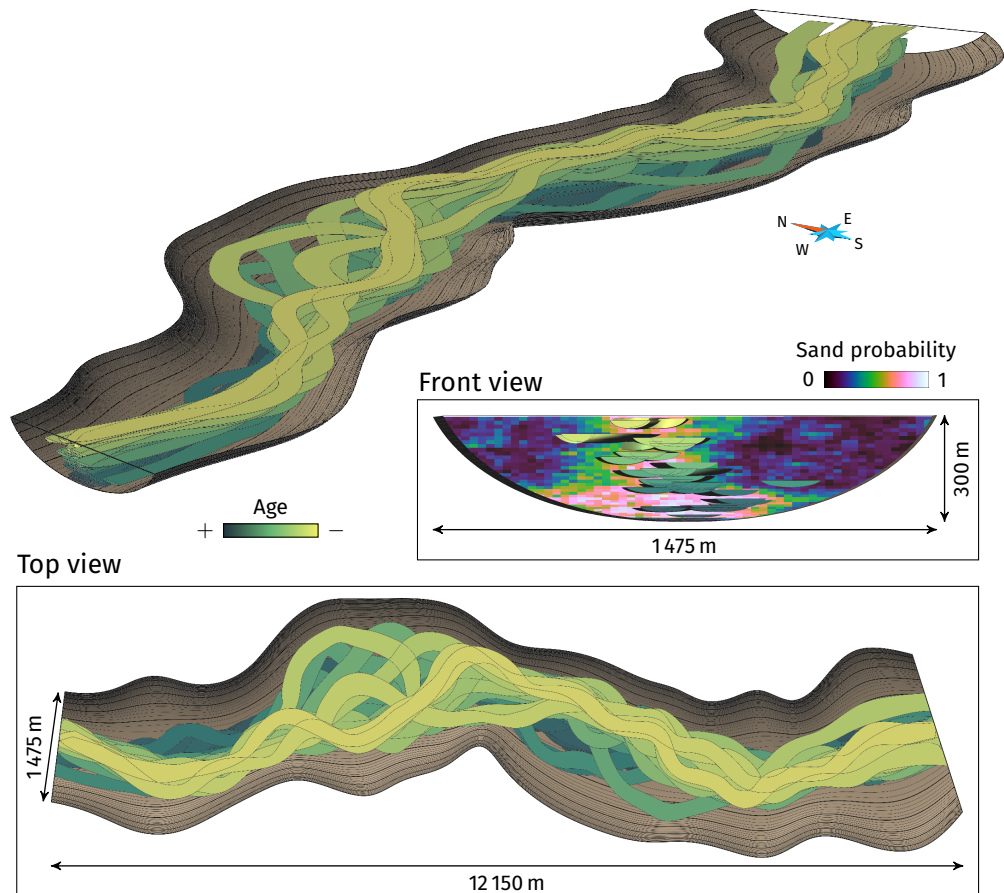


**Figure 3.29** Example of a realization containing 40 channels conditioned to a sand probability cube within a master channel.

The purpose remains to preserve the channel morphology while respecting all those constraints. Figure 3.33 illustrates this aspect with the top channel of a realization. This channel must go through the entire master channel, without going outside the master channel margins, without conditioning one of the 14 inter-channel data and with 6 channel data that it may condition.

The channel centerlines never go outside the master channel margins, but locally the channel objects can go outside. This is often due to some inter-channel data close to the margins (figure 3.34): the space is maybe not enough for a channel to go through it, but the channel still does it. The influence of the sand probability is still noticeable (figure 3.35), with a subtle lateral development at the grid bottom due to the channel margin repulsion and a

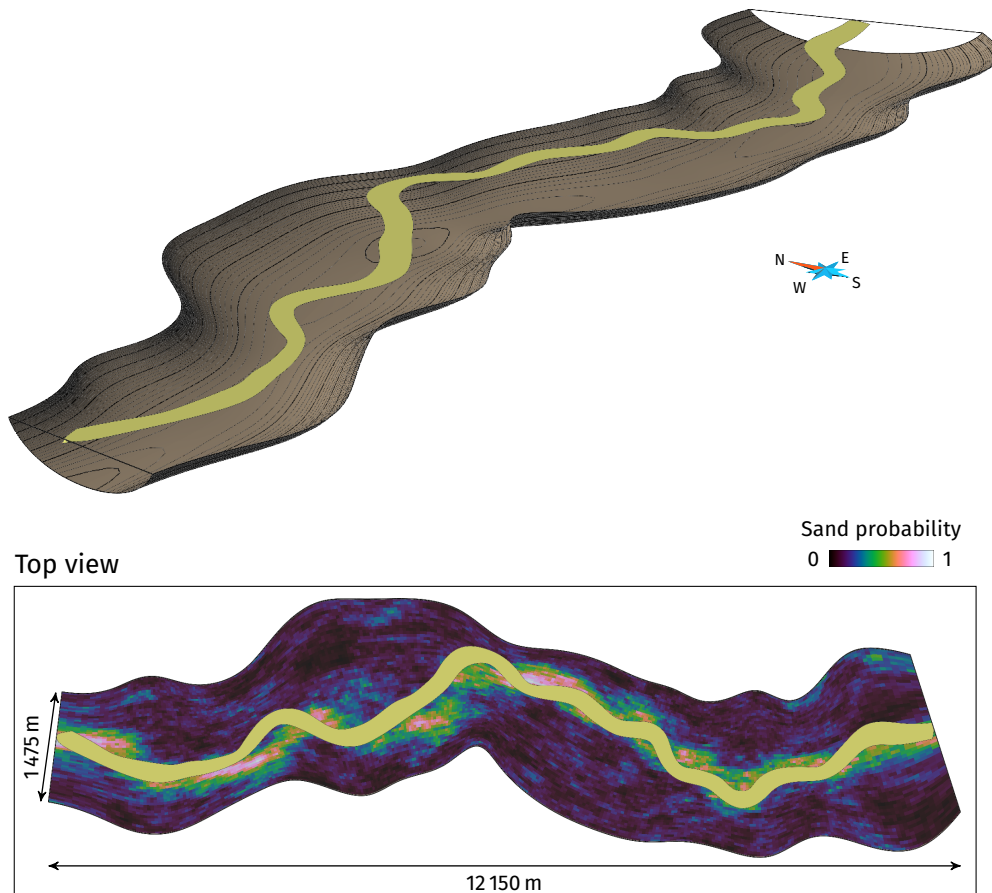


**Figure 3.30** Channel at the top of the realization in figure 3.29.

pronounced vertical trend at the grid top. The channels honor all the channel data, as the simulation process would not stop if it was not the case. But the conditioning area is based on a horizontal and a vertical criterion. Thus, this area is rectangular and not channel-shaped (figure 3.36, c). Over 234 channel data points, 15 are outside a channel and would require a post-process to strictly condition them. Similarly, some channels condition to inter-channel data: over 391 inter-channel data points, 30 are conditioned by a channel. This is either a failure of the repulsive process (figure 3.36, b), or a channel that conditions a channel data and at the end also conditions an inter-channel data (figure 3.36, a). This last case mainly arises because the simulation process is meant to favor channel data conditioning. Thus, if an inter-channel data is right below the channel data to condition, the inter-channel data is ignored.

### 3 Stochastic simulation of channelized sedimentary bodies

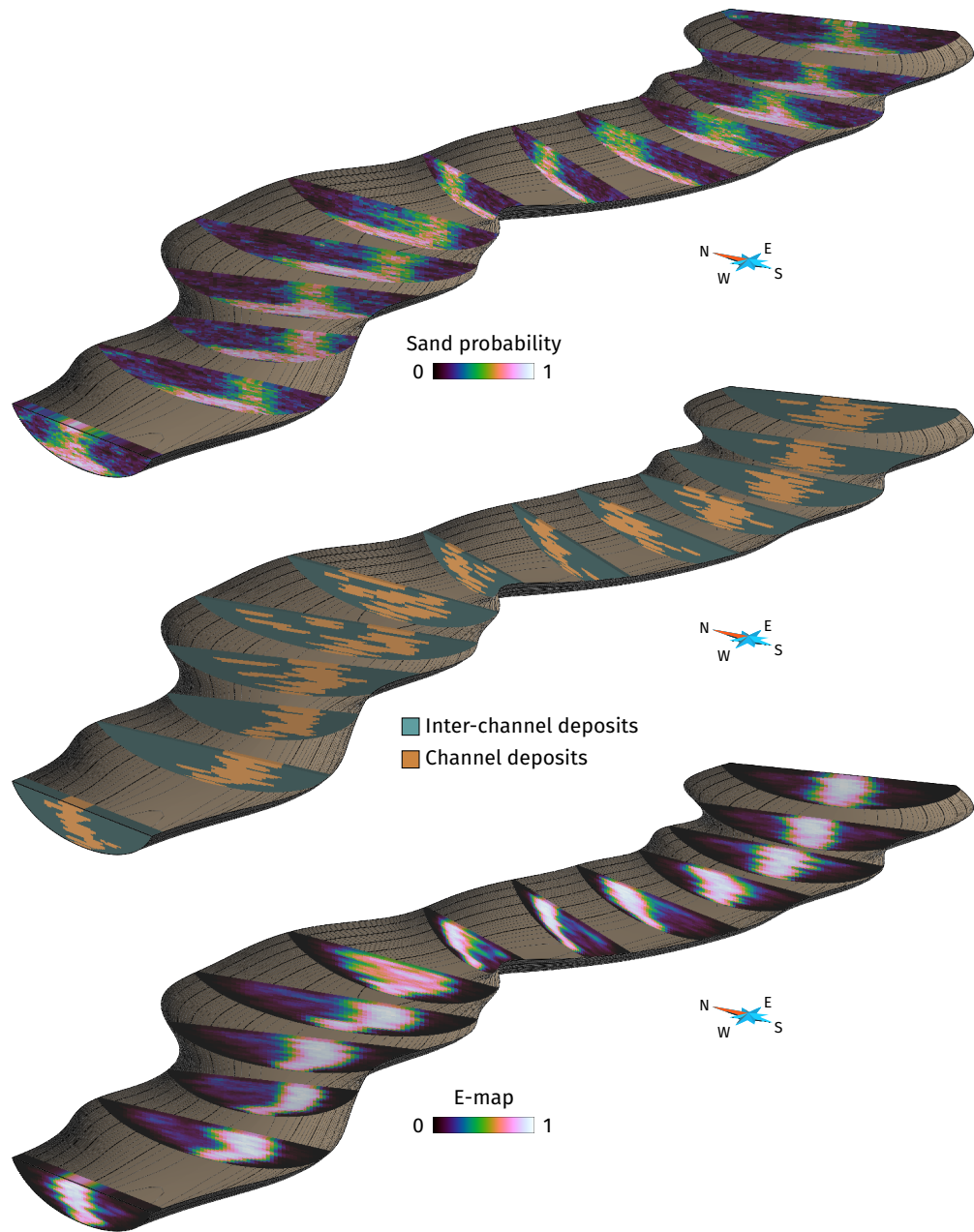


**Figure 3.31** Details on the channel trend of the realization in figure 3.29 rasterized in the master channel grid. The sand property cube along the same sections is here for comparison. The E-map illustrates the mean channel distribution over the 100 unconditional realizations.

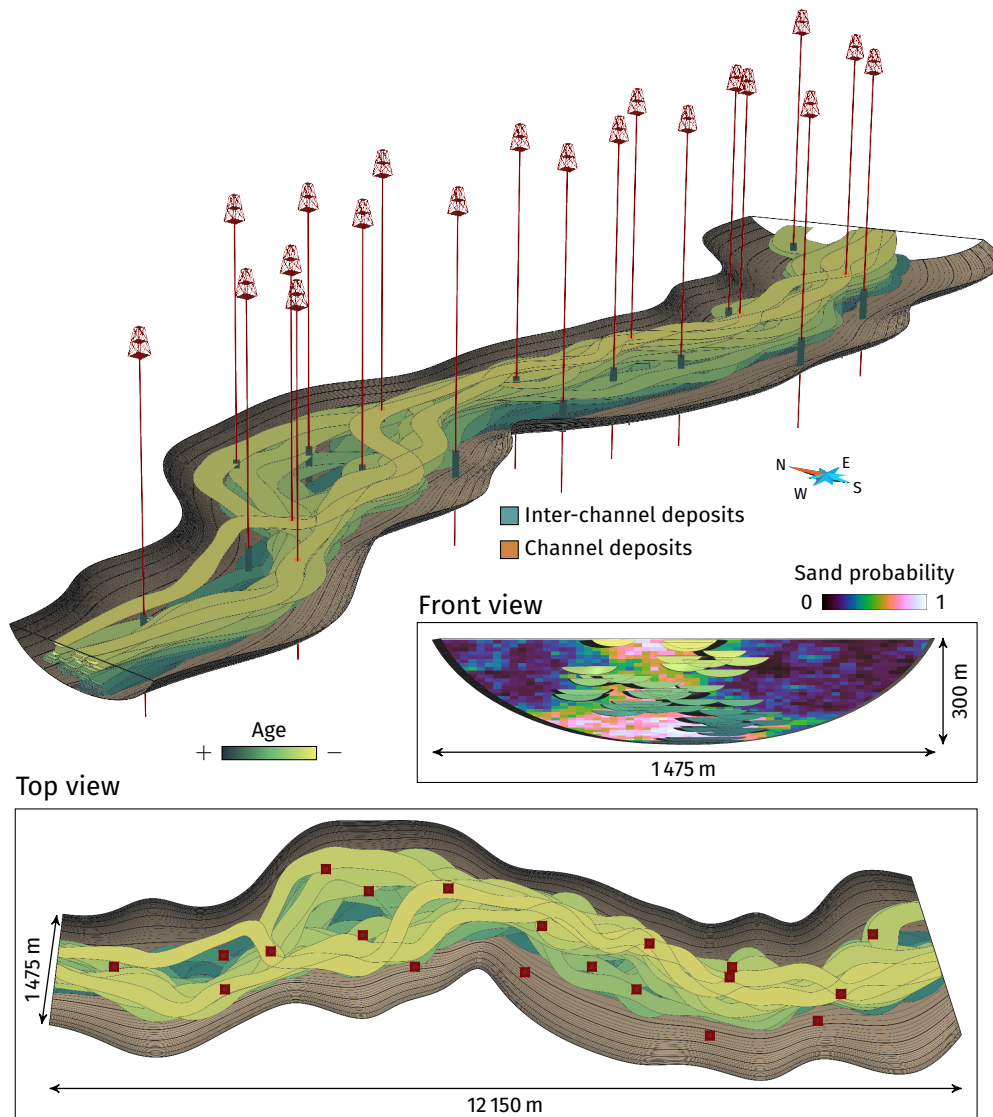


**Figure 3.32** Example of a realization containing channels conditioned to a sand probability cube and well sedimentary data within a master channel.

The well data come from a realization of 40 channels. On average one realization contains 59,38 channels, with a standard deviation of 3.64. There is a clear increase due to the conditioning: none of the realizations has been able to condition all the channel data with less than 49 channels.

### 3 Stochastic simulation of channelized sedimentary bodies

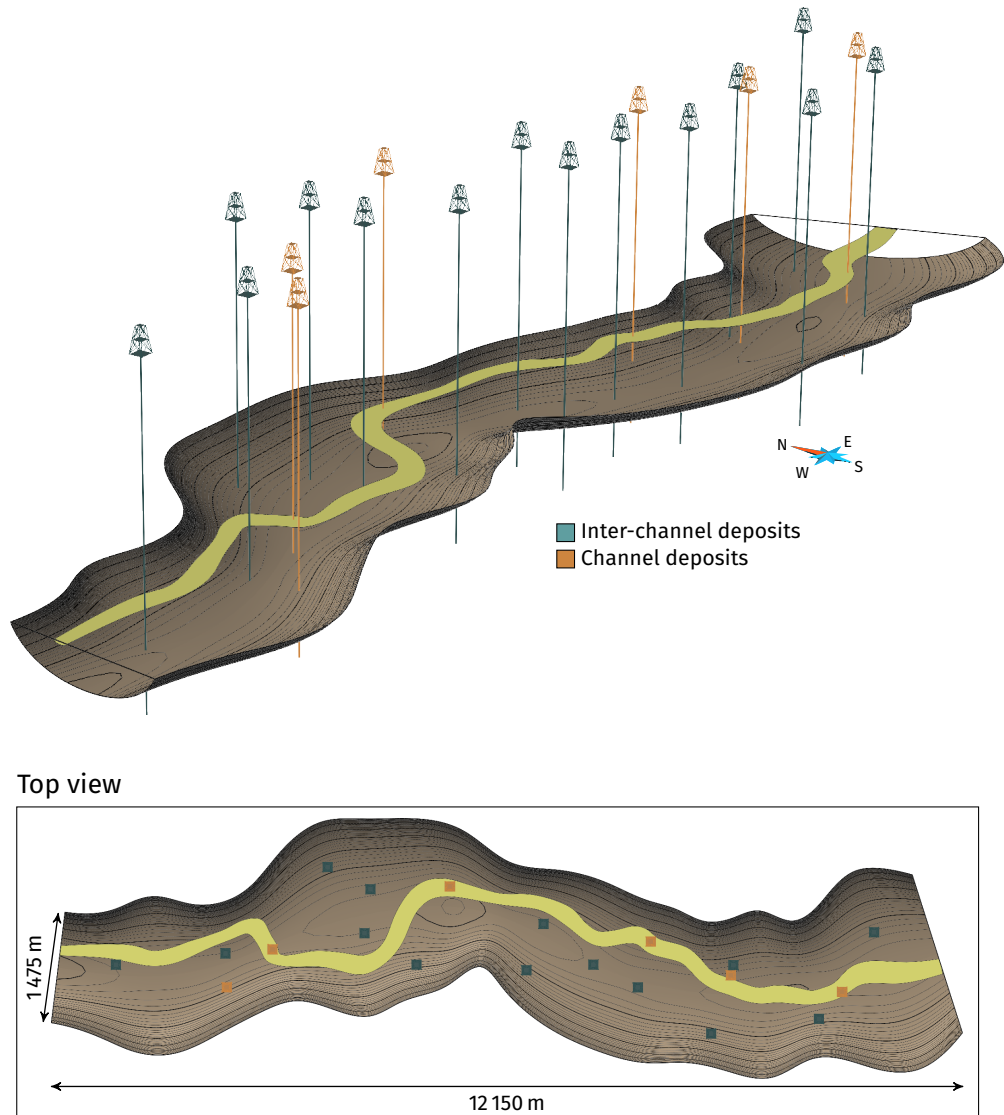


**Figure 3.33** Channel at the top of the realization in figure 3.32. The wells are colored depending on their facies data for the channel.

## 3.7 Discussion and perspectives

All the previous synthetic cases illustrate the method ability to simulate channels while taking into account various and numerous data. This section discusses some aspects of the simulation process.

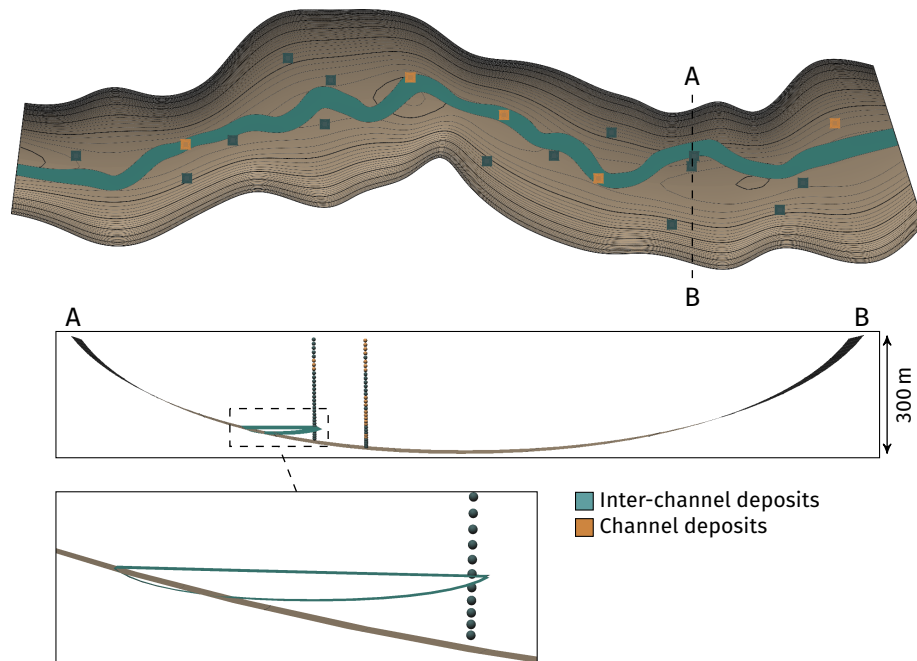


Figure 3.34 Example of incompatibility between the data and the L-system path.

### 3.7.1 About the channel morphology

With both the bend length and the curvature or the bend half-wavelength, bend amplitude and deviation angle, channel of various morphologies can be simulated, from straight to sinuous channels. The bends simulated with the current L-system rules follow a circular curve. In fluvial systems, bends are closer to a sine-generated curve than a circular curve [Langbein and Leopold, 1966], i.e., the angles between two successive segments evolve as a sine function of the channel distance, also called fattening. The bend shape also tends to be asymmetric or skewed depending on the global flow direction [e.g., Kinoshita, 1961, Brice, 1974, Carson and Lapointe, 1983]. Such asymmetry is also observable on turbiditic channels [Kolla et al., 2001] (figure 3.37). Kinoshita [1961] proposes a formula for the curvature of channel as a function of the channel distance, the bend wavelength and fattening and skewing coefficients. If necessary, the L-system rules can be easily modified to simulate bends based on a sine-generated curve or Kinoshita equation. Thanks to the L-system, the channel morphology is not a fixed feature of the method and can be changed at will.

The current process is still able to simulate asymmetric bend through two

### 3 Stochastic simulation of channelized sedimentary bodies

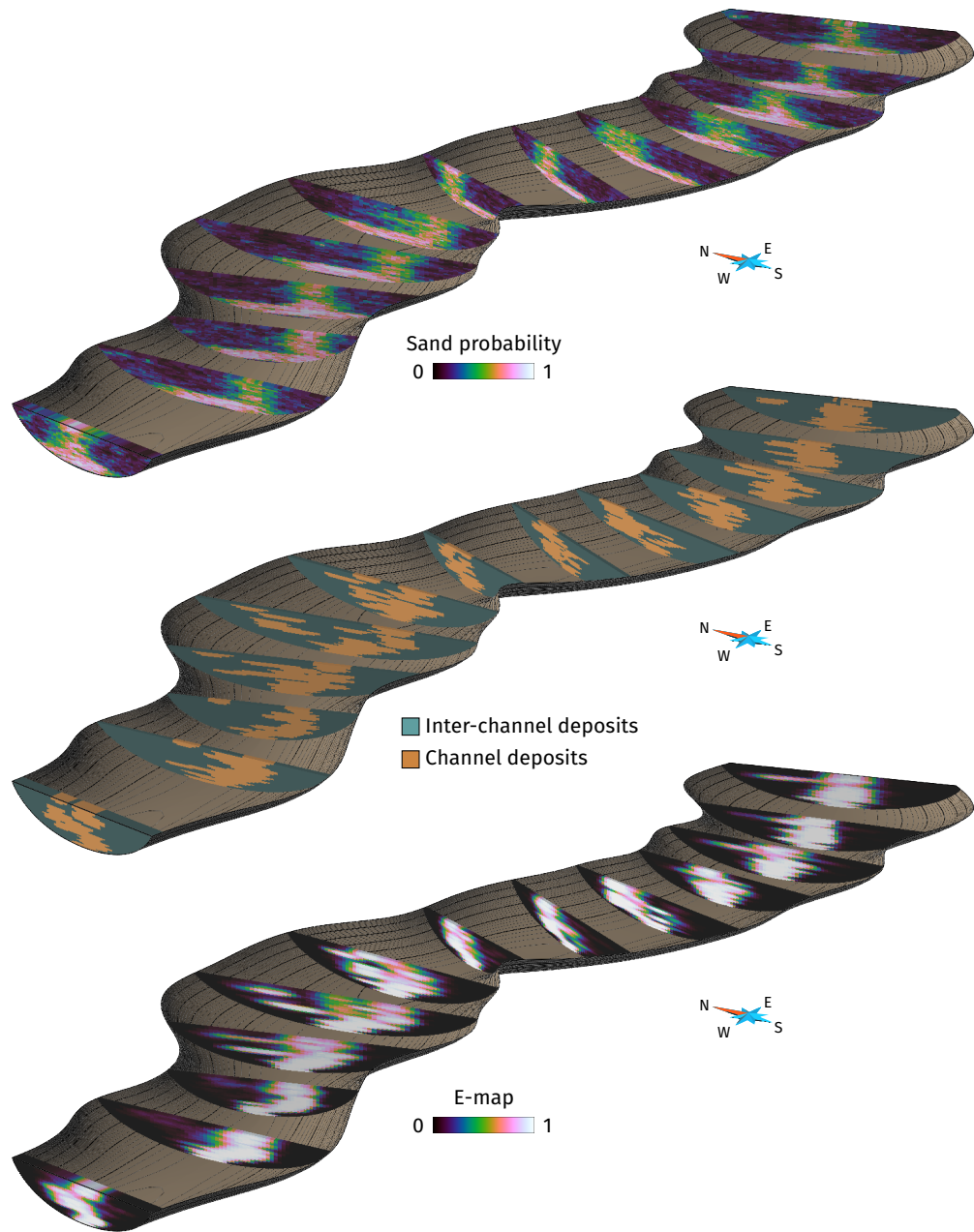


**Figure 3.35** Details on the channel trend of the realization in figure 3.32 rasterized in the master channel grid. The sand property cube along the same sections is here for comparison. The E-map illustrates the mean channel distribution over the 100 unconditional realizations.

### 3.7 Discussion and perspectives

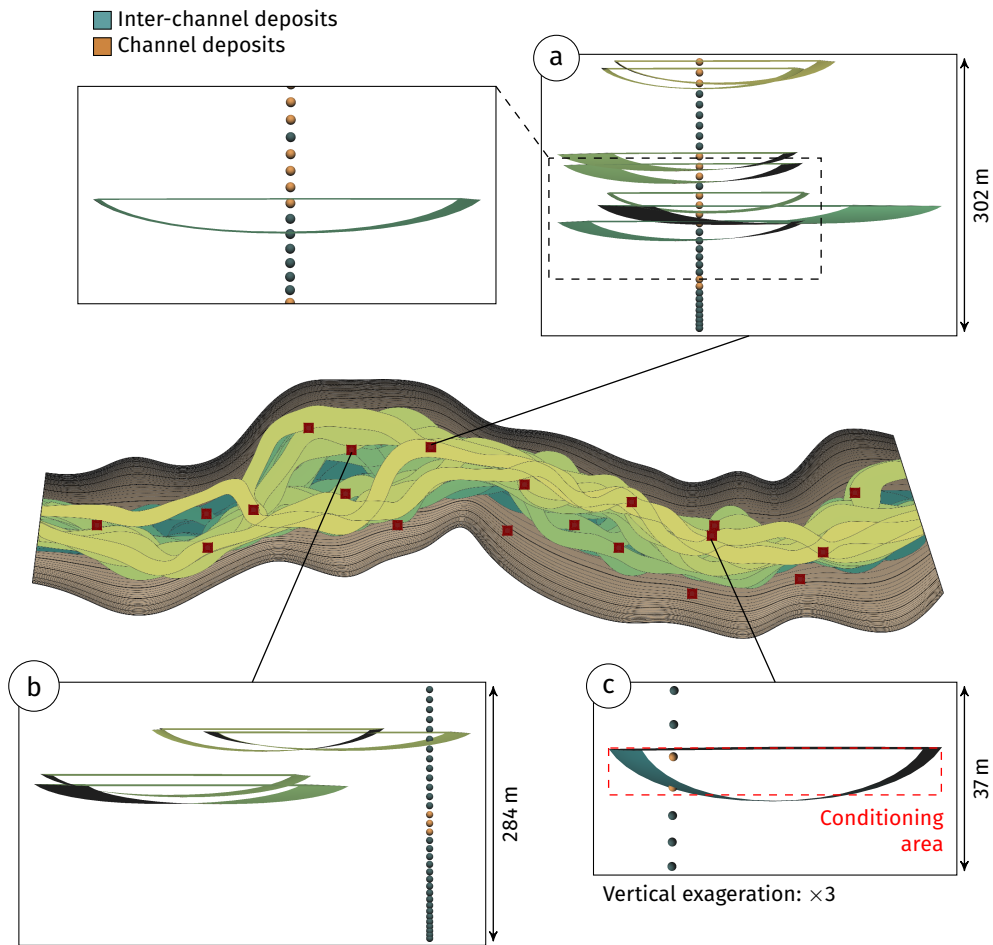


**Figure 3.36** Details on the well conditioning of the realization in figure 3.32. All the channels passing at or near the wells are not showed for clarity. a. The four channels at the top of the well perfectly condition the channel data. At the middle of the well, the last channel condition both a channel data and an inter-channel data. Indeed, the process is currently not able to precisely condition the channel so that the channel data remains inside the channel and the inter-channel data remains outside. b. 5 channels are close to a set of inter-channel data along a well. One of those channels condition the inter-channel data. This case shows a failure in the repulsion process. c. The channel conditions the two channel data of the interval as defined in the simulation process. However, the channel data at the bottom is not within the channel and not conditioned *stricto sensu*.



### 3 Stochastic simulation of channelized sedimentary bodies

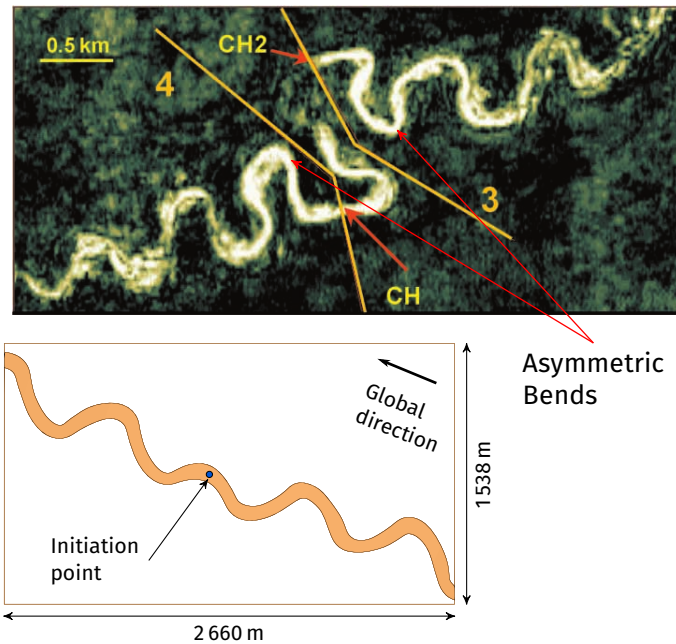


**Figure 3.37** Examples of asymmetric bends on a seismic section from Angola, West Africa (modified from Kolla et al. [2001]) and below example of channel simulated with a L-system showing opposite bend asymmetries from the initiation point.

features. First when using the curvature, asymmetry can appear thanks to the stochastic process. However, such shapes do not appear at will. The channel global direction tend to skew more or less the bends depending on the global direction weight. It also tends to make the channels straighter. Here the control is more clear. However, the bends are deformed depending on the constraint direction, which is not necessarily oriented along the global flow direction. This results in one branch with bends deformed in the opposite direction than the bends of the other branch (figure 3.37). Such setting is unnatural. For now no solution has been found to control the bend asymmetry due to the global direction.

Similar issue is noticeable with the other constraints. The relative constraint setting has been developed with the idea of minimizing the deformation induced by a constraint. However when simulating channels the two most important aspects are:

- Conditioning to all the available data, as they give information about the real setting of the domain of interest.

- Preserving the channel continuity, as it has more impact on the flow than the channel sinuosity.

Currently, the method is able to satisfy both aspects. Better reproducing real channel morphology and better controlling the constraint impact still call for improvements. In this perspective, comparing the simulated morphology with real channels should give an insight on the method ability to simulate realistic bends.

When simulating channels with a high sinuosity, channel self-intersections may happen despite the global direction and the self-repulsion. The speed of the simulation process (see section 3.7.12) makes conceivable to simply re-simulate the channel. Another solution is to suppress the loop formed by the self-intersection.

### 3.7.2 About constraints and conditioning

Constraints are able to handle a wide variety of constraining elements, from well data to probability cubes or seismic interpreted objects. This conditioning relies on the sum of vectors. Thus, it is a simple and fast process (see section 3.7.12). Getting the constraining vector is the only aspect that may slow down the conditioning process.

The main idea is to add as few constraints as possible, so that each constraint is expressed and taken into account at best. Adding few constraints helps to better preserve the channel morphology by limiting the deformations induced by the constraints.

A comparison with a conditioning by rejection sampling has been made to further analyze the bias introduced by the constraints on the channel morphology (figure 3.38). The rejection sampling is a simplistic conditioning process: an unconditional channel is simulated, if it fits the data it is kept, otherwise a new channel is simulated. Here the example is quite simple with two well channel data to condition. The channel parts within the inter-well area appear slightly less variable with the constraint than with the rejection sampling. It comes from the straighter morphology of the channels due to the constraint. This bias could be reduced by adapting the constraint setting, especially the magnitude, depending on the studied case.

The channel segment length has also a significant impact on the conditioning by the constraints. For a given channel length, a lower segment length means more channel segments and an easier conditioning. This is equivalent to the speed in robot motion planning: the higher the speed is, i.e., the longer the segment length is, the more the obstacle avoidance requires anticipation. This can be an issue as decreasing the channel segment length is computationally

### 3 Stochastic simulation of channelized sedimentary bodies

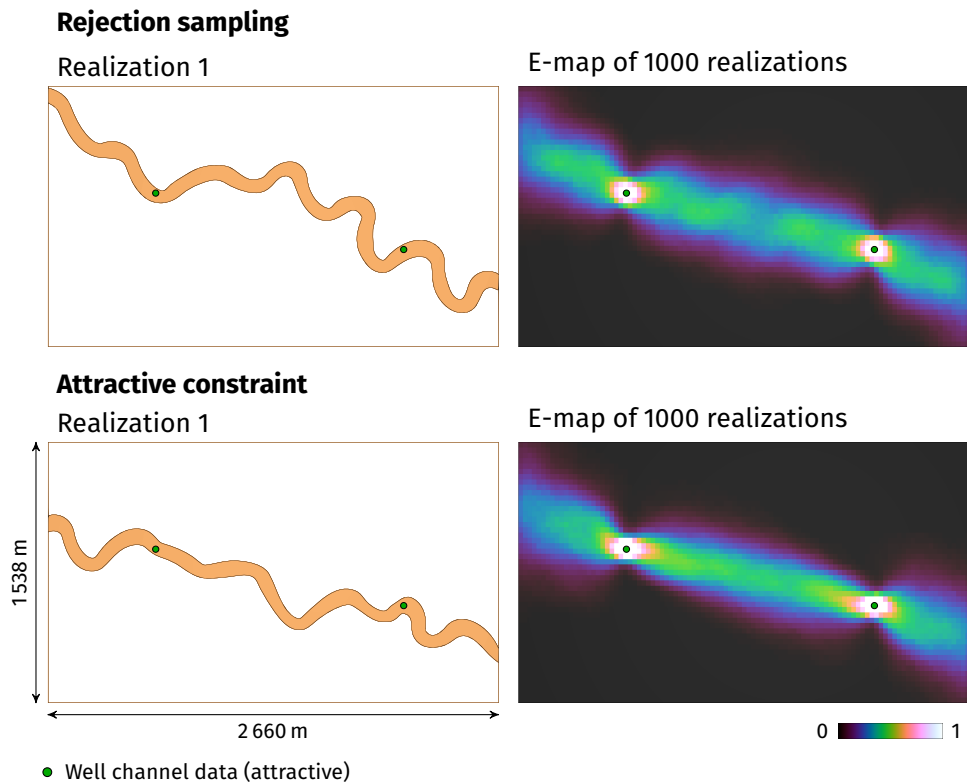


**Figure 3.38** Examples of realizations conditioned to well sedimentary data using two different conditioning processes and associated E-maps of 1 000 realizations. L-system weight: 1; global direction weight: 0.2 (rejection sampling). L-system weight: 1; global direction weight: 0.2; channel data weight: 1 (attractive constraint).

demanding. Thus, the constraint magnitudes should depend on the segment length, which is not the case for now.

Similar conditioning process is already applied in channel simulation [Lopez, 2003, Pyrcz et al., 2009] through a lateral deformation. Here the constraints are directly oriented toward the data as the channel grows. The deformation is then more easily distributed along the channel. A channel can also go straightly from one data to the other to ensure more easily the conditioning. Compared to conditioning based on a rejection procedure [e.g., Deutsch and Tran, 2002, Hassanpour et al., 2013], constraints are faster and more flexible, especially if the channel morphology specified as input is not consistent with the data. The conditioning of other data types than wells, e.g., property cubes, is also far easier. Compared to MPS, which can be seen as a conditioning solution

for object-based simulation, constraints ensure the preservation of the channel continuity and shape.

### **3.7.3 Post-processing the conditioning**

The L-system globally condition to the data, but a precise conditioning is difficult to achieve. For instance a L-system may not precisely condition to a well interval with the channel shape. If some improvements are undoubtedly possible, other solutions exist to ensure the conditioning of data.

A simple solution is to suppress the channel and to re-simulate a new one. This is worth considering with significant conditioning errors, as the simulation process is fast (see section 3.7.12). However, this is not conceivable for precise conditioning at a very local scale. Another possibility is to re-simulate the channel width or thickness. This is useful if a channel goes slightly outside its confinement for instance. Finally, the last possibility is to rely on the NURBS, which are very easy to deform. Such deformation process could be useful for the conditioning of other types of data, such as channel orientation data on a well.

### **3.7.4 Better introducing the channel width and thickness in the conditioning**

The better integration of the channel width and thickness in the constraints could be a significant improvement in the simulation process. Both the channel width and the thickness influence the conditioning through the constraint magnitude and perception area. For both features, the minimal and maximal values of the width and thickness are used. It helps to ensure the conditioning. However, it is rather strict and it would be better to use the local width and thickness of the channel.

Currently the width and the thickness are simulated at the end, when the conditioning process is already over. Nothing prevents the width and thickness to be simulated during the channel development. Due to the linear development of L-systems, the simulation path could not be random any more, but linear. This limits the stochasticity of the sequential Gaussian simulation, and could be a drawback of such process. On the other hand, it influences several aspects of the simulation process, such as the number of channels that condition to a set of channel data.

### **3.7.5 Conditioning to well sedimentary data**

The conditioning of well channel data is done from one data to the other. Thus, a channel can condition to any number of channel data. The only restriction is to have a channel segment length lower than the inter-well space. Limiting the perception area, combined with the stochastic development of the L-system, allows to stochastically correlate the wells with some control on the resulting correlation. The main force of this process is its ability to easily ensure channel data conditioning. Increasing the constraint weight makes the channel go straightly to the data. As demonstrated with connectivity data, the conditioning can be further forced by memorizing the data to condition until its conditioning.

Inter-channel data are more difficult to take into account. To ensure their non-conditioning, the repulsion magnitude must be high. Thus, a channel has difficulty to handle numerous inter-channel data, due to their combined repulsive action. In such cases, it is better to lower the weight related to the inter-channel data and to post-process those which are conditioned.

Here inter-channel data are considered as a homogeneous environment. In fact, it is constituted by several sedimentary bodies, for instance to levees or lobes. These data imply a channel close to them. A channel must pass at a certain distance of the data, without impinging on the sedimentary object related to that data. Modifying the magnitude by separating the inner area in two, one forbidden inner area and one outer area to condition, does not lead to satisfying results for now. Another solution is to add false channel data at a certain distance from the inter-channel data, or to rely on a NURBS deformation in post-processing.

### **3.7.6 Conditioning to well connectivity data**

Integrating connectivity data remains for now quite simple: when two wells need to be connected, a single channel correlates them. However two wells may be connected by different channels and not just one as described. The same principle of attraction can be used, but on a previously simulated channel conditioning the well and not on the well itself. Such process requires to better handle the relationships between the channels. It also implies to preserve the connectivity of the two wells when simulating the channel fill.

The non-connectivity of the wells are only handled by repulsing the channels from the wells. It can be better handled through the repulsion of the channel that condition to the non-connected data by the channels that condition the connected data.

The simulation of the channel fill is also essential to further control both the

connectivity and non-connectivity between several channels and several wells. When two wells are connected, the channel fill should ensure the preservation of the connectivity from one well to the other. Similarly, if a path of channels exist between two non-connected wells, the channel fill can ensure the non-connectivity of the wells.

When two wells are connected, the precise parts along the wells assuring the connection are not necessarily known. For now those parts are a user-defined property. Some work could be done to explore a more automatic and stochastic process to define the parts of two well that must be connected.

### 3.7.7 Conditioning to a sand probability cube

An interesting aspect of the constraints is the ability given to the L-system to condition property cubes with complex variations. The method is able to influence the channels during their development, so that they follow the high probability areas. The constraint weight enables to adjust this influence of the high probability areas.

Most of the time the purpose is to have the E-map of many realizations reproducing the probability cube. Better reproducing the probability cube requires adjusting the weight for this constraint, which must not necessarily be high compared to the other constraints. The process could still be improved to better reproduce the property cube with a low weight to better preserve the channel morphology.

With the application to a sand probability, it should be remembered that it is not a channel probability. Channel filling is not homogeneous and should also be taken into account to further analyze the probability reproduction by the simulation. If channels are continuous objects, discontinuities between the high probability areas can appear in the E-map. If these discontinuities do not reproduce precisely enough the probability cube, simulating channel objects is maybe not the best option. Other solutions, such as simulating point bar packages such as proposed by [Hill and Griffiths \[2009\]](#) or [Hassanpour et al. \[2013\]](#), should be considered.

### 3.7.8 Integrating seismic-interpreted objects

The application of channel simulation within a master channel illustrates the constraint ability to handle a confinement. The channel centerlines never go outside the confinement. This aspect calls for a significant repulsion, which perturbs the channel distribution. Further limiting the effect of the repulsion away from the confinement should improve the uniformity of the channel distri-

bution. Locally, the channel shape may go outside. This local miss-conditioning is pretty easy to correct by re-simulating the channel width or thickness or deforming the NURBS surfaces.

Another object that could be interpreted on seismic data are channels or channel parts. Complete channels do not require further treatment from the simulation process. Channel parts should be integrated as conditioning data. They could be treated similarly to the well channel data. A channel part is randomly selected to initiate a channel. Two branches grow from the two extremities of the channel part. Then the extremities of the other channel parts are considered as attractive data. The deformation aptitude of the NURBS can be used to avoid an abrupt curvature transition between the simulated channel and an interpreted channel part.

#### **3.7.9 About the parameterization**

The channel section parameters are quite classical in object-based simulation of channels [e.g., [Deutsch and Tran, 2002](#)]. The width and thickness are simple parameters. The ranges and curvature weights are more complex to infer. By default, the ranges can still be chosen equal to the bend length. It is more difficult to choose a default value for the curvature weight, as both the width and thickness do not necessarily vary following the curvature.

The bend length and curvature are unusual parameters in object-based simulations of channels. The curvature is less easy to infer than a bend length, half-wavelength or amplitude. However, the resulting channel morphology varies more, with more small scale variations along a bend. The bend half-wavelength and amplitude are more common parameters, both in object-based simulations and in the geomorphological description of channels. The deviation angle is quite secondary compared to the bend half-wavelength and the bend amplitude. Its purpose is to reintroduce the bend shape variability allowed by the curvature. Nevertheless, when the deviation angle is high, it perturbs both the half-wavelength and amplitude, which does not necessarily correspond to the input values any more. Moreover, this parameter is quite complex to infer. If the half-wavelength and the amplitude are used for their inference simplicity, the deviation angle can be avoided by setting it to zero.

Compared to other object-based methods [e.g., [Viseur, 2001](#), [Deutsch and Tran, 2002](#), [Hassanpour et al., 2013](#)], the main difference in the parameterization comes from the constraints. These constraints call for numerous parameters. Thus asking the user to set all those parameters is not really possible, especially for several constraints. Furthermore, some parameters such as the perception area are not necessarily easy to determine. The solution proposed

here is to predefined as much as possible the constraints and their parameters. However, depending on the studied case and the number of constraints, these parameters may be not compatible enough, leading to a poor conditioning. In such cases, the user can still modify the parameter values. All this requires more work to try to reduce the number of constraint parameters or, if possible, to infer some of them automatically.

### 3.7.10 About the use of L-systems

One main advantage of using L-systems is the possibility for the user to change the L-system rules. Modifying the channel morphology or introducing non-stationarity along the channel path is then easy once the L-system formalism is known. This brings more flexibility in the object definition than in other object-based approaches [e.g., [Viseur, 2001](#), [Deutsch and Tran, 2002](#), [Hassanpour et al., 2013](#)].

[Hill and Griffiths \[2009\]](#) use a different kind of formal grammar to simulate channels: the plex grammar [[Feder, 1971](#)]. In the L-system formalism, a symbol in a string can have a left and a right symbol. Visually, it has two attaching points, one to the left symbol and one to the right symbol. The plex grammar generalizes this principle by enabling connections between an arbitrary number of symbols. While three-dimensional shapes are better handled by such grammar, the rules can become quickly unwieldy. [Hill and Griffiths \[2009\]](#) simulate channels from a training channel, similarly to MPS. Thus, the rules are automatically deduced from the training channel and the user do not manipulate them directly.

Using a training model makes possible to fully exploit analog data, if available, while limiting the parameterization. However, the training model should be large enough to capture all the channel morphology variations. While a L-system and the associated constraints call for multiple parameters, they give the possibility to simulate channels from scratch. The L-system rules to build a bend give also a more compact representation of the channel morphology. This facilitates the interaction with the user. The L-system could also get its parameter values from analog data. In this case, it does not necessarily call for a complete training model, which may be difficult to get.

To build the rules of the plex grammar, the training model is cut into smaller segments. The principle is to find the smallest set of segments describing the model. The resulting segments tend then to be as long as possible, with one or several bends corresponding to a segment. While this facilitates the rule definition, conditioning to data is less easy than with a L-system, which can use smaller segments without complicating the rules.



**Table 3.10** Simulation time for a realization containing one channel. All the channels are simulated from the same location in the same domain as in section 3.5.3. The given values are the average time over 1 000 realizations and the standard deviation. The first set of realizations have no data. The second set is conditioned to the well sedimentary data of section 3.5.3. The last set is conditioned to the probability cube of section 3.5.3.

Simulation set	L-system simulation (in s)	NURBS generation (in s)
No data	$0.132 \pm 0.020$	$0.780 \pm 0.107$
Well data	$0.144 \pm 0.013$	$0.843 \pm 0.063$
Probability cube	$0.141 \pm 0.009$	$0.803 \pm 0.041$

### 3.7.11 About the simulation process

The current simulation process is able to simulate any number of channels while handling numerous data. The main source of improvement concerns the simulation stopping criterion. For now this criterion is a target number of channels. The simulation process completely ignores that target number of channels if some channel data are still not conditioned. This is worrying as the process tend to require many channels to condition all the channel data. Moreover, the number of channel data points influence the final number of channels. It could be appreciable to influence the conditioning and stay closer to the target number of channels.

Such process could give some leads to respect a channel proportion or a net-to-gross instead of a number of channels. Indeed, while the number of channels is difficult to infer, a channel proportion or a net-to-gross can be estimated from the data. Moreover, the channel proportion and the net-to-gross have a significant impact on the flow simulations. These parameters are often fitted through an iterative process in other object-based methods [e.g., [Viseur, 2001](#), [Deutsch and Tran, 2002](#)].

### 3.7.12 Numerical aspects

The realizations were simulated on a 64-bit Linux system with a 2.10 GHz processor Intel® Core™ i7-3612QM and 6 GB of RAM.

The L-system process in itself is quite fast (table 3.10). Adding conditioning data does not increase much the computation time on those simple examples. Indeed, the constraints rely on the sum of vectors to condition. For the conditioning process in itself, the only aspect that increases the computation time is to determine those vectors. The constraints also influence the computation time as the channels tend to be straighter or need to be longer to match the

**Table 3.11** Simulation time for a realization containing one channel with two different conditioning processes. The realizations are those illustrated by the figure 3.38. The given values are the average time over 1 000 realizations and the standard deviation.

Conditioning type	L-system simulation (in s)	NURBS generation (in s)
Rejection sampling	$15.494 \pm 15.489$	$0.834 \pm 0.048$
Attractive constraint	$0.130 \pm 0.008$	$0.770 \pm 0.039$

**Table 3.12** Simulation time for a realization for each set of realizations in the master channel. The only difference between each set are the data: Set 1. Confinement only; Set 2. Confinement and probability cube ; Set 3. Confinement, probability cube and well data. The given values are the average time over 100 realizations and the standard deviation.

Simulation set	L-system simulation (in s)	NURBS generation (in s)
Set 1	$3.17 \pm 0.15$	$16.24 \pm 0.22$
Set 2	$4.73 \pm 0.10$	$14.57 \pm 0.15$
Set 3	$6.64 \pm 0.45$	$21.47 \pm 1.31$

data. For instance, some channels have a more tortuous aspect due to their path to escape the repulsive data. This increases the computation time. The generation of the NURBS is the most time consuming part of the process, with computation time about six times higher than the L-system simulation times.

The comparison with a simplistic rejection sampling for conditioning also highlights the significant speed of the conditioning process by constraints (table 3.11). On average, the constraint is 100 times faster than the rejection sampling. The computation times of the NURBS surfaces in the two cases illustrate the straighter channels simulated under the constraint influence.

The simulation process of several channels is also quite fast (table 3.12). Here adding a probability cube significantly increases the computation time. It is due to the perception area size, which increases with the channel segment length. In the simple cases the segment length is about 1 grid cell and in the master channel case it is about 6 grid cells. The time increase when adding well data mainly comes from the higher number of simulated channels to condition all the channel data. The generation of the NURBS is again the most time consuming part of the process, with computation time three to five times higher than the L-system simulation times. The increase in set 3 compared to the set 1

is also due to the higher number of simulated channels. Adding a probability cube tends to form straighter channels. This decreases the computation time of the corresponding NURBS.

The conditioning process and its efficiency highly depend on the segment length. For a given channel length, smaller channel segments means more segments, which impacts the computation time. It also means heavier NURBS surfaces at the end. In such case, a re-parameterization function to use the minimal number of control points on a NURBS surface while preserving at best its shape is useful. This function is already proposed by [Parquer et al. \[2015\]](#) for channel modeling with NURBS.

## 3.8 Conclusions

This work introduces a new method for channel simulation through a formal grammar. The formal grammar, called the Lindenmayer system, simulates the channel morphology. This morphology is then wrapped with non-uniform rational B-spline surfaces to obtain the final channel object. The simulated morphologies are defined thanks to the rewriting rules of the L-system. Predefined rules are proposed to simulate straight to sinuous channels. These rules can be modified to simulate different morphologies, to add branches or to obtain non-stationary channels.

External constraints ensure the channel conditioning. They are determined from a constraining element, for instance a well data, a property cube or a seismic-interpreted object. A constraint is attractive or repulsive and is added to the L-system to influence the channel development by the related constraining element. Here some constraints related to classical conditioning data are presented: well sedimentary and connectivity data, sand probability cube and seismic interpreted sedimentary objects. As their parameterization is quite significant, most of the parameters are predefined to ensure the conditioning in most cases without much work for the user.

Object-based methods usually lack of flexibility for both well data or seismic-derived data conditioning. Here the process integrates data conditioning directly in the channel development. The conditioning then competes with the channel morphology. This induces a deformation of that morphology, and probably a statistical bias due to the conditioning. On the other side it ensures the conditioning: if the priority is given to the data condition, the channel straightly goes to the data, or avoids it depending on the constraint type. This illustrates that when data conditioning is the focus of the simulation process, that conditioning can always be achieved, similarly to cell-based methods. Using channel

objects always preserves the channel continuity, contrary to cell-based methods. The channel sinuosity can be lost, but it is less essential in flow simulation than the channel continuity.

Many improvements are still possible. First some work could be done around NURBS deformation to perfectly fit the data at a local scale. Then the conditioning process could be improved to deform less the channel morphology. This includes influencing the deformation direction of the bends so that it follows the global channel direction and not the constraint direction. It also includes a better management of different constraints with different types. From this point of view, a lot can be borrowed from robot motion planning, as the principles are pretty similar. Other sedimentary structures should be added to the process, such as lobes or levees. A NURBS parameterization already exists for those structures [Ruiu et al., 2015b]. Their development has to be integrated within the L-system rules.



## Chapter 4

# A geostatistical approach to the simulation of stacked channels

**Abstract** Turbiditic channels evolve continuously in relation to erosion-deposition events. They are often gathered into complexes and display various stacking patterns. These particular architectures have a direct impact on the connectivity of sand-rich deposits. Being able to reproduce these patterns in stochastic simulations is thus of significant importance. We propose a geometrical and descriptive approach to stochastically control the channel stacking patterns. This approach relies on the simulation of an initial channel using a Lindenmayer system. This system migrates proportionally to a migration factor through either a forward or a backward migration process. The migration factor is simulated with a sequential Gaussian simulation or a multiple-point simulation. Global avulsions are performed using a Lindenmayer system, such as the initial channel simulation. This methodology brings a control on the connectivity between the channels by adjusting the extension of the migrating areas and the migration patterns. If some aspects such as the smoothing of the migration factor or data conditioning require further work, this method furnishes encouraging results with both forward and backward migration processes.

## 4.1 Introduction

Facies heterogeneities within a reservoir or an aquifer can have a dramatic impact on the flow. The Shiehallion field is a perfect illustration of such impact in an oil field [e.g., [Gainski et al., 2010](#)]. When the production started, its reservoir compartments appear far less inter-connected compared to the initial expectations. Sand-rich deposits within turbiditic channels form the reservoir compartments, but the channel fills are not homogeneous. Some flow barriers can appear along the channel top, sides and bottom due to mud-rich deposits, e.g., margin drapes or slumps. These elements are too small to be visible on the data, especially seismic data.

The impact of mud-rich deposits on the flow depends on the stacking pattern [[Labourdette et al., 2006](#)], i.e., how channels position themselves in relation to each others. The stacking pattern determines if a margin drape prevents any flow circulation between two channels or if it has no impact at all. This is especially important when considering turbiditic channels, as significant changes in the stacking pattern can be observed even over short distances [[Mayall and O'Byrne, 2002](#)], with a non-negligible impact on the reservoir connectivity. Thus channel stacking has to be taken into account when simulating channels for reservoir modeling. A common strategy is to simulate or mimic the processes that control the stacking.

Channel stacking is the result of the channel evolution. This evolution implies two main processes: channel migration and avulsion. The migration comes from the erosion and deposition processes due to density current circulation that forms the channel. Four main migration patterns are observed:

- A lateral channel bend migration or swing, which shifts the bend laterally and increases the channel sinuosity [[Peakall et al., 2000](#), [Posamentier, 2003](#)] (figure 4.1).
- A downsystem channel bend migration or sweep, which shifts the bend downward [[Peakall et al., 2000](#), [Posamentier, 2003](#)] (figure 4.1).
- A channel bend retro-migration, which decreases the channel sinuosity [[Nakajima et al., 2009](#)].
- A vertical channel migration or aggradation, which shifts the channel upward [[Peakall et al., 2000](#)] (figure 4.1).

Migration of turbiditic channels is continuous, forming accretion packages [e.g., [Abreu et al., 2003](#), [Arnott, 2007](#), [Nakajima et al., 2009](#)], or discrete, due to abrupt migrations which correspond to local avulsion [e.g., [Abreu et al., 2003](#),

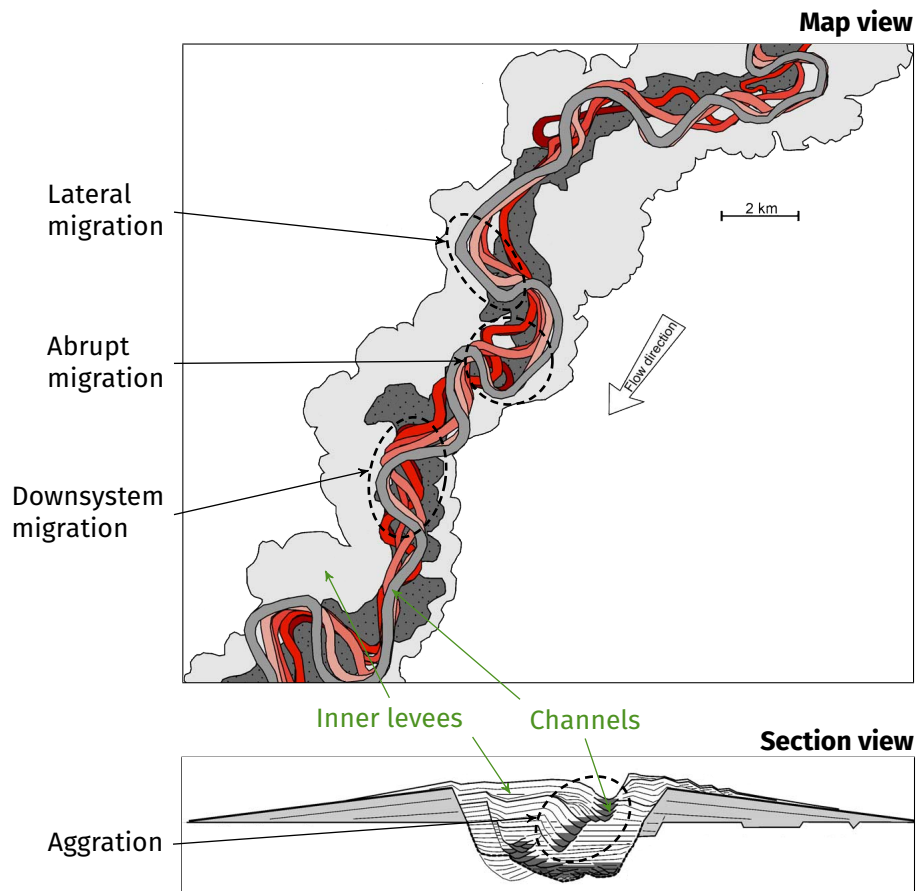


**Figure 4.1** Example of migration patterns on channels interpreted on seismic data from the Benin-major channel-belt, near the Niger Delta (modified from [Deptuck et al. \[2003\]](#)).

[Deptuck et al., 2003](#)]. Avulsion occurs when the currents exceed the channel capacity to contain them: the flow leaves the channel and forms another course. Contrary to abrupt migrations, regional avulsions are often a definitive abandonment of the previous course.

Mimicking migration and avulsion in stochastic simulation methods is a topical subject of study to better control the channel stacking. Whatever the method, avulsions rely on a statistical framework, due to the lack of knowledge to genetically model their initiation. Regional avulsions are handled through a probability associated to the development of a new channel. Channel migration has been more widely studied, with numerous works attempting to develop a



physical model of the migration.

In fluvial systems, the more widespread methods are two-dimensional physical simulations. They link the migration to the asymmetry in the flow field induced by the channel curvature and responsible for bank erosion [Ikeda et al., 1981]. These methods have been extended to a stochastic simulation framework by Lopez [2003] and Pyrcz et al. [2009]. If they manage to produce realistic-looking channels, such method predictions can be far from the reality depending on the simplifications introduced in the physical model [Camporeale et al., 2007]. Models with fewer simplifications call for a heavier parameterization and possibly a more important computational effort, which may not be practical in a stochastic reservoir simulation context. Data conditioning remains also a challenge.

These two-dimensional physical methods have been applied to turbiditic environments [McHargue et al., 2011]. Imran et al. [1999] even adapt them to the migration of submarine channels. However, the physical processes behind submarine channels have been, and still are, a source of controversy. The main controversy concerns the rotation direction of the secondary flow and the factors that determine this direction [e.g., Corney et al., 2006, Imran et al., 2008, Corney et al., 2008]. This aspect is a major concern because the rotation of the secondary flow controls the channel migration. Lately, Dorrell et al. [2013] argue that two-dimensional physical models are not accurate enough to capture the full three-dimensional structure of the flow field. Beside their validity, which remain questionable and questioned [e.g., Sumner et al., 2014], three-dimensional models are also computationally demanding. Thus, their convenience in a stochastic framework is doubtful. Moreover, the last channel of a system is often observable on seismic data due to its argileous fill. In such a configuration, initiating the process from this last channel, so from the youngest channel, and migrating backward to the oldest channel is more appropriate, as it starts directly from the available data [Labourdette, 2008]. Then the migration divides in two processes:

- A forward migration, which is the normal or classical migration. It starts from the oldest channel which migrates to obtain the youngest channel.
- A backward migration, which is a reverse migration. It starts from the youngest channel which migrates to obtain the oldest channel.

In the stochastic simulation of channels, most approaches are descriptive: their goal is to directly simulate the sedimentary bodies resulting from the flow processes, not the flow processes themselves. For now, very few works have tackled the migration in a descriptive manner.

Viseur [2001] and Ruiu et al. [2015b] use a forward migration process by defining migration vectors from a weighted linear combination of vectors for lateral migration, downsystem migration, bend rotation and more recently vertical migration thanks to Parquer et al. [2015]. This method gives an important control over the migration pattern. However, the migration pattern is for now identical over the whole channel and the migration is deterministic whereas not relying on physical principles. The weights in the linear combination may also be hard to define. Concerning backward migration, Ruiu et al. [2015b] lay the foundations for process to reconstruct point bars from channels interpreted on seismic data. But this process is still at an early stage and is also purely deterministic.

In a fluvial setting, Teles et al. [1998] rely on an empirical law giving the migration displacement as a function of the curvature and the channel width. Labourdette [2008] proposes a workflow based on the occurrence of channels within a confinement, a configuration often seen in turbiditic reservoirs. Starting from the last channel of the migration process, he performs a backward migration based on empirical laws deduced from analogs to determine the distance between the channel centerline and the canyon border. However, this workflow is deterministic, limited to channels within a confinement and to the representativeness of the analog data.

We propose a different approach for channel migration, based on a descriptive stochastic simulation approach to avoid the use of too complex and incomplete physical models. The global process is similar to the principle of two-dimensional physical methods. It starts with the collection of a channel to initiate the evolution process (section 4.2). A Lindenmayer system simulates the new channel path following an avulsion. Channel migration is divided into two elements:

- The lateral and downsystem migrations and the retro-migration are the horizontal components of the migration. For the rest of this chapter, the horizontal migration is referred as migration.
- The vertical migration is the vertical component of the migration. It is referred as aggradation for the rest of this chapter.

A vertical shift of the channel simulates the aggradation. The stochastic simulation of a migration factor allows the migration. This stochastic simulation uses either a sequential Gaussian simulation (SGS) (section 4.3) or a multiple-point simulation (MPS) method (section 4.4). With some other considerations (section 4.5), all this lays the foundations of a process to simulate both forward and backward channel migration (section 4.6). The process is applied to a synthetic

case with turbiditic channels migrating within a canyon (section 4.7), which lead to some discussions and perspectives (section 4.8).

The whole method was implemented in C++ within the Gocad plug-in ConnectO. The channel envelopes with NURBS were implemented by J  r  my Ruiu within the Gocad plug-in GoNURBS [Ruiu et al., 2015b].

## 4.2 New channel generation

Performing either a forward or backward migration calls for a channel to initiate the process. This initiation occurs at two steps: at the beginning of the whole process and when a new channel path develops.

### 4.2.1 Channel initiation

Two main options are considered. When the data can not provide an initial channel, a channel path is stochastically simulated. Sometimes channels are interpretable on seismic data. These channels can initiate the process.

#### From L-system

L-systems offer a way to stochastically simulate the initiating channel. The simulation process is exactly that described in the previous chapter. A set of L-system rules handles the channel morphology by simulating a channel centerline. The centerline is a set of locations through which the channel passes. Each location knows the channel width, thickness and asymmetry at that location. Non Uniform Rational B-Spline (NURBS) surfaces dress the L-system to obtain the final channel shape. Data conditioning, either for well or seismic data, is done through constraints applied during the channel growth. The constraints attract or repulse the channel from the data.

This method simulates various meandering patterns, from straight channels to highly sinuous patterns (figure 4.2). It is suitable for both forward migration, which classically requires starting with a quite straight channel, and backward migration, which requires an initial channel with a high sinuosity. The parameters needed by the method, i.e., channel width, thickness and bend length, curvature or half-wavelength, amplitude, can be retrieved from wells or from a seismic, if available, or on analog data coming from seismic or field studies.

#### From interpreted seismic data

Another way to obtain this initial channel is to interpret it directly on a seismic. Ruiu et al. [2015a] propose a method to interpret channels in a semiautomatic

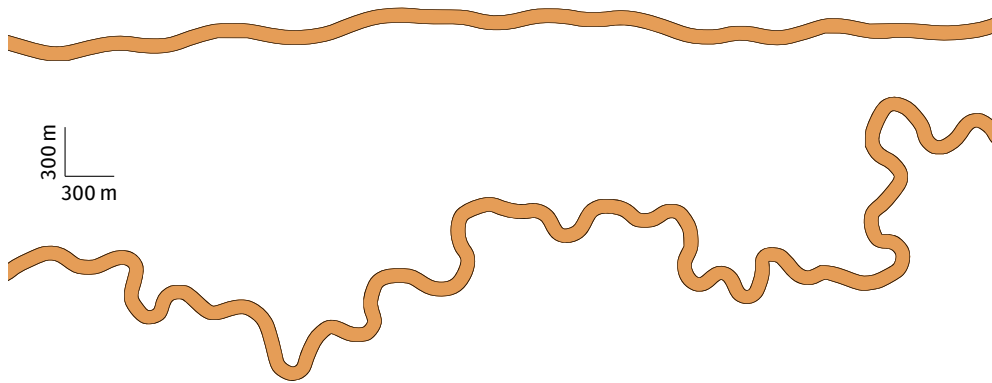


**Figure 4.2** Example of a straight channel (top) and a highly sinuous channel (bottom) simulated with L-system and wrapped with NURBS. The input parameters are given in table C.1, appendix C.

way. It requires to approximately arrange a channel representation based on Non-Rational Uniform B-Splines (NURBS) surfaces within a channel identified on the seismic. Then an automatic optimization fits the NURBS surfaces to the most relevant edges delimiting the channel, determined through custom edge detection. This method can be used when seismic data are available with a sufficient resolution. This is often the case in turbiditic context, where the last channel of a complex is usually filled by a highly argillaceous content and stands out on the seismic. It could require converting the resulting channel object into an L-system formalism depending on the implementation choices, i.e., if the migration is performed on the L-system or on the NURBS.

If channels are partially interpretable, the blanks between the interpreted channel parts can be simulated using L-systems. An extremity of a part is defined as an initiation point for the L-system, and the extremity of the following part is defined as an attractive data. Thus, the simulated system can stochastically link the two parts.

### 4.2.2 Regional avulsion

Regional avulsion is a key event widely observed on both fluvial and turbiditic systems. When an avulsion occurs, the channel is abruptly abandoned at a given location (figure 4.3). Upstream the flow remains in the old channel, whereas downstream a new channel is formed. However, its triggering conditions remain poorly understood due to the complexity of this process. Avulsion is so often statistically handled in simulation methods: a probability of avulsion

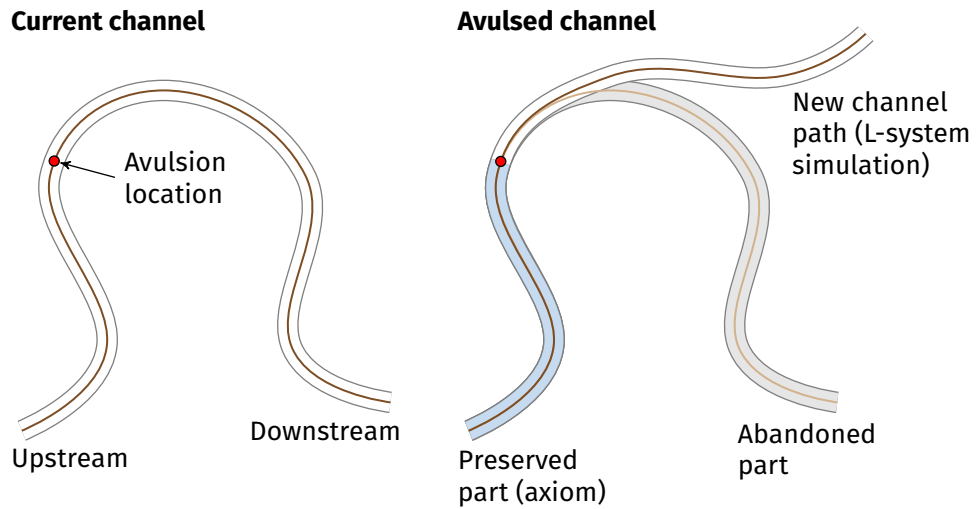


**Figure 4.3** Principle of global avulsion based on L-system.

controls the development of a new channel. This process can be influenced by the curvature, as a high curvature tends to favor an avulsion.

The approach for global avulsion is similar to the one defined by [Pyrzcz et al. \[2009\]](#). The avulsion starts by computing the sum of the curvatures at each channel section. A threshold is randomly drawn between zero and the sum of curvatures. The channel is then scanned from its most upstream part to the downstream part. At each section, the curvature is subtracted from the threshold. A section initiates an avulsion or not depending on two factors:

- An input probability of avulsion.
- The random curvature threshold, which should be lower than the section curvature to trigger an avulsion.

Thus the avulsion initiation at a given section is a probabilistic choice influenced by the curvature at the section location.

Then the upstream part of the L-system is isolated. The obtained string serves as axiom to simulate the new post-avulsion channel ([figure 4.3](#)). This channel is based on the same parameters as the initial channel, but different parameter values may be used. A repulsion constraint with the pre-avulsion channel can be set to avoid intersections between the two channels.

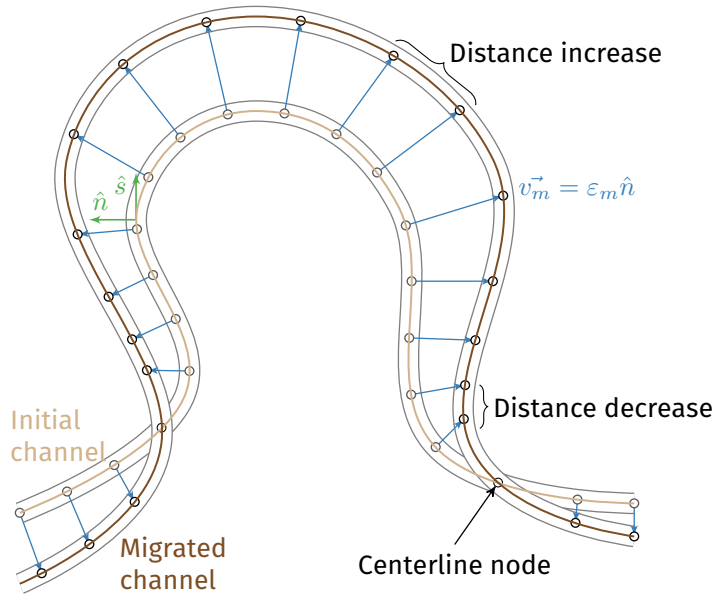


**Figure 4.4** Migration principle: the centerline nodes are moved along a migration vector  $v_m^{\vec{}}$  based on the normal  $\hat{n}$  to the centerline and a migration factor  $\varepsilon_m$ .  $\hat{s}$  is the normalized vector along the streamwise direction.

### 4.3 SGS for forward or backward migration

The first process we propose to simulate both forward and backward migration is based on sequential Gaussian simulation (SGS). It uses a migration factor statistically simulated by the SGS.

#### 4.3.1 Principle

Channel migration is deeply linked to the channel curvature. Other elements come into consideration, such as soil properties or flow fluctuations. However, the physical processes behind bend evolution are complex and still not completely understood. Moreover, they differ from turbiditic to fluvial environments.

This is why we propose to rely on a more descriptive approach based on geostatistics. In physical approaches, a migration factor is computed along the nodes of a channel centerline based on fluid flow equations. Then the nodes are moved based on that factor along the normal to the centerline (figure 4.4).

We rely on a similar approach based on moving the node along the normal to the centerline to migrate a channel. Here the Euclidean distance  $d$  of

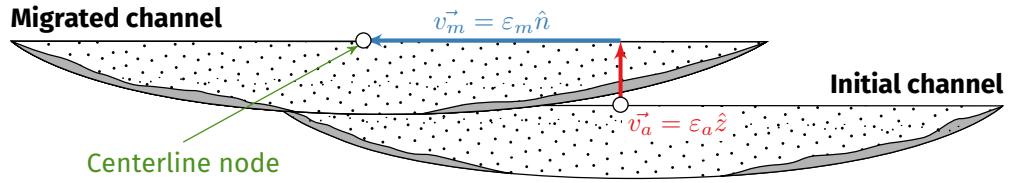


**Figure 4.5** Components of the displacement vector for channel migration.  $\vec{v}_a$  is the aggradation component along the vertical direction symbolized by the normalized vector  $\hat{z}$ . The aggradation factor  $\epsilon_a$  determine the vertical displacement.  $\vec{v}_m$  is the migration component along the normal direction to the centerline symbolized by the normalized vector  $\hat{n}$ . The migration factor  $\epsilon_m$  determine the horizontal displacement.

displacement for a node is the length of a displacement vector  $\vec{v}$ :

$$d = \|\vec{v}\| \quad (4.1)$$

The displacement vector divides in two components (figure 4.5):

- A vertical component for the aggradation. Aggradation is simply done by shifting the new channel vertically by an aggradation factor  $\epsilon_a$ , which is the same for all the channel nodes.
- An horizontal component defined by a migration factor  $\epsilon_m$  computed using sequential Gaussian simulation.

The SGS simulates a migration factor value for each node of the centerline in a sequential manner [e.g., [Deutsch and Journel, 1992](#)]:

1. A random path is defined to visit all the centerline nodes.
2. At a given node:
  - a) If some nodes in a given neighborhood already have a value:
    - i. A kriging system determines the Gaussian complementary cumulative distribution function (ccdf) using the data, i.e., the nodes with a value given in input, and the previously simulated nodes within the neighborhood.
    - ii. A simulated value for the given node is drawn within the ccdf.
  - b) Otherwise, the simulated value is drawn from an input distribution of migration factor.
3. Return to step 2 until all the nodes of the path have been visited.

The SGS requires the migration factor to be a Gaussian variable. If not, a normal score transform of the input distribution and of the data is introduced before step 1. A back transform is done at the end of the simulation process.

Using directly SGS with simple kriging involves that the migrating area appears anywhere along the channel. But a migrating area is often related to a bend and is greatly influenced by the channel curvature. This aspect is taken into account by using intrinsic collocated cokriging [Babak and Deutsch, 2009] instead of simple kriging. The channel curvature is integrated as a secondary variable in the simulation process, influencing the spatial structure of the migration factor. The intrinsic collocated cokriging enables to adjust the influence of the curvature through a weight: when that weight is positive, the channel tends to migrate, when it is negative, the channel tends to retro-migrate. This weight represents the correlation between the primary variable, i.e., the migration factor, and the secondary variable, i.e., the curvature. Thus, simply by changing the curvature weight symbol the same workflow achieves both forward and backward migration processes.

#### 4.3.2 Parameter set

Four parameters are required to perform a migration through SGS (figure 4.6): a migration factor distribution, an aggradation factor distribution, a variogram and a curvature weight.

#### Migration and aggradation factor distributions

Two migration factor distributions control directly the distances between two successive channels in the migration process: one for the horizontal component of the migration and one for the vertical component. These distributions can be obtained by interpreting horizontal and vertical distances between channels or point bars on seismic of field analogs for instance. They are geometrical parameters. The horizontal factor should be chosen as small as possible, as it tends to increase the impact of the small scale distance variations on the horizontal migration. The vertical factor is unique for all the modules of a given channel but may vary between channels, hence the need for a distribution.

#### Variogram

The variogram informs about the spatial model of a variable [e.g., Gringarten and Deutsch, 2001]. It is usually inferred from the data. These data can come from the partial interpretation of migrating channels on a seismic to get migration factor values along the interpreted channel parts.



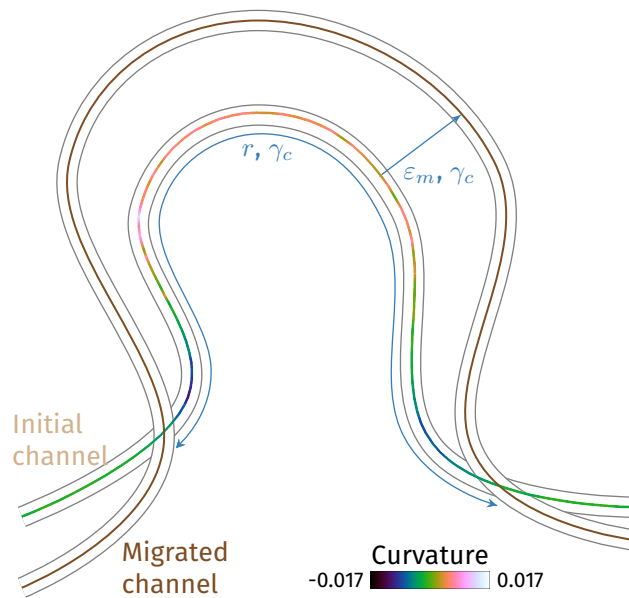


**Figure 4.6** Main parameters used for horizontal bend migration with SGS.  $\epsilon_m$  is the migration factor,  $r$  the variogram range and  $\gamma_c$  the curvature weight. The later perturbs the two other parameters by fitting more or less the migration spatial structure to the curvature spatial structure.

If no data is available, the migration factor is considered as a Gaussian variable. The purpose is to have a migration factor that evolves as smoothly as possible to avoid small-scale perturbations during the migration. The variogram model is then chosen Gaussian. The nugget effect adds noise to the realizations and is kept to 0. The sill is fixed to 1.

This leaves one parameter: the variogram range. This parameter represents the horizontal extension of a migration area, which can stretch over several bends (figure 4.7). It has a main impact on the migration. By default, it must be close to the wanted bend length for the bends that develop through the process. A range smaller than the bend length leads to the development of smaller-length bends through the migration. A range larger than the bend length makes the migration occur over several bends. Thus some bends seem to migrate and other to retro-migrate.

### Curvature weight

The curvature weight adjusts the curvature influence on the spatial structure of the migration factor (figure 4.7). When equals to  $(-)$ 1, the migration factor

### 4.3 SGS for forward or backward migration

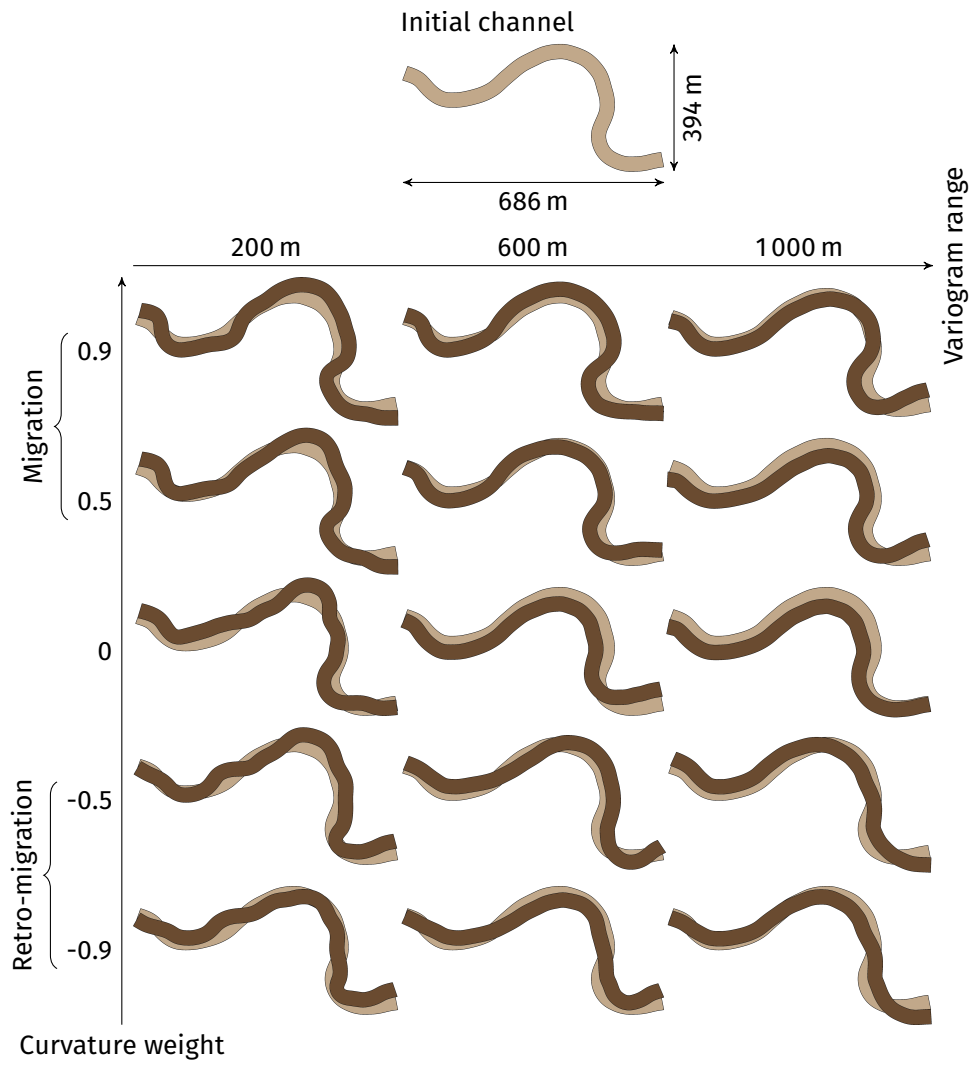


**Figure 4.7** Effect of the variogram range and of the curvature weight on bend migration with SGS.

follows strictly the curvature spatial structure, favoring lateral migration. When equals to 0, the migration factor is independent from the curvature and more various migration patterns appear: lateral migration, downsystem migration and even their counterparts in retro-migration. The curvature weight is so related to the stability of the system: when a system is unstable, channel stacking patterns are highly variable as the influence of the previous channel over the next one is weaker.

This parameter is the harder to adjust. It depends on the wanted migration patterns, which can be deduced from a seismic or from analogs. However, the lateral migration is the only pattern that can be favored in the current form of the method: having only lateral migration is possible, but having only downsystem migration is not.

## 4.4 MPS for forward or backward migration

Multiple-point simulation (MPS) is another approach to perform a migration. The idea is to rely on a more complete model than a variogram to define the spatial structure of the migration.

### 4.4.1 Principle

Simulation methods such as the SGS rely on a histogram and a variogram inferred from the data. Thus, they only catch the one- and two-point statistics and miss all the higher-order statistics. But higher-order statistics are difficult if not impossible to infer from data. Multiple-point simulation [[Guardiano and Srivastava, 1993](#)] attempts to overcome such limitation by relying on an external representation of the structures of interest, the training image. Using MPS instead of SGS in the migration process can give more realistic migrations.

The global principle is similar to the one introduced for the SGS: each node of the channel centerline migrates following a migration factor and an aggradation factor. The values of those factors are borrowed from a training set, i.e., a set of migrating channels. This training set can come from a seismic or field analog. The migration and aggradation factors are computed all along the channels of the training set. No factors can be computed for the last channel, which is excluded from the set.

For a given channel, the aggradation factor is supposed to be the same for all the centerline nodes. A value is then randomly drawn amongst the training set and attributed to all the nodes of the channel to migrate. This channel migrates simply by shifting it vertically following the aggradation factor. The migration factor is computed using a MPS method, the Direct Sampling (DS) [[Mariethoz](#)

et al., 2010]. This method has the advantage of easily handling continuous properties and secondary data. Again, the curvature serves as secondary data to influence the migration.

The whole training set is not necessary used to simulate the migration of a channel. The process relies on a training model, which can be (figure 4.8):

- Directly the whole training set. In this case, each simulated migration step is influenced by all the migration steps within the training set.
- A single migration step within the training set:
  - Drawn randomly among all the migration steps of the training set.
  - That follows the migration order of the training set. In that case, each simulated migration step corresponds to a particular migration step within the training set. With that option, the number of migration steps in the training set limits the number of simulated migration steps.

Both the migration factor and the curvature are known in the training model (figure 4.8). The migration process starts from an initial channel, whose curvature is known. The principle is then to simulate the migration factor on the initial channel based on the training model. The curvature ensures the link between the spatial variations of the migration factor in the training model and that on the simulation.

At a node to simulate, the  $n$  closest nodes with already a value form a data event  $N_x$  (figure 4.9). The principle of the DS method is to try to find these data event in the training model. A position is randomly chosen, either in the whole training set or only within a given migration step depending on the retained option. Then the process scans the training model. At each node, a distance  $d_{D,P}$  is computed between the current pattern  $N_y$  and the data event  $N_x$ :

$$d_{D,P}(N_x, N_y) = \frac{1}{n} \sum_{i=1}^n \frac{|Z(x_i) - Z(y_i)|}{\max_{y \in TS} (Z(y)) - \min_{y \in TS} (Z(y))} \quad (4.2)$$

with  $d_{D,P} \in [0, 1]$ ,  $n$  the number of nodes in the data event,  $Z$  the compared property,  $x$  a node in the data event,  $y$  a node in the training set pattern and  $TS$  is the whole training set or just a single migration step of the training set. The process stops if the distance is lower than a given threshold. The simulated node gets the value of the central node associated to the training set pattern. During the process, the value corresponding to the lowest distance value is

4 A geostatistical approach to the simulation of stacked channels

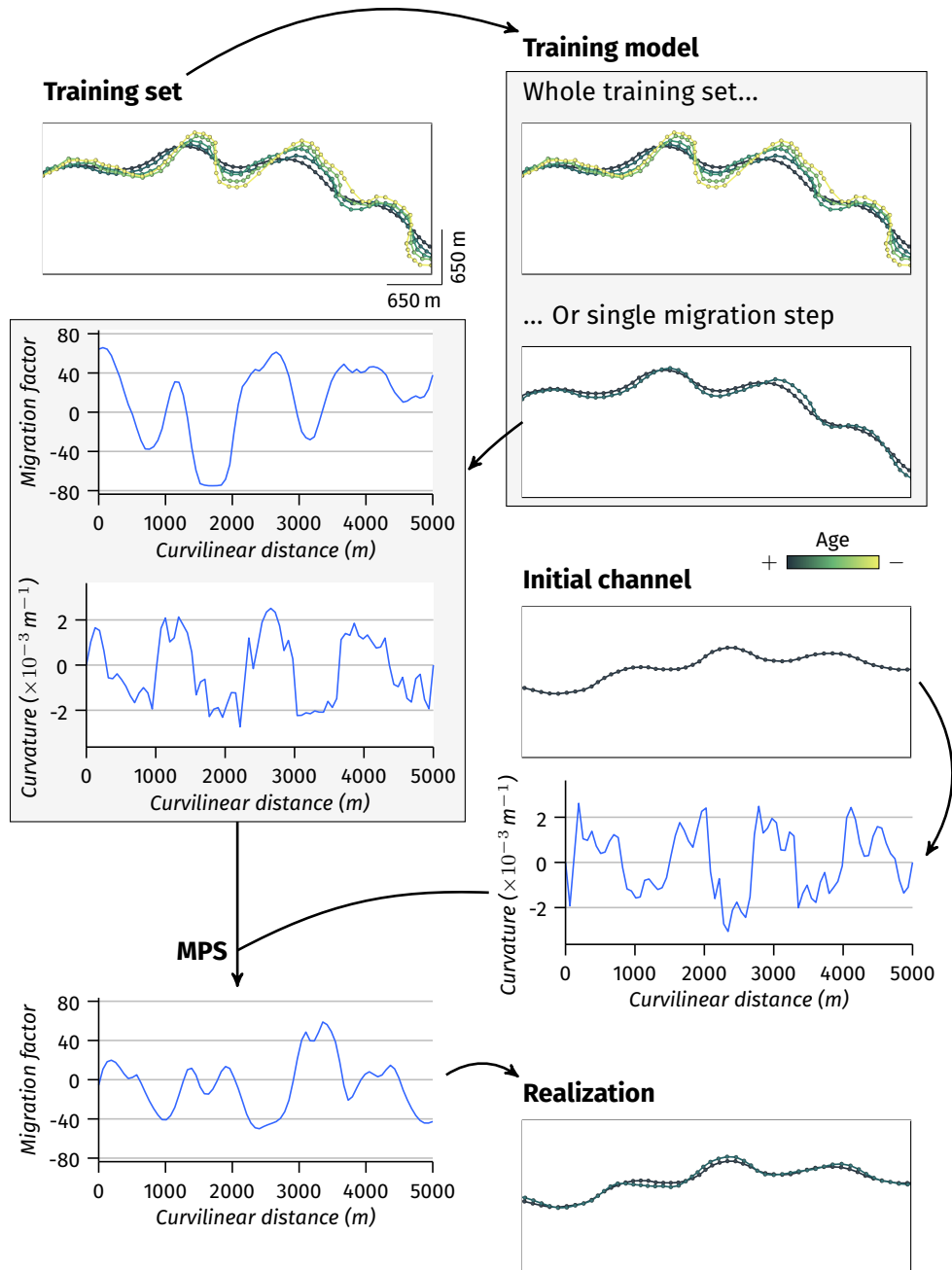
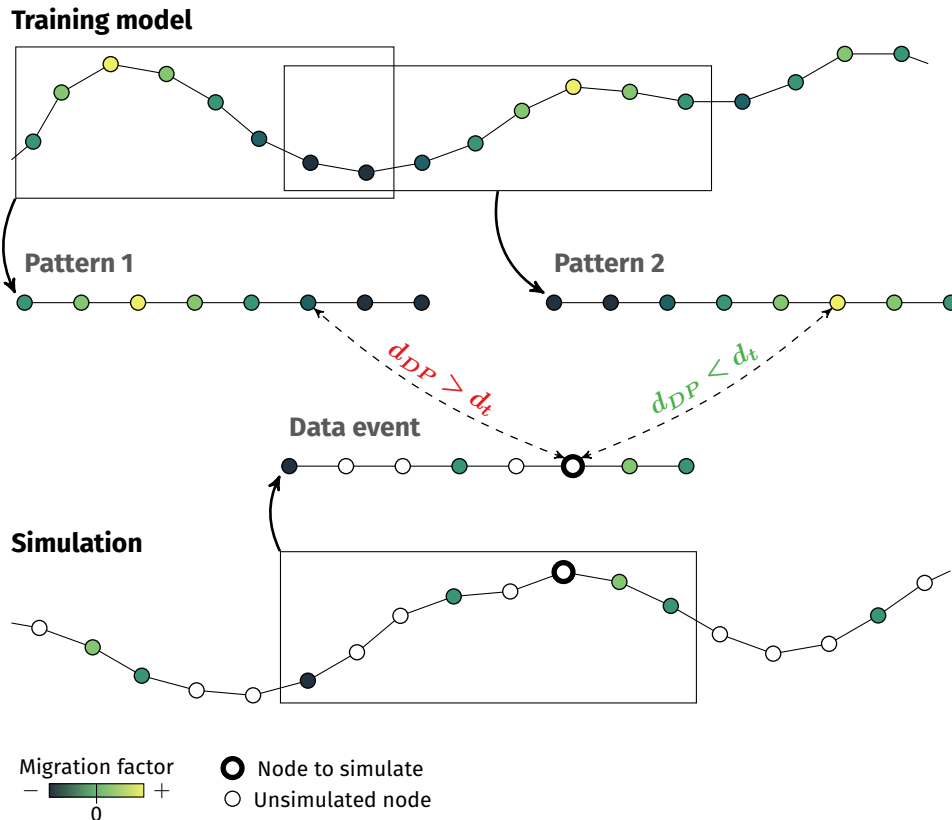


Figure 4.8 Framework for the simulation of the migration factor  $\varepsilon_m$  with MPS.



**Figure 4.9** DS simulation principle: the neighboring configuration around the node to simulate, the data event, is sought within the similar configurations in the training model, the patterns. Here the neighboring configurations contains the four nodes with a known value that are the closest to the node to simulate. When the distance  $D_{DP}$  between the data event and a pattern is lower than a given threshold  $d_t$ , the process stops and the node to simulate gets the value at the same location within the pattern.

kept. If no distance lower than the threshold is found at the end of the scan, the simulated node gets that value.

The migration process involves two data events: one data event contains the migration factor values and another data event contains the curvature values that influence the spatial structure of the simulated migration factor. The distance computation is applied on both the migration factor and the curvature, each one with its own threshold. A value is only retained when the two distances are lower than their respective thresholds.

#### 4.4.2 Parameter set

Besides from the training set, the DS method does not require much parameters. Most of these parameters balance the realization quality and the speed of the process. For more details about those parameters and their effect, see [Meerschman et al. \[2012\]](#).

#### 4.4.3 Size parameters

Two parameters have a direct impact on the simulation speed: the maximal number of nodes in a data event and the maximal proportion of the training model to scan.

The maximal number of nodes in the data event is simply the maximal number  $n_{max}$  of nodes with a value to consider in a data event. All these nodes are the closest to the node to simulate. A low number speeds up the simulation, but it may be at the cost of the realization quality. A high number does not necessarily means a good quality. Indeed, the size of the data event limits the number of potential patterns in the training set. It is then more difficult to find a pattern similar enough to the data event.

The maximal proportion to scan determines how much of the training model to scan before stopping the process. The training model is either the whole training set, or only one migration step of that training set. This parameter stops the process when no satisfying pattern is found. It speeds up the simulation, but it may be at the cost of the realization quality.

#### 4.4.4 Threshold parameters

The migration process based on the DS calls for two thresholds: one for the horizontal migration factor, one for the curvature. When a threshold is close to 0, the retained pattern has to be highly similar to the data event. A threshold closer to 1 authorizes more dissimilar patterns, at the cost of the realization quality.

Those parameters have two roles. First they have an impact on the simulation speed: the higher the threshold, the faster the simulation. The second role is similar to the role of the curvature weight with the SGS: it controls the impact of the curvature on the migration (figure 4.10). If the curvature threshold is far higher than the migration factor threshold, the curvature impacts less the process. If the two thresholds have similar values, the curvature influence is more noticeable. Contrary to the curvature weight of the SGS, a threshold is always positive. Thus, a threshold gives no control on migration or retro-migration trends. Only the training set controls such trends.

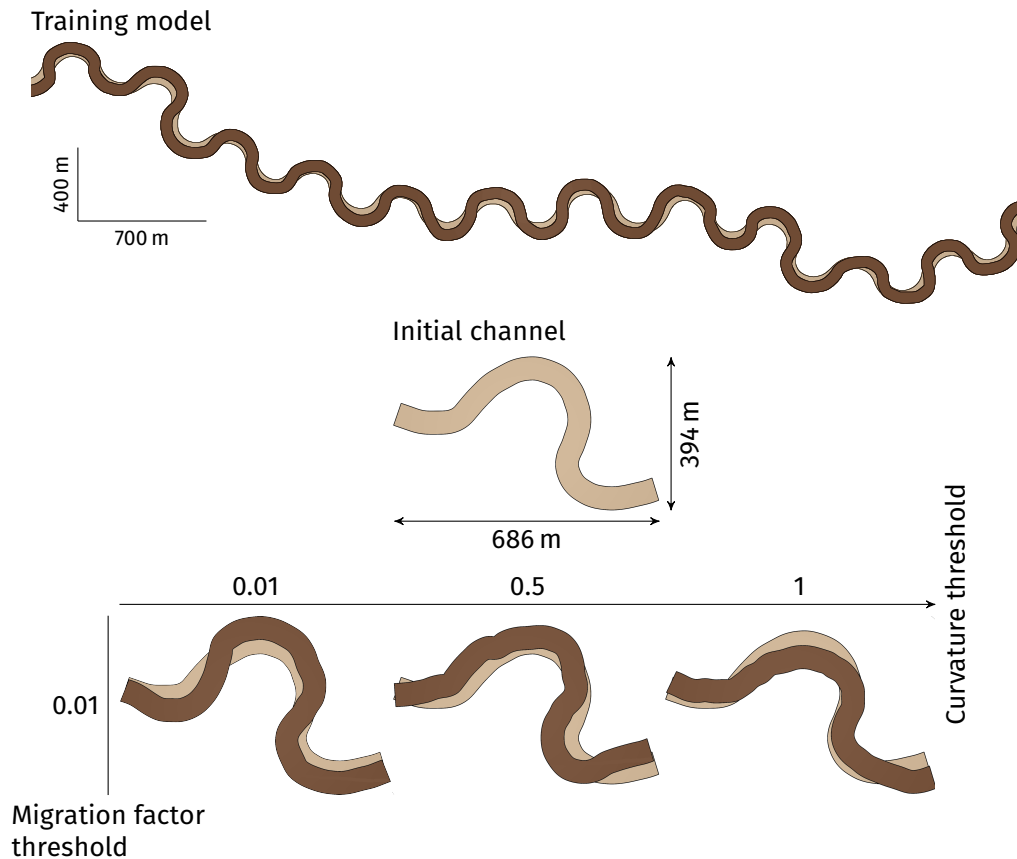


**Figure 4.10** Effect of the curvature threshold on bend migration with MPS. Here lateral migration dominates the training model. When the curvature threshold decreases, the initial channel has less influence on the migration. Other migration patterns than lateral migration may appear.

## 4.5 Numerical aspects

One key aspect of this method is shared with physical simulation methods: the horizontal migration factor has to be relatively smooth to avoid small-scale perturbations. Indeed, these perturbations tend to have a huge impact on the migration structures and can lead to inconsistencies.

### 4.5.1 Curvature computation

In our process, curvature values have no impact on the horizontal migration factor values themselves, only on their spatial structures. But having a curvature



which evolves smoothly remains as important as in physical simulation methods. These methods usually smooth the curvature, either following a weighted average or based on cubic spline interpolation [Crosato, 2007].

Schwenk et al. [2015] underline these inaccuracies in the curvature computation and propose to use a stabler curvature formula to avoid a smoothing phase. This formula is used here to compute the channel curvature  $\kappa$  at a centerline node  $i$ :

$$\kappa = \frac{2(a_y b_x - a_x b_y)}{\sqrt{(a_x^2 - a_y^2)(b_x^2 - b_y^2)(c_x^2 - c_y^2)}}$$

with  $a_x = x_i - x_{i-1}$ ,  $b_x = x_{i+1} - x_{i-1}$ ,  $c_x = x_{i+1} - x_i$  and equivalently for  $y$ .

### 4.5.2 Regridding

The regridding is a key step in channel migration. Indeed, as the bends migrate, the distance between two successive channel nodes can increase or decrease, as noticeable on figure 4.4. These variations lead to instabilities in the resulting migration. A regridding step is required to prevent too many variations of the inter-node distance.

This regridding step is the same as in physical methods [e.g., Schwenk et al., 2015]:

- If the distance between two successive nodes is higher than  $\frac{4}{3}l_d$ , with  $l_d$  the default channel length of the L-system, a new node is added. The parameters of this new node are deduced from the interpolation of its position. This interpolation uses a natural monotonic cubic spline interpolation of both coordinates  $x$  and  $y$  following the curvilinear coordinate.
- If the distance between two successive nodes is smaller than  $\frac{1}{3}l_d$ , with  $l_d$  the default channel length of the L-system, the second node is suppressed from the L-system string.

During the migration, two successive migration vectors may also cross each other, leading to an unwanted channel self-intersection. The migration vectors are so checked for intersection. If an intersection may happen, the two nodes are suppressed to eliminate the possible cycle.

### 4.5.3 Smoothing

If the curvature computation does not require any smoothing step, the migration factor realizations can display small-scale perturbations that have a huge, and sometimes unwanted, impact on the migration. This is especially the case

when using a non-Gaussian variogram model and/or a curvature weight equals to  $\pm 1$  in the SGS. The simulated horizontal migration factor is smoothed right before the migration step. The smoothing procedure uses the weighted average defined by [Crosato \[2007\]](#):

$$\varepsilon_i = \frac{\varepsilon_{i-1} + 2\varepsilon_i + \varepsilon_{i+1}}{4}$$

with  $\varepsilon_i$  the (retro-)migration factor of the module  $i$ . It can be applied several times depending on the wanted smoothness.

#### 4.5.4 Neck cutoff determination

As the channel sinuosity increases, the two extremities of a bend come closer one to the other until the flow bypasses the bend. This is a neck cutoff, leading to the abandonment of the bypassed bend.

As done in physical simulations [e.g., [Howard, 1992](#), [Camporeale et al., 2005](#), [Schwenk et al., 2015](#)], neck cut-offs are simply identified when two non-successive nodes of the centerline are closer than a given threshold. The lower possible threshold is the channel width, as the margins of the two bend extremities come in contact. However, this threshold is quite restrictive and not so realistic [[Camporeale et al., 2005](#)]. Here the threshold is set to 1.2 times the maximal channel width.

The search for cut-off starts upstream and continues to the most downstream part of the channel. The distance between a given node and another non-successive node of the centerline is compared with the threshold. When the distance is lower, those two nodes and all the nodes in-between are suppressed. The cutting path is then symbolized by two nodes. A new node is added along that path [[Schwenk et al., 2015](#)], using a cubic spline interpolation such as in the regriding.

This method of neck cutoff determination is simple but rather time-consuming. More efficient methods exist to reduce the computation time [e.g., [Camporeale et al., 2005](#), [Schwenk et al., 2015](#)]. For now only the forward migration process handles the formation of neck cutoffs. Indeed, the cutoffs appear naturally with the sinuosity increase. In the backward process, there is no such sinuosity increase, but a sinuosity decrease. Introducing neck cutoffs in such process calls for a different method.

## 4.6 Simple applications

This method was implemented to make L-system strings migrate. However, the whole method is still valid for any channel representation and could be

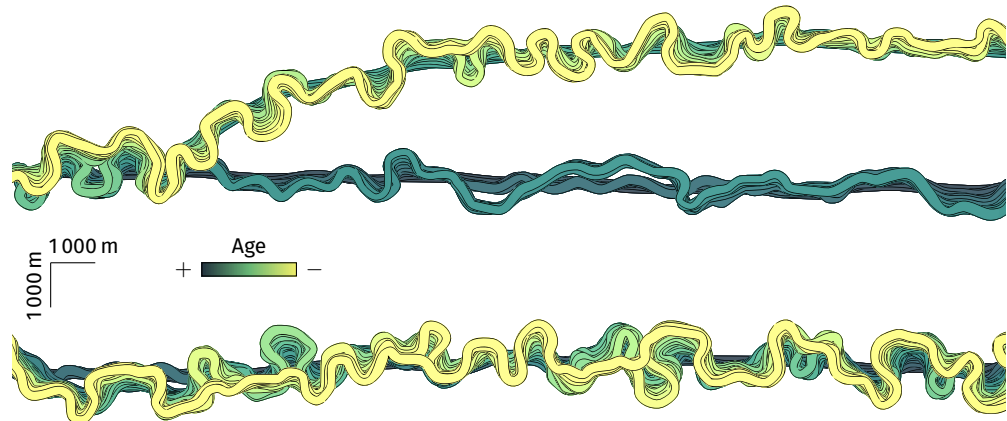


**Figure 4.11** Application of a forward migration process based on SGS to two channels generated with L-system. The input parameters are given in table C.2, appendix C.

modified to be done on curves or on NURBS. L-systems have the advantage that their manipulation requires a low computational cost. This is especially useful when working with numerous and long channels composed of small channel segments.

The method was used to generate two models: one following a forward migration process (figure 4.11) and one following a backward migration process (figure 4.13). Both processes are able to reproduce various migration patterns, from lateral to downsystem migration, with even areas of retro-migration (figure 4.12 and 4.14). Some bends also evolve to complex bends constituted by several bends: this lead to the formation of new meanders(figure 4.15). These synthetic cases have been developed without any data. The variogram parameters for the migration are those predefined. The range is chosen similar to the bend length. The curvature weight is kept high, giving a dominant lateral migration. At the end few parameters are required for the migration process itself. The forward model can continue over more migration steps without any trouble: neck cutoffs tend to keep the channel within a restrained area. The backward process does not migrate much after a few steps when the channel starts to miss significant bends. A regional avulsion and sometimes an abrupt migration can still revitalize the system.

Abrupt migrations are handled by introducing a second set of migration parameters. The channel centerline is scanned upstream to downstream. A probability of abrupt migration defines if an abrupt migration occurs. The appearance of an abrupt migration is also weighted by the channel curvature. When an

## 4.6 Simple applications

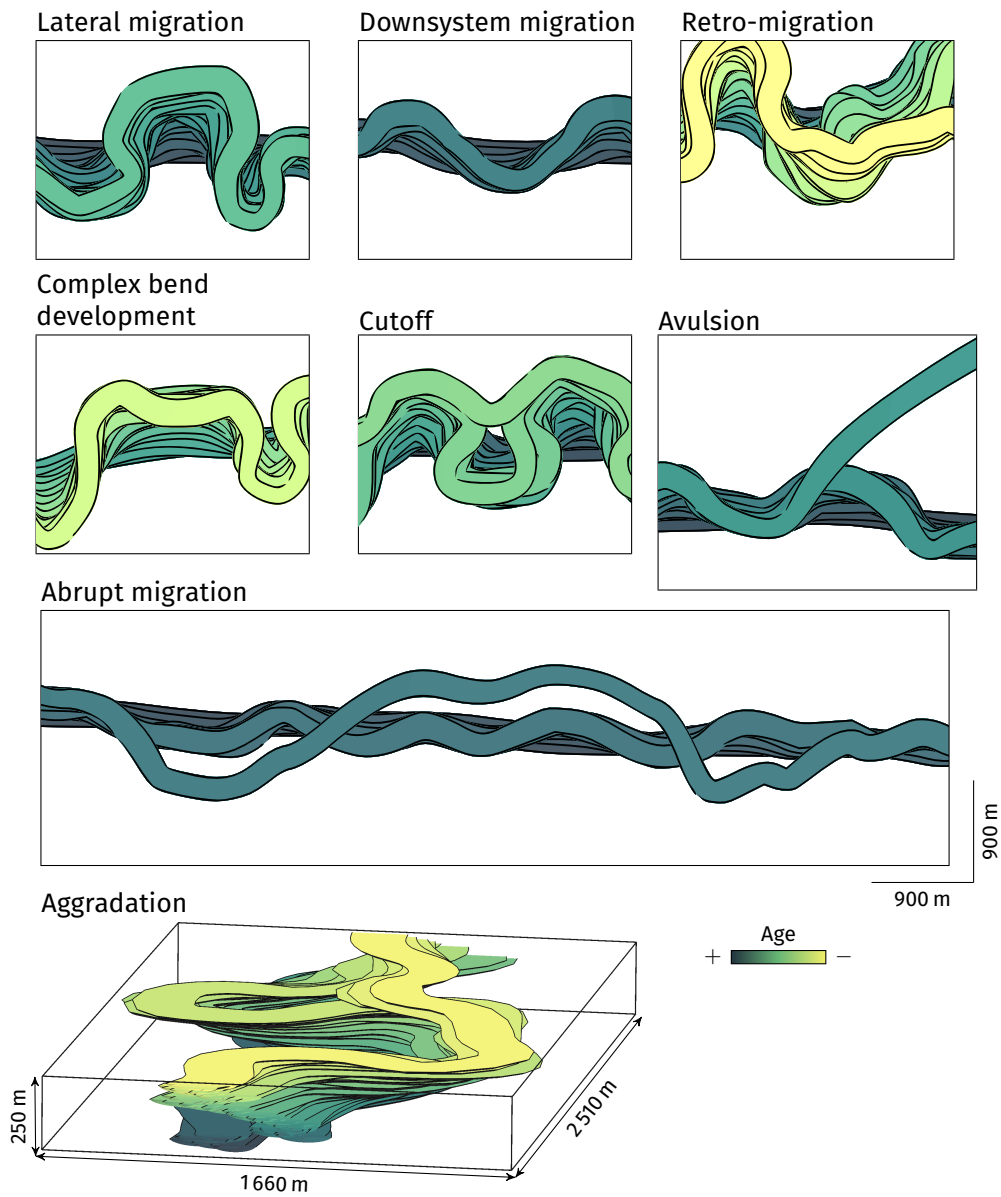


**Figure 4.12** Enlargements on some areas of the channels on figure 4.11 illustrating different aspect of channel evolution reproduced by the method.

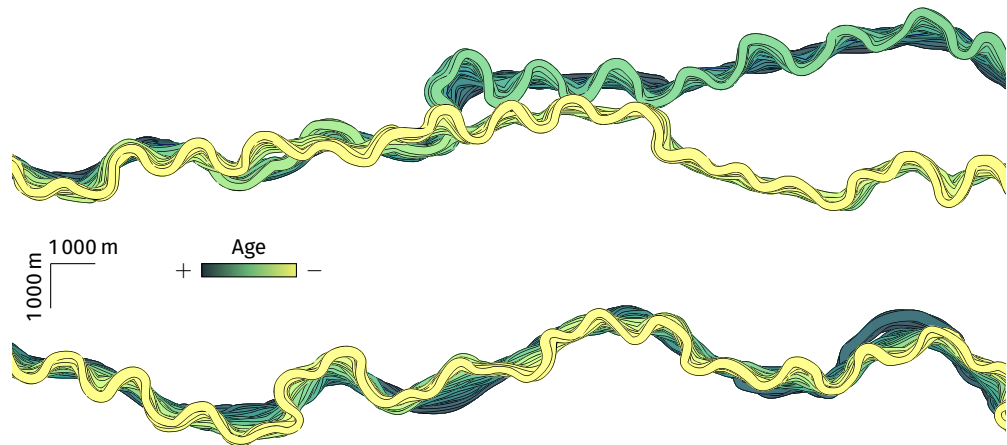


**Figure 4.13** Application of a backward migration process based on SGS to two channels generated with L-system. The input parameters are given in table C.2, appendix C.

abrupt migration occurs, an abrupt migration length is drawn from an input distribution. All the nodes along the drawn length migrate following the second set of migration parameters. Such abrupt migration process tends to introduce a spatial discontinuity with the previous channel (figure 4.12 and 4.14).

Regional avulsions momentarily stops the migration process, which starts again on the new channel. The continuity between the upstream part to the avulsion location and the newly simulated channel is finely preserved (figure 4.12 and 4.14). The use of the curvature to weight the abrupt migration and avulsion process tend to make them less appear in the backward process. This is due to the sinuosity decrease induced by such process. In this case higher probabilities are used.

Neck cutoffs appear naturally during the forward process as the sinuosity increases (figure 4.12). The backward process is unable to generate cutoffs. As the migration advances, the channel just gets straighter. It does not evolve to a complete straight line, but continuing the process does not lead to an increase of the sinuosity: the channel remains in a steady-state.

To test the method with MPS, a training set was simulated with a SGS-based process (figure 4.16). This training set only have 9 migrating steps. Lateral migration dominates the system, with several abrupt migrations all along it. Each migration step can only look for its values in the corresponding step in the training set, and not in the whole training set. The parameters for the MPS favor the quality over the speed, with the two thresholds at zero and maximal

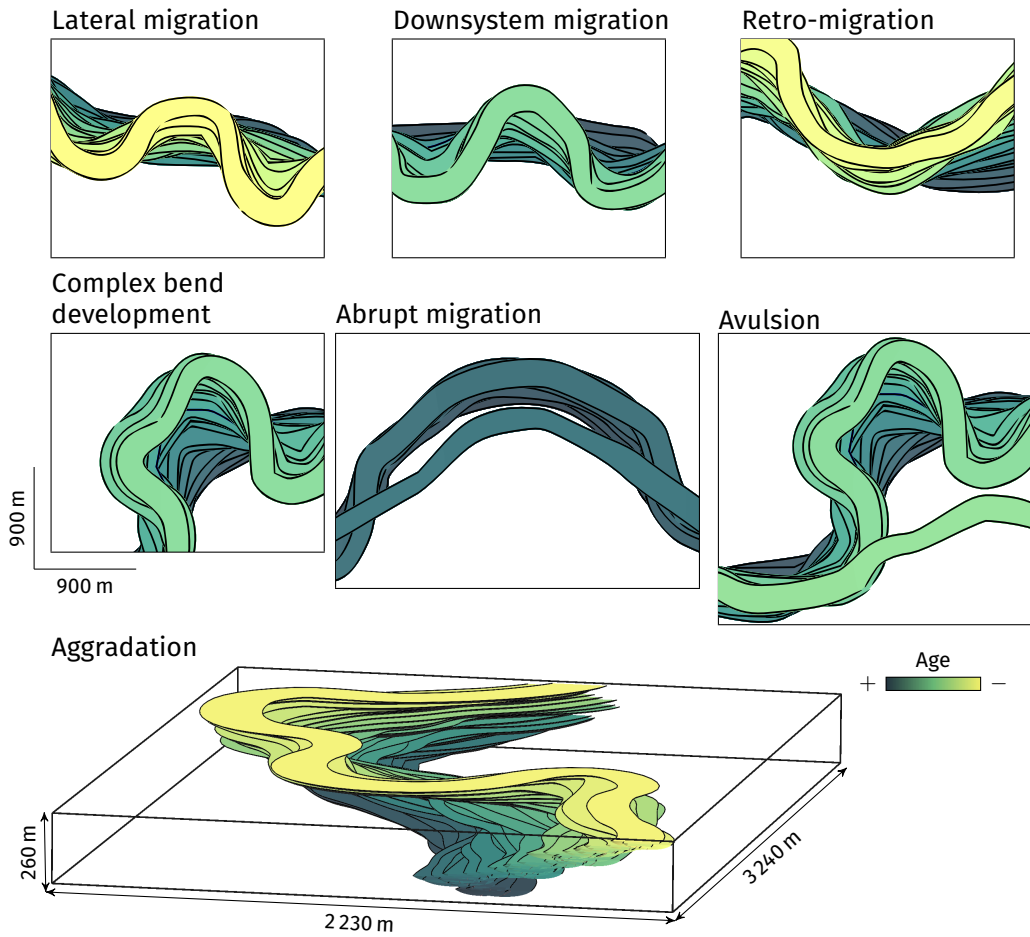


**Figure 4.14** Enlargements on some areas of the channels on figure 4.13 illustrating different aspect of channel evolution reproduced by the method.

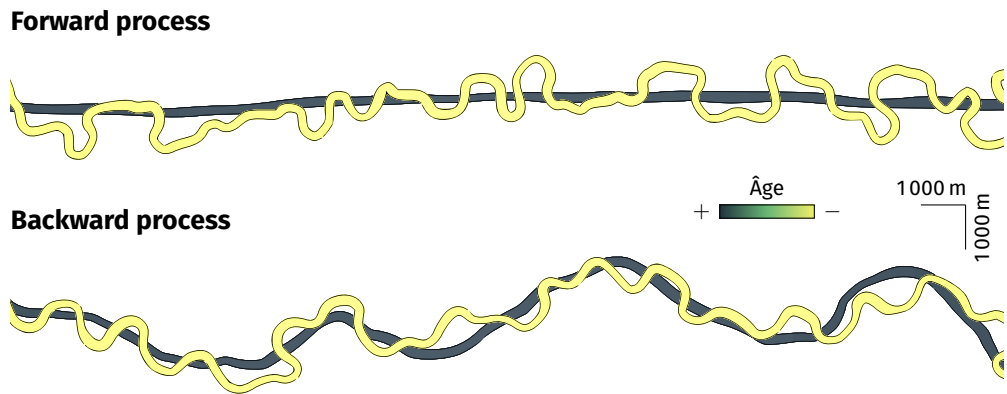


**Figure 4.15** First and last channel of a forward and backward migration with SGS. The channels for the forward process come from the bottom migrating system of figure 4.11 and the initial channel is the older. The channels for the backward process come from the bottom migrating system of figure 4.13 and the initial channel is the younger. The input parameters are given in table C.2, appendix C.

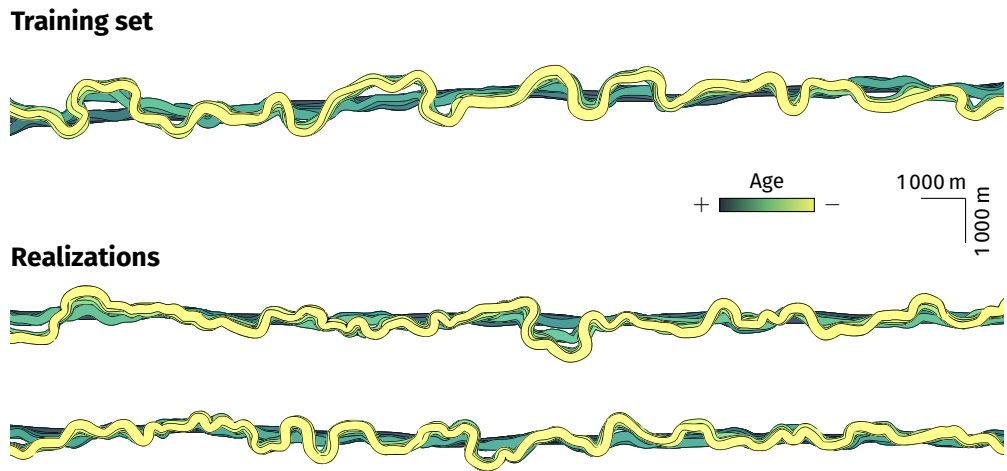


**Figure 4.16** Application of a forward migration process based on MPS to two channels generated with L-system. The input parameters are given in table C.3, appendix C.

scanned fraction of the training model of 0.75. As the simulated migration factors are quite perturbed, two smoothing iterations are added at the end of each simulation. This counterbalance the inability of the simulation process to find a pattern with a distance value consistent with the threshold.

At the end the lateral migrations is still dominant in the simulations. Abrupt migrations are also reproduced by the simulation process. However, they tend to be less frequent. They also tend to be smaller, both in length and in migration factor, than in the training set. This comes from both the inability to find the right pattern in the training set and from the smoothing.

### **4.7 Comparison of different channel stacking in terms of connectivity**

The purpose of this section is to highlight the impact of the migration process on the connectivity of the simulated channels. Three sets of realizations represent different channel stacking and are compared with a focus on the connectivity.

This comparison relies on the indicators introduced in chapter 2. The table 4.1 recalls the set of indicators. The indicators are based on the connected components of the realizations. To facilitate the realization comparison, they are used to compute dissimilarity values between all the realizations by means of a heterogeneous Euclidean/Jensen-Shannon metric.

#### **4.7.1 Case study**

This case study uses that of the third chapter (section 3.6), with turbiditic channels evolving within a master channel, gradually filling the master channel. The data set includes a hexahedral grid representing the master channel (figure 4.17). This grid comes from the NURBS volume of a channel simulated by a L-system process. A sand probability cube is defined within the whole master channel. This cube informs about the channel evolution within the master channel:

- Lateral migration dominates the first phase of the master channel filling. The channels migrate within the whole master channel width, with a low aggradation and some abrupt lateral migration. This results in the deposition of sand-rich deposits over the whole bottom of the master channel.
- Aggradation dominates the second phase of the master filling. The lateral migration is less significant compared with the first phase, without any



**Table 4.1** Set of indicators and associated weights used for the case study. The indicator descriptions are in section 2.2, chapter 2.

Set	Subset	Indicator	Symbol	Weight
Global analysis (measures on all the components)		Facies proportion	$p$	1
		Facies adjacency proportion	$p^a$	1
		Facies connection probability	$\Gamma$	1
		Corrected connected component density	$\epsilon$	1
		Unit connected component proportion	$p^u$	1
		Traversing connected component proportion	$p^c$	1
Detailed analysis (measures on each component)	Shape indicators	Corrected number of connected component cells	$n$	1
		Box ratio	$\beta$	1
		Faces/cells ratio	$\zeta$	1
		Sphericity	$\phi$	1
	Skeleton indicators	Node degree proportions	$p^n$	1
	Branch inverse tortuosity	$t$	1	

abrupt migration. This results in the deposition of sand-rich deposits in a limited area within the top of the master channel. The rest of the master channel is filled with inter-channel deposits, in particular inner levees whose development induces the limited lateral migration.

Three set of 100 realizations are simulated within the master channel grid, with each realization containing 40 channels:

- The first set comprises L-system realizations without data except the confinement from the master channel margins (figure 4.18). The channels are randomly placed inside the grid and are free to develop in the whole canyon, without any constraint on the position of each channel relative to the others. The channels from this set have a disorganized stacking. The input parameters for this set are those of the set 1 in table B.3, appendix B.
- The second set comprises L-system realizations conditioned to the master channel margins and the sand property cube (figure 4.19). The channel

#### 4.7 Comparison of different channel stacking in terms of connectivity

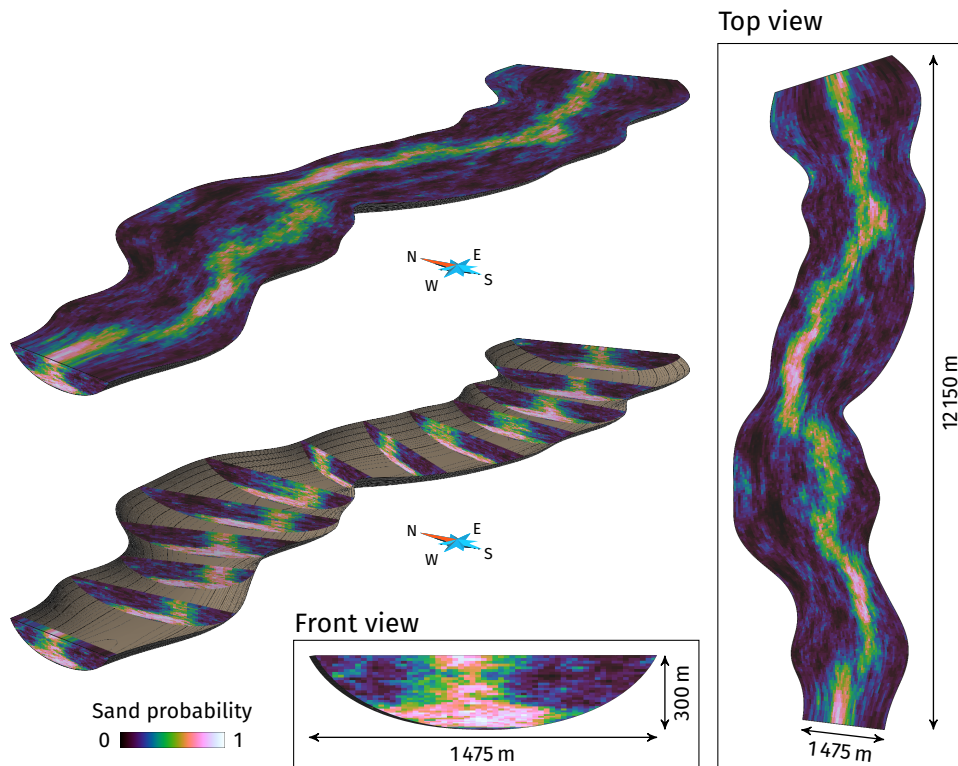


**Figure 4.17** Dataset of the application: a curvilinear grid representing a master channel with a sand probability cube.

random initial position and the channel development are both influenced by the sand probability cube. This influences the relative positions of the channels, but without a direct control on the channel relationships. The channels from this set have a conditioned disorganized stacking. The input parameters for this set are those of the set 2 in table B.3, appendix B.

- The last set comprises realizations from a forward SGS-based migration from an initial channel simulated with a L-system (figure 4.20). The initial position of the first channel is randomly drawn at a fixed vertical coordinate along the bottom of the canyon. The migration process includes two phases to reproduce the global channel evolution. A first set of parameters simulates 27 migration steps, with a high lateral migration, some abrupt migration and few aggradation. This first phase is initiated with a channel simulated with a L-system. The next 12 steps simulate a

#### 4 A geostatistical approach to the simulation of stacked channels

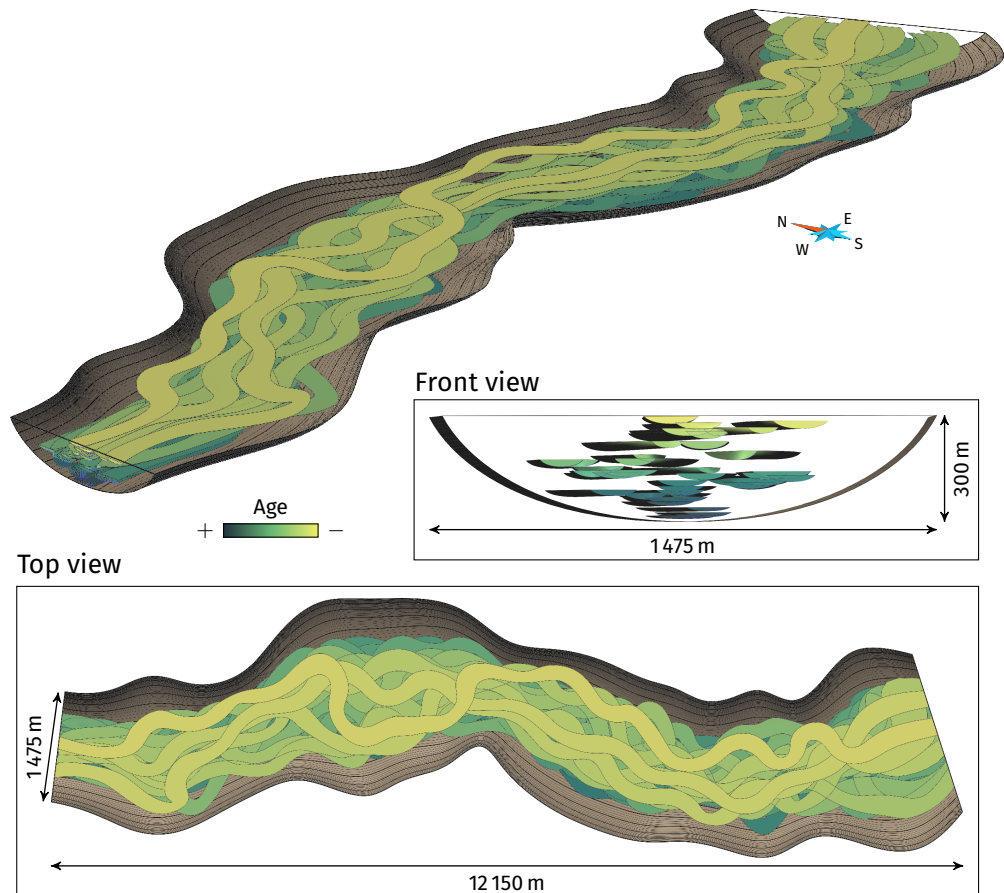


**Figure 4.18** Example of a realization from the disorganized stacking set. The realization contains 40 channels within a master channel.

small lateral migration with a significant aggradation. This second phase is initiated with the last channel of the first phase. If a migration will lead a channel node to go outside the master channel, the migration factor is decreased so that the channel remains within the master channel. The channels from this set have an organized stacking. The input parameters for this set are given in table C.4, appendix C.

#### 4.7.2 Indicator results

All the indicators get the same weight of 1. Only the channels are considered, and not the inter-channel deposits within the master channel. Three indicators

#### 4.7 Comparison of different channel stacking in terms of connectivity

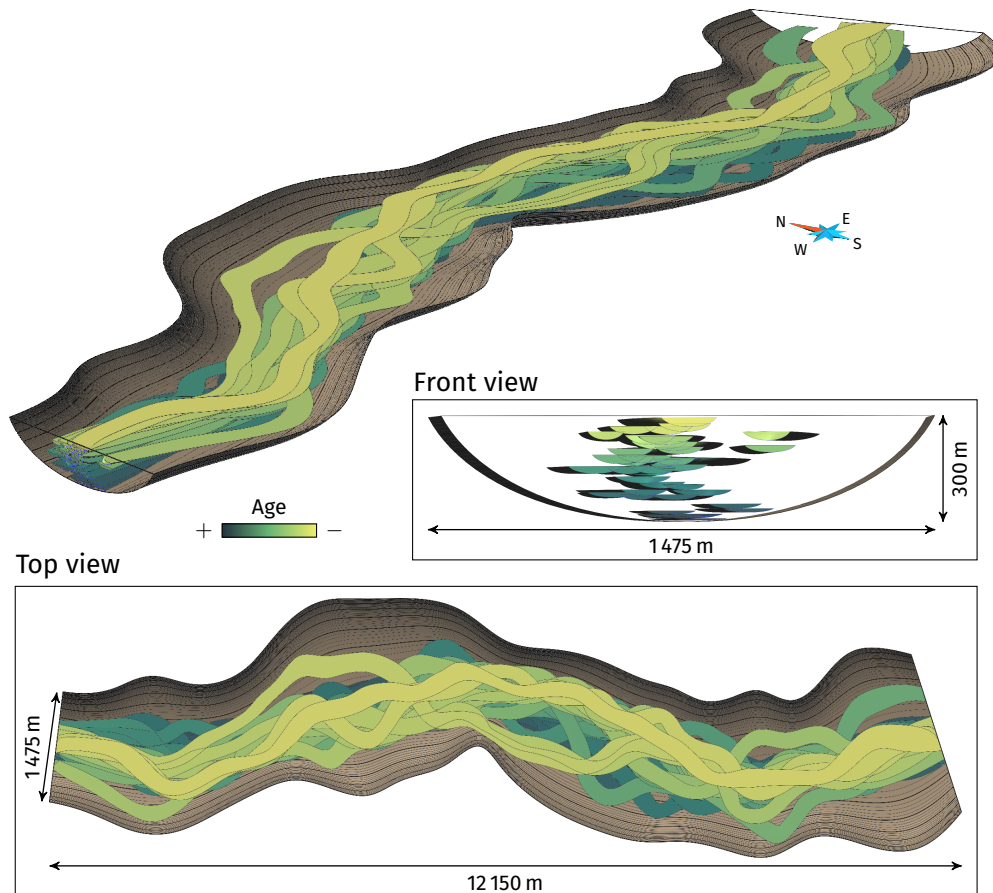


**Figure 4.19** Example of a realization from the conditioned disorganized stacking set. The realization contains 40 channels conditioned to a sand probability cube within a master channel.

appear to be non-discriminant in this case study:

- The facies adjacency proportions, because the realizations only contain two facies.
- The unit connected component proportion, because the rasterized objects do not lead to any connected component of one cell.
- The traversing connected component proportion, because all the channel objects go through the entire master channel and are all traversing.

#### 4 A geostatistical approach to the simulation of stacked channels

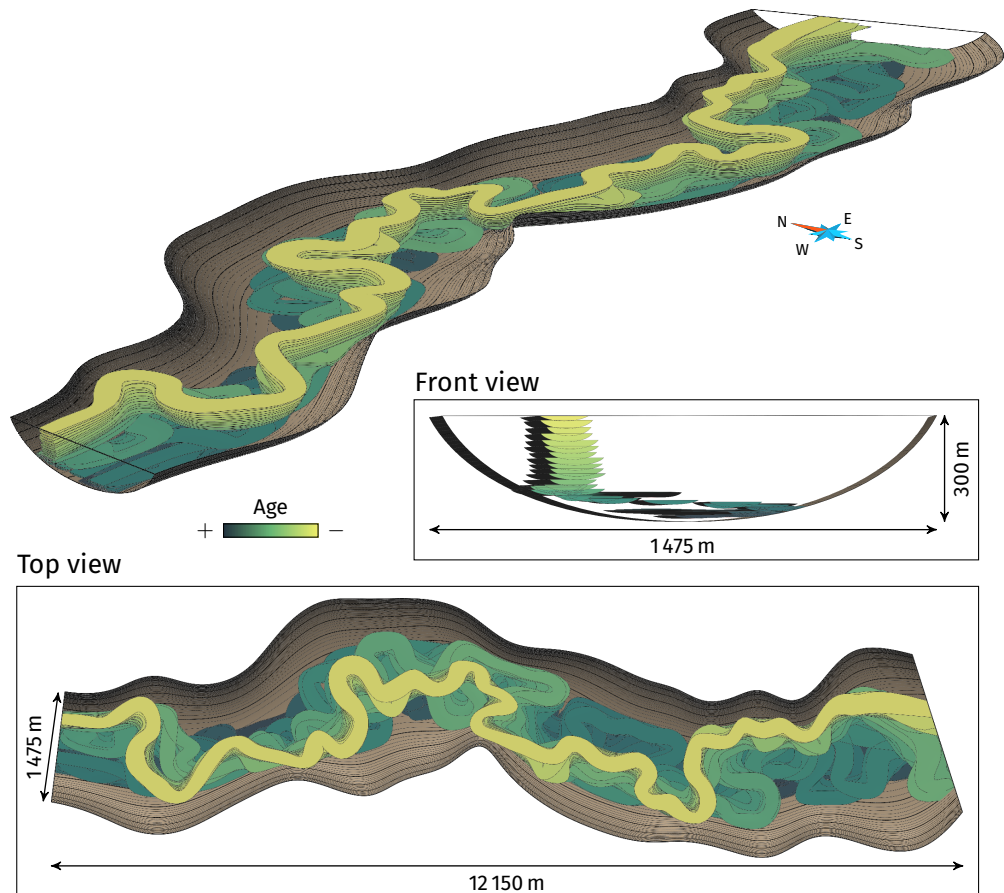


**Figure 4.20** Example of a realization from the organized stacking set. The realization contains 40 channels within a master channel.

The dissimilarities are represented by a multidimensional scaling (MDS) (figure 4.21). The purpose is to represent the realizations as points, the distances between the points being as close as possible to the dissimilarities between the realizations. Here the Shepard diagram and the scree plot help to see the MDS ability to reproduce the dissimilarities. A two-dimensional representation given by the MDS is sufficient. Three dimensions would have been a bit better, but more difficult to analyze.

The dissimilarities clearly divide the realizations in two groups. The first group contains all the 100 organized stacking realizations, 47 conditioned disorganized stacking realizations and 58 disorganized realizations. The realizations of the different sets do not mix much, with three sub-groups, one per

4.7 Comparison of different channel stacking in terms of connectivity

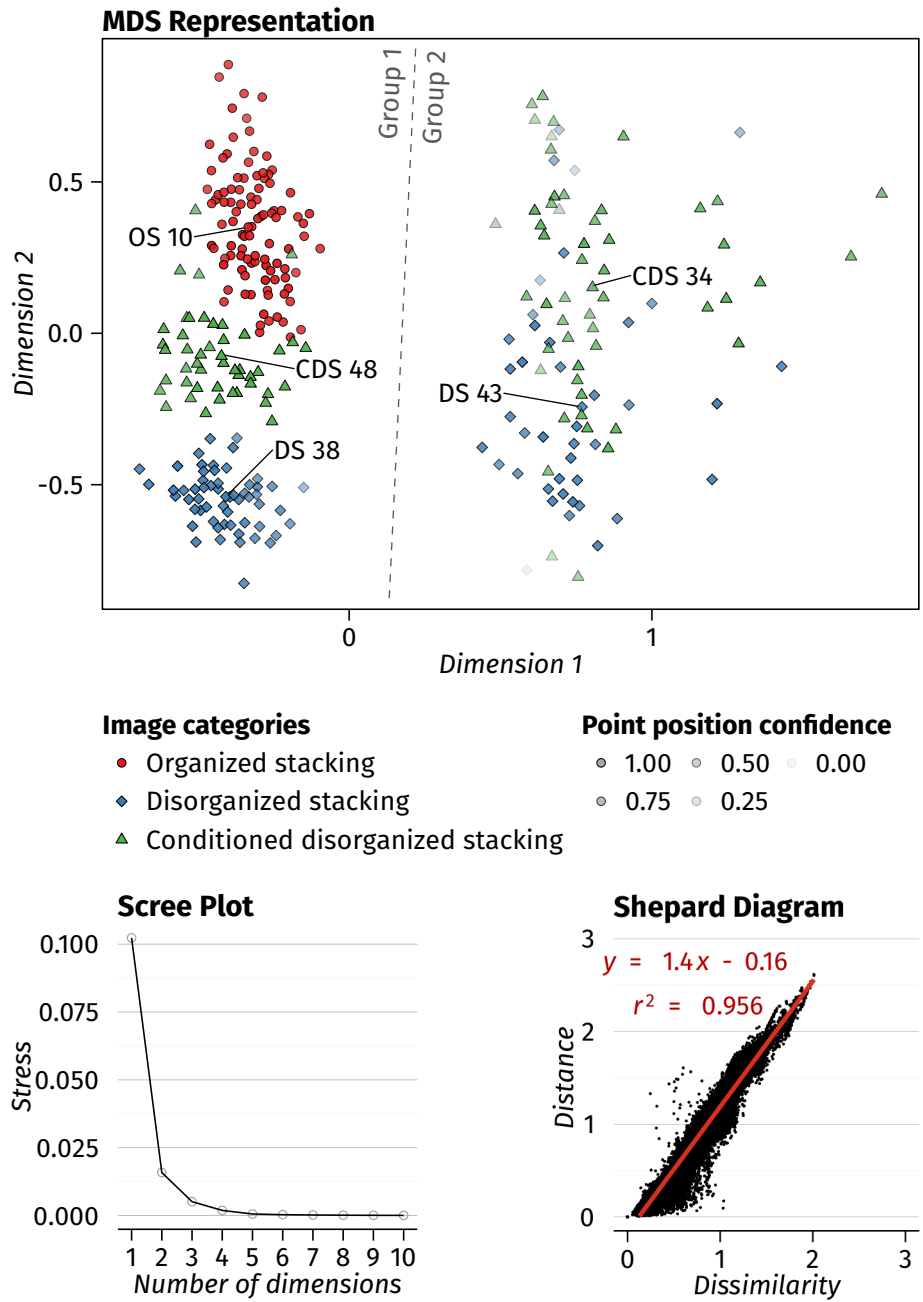


**Figure 4.21** Multidimensional scaling representation comparing three set of realizations with different methods and parameters. The identified realizations are shown in figure 4.22.

#### 4 A geostatistical approach to the simulation of stacked channels

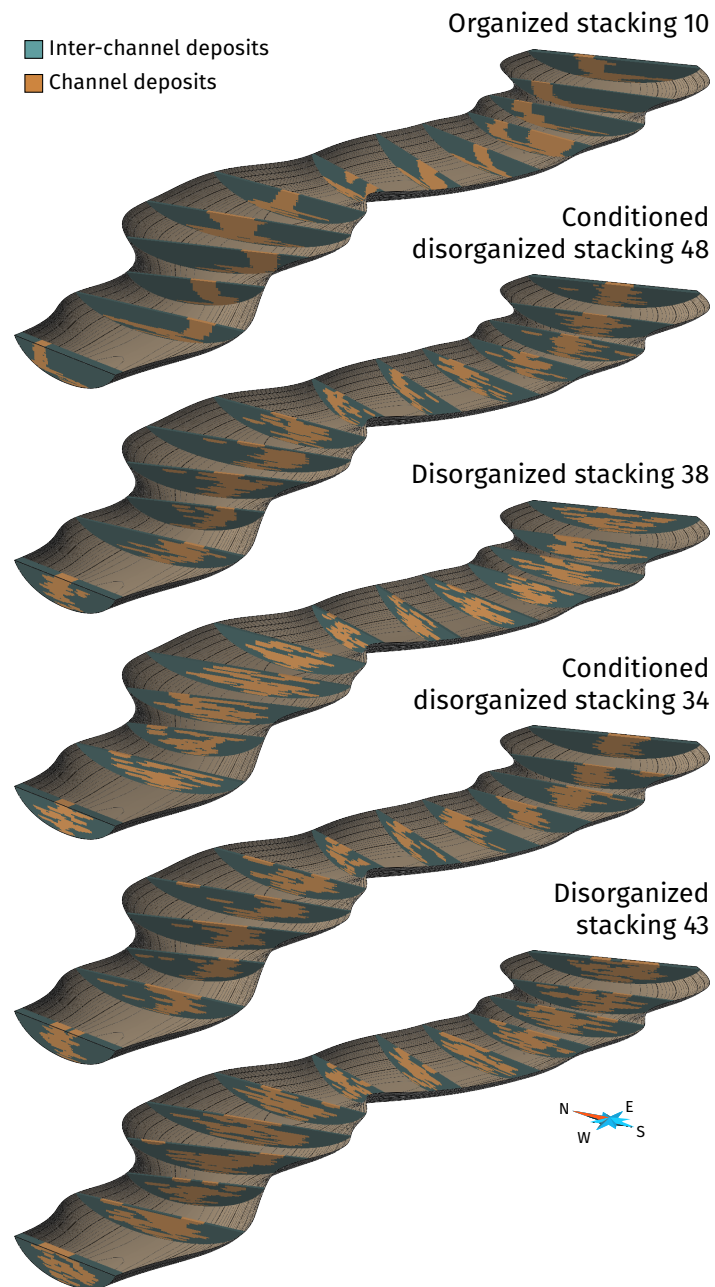


**Figure 4.22** Realizations of for each set within the two groups separated by the dissimilarities. Each realization is the closest to the mean MDS point of its set and group.

#### 4.7 Comparison of different channel stacking in terms of connectivity

realization set. The conditioned disorganized stacking realizations are closer to the organized stacking realizations than the disorganized stacking realizations. The second group contains 53 conditioned disorganized stacking realizations and 42 disorganized stacking realizations. Compared to the first group, the realizations are a bit more mixed, with a significant variability between the realizations.

Visually, the difference between the realizations of the different sets is quite clear (figure 4.22). However, examining realizations of the same set belonging to different groups does not show any significant difference.

Examining the indicators gives an explanation of the separation into two groups (figure 4.23). Realizations of the second group have lower facies connection probability, a higher component density and a lower average number of component cells than the realizations of the first group. Moreover, the realizations of the first group all have a facies connection probability of one. These realizations have channels that form a single connected component. The second group contains all the realizations with more than one connected component. This highlights the continuity of the migration process: having a non-connection between two successive channels requires an avulsion, otherwise the channels are always connected. Without migration, the control of the channel connectivity is less obvious.

Within the first group, the disorganized stacking realizations are clearly different from the other realizations. This is especially visible on the facies proportion and on the average number of component cells. Due to the disorganized stacking, the connected components of these realizations are larger than those of the other sets. On the other hand, the conditioned disorganized stacking and organized stacking realizations have similar facies proportions and average numbers of component cells. Their difference appears on the other indicators, such as the average faces/cells ratio or the average sphericity: even if the channels of the two sets occupy similar volumes within the grid, their shapes are different. The low faces/cells ratio of the organized stacking realizations highlights their organized stacking: the channels are significantly stacked over long distances, what decreases more the number of faces of the components than their number of cells. The average sphericity of these realizations is quite high compared to that of the conditioned disorganized realizations. This comes from their respect of the channel evolution: they occupy the whole width of the master channel bottom, and vertically they evolve to the top of the master channel. This also comes from the management of the channel margins: the migration is simply blocked by the channel margins, what is less constraining than the margin repulsion, especially at the bottom of the grid.



4 A geostatistical approach to the simulation of stacked channels

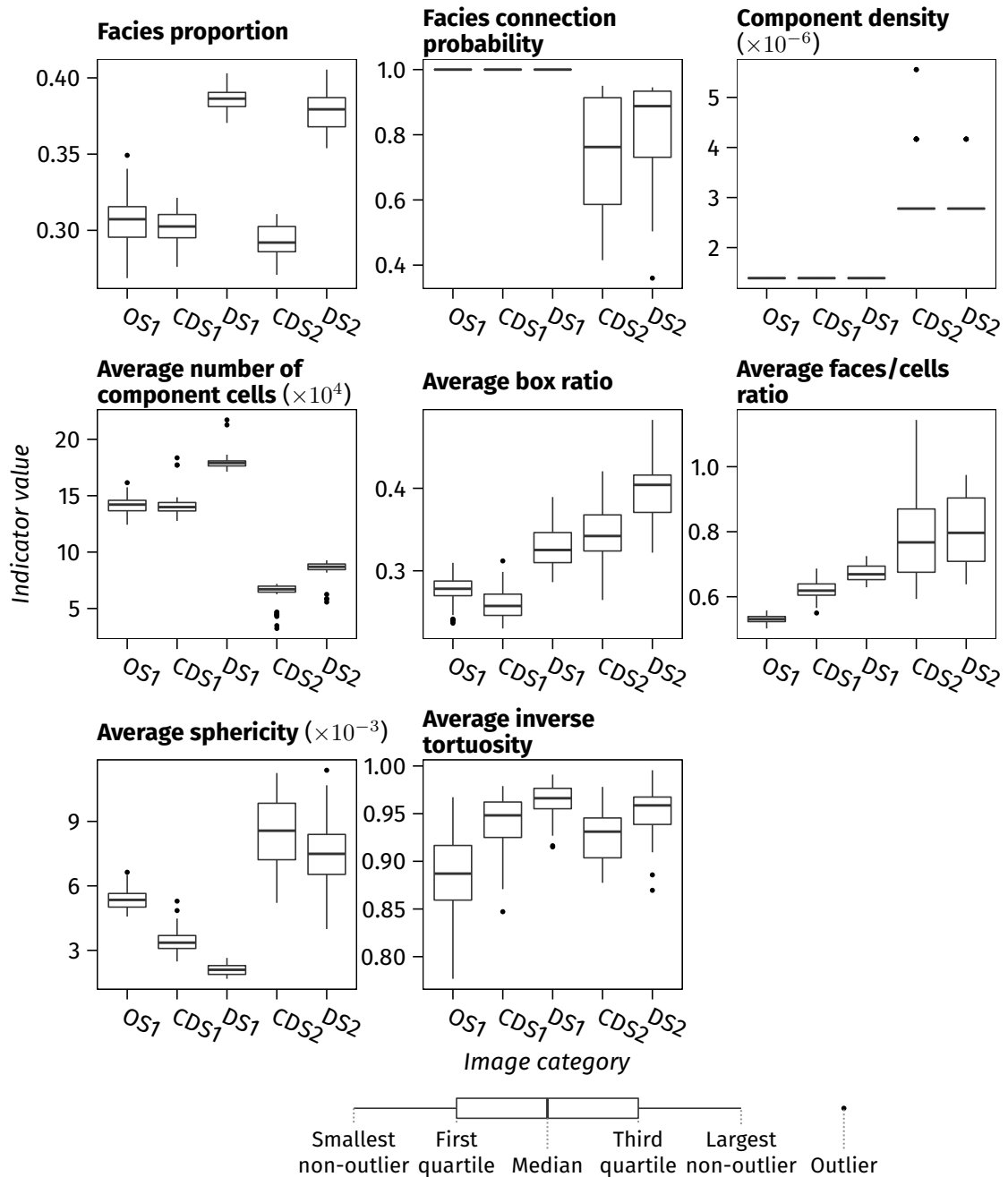


**Figure 4.23** Box-plots comparing the range of indicators – except the node degree proportions – computed on three sets of realizations with different methods and parameters.  $OS_1$ . Organized stacking realizations within the group 1;  $CDS_1$  and  $CDS_2$ . Conditioned disorganized stacking realizations within the groups 1 and 2;  $DS_1$  and  $DS_2$ . Disorganized stacking realizations within the groups 1 and 2;

The difference between the realization sets within the first group is also visible on the skeletons (figure 4.24). The disorganized stacking realizations have higher proportions for the node degrees larger than 3 compared to the realizations of the other sets. This highlights channels that locally cross each other but are globally disconnected. This tend to generate many small branches all along the skeleton, with many loops (figures 4.26 and 4.26). The difference between the conditioned disorganized stacking and the organized stacking realizations of the first group is less significant than on the other indicators. However, the conditioned disorganized stacking realizations have higher proportions for the node degrees larger than 3. Again, this highlights the tendency of their channels to cross each other without really stack within each other (figure 4.25). This is striking when visually comparing the skeletons (figure 4.26): the conditioned disorganized stacking realizations have many small branches forming loops, similarly to the disorganized stacking realizations. The organized stacking realizations have far less of those small branches. These small branches also tend to be straight, so to have a inverse tortuosity close to one. From this perspective, the evolution from the disorganized stacking to the conditioned disorganized stacking and the organized stacking is clear on the average inverse tortuosity: as the stacking increases, the inverse tortuosity decreases due to less straight branches.

It should be noticed that the skeletons do not capture the complete shape of the connected components in all its complexity. For instance in the organized stacking realizations, the distinction between the lateral migration at the master channel bottom and the aggradation at the top is not captured. This highlights the difficulty to determine the skeleton of an object.

Nevertheless, the differences between the three sets are clear on the indicators. The difference in stacking impacts directly the shape of the connected components and their connectivity. Adding a sand probability cube clearly helps to control the connectivity between the channels. However, the resulting channel organization is far from the clear stacking offered by the migration. Furthermore, the migration process gives a better control on the stacking and prevent non-connections if required.

## 4.8 Discussion and perspectives

The previous applications highlight the relevance of this approach. The next sections discuss some aspects of the method, leading to some perspectives.

4 A geostatistical approach to the simulation of stacked channels

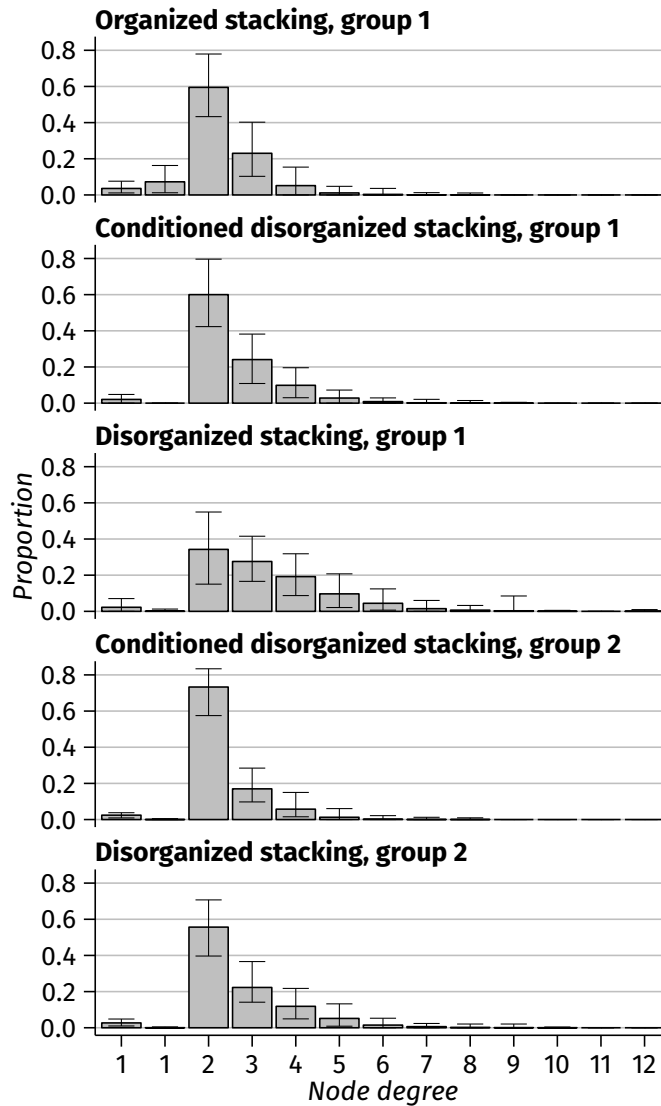


**Figure 4.24** Mean node degree proportions of the levee skeletons for each set and group. The error bars display the minimum and maximum proportions. The first 1 node degree corresponds to the nodes of degree one along a grid border. The second 1 node degree corresponds to the nodes of degree one inside the grid.

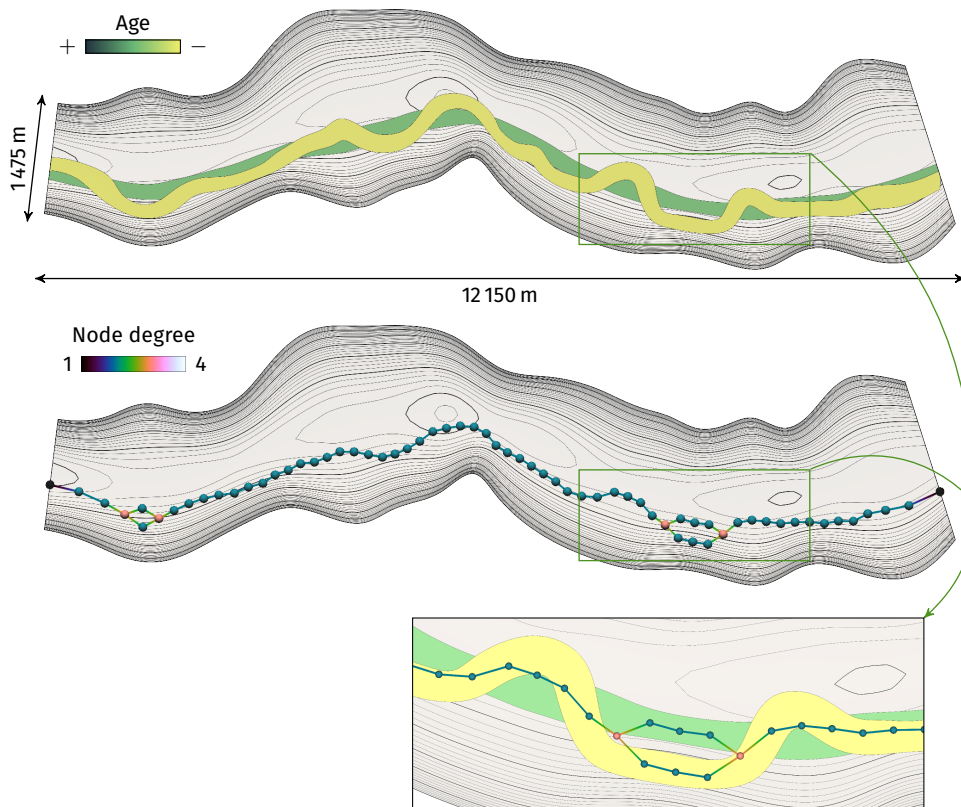


**Figure 4.25** Two migrating channels with two local abrupt migrations and associated skeletons. An organized stacking of the two channels results in a single branch on the skeleton. The areas of abrupt migration, where the channels are not stacked anymore, results in a loop on the skeleton.

#### 4.8.1 About the migration pattern simulation

As defined, the process based on SGS leads to a dominant lateral migration through the influence of the curvature. Using a low curvature weight leads to the simulation of other patterns. However, it is not possible to choose another dominant migration pattern, such as a downsystem migration. This is not an issue for turbiditic channels, which tend to have little downsystem migration [e.g., Nakajima et al., 2009]. However, if another dominant pattern is required, the method has to be adapted. A simple solution is to modify the vector of migration by adding a downsystem component, such as done by Teles et al. [1998] or Viseur [2001]. Another solution is to change the secondary data influencing the migration. The curvature could be modified, or a different property would

4 A geostatistical approach to the simulation of stacked channels

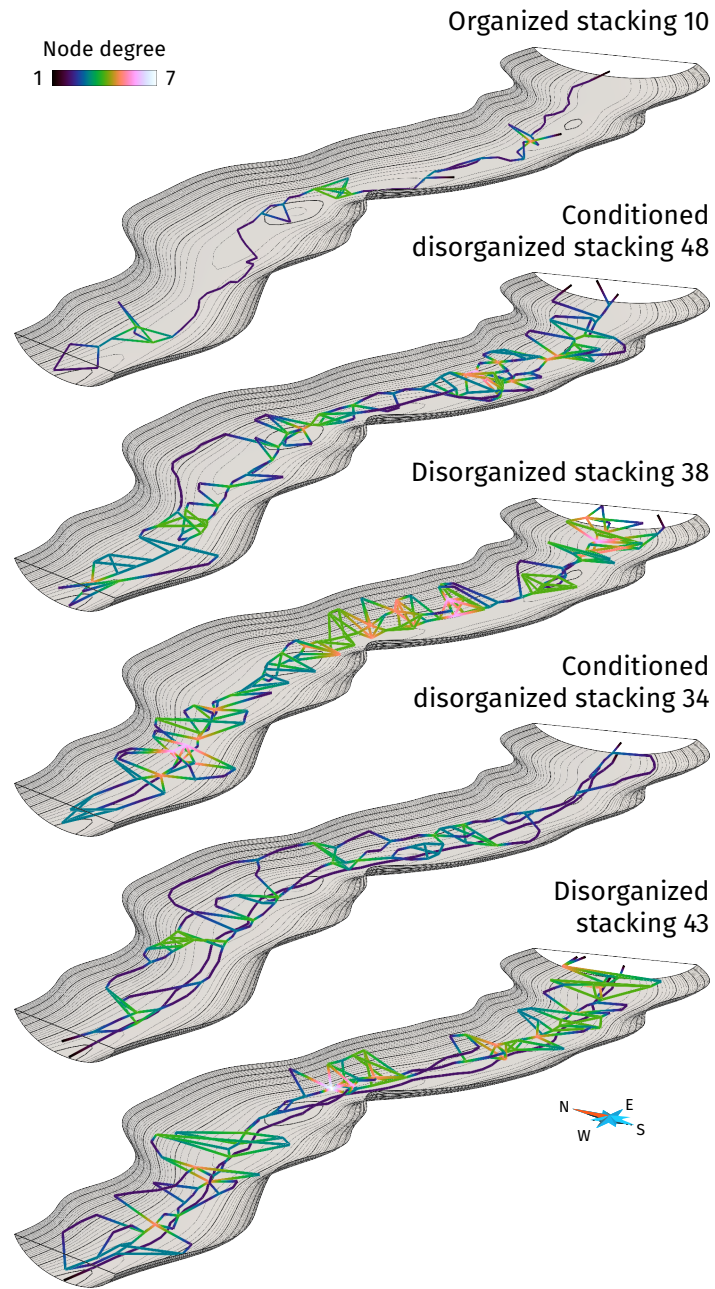


**Figure 4.26** Skeletons of the channel connected components of the realizations showed in figure 4.22.

have to be used. From this point of view, MPS have the advantage that the training set controls the migration pattern.

Globally, the SGS remains able to reproduce various migration patterns. Most of the time, no smoothing is really required. The MPS would require more work to improve the reproduction of the migration pattern from the training set. MPS seem to difficultly develop large bends. Several bends at a smaller scale than those in the training set tend to appear. For now smoothing steps are required to obtain satisfying results. From this point of view, the training set used in the example is not optimal as the channels have roughly the same length as in the realizations. Longer channels within the training set increase the repeatability of the patterns and improve the realization quality.

The bends should also be compared with their counterparts from real cases to assess the method ability to develop a realistic migration. When using a real case as training set, MPS should be one step ahead. But this need to be further tested. To compare the channels through the migration, statistics such as those of [Howard and Hemberger \[1991\]](#) can be used. But they are not directly defined to analyze the migration. Histogram and variogram of the migration factor can give a first insight, but further indicators should be developed to objectively analyze and compare migration patterns.

A comparison could then be done with physical simulation methods, especially the stochastic ones [[Lopez, 2003](#), [Pyrz et al., 2009](#)]. The main interrogation comes from the physical model ability to explore all the possible migrations. This questions the variety of stacking pattern that can be simulated. For instance here some retro-migrating areas can appear. These areas form outer-bank bars, which are potential reservoir areas [[Nakajima et al., 2009](#)]. Such bars have no equivalent in fluvial processes, whereas all the physical methods for the migration are developed for the fluvial environment. Thus, they may not be able to develop such migration patterns. Comparing the results of the forward and the backward migration processes would be also an interesting development.

#### **4.8.2 About the discrete process simulation**

For the SGS process, abrupt migration are introduced by a second set of migration parameters. Channels tend then to develop discontinuities from the previous channels. However, they tend to follow a similar migration pattern. Abrupt migrations and even local avulsions could also be simulated using L-systems. The initiation process would be the same as for the global avulsion. The newly simulated part would be attracted to a downstream location of the initial channel. This process is similar to the one developed by [Anquez et al.](#)

[2015] to simulate anastomotic karst networks. It would possibly simulate bends completely independent from the previous channel.

MPS have shown their ability to reproduce abrupt migrations from the training set. Here again it facilitates the work for the user once a training set is available. The only drawback is when regional avulsions or cutoffs are present in the training set. For now they are not handled, but they could be used to better simulate such processes.

The appearance of neck cutoff is not a problem in a forward process with SGS. With SGS in a backward process, neck cutoff should be simulated during the process. This would help the migration to continue whatever the number of migration steps.

### 4.8.3 About the parameterization

Using SGS does not call for an intensive parameterization, with only four parameters required for a simulation. The aggradation and migration factors are directly related to the vertical and horizontal distances between two successive channels. They are thus pretty easy to define. The curvature weight is a bit harder to define. A weight of 1 gives a significant influence to the curvature. By default, a weight around 0.8 gives a dominant lateral migration but lets some other migration patterns appear. Starting with a range around the wanted bend length at the end of the process gives satisfying results.

No use of data has been done yet to find the parameter values. This could be done for instance thanks to an interpretation of channels on seismic data. If all the channels are often not discernible on seismic data, some of them could give indications on the possible parameter values, for the factor distributions, the variogram parameters and even the curvature weight by comparing the channel curvature with the migration distance.

One possibility to reduce a bit more the number of parameters is to use the bend length as range. The range then varies following the channel bends and the migration step. However, the channels often tend to develop small-scale variations that perturb the bend identification and thus the bend length computation. No significant migration can be obtained with such parameterization. One possibility is to smooth the simulated migration factors or the bend lengths. A better solution would be to better identify the bends and avoid the small-scale variations. The work of [O'Neill and Abrahams \[1986\]](#) for instance could be a first lead.

Compared to physical methods [e.g., [Ikeda et al., 1981](#), [Parker et al., 2011](#), [Lopez, 2003](#)], the parameterization is far simpler when the purpose is to model the current aspect of the geology. This requires working on old channels that

have been deformed. Thus the physical parameters that lead to the channel formation are difficult if not impossible to infer. [Pyrzcz et al. \[2009\]](#) manage to reduce the number of parameters to a single maximum distance to reach by a standardization process. The impact of such standardization on the migration process and thus on the stacking patterns is not discussed. This parameterization is easier to infer, but less flexible if the migration patterns are not satisfying. The parameters used here give a finer control to the user on the migration patterns. Furthermore, they are mainly descriptive and can be inferred from the available data.

The more processes are introduced, e.g., abrupt migration, the heavier tend to be the parameterization. The MPS approach is then pretty useful. The few parameters are more related to the ratio between the simulation quality and the simulation speed. However, the training set dictates the geological considerations, such as the presence of abrupt migrations or the dominant migration patterns. The main issue is to find a training set. The most interesting option is to find one from an analog, either seismic data such as done by [Labourdette \[2008\]](#) or possibly an outcrop. In a fluvial system, satellite images are interesting sources of training sets.

#### 4.8.4 About small-scale variations and smoothing

With both SGS and MPS, the migration factor is not always completely smooth. This induces some small-scale variations that can form inflexions. Such inflexions prevent from using directly the bend length as range for the SGS, as discussed in section 4.8.3. They also tend to further develop during the migration, forming new bends at a smaller-scale than initially desired.

The emergence of such features still needs to be explored. They may come from the prior model, i.e., the variogram or the training set, as it is not necessarily smooth. The question is then if this local sharpness should affect the migration. It may also come from a failure of the simulation process, especially with MPS with too high thresholds.

The smoothing of the migration factor gives a control on the small-scale variations by eliminating their influence on the migration. However, the smoothing impact is quite significant, as discussed by [Crosato \[2007\]](#) on the curvature. Four to five smoothing steps can be enough to completely modify the migration structure. It should then be used carefully.



#### 4.8.5 About the usefulness of the migration process

The comparison with object-based simulations without migration process highlights the differences in term of connectivity. This migration process gives a more important control on the stacking pattern. This is especially useful knowing the significant influence of the stacking pattern on the connectivity. By adding secondary data to an object-based process, it is possible to get closer to the migration results. However, the difference in terms of connectivity remains significant.

The analysis of the connectivity could be further developed by introducing the channel filling. In particular shale drapes have a significant impact on the connectivity. And in such case controlling the stacking pattern is even more important.

#### 4.8.6 About the simulation process with migration

L-system are interesting to develop the initial channel, especially for their ability to develop channels with various sinuosity. In the MPS case, method such as the one of [Mariethoz et al. \[2014\]](#) could also be interesting. They simulate channel centerline based on MPS in a similar process that the one used for migration. The initial channel could then be simulated based on the first channel of the training set.

Both SGS and MPS are able to simulate a forward or a backward migration. This backward process is really useful, as the last channel of a migrating sequence is far more often interpretable on seismic data than the first one [[Labourdette, 2008](#)]. This allows initiating the process from the real data, instead starting from an unknown state and trying to condition the process to the last channel.

Some elements would be interesting to go further in the process. For now the channel width and thickness are simulated at the end of each migration step. As the width in particular has an impact on the migration, it could be interesting to simulate them earlier. With MPS, the channel width and thickness could also be simulated from the training set instead of using SGS such as done in the case studies. Other geological elements could be integrated, such as the channel filling. This is especially important due to their impact on the connectivity. Levees also need to be introduced. And when the channels migrate within a confinement such as a canyon, they can erode that confinement. Thus, they modify the confinement morphology, which could be taken into account.

### 4.8.7 About data conditioning

Data conditioning of the migration process has not been explored yet. Thanks to both SGS and MPS, data conditioning is pretty easy if the data are at a distance compatible with the migration factor distributions. Data can then be directly integrated into the spatial structure of the migrated channel. To preserve the conditioning, smoothing can not be performed at the data locations.

However, the process is more difficult when the data are away from the channel: the migration can not condition the data if the channel does not come close enough. One solution is to introduce a constraint that attracts the migrating channel to the data, similarly to the initial channel conditioning or to the conditioning of Flumy [Lopez, 2003]. This implies to adjust the appearance of discrete migrations and avulsions depending on the data and their location.

It is also important to notice that the overall methodology requires an important work of data interpretation and sorting to possibly pre-attribute them to each migrating system. Conditioning to a sand probability cube is also problematic, especially to handle avulsions. This may require identifying the large-scale trends within the cube.

### 4.8.8 Numerical aspects

The realization were simulated on a 64-bit Linux system with a 2.10 GHz processor Intel® Core™ i7-3612QM and 6 GB of RAM.

The migration process in itself is really fast. In the master channel, it took  $2.79 \pm 0.20$  s to simulate the initial channel and to perform the 39 steps of migrations. Here the first and last nodes of the channels are free to migrate. Thus, the initial channel length has to be chosen large enough so that the migrating channels continue to spread across the whole master channel length. Setting the migration factor to zero for the first and last nodes of the migrating channels could prevent those channel to have their extremity migrating inside the master channel. This would reduce the computation time by enabling the use of a smaller initial channel length.

The generation of the NURBS is the most time consuming part of the process, with  $20.03 \pm 1.17$  s to materialize the 40 channels of a realization. On the migration process itself, the most time consuming parts are the regridding and the neck cutoff generation. However, more efficient solutions than the one used here exists for the neck cutoff generation [e.g., Camporeale et al., 2005, Schwenk et al., 2015].

Globally the process gives nicer results with smoother migrations as the resolution increase. Increasing the resolution means using a small element resolu-

tion and a small migration factor. This potentially induces more channels with more elements. [Parquer et al. \[2015\]](#) develop a re-parameterization function to use the minimal number of control points on a NURBS surface while preserving at best its shape. This can be useful to limit the weight of the NURBS surfaces.

## 4.9 Conclusions

This work provides a basis for a more descriptive approach of channel migration to control channel stacking. A single approach stochastically simulates either forward or backward channel migration, starting with an initial channel simulated by L-system or directly interpreted on seismic data. The migration process is based on simulating a migration factor by SGS or MPS with the curvature as secondary data. Four parameters are required by the SGS approach to adjust the migration patterns. The MPS approach calls for four parameters related to the simulation speed and quality and a training set that controls the migration patterns. Global avulsion is done by L-system simulation, as the initial channel.

The first results are encouraging, with a significant difference in connectivity from a process with no direct control on the channel stacking. Some deeper work is required on particular points, as using the bend length as variogram range by default. Conditioning to already interpreted accretion packages is possible thanks to both SGS and MPS conditioning ability, but only if these packages are not too far from the channel. Further managing accretion packages could be done with potential fields for instance, as done for initial channel conditioning or with physical methods [e.g., [Lopez, 2003](#)]. Neck cut-offs remain to be introduced in the backward process with SGS. The training set required by MPS could be better used to take into account cutoffs and possibly avulsion, both regional or local. The channel fill should also be simulated to better assess the impact on the connectivity. If the method is introduced from the point of view of the turbiditic environment, its use of prior statistical models to migrate in a descriptive process makes the method valid for fluvial applications.

# Conclusions

## 1 Contributions

The connectivity between sand-rich deposits is a main factor controlling flow behavior within a reservoir or an aquifer related to a channelized system. From this point of view, channels are fundamental sedimentary structures, both for their role in sediment transport and their own deposits, whose permeability enables fluid circulation. Turbiditic systems are a perfect example of how the complex architectures related to channels influence the connectivity at various scales. Based on those considerations, two strategies have been developed to better take into account the connectivity in stochastic simulations:

- A strategy to analyze the connectivity of a realization through indicators. This enables the objective comparison of realizations in terms of connectivity.
- A strategy to better model the connectivity through a better reproduction of channels while conditioning to the available data and through a better reproduction of the channel relationships.

The following sections summarize the main contributions of this thesis around those strategies.

### **1.1 Indicators and an analysis process to compare stochastic simulations of sedimentary bodies by focusing on the connectivity**

Being able to compare realizations in terms of connectivity is of significant interest as the final purpose of these realizations is to better understand the flow behavior within the studied domain. Furthermore, geostatistical simulation methods mostly rely on the reproduction of statistics and do not directly take into account the connectivity.

The method developed in this thesis to analyze the connectivity applies on categorical images representing sedimentary bodies. It relies on a set of indicators that further develop the use of connected components compared to previous work [e.g., [Deutsch, 1998](#), [De Iaco and Maggio, 2011](#)]. The indicators measure for instance the component size, shape, density or the node degrees of the component skeleton. They are used to compute dissimilarities between different realizations and/or conceptual models. Such dissimilarities facilitate the analysis process by integrating all the indicators in a single value.

However, the resulting dissimilarity matrix is unreadable when dealing with hundreds of realizations, as it is usually done in stochastic modeling. Multi-dimensional scaling is a really powerful visualization technique which significantly facilitates the analysis process. It raises an increasing interest in the literature to compare realizations [e.g., [Tahmasebi et al., 2014](#), [Yang et al., 2016](#)], without always enough care at the validity of the representation in a low dimensional space. Indeed, it is only a partial view of the dissimilarities which can be misleading in some circumstances. From our tests, no case has been encountered where the MDS is completely wrong in its representation of the dissimilarities, at least for a global analysis. The heat map is harder to analyze, but it represents the real dissimilarity values. It is then an interesting tool to verify the observations done on the MDS representation. In any case, going back to the indicators should be always done, at least as a precaution.

The application of the proposed method to a synthetic case results in a different ranking than the one obtained by a visual analysis. Nevertheless, a detailed analysis shows the consistency of the indicator behavior. These indicators are simple to analyze, and not computationally demanding. Using the skeletons is appealing because they capture more directly the connectivity through the topology of the connected components.

### **1.2 A method to stochastically simulate channelized bodies using a constrained L-system**

The approach developed to stochastically simulate channels relies on a formal grammar, the Lindenmayer system. Predefined rules control the development of the channel morphology to simulate straight to sinuous channels. During that development, constraints attract or repulse the channel to condition the available data.

This approach is really fast, both for the simulation of channel and for their conditioning. Applying the constraints gradually during the channel development appear to be flexible enough to handle numerous data simultaneously. It also gives the possibility to always condition a data. Thus, the method can sim-

ulate conditional channels even if the chosen parameter values lead to channels not conform to the data configuration. In object-based simulation, a focus is often done on well sedimentary data conditioning [e.g., [Oliver, 2002](#), [Hassanpour et al., 2013](#), [Mariethoz et al., 2014](#)]. Here the method is able to handle far more data types, including well connectivity data, a sand probability cube or any kind of property cube and even a confinement. Weights give further control on the impact of each constraint.

The constraints induce a deformation of the initial channel morphology, including the sinuosity. They have been developed with the purpose to keep that deformation as small as possible. However, the channel sinuosity has less impact on flow circulations than the channel continuity. This approach never degrades the continuity of the channel, contrary to cell-based methods.

### **1.3 A method to stochastically simulate stacked channelized bodies using a geostatistical approach**

The channels simulated with a L-system are not able reproduce the complex organization of the relations between the channels as seen on outcrops or seismic images. That organization comes from migration and avulsion of the channels.

This is why the approach has been extended to include such types of controls. The proposed method relies on mimicking both migration and avulsion processes. It starts from an initial channel, either simulated with a L-system or interpreted on seismic data. Avulsion consists in simulating a new channel with a Lindenmayer system after a randomly chosen avulsion location. Migration is introduced through a geostatistical framework. This framework relies on the simulation of a migration factor with a sequential Gaussian simulation or a multiple-point simulation if a training set is available. With a training set the migration patterns can be directly borrowed from real data.

The current stochastic approaches of the migration [[Lopez, 2003](#), [Pyrzcz et al., 2009](#)] rely on physical models that are a controversial topic, especially with turbiditic systems. Here the method offers a more descriptive approach to control the stacking pattern resulting from migration and avulsion. The migration is controlled by means of a prior, which can come either from field data or from analog data. Furthermore, it is able to stochastically simulate both forward and backward migration. A backward process allows starting from the data, as the last channel of a complex is often interpretable on seismic data but not the first channel. Thus, this approach refocuses the migration process on the data.

Three realization sets have been compared to highlight the interest of integrating a migration process within stochastic simulations of channels. The first

set contains realizations without migration process, so simple L-system realizations. The second set does not integrate the migration process, but condition to a sand probability cube representing the result of the channel evolution. The last set contains realizations with migration process. Using the indicators (section 1.1) highlight the significant difference of connectivity between the different sets. It also highlights the poor control on the channel stacking without migration process. This can lead to complete – and unwanted – disconnections between some channels, so a significant impact on the connectivity.

## 2 Perspectives

Besides the technical improvements, several lines of research would be meaningful to further explore the integration of connectivity within stochastic simulations of channels.

### 2.1 Sensitivity tests and application to real data

All the methods have been tested on synthetic cases of different dimensions and settings, especially considering the types of data to take into account. Those cases have allowed exploring the possibilities offered by the methods. But the impact of the parameters on the resulting channels has only be slightly developed.

In particular, it has consequences on the conditioning of L-systems. Indeed, constraints involve many parameters, with several of them predefined to facilitate the task for the user. The ability of the predefined set to handle all, or at least most, cases has to be questioned. Sensitivity tests could also be done to explore the possible migration patterns developed thanks to the SGS or MPS. A comparison with real migrations is also a quite interesting perspective. This is especially true for the MPS-based process, which has a far higher interest when used with a training set from real data.

This aspect raises the question of the application on real data. If the synthetic cases have been developed with the idea of getting close to real cases, there are always differences with the reality. The application of all the methods proposed in this thesis on a real case would be of prime importance to either validate or further improve the chosen approaches.

### 2.2 Improvements of the indicators

Computing the indicators on sub-grids could be a significant development. Indeed, it would bypass the issue of comparing realizations within grids of dif-

ferent dimensions. This should improve the indicator efficiency to capture the connected component shape. It could also enable to capture a potential non-stationarity within the realizations.

Despite the interesting aspect of skeletons, their extraction from a component is difficult in three dimensions. Only two methods have been tested in this thesis and more exists [e.g., [Cornea et al., 2007](#)]. Using other methods could help to better capture the component topology and most importantly the component geometry.

### 2.3 Further use of L-systems

For now the simulation of channels is far from using the full potential of L-systems. Some examples illustrate the possibility of modifying the rules. Other possibilities include the simulation of lobes or of abandoned bends. These abandoned bends could be integrated in the backward migration process. This would complete the process, as neck cut-offs is the only missing feature compared with the forward process. Using L-systems for abrupt-migration should also improve the appearance of a disorganized stacking.

One exciting aspect of L-systems is all the developments done in numerical biology. For instance, L-systems are not only used to simulate tree morphologies, but also leaves, fruits and whole plants in three dimensions from a set of rules and the related interpretation [e.g., [Prusinkiewicz et al., 2001](#)]. Thus, the user can define its own three-dimensional objects. This aspect could be of significant interest for object-based modeling. Indeed, one limitation is to have a parameterization that defines a sedimentary object. From a user perspective, it is always annoying if that parameterization does not exist or is not satisfying. Some sedimentary objects could be then proposed by default. And if the user needs different or new objects, he would have the possibility to define them relatively easily. These developments should start by simulating the whole channel object with L-systems, and not just the channel morphology.

### 2.4 Better management of the data

Data conditioning is a key aspect in stochastic simulations. It could be introduced in the indicators to quantify the integration of data in the realizations. With cell-based methods, a cell with a channel value can remain without any channel cells in its neighborhood. Thus, no channel object passes through that cell, with an impact on the connectivity. Even if the data is conditioned *stricto sensu*, such configuration should be avoided.

Within the L-system process, the preservation of the channel morphology is a



main concern. That preservation significantly varies following the channel segment length. This parameter should be introduced in the constraint magnitude computation. The accuracy of conditioning by the constraints is not always good enough, even if the misfit remains at a very local scale. From this point of view, the deformation ability of NURBS is highly interesting, but still has to be tested. Conditioning to a global channel proportion or a net-to-gross would also be a significant improvement.

An interesting aspect of the constraints is their ability to take into account various types of data, including connectivity data. For now their integration is quite rough: one channel must condition a whole set of connected data. In reality, the connection may concern several channels. This just implies to better handle the relationships between the channels. For instance, a first channel conditions to a data. Another channel conditions another data, which should be connected to the first data. Then that second channel is attracted to a channel section of the first channel instead of the first data itself.

A last aspect is data conditioning in the migration process. All the methods used for avulsion and migration are able to condition. For migration, conditioning is easy at a distance less than the maximal migration distance. For larger distance, it requires another process. The bends could be attracted or repulsed, similarly as with the L-system or as done by [Lopez \[2003\]](#) or [Pyrz et al. \[2009\]](#). For avulsion, its triggering should be conditioned by the trend in the distance between the current channel and the data.

## 2.5 Introduction of the channel fill

Channel stacking is a main aspect influencing the connectivity of turbiditic systems. But the channel fill is another one. It could be highly interesting to test the indicators not on the sedimentary objects, but on the permeable deposits within those objects. The resulting shapes would be much more variable, but the analysis would be directly on the connectivity of the reservoir deposits.

For both channel and migration simulation, the use of NURBS gives access to curvilinear grids that can follow various fill geometries [[Ruiu et al., 2015b](#)]. It gives the opportunity to precisely simulate the channel fill. This simulation can relate on more classical geostatistical methods such as sequential indicator simulation. One aspect is how to combine the results from all the individual channels. One possibility is to transfer the fill properties into a curvilinear grid including all the channels, such as done with the master canyon in the synthetic cases. This leads to lose some more or less details of the fill depending on the master grid resolution. A better solution would be to generate a hexahedral grid conform to all the channels. However, this task is currently far beyond our

reach.

## **2.6 Link with fluvial systems**

Both fluvial and turbiditic environments raise similar interests, with similar issues around fluids circulating in deposits from channelized structures. Both systems are based on a morphologically similar element: the channel. However, in terms of sedimentology, similarities between fluvial and turbiditic environments is a huge subject of controversy [e.g., [Kolla, 2007](#), [Wynn et al., 2007](#)]. This controversy is nowadays mainly focused on the physics driving the current circulation within a channel.

If the global dimensions and architecture of fluvial and turbiditic deposits are significantly different, the methods illustrated here with turbiditic cases remains valid from a fluvial perspective. Indeed, we do not rely on the physical process underlying channelized deposits, only on the description of those deposits.



## Appendix A

# Simulation parameters of chapter 2

**Table A.1** Parameters used to simulate the channelized environment with DeeSse.

Parameters	Values
Maximum number of neighbors	64
Acceptance threshold	0.05
Maximal scan fraction of the TI	0.33

**Table A.2** Parameters used to simulate the channelized environment with IMPALA.

Parameters	Values
Number of multi-grids	4
Number of multi-grid levels in each direction	$4 \times 4 \times 1$
Search template type	Elliptic
Size of the search template (radii in m)	$7 \times 7 \times 4$
Maximal number of neighbors in the template	64

A Simulation parameters of chapter 2

**Table A.3** Parameters used to simulate the channelized environment with the object-based method of Petrel. The distributions used are all triangular.

<b>Simulation parameters</b>	<b>min</b>	<b>mode</b>	<b>max</b>
<b>Channels</b>			
Proportion (in %)	21.21	21.21	21.21
Orientation (in °)	0	0	0
Amplitude (in m)	10	15	40
Wavelength (in m)	60	70	100
Width (in m)	7	10	13
Thickness (in m)	1.5	2	4
<b>Levees</b>			
Proportion (in %)	8.79	8.79	8.79
Width (in m)	4	7	11
Thickness (relative to channel thickness)	0.25	0.35	0.6

**Table A.4** Variogram parameters used to simulate the channelized environment with SIS.

<b>Variogram parameters</b>	<b>Channels</b>	<b>Levees</b>	<b>Mudstone environment</b>
Azimuth (in °)	0	0	0
Dip (in °)	0	0	0
Sill	0.145	0.109	0.210
Nugget	0	0	0
Range 1 (in m)	23	26	70
Range 2 (in m)	12	14	34
Range 3 (in m)	3	1	2.5
Type	Spherical	Exponential	Exponential

## Appendix B

# Simulation parameters and L-system rules of chapter 3

**Table B.1** Parameters used to simulate the non-stationary channels.  $\mathcal{T}$  is a triangular distribution with a minimum, a mode and a maximum.

Simulation parameters	Decreasing sinuosity	Branching
Global direction (in $^{\circ}$ )	90	90
Global direction weight	0.25	0.25
Default segment length (in m)	100	100
Channel length (in m)	20 000	30 000
Half-wavelength (in m)	$\mathcal{T}(300,400,600)$	$\mathcal{T}(300,400,600)$
Amplitude (in m)	$\mathcal{T}(0,150,200)$	$\mathcal{T}(0,150,200)$
Deviation angle (in $^{\circ}$ )	$\mathcal{T}(0,0.057,0.57)$	$\mathcal{T}(0,0.057,0.57)$
L-system weight	1	1
Channel self-repulsion weight	1	1
Channel width (in m)	$\mathcal{T}(75,100,125)$	$\mathcal{T}(75,100,125)$
Channel width range (in m)	$\mathcal{T}(400,500,600)$	$\mathcal{T}(400,500,600)$
Curvature weight	0.85	0.85
Channel thickness (in m)	$\mathcal{T}(5,7,10)$	$\mathcal{T}(5,7,10)$
Channel thickness range (in m)	$\mathcal{T}(400,500,600)$	$\mathcal{T}(400,500,600)$
Curvature weight	0.85	0.85
Asymmetry aspect ratio	0.5	0.5

## B Simulation parameters and L-system rules of chapter 3

**Table B.2** Parameters used to simulate the channels of the figures 3.17, 3.18 and 3.23. Realizations in figures 3.21, 3.22, 3.15, 3.20 and 3.24 have the same parameters except the weights.  $\mathcal{T}$  is a triangular distribution with a minimum, a mode and a maximum.

Simulation parameters	Figure 3.17	Figure 3.18	Figure 3.23
Global direction (in °)	70	70	70
Global direction weight	0.2	0.2	0.2
Default segment length (in cell)	1	1	1
Channel length (in cell)	–	–	–
Half-wavelength (in cell)	$\mathcal{T}(4,7,12)$	$\mathcal{T}(4,7,12)$	$\mathcal{T}(4,7,12)$
Amplitude (in cell)	$\mathcal{T}(0,3.5,6)$	$\mathcal{T}(0,3.5,6)$	$\mathcal{T}(0,3.5,6)$
Deviation angle (in °)	$\mathcal{T}(0,0.057,0.57)$	$\mathcal{T}(0,0.057,0.57)$	$\mathcal{T}(0,0.057,0.57)$
L-system weight	1	1	1
Channel self-repulsion weight	0	0	0
Channel width (in cell)	$\mathcal{T}(2,2.75,3.5)$	$\mathcal{T}(2,2.75,3.5)$	$\mathcal{T}(2,2.75,3.5)$
Channel width range (in cell)	$\mathcal{T}(7,15,25)$	$\mathcal{T}(7,15,25)$	$\mathcal{T}(7,15,25)$
Curvature weight	0.75	0.75	0.75
Channel thickness (in cell)	1	1	1
Channel thickness range (in cell)	–	–	–
Curvature weight	0.75	0.75	0.75
Asymmetry aspect ratio	0.5	0.5	0.5
Domain	Yes	Yes	Yes
Confinement weight	0	0	0
Well sedimentary data	No	Yes	No
Channel data weight	–	1	–
Channel data bandwidth (in cell)	–	1 000	–
Inter-channel data weight	–	1	–
Well connectivity data	No	No	No
Sand probability cube	No	No	Yes
Sand probability weight	–	–	0.2

**Table B.3** Parameters used to simulate the channels within the master channel of the synthetic case.  $\mathcal{T}$  is a triangular distribution with a minimum, a mode and a maximum.

Simulation parameters	Set 1	Set 2	Set 3
Global direction (in °)	90	90	90
Global direction weight	0.25	0.25	0.25
Default segment length (in cell)	6	6	6
Half-wavelength (in cell)	$\mathcal{T}(10,15,25)$	$\mathcal{T}(10,15,25)$	$\mathcal{T}(10,15,25)$
Amplitude (in cell)	$\mathcal{T}(0,4,7)$	$\mathcal{T}(0,4,7)$	$\mathcal{T}(0,4,7)$
Deviation angle (in °)	$\mathcal{T}(0,0.57,5.7)$	$\mathcal{T}(0,0.57,5.7)$	$\mathcal{T}(0,0.57,5.7)$
L-system weight	1	1	1
Channel self-repulsion weight	0	0	0
Channel width (in cell)	$\mathcal{T}(5,6,8)$	$\mathcal{T}(5,6,8)$	$\mathcal{T}(5,6,8)$
Channel width range (in cell)	$\mathcal{T}(10,15,20)$	$\mathcal{T}(10,15,20)$	$\mathcal{T}(10,15,20)$
Curvature weight	0.75	0.75	0.75
Channel thickness (in cell)	$\mathcal{T}(1.5,2,2.5)$	$\mathcal{T}(1.5,2,2.5)$	$\mathcal{T}(1.5,2,2.5)$
Channel thickness range (in cell)	$\mathcal{T}(10,15,20)$	$\mathcal{T}(10,15,20)$	$\mathcal{T}(10,15,20)$
Curvature weight	0.75	0.75	0.75
Asymmetry aspect ratio	0.5	0.5	0.5
Domain	Yes	Yes	Yes
Confinement weight	1	1	1
Well sedimentary data	No	No	Yes
Channel data weight	–	–	1
Channel data bandwidth (in cell)	–	–	30
Inter-channel data weight	–	–	1
Well connectivity data	No	No	No
Sand probability cube	No	Yes	Yes
Sand probability weight	–	1	1



**Table B.4** Rules used to simulate channels with a bend length  $l_B$  from a distribution  $F_{l_B}$  and a curvature  $c$  from a distribution  $F_c$ .  $l_d$  is the channel default segment length,  $l_C$  the wanted channel length,  $l_c$  the current channel length,  $l_s$  and  $l_o$  are the distance between two channel sections,  $n_{s_u}$  are numbers of channel elements,  $\alpha$  is the angle between two channel sections and  $o$  is the branch orientation, equal to 1 if the channel follow the global direction,  $-1$  if the branch follow the opposite direction.

Global parameters:  $l_d, l_C, F_{l_B}, F_c, l_c = 0, l_B = 0, i = 1, n_{s_o} = 0$

$\omega$	:	$T_0$						
$p_1$	:	$T_0$	$\{l_B = draw(F_{l_B})\}$	$: l_c + l_B \leq l_C$	$\{n_s = \lceil l_B/l_d \rceil;$ $n_{s_1} = udraw(1, n_s - 1);$ $n_{s_2} = n_s - n_{s_1};$ $l_s = l_B/n_s\}$	$\xrightarrow{0.5}$	$[+C\{+C\}^{n_{s_1}-1}T_1] + (180) - C\{-C\}^{n_{s_2}}T_1$	} Initialization
$p_2$	:	$T_0$	$\{l_B = draw(F_{l_B})\}$	$: l_c + l_B \leq l_C$	$\{n_s = \lceil l_B/l_d \rceil;$ $n_{s_1} = udraw(1, n_s - 1);$ $n_{s_2} = n_s - n_{s_1};$ $l_s = l_B/n_s\}$	$\xrightarrow{0.5}$	$[-C\{-C\}^{n_{s_1}-1}T_1] + (180) + C\{+C\}^{n_{s_2}}T_1$	
$p_3$	:	$-C < T_i$	$\{l_B = draw(F_{l_B})\}$	$: l_c + l_B \leq l_C$	$\{n_s = \lceil l_B/l_d \rceil;$ $l_s = l_B/n_s\}$	$\rightarrow$	$+C\{+C\}^{n_s-1}T_{i+1}$	} Development
$p_4$	:	$+C < T_i$	$\{l_B = draw(F_{l_B})\}$	$: l_c + l_B \leq l_C$	$\{n_s = \lceil l_B/l_d \rceil;$ $l_s = l_B/n_s\}$	$\rightarrow$	$-C\{-C\}^{n_s-1}T_{i+1}$	
$p_5$	:	$-C < T_i$		$: l_c + l_B > l_C$	$\{l_B = l_C - l_c;$ $n_s = \lceil l_B/l_d \rceil;$ $n_{s_n} = i \times udraw(0, n_s) + n_{s_o};$ $l_s = l_B/n_s\}$	$\rightarrow$	$+C\{+C\}^{n_{s_n}-1}$	} Closure
$p_6$	:	$+C < T_i$		$: l_c + l_B > l_C$	$\{l_B = l_C - l_c;$ $n_s = \lceil l_B/l_d \rceil;$ $n_{s_n} = i \times udraw(0, n_s) + n_{s_o};$ $l_s = l_B/n_s\}$	$\rightarrow$	$-C\{-C\}^{n_{s_n}-1}$	
Left context:		$p_3, p_4, p_5, p_6$			$\pm(\alpha, o, l_o, l_B)C(l_s, o, l_c)$			
Successor		$p_1, p_2$			$\pm(draw(F_c) \times l_s \frac{180}{\pi} \times (\frac{n_s}{2} - n_{s_1} + 1), 1, l_s, l_B)C(l_s, 1, l_c + l_s)\{\pm(draw(F_c) \times l_s \frac{180}{\pi} \times (\frac{n_s}{2} - n_{s_2}), -1, l_s, l_B)C(l_s, -1, l_c + l_s)\}$			
Successor:		$p_3, p_4, p_5, p_6$			$\pm(draw(F_c) \times \frac{l_s + l_o}{2} \frac{180}{\pi}, o, l_s, l_B)C(l_s, o, l_c + l_s)\{\pm(draw(F_c) \times l_s \frac{180}{\pi}, o, l_s, l_B)C(l_s, o, l_c + l_s)\}$			

End condition:  $l_c \geq l_C$

## Appendix C

# Simulation parameters of chapter 4

**Table C.1** Parameters used to simulate the channels of figure 4.2.  $\mathcal{T}$  is a triangular distribution with a minimum, a mode and a maximum.  $\mathcal{U}$  is a uniform distribution with a minimum and a maximum.

Simulation parameters	Straight channel	Sinuoues channel
Global direction (in $^{\circ}$ )	90	90
Global direction weight	0.25	0.25
Default segment length (in m)	50	50
Channel length (in m)	$\mathcal{U}(6\,000,6\,500)$	$\mathcal{U}(10\,000,10\,500)$
Bend length (in m)	$\mathcal{U}(150,500)$	$\mathcal{U}(150,500)$
Curvature (in $\text{m}^{-1}$ )	$\mathcal{T}(0,0.001,0.005)$	$\mathcal{T}(0,0.001,0.025)$
L-system weight	1	1
Channel self-repulsion weight	0	0
Channel width (in m)	80	80
Channel thickness (in m)	5	5
Asymmetry aspect ratio	0.5	0.5

C Simulation parameters of chapter 4

**Table C.2** Parameters used to simulate the SGS-based migrations in the simple cases.  $\mathcal{T}$  is a triangular distribution with a minimum, a mode and a maximum.  $\mathcal{U}$  is a uniform distribution with a minimum and a maximum.

Simulation parameters	Forward migration	Backward migration
<b>Initial channel and avulsions</b>		
Global direction (in °)	90	90
Global direction weight	0.05	0.2
Default segment length (in m)	100	100
Channel length (in m)	30 000	35 000
Bend length (in m)	$\mathcal{T}(500,1\,000,2\,000)$	$\mathcal{U}(500,1\,500)$
Curvature (in $\text{m}^{-1}$ )	$\mathcal{T}(0,0.0001,0.0003)$	$\mathcal{T}(0,0.002,0.007)$
L-system weight	1	1
Channel self-repulsion weight	0	0
Channel width (in m)	$\mathcal{T}(150,200,250)$	$\mathcal{T}(150,200,250)$
Channel width range (in m)	$\mathcal{T}(2\,000,3\,000,5\,000)$	$\mathcal{T}(2\,000,3\,000,5\,000)$
Curvature weight	0.75	0.75
Channel thickness (in m)	$\mathcal{T}(15,20,25)$	$\mathcal{T}(15,20,25)$
Channel thickness range (in m)	$\mathcal{T}(2\,000,3\,000,5\,000)$	$\mathcal{T}(2\,000,3\,000,5\,000)$
Curvature weight	0.75	0.75
Asymmetry aspect ratio	0.5	0.5
<b>Migrated channels</b>		
Number of migration steps	29	29
Aggradation factor	$\mathcal{U}(5,10)$	$\mathcal{U}(-10,-5)$
Migration curvature weight	0.75	-0.75
Migration factor	$\mathcal{U}(-75,75)$	$\mathcal{U}(-75,75)$
Migration range (in m)	3 000	3 000
Abrupt migration probability	0.001	0.001
Abrupt migration length (in m)	$\mathcal{T}(5\,000,6\,000,8\,000)$	$\mathcal{T}(5\,000,6\,000,8\,000)$
Abrupt migration curvature weight	-0.25	0.25
Abrupt migration factor	$\mathcal{U}(-400,400)$	$\mathcal{U}(-400,400)$
Abrupt migration range (in m)	4 000	4 000
Regional avulsion probability	0.0007	0.0007

**Table C.3** Parameters used to simulate the MPS-based migrations in the simple cases.  $\mathcal{T}$  is a triangular distribution with a minimum, a mode and a maximum.  $\mathcal{U}$  is a uniform distribution with a minimum and a maximum.

Simulation parameters	Training set	Realization
<b>Initial channel and avulsions</b>		
Global direction (in $^{\circ}$ )	90	90
Global direction weight	0.05	0.05
Default segment length (in m)	100	100
Channel length (in m)	30 000	30 000
Bend length (in m)	$\mathcal{T}(500,1\ 000,2\ 000)$	$\mathcal{T}(500,1\ 000,2\ 000)$
Curvature (in $\text{m}^{-1}$ )	$\mathcal{T}(0,0.0001,0.0003)$	$\mathcal{T}(0,0.0001,0.0003)$
L-system weight	1	1
Channel self-repulsion weight	0	0
Channel width (in m)	$\mathcal{T}(150,200,250)$	$\mathcal{T}(150,200,250)$
Channel width range (in m)	$\mathcal{T}(2\ 000,3\ 000,5\ 000)$	$\mathcal{T}(2\ 000,3\ 000,5\ 000)$
Curvature weight	0.75	0.75
Channel thickness (in m)	$\mathcal{T}(15,20,25)$	$\mathcal{T}(15,20,25)$
Channel thickness range (in m)	$\mathcal{T}(2\ 000,3\ 000,5\ 000)$	$\mathcal{T}(2\ 000,3\ 000,5\ 000)$
Curvature weight	0.75	0.75
Asymmetry aspect ratio	0.5	0.5
<b>Migrated channels (SGS)</b>		
Number of migration steps	9	–
Aggradation factor	$\mathcal{U}(5,10)$	–
Migration curvature weight	0.75	–
Migration factor	$\mathcal{U}(-75,75)$	–
Migration range (in m)	3 000	–
Abrupt migration probability	0.1	–
Abrupt migration length (in m)	$\mathcal{T}(5\ 000,6\ 000,8\ 000)$	–
Abrupt migration curvature weight	-0.25	–
Abrupt migration factor	$\mathcal{U}(-400,400)$	–
Abrupt migration range (in m)	3 000	–
Regional avulsion probability	0	–
<b>Migrated channels (MPS)</b>		
Number of migration steps	–	9
Whole training set as training model	–	No
Maximum scan fraction	–	0.75
Maximum neighbor number	–	7
Migration factor acceptance threshold	–	0
Curvature factor acceptance threshold	–	0

**Table C.4** Parameters used to simulate the organized stacking realizations.  $\mathcal{T}$  is a triangular distribution with a minimum, a mode and a maximum.  $\mathcal{U}$  is a uniform distribution with a minimum and a maximum.

<b>Simulation parameters</b>	<b>First phase</b>	<b>Second phase</b>
<b>Initial channel and avulsions</b>		
Initial location (in cell)	150, -, 8	-
Global direction (in °)	90	-
Global direction weight	0.25	-
Default segment length (in cell)	6	-
Channel length (in cell)	450	-
Bend half-wavelength (in cell)	$\mathcal{T}(15,20,30)$	-
Amplitude (in cell)	$\mathcal{T}(0,0.5,1)$	-
Deviation angle (in °)	$\mathcal{T}(0,0.57,5.7)$	-
L-system weight	1	-
Channel self-repulsion weight	0	-
Channel width (in cell)	$\mathcal{T}(5,6,8)$	-
Channel width range (in cell)	$\mathcal{T}(10,15,20)$	-
Curvature weight	0.75	-
Channel thickness (in cell)	$\mathcal{T}(1.5,2,2.5)$	-
Channel thickness range (in cell)	$\mathcal{T}(10,15,20)$	-
Curvature weight	0.75	-
Asymmetry aspect ratio	0.5	-
<b>Migrated channels</b>		
Number of migration steps	27	12
Aggradation factor	$\mathcal{T}(0,0.5,1)$	$\mathcal{T}(1.25,1.65,2)$
Migration curvature weight	0.75	0.95
Migration factor	$\mathcal{U}(-3,3)$	$\mathcal{U}(-0.5,0.5)$
Migration range (in cell)	50	50
Abrupt migration probability	0.2	0
Abrupt migration length (in cell)	$\mathcal{T}(60,70,80)$	-
Abrupt migration curvature weight	0.75	-
Abrupt migration factor	$\mathcal{U}(-8,8)$	-
Abrupt migration range (in cell)	70	-
Regional avulsion probability	0	0

## Appendix D

# Karst network simulation with L-systems

**Context** The following proceeding article comes from the master project of Pierre Anquez, supervised during the thesis work. The project purpose was to apply the Lindenmayer system to the stochastic simulation of karst networks. It led to the definition of L-system rules integrated in a process to simulate branchwork to anastomotic karst networks.

P. Anquez, G. Rongier, P. Collon (2015) *Stochastic simulations of karst networks with Lindenmayer systems*, 35<sup>th</sup> Gocad Meeting, Nancy, France

# Stochastic simulations of karst networks with Lindenmayer systems

Pierre Anquez<sup>1</sup>, Guillaume Rongier<sup>1,2</sup>, and Pauline Collon<sup>1</sup>

<sup>1</sup>*GeoRessources - RING, Université de Lorraine - ENSG / CNRS /CREGU. ENSG, 2 rue du Doyen Marcel Roubault, F-54518, Vandoeuvre-lès-Nancy, France*

<sup>2</sup>*Centre d'Hydrogéologie et de Géothermie, Université de Neuchâtel, 11 rue Emile-Argand, 2000 Neuchâtel, Switzerland*

*pierre.anquez3@etu.univ-lorraine.fr ; guillaume.rongier@univ-lorraine.fr ;  
pauline.collon@univ-lorraine.fr*

September 2015

## Abstract

Some major hydrocarbon reservoirs are contained within paleokarsts and are influenced by the highly complex network geometries of the past karstic conduits. Those geometries are most of the time unknown and numerical simulations allow to better assess the uncertainty associated to those reservoirs. Several methods have been developed to simulate karstic systems but they mainly focus on branchwork karst networks. Anastomotic patterns are also observed in a significant proportion of karstic networks. Their singular connectivity implies a different response in the oil extraction process, and, thus, needs to be considered. This paper introduces a new object-based method to stochastically simulate karst networks with both branchwork and anastomotic patterns. Based on the Lindenmayer system (L-system), this method is composed of two steps. First, an intermediate karst network with only branchwork pattern is simulated. In a second time, some conduits are reconnected one by one on other conduits of the intermediate network. The very first results are two dimensional karst networks composed of some branching parts and anastomoses. This object-based method allows to generate several models reproducing the particular connectivity of complex karst networks mixing different patterns. Uncontrolled intersections between conduits sometimes appear. They could besides be limited by introducing a repulsion between the conduits. This work gives a basis for the simulation of 2.5D karst networks with possible integration of hard and soft data.

## Introduction

Karstic systems are underground networks deeply related to fluid circulation as they result from the dissolution of carbonated rocks by groundwater. Some of them later constitute important hydrocarbon reservoirs. For instance, the Tarim basin and its Ordovician limestone and dolostone account for the fifth of the Chinese hydrocarbon resources [Zeng et al., 2011]. Karst development leads to very complex heterogeneities at various scales, with a huge impact on fluid flows. Predicting these heterogeneities is quite challenging but necessary to better characterize karstified reservoirs.

In order to study the flows in karstic systems, numerical models are a valuable support. Many information about karsts can be drawn from speleologist explorations. However speleology is limited to conduits that are accessible to humans: some parts of the networks can not be explored, for instance because of small or collapsed conduits. In case of shallow karsts or paleo-karsts, speleology is impossible. It leads to a lack of information which can be partially overcome with wells and seismic data. Stochastic simulations are a way to fill the remaining gaps and to better assess the uncertainties in the unexplored parts of the karst networks.

There are different approaches for karst network simulations which could be gathered in three groups:

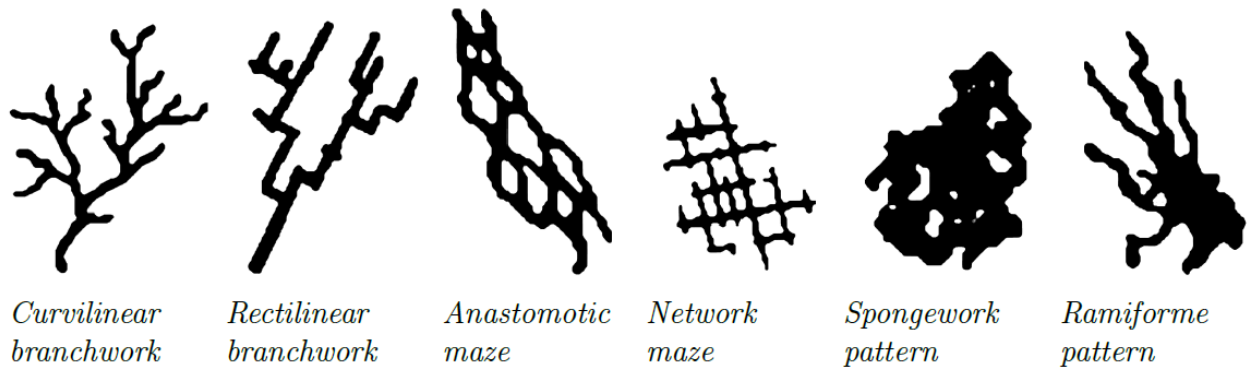


Figure 1: *Classification of patterns found in karstic networks (modified from [Palmer, 2002]).*

- *Genetic methods* compose the first group. They try to reproduce physical and chemical processes that lead to the formation of karst systems. Unfortunately those methods need long run-time and numerous parameters sometimes uneasy to define. Most of them are deterministic methods [e.g., Siemers and Dreybrodt, 1998, Bauer et al., 2000, Kaufmann and Braun, 2000], and are hard, if not impossible, to condition with available data.
- *Object-based methods* aim to describe the karst network morphology at a given time, without considering the processes at the origin of the network geometry [e.g., Pardo-Igúzquiza et al., 2012, Barthélemy and Collon-Drouaillet, 2013]. An advantage of object-based methods is the possibility to explore the uncertainties considering the data.
- *Pseudo-genetic methods* are the intersection of the previous groups: they try to preserve the strengths of both genetic and object-based methods. These methods use several models of karst morphology and karst evolution. They are based on a set of simple assumptions of the karstification physical processes that they try to honor [e.g., Jaquet et al., 2004, Borghi et al., 2012, Collon-Drouaillet et al., 2012]. They can also often take data into account in the simulation process, although this aspect remains quite limited.

To assess the heterogeneities and their impact on flow, the study of karst network connectivity at the largest scale is necessary. Palmer’s classification [Palmer, 2002], based on a study on the connectivity and geometry of several karst networks, can be a source of inspiration. This classification ranges karst networks depending on recurrent patterns that can be related to speleogenetical processes (Figure 1).

A huge part of karst network simulation methods have been developed to reproduce the geometry of branchwork karsts. The anastomotic maze pattern has particular geometries composed of loops and reconnections between conduits that strongly influence fluid flows. But only few methods are able to simulate this kind of pattern [e.g., Jaquet et al., 2004, Barthélemy and Collon-Drouaillet, 2013]. Moreover, Palmer’s classification remains general and a single karst network is often a mix of the various patterns. It is thus important to integrate the possibility of loop generations in a karst simulation workflow.

Lindenmayer systems, also known as L-system [Lindenmayer, 1968], are a formal grammar which consists in string rewriting from an initial string and rewriting rules. Each character of the final string can then be interpreted geometrically to obtain a simulated object. The L-system formalism has been extensively developed through the years. It is so possible to generate different final strings from a given set of rules and thus to simulate multiple objects from the same L-system.

This work is dedicated to stochastically simulate karst networks with a new object-based method based on L-systems. Different rules have been defined to simulate karst networks mixing branchwork and anastomotic patterns. This method gives multiple stochastic realisations while respecting the global topology of such networks.



# 1 L-system principles

A L-system is a formal grammar system based on string rewriting. A string is composed of characters, which could be letters or symbols. The set of characters used in a L-system is called the alphabet. The string can then be interpreted geometrically.

A L-system is so composed of four elements [Prezemyslaw and Lindenmayer, 1996]:

- An alphabet of characters (Table 1);
- An initial string, the axiom  $\omega$ , with which the L-system starts;
- A set of production rules ( $p_i, i \in [1, n]$ ,  $n$  being the number of rules), which are the rewriting rules of a *predecessor* by a *successor*;
- An order, the number of iterations, in other words the number of rewriting of the whole string.

## 1.1 Basic L-systems [Lindenmayer, 1968]

In the simplest L-systems, the production rules are only made of a predecessor and a successor:

$$\text{predecessor} \longrightarrow \text{successor}$$

For each production step  $i$ , each character is read and compared with the predecessors of the production rules. If the character matches a predecessor, it is replaced by the corresponding successor. If the current character does not match any predecessor in the production rules, the character is simply copied in the next string. For example, if a L-system is defined by the following axiom and production rules:

$$\begin{aligned} \omega & : b \\ p_1 & : a \longrightarrow abc \\ p_2 & : b \longrightarrow a \end{aligned}$$

The results for an order equal to five is:

$$\begin{aligned} 0 & : b \\ 1 & : a \\ 2 & : abc \\ 3 & : abcac \\ 4 & : abcacabcc \\ 5 & : abcacabccabcacc \end{aligned}$$

These basic principles are the most simple formalism of L-system. Due to the great flexibility of this formalism, more complex rules have been added and so expand the L-system possibilities.

## 1.2 Geometrical interpretation of strings

The geometrical interpretation is the transcription of generated L-system strings into an image, a graph or an object. Each character of the string corresponds to a geometrical action (Table 1). Several geometrical interpretations exist but the most often used is the *turtle interpretation* [Prezemyslaw and Lindenmayer, 1996].

The principle is to translate the L-system final string, character after character, by a turtle advance. The final string is the string obtained when the number of rewriting steps are equal to the order. The turtle is represented by three unit orthogonal vectors,  $\vec{H}$ ,  $\vec{L}$  and  $\vec{U}$ , corresponding respectively to the direction of the turtle head, the direction of its left and the upward direction. These three vectors are updated during string interpretation.

The turtle can make two kinds of movements: turning of a given angle  $\alpha$  around one of the three axis determined by  $\vec{H}$ ,  $\vec{L}$  and  $\vec{U}$ , or moving forward of a given length  $l_{C_i}$  in the direction to the

Table 1: *Classical geometrical interpretation of L-system characters*

Symbols	Geometrical interpretation
F	Move forward of a given length, draw a segment
f	Move forward on a given length without drawing a segment
+	Turn left by a given angle around the vector $\vec{U}$
-	Turn right by a given angle around the vector $\vec{U}$
[	Start a branch and save the position and state of the turtle
]	End a branch and replace the turtle in the latest saved position

head vector  $\vec{H}$ . Interpreting a L-system string consists of a suite of actions based on movements and motionless rotations (Table 1).

### 1.3 Stochastic L-systems

Basic L-systems are deterministic: at a given order, the resulting string of a given system is always the same. There are two ways to give stochastic results from a single L-system definition:

- By randomizing the geometrical interpretation of the final string. Only the geometry will vary, the topology remains the same.
- By defining several production rules for the same predecessor and associating a probability of application to each. Both the geometry and the topology of the final object will vary.

In the following example, when the character  $a$  is read in the string, its probability to be rewritten with  $abc$  is 75% and its probability to be rewritten with  $bbb$  is 25%.

$$\begin{aligned}
 \omega & : b \\
 p_1 & : a \xrightarrow{0.75} abc \\
 p_2 & : a \xrightarrow{0.25} bbb \\
 p_3 & : b \longrightarrow a
 \end{aligned}$$

### 1.4 Parametric L-systems

It is possible to affect one or more parameters to a character. Parameters could be used in two different ways:

- To define some needed values in the geometrical interpretation, particularly the length of each drawn segment and the angle between two successive segments;
- To condition the application of production rules. A rule is only applied if all the conditions concerning the parameters are valid.

In the following parametric L-system, validating the condition in the production rule  $p_2$  is necessary to apply the rule:

$$\begin{aligned}
 h & = 0 \\
 \omega & : b(h) \\
 p_1 & : a \longrightarrow ab(h + 0.1) \\
 p_2 & : b(h) : h \leq 1 \longrightarrow a
 \end{aligned}$$

$h$  is a global parameter, which means that it is never reset to 0 during the rewriting process. The rule  $p_2$  is applied as long as  $h$  is lower or equal to 1. If an other production rule  $p_3$  is defined with the

condition  $h > 1$ , the production rule  $p_2$  is first applied until  $h$  reaches 1 and then the production rule  $p_3$  is applied.

These two additional formalisms used together allow L-systems to simulate various forms and objects. Only few of the numerous L-system definitions and possibilities have been presented in this paper, for more details see Prezemyślak and Lindenmayer [1996].

## 2 Karst network simulations using L-systems

We propose a new method for karst network simulation based on L-systems. Karst networks can be described by the geometry of conduits and their connections to each others. In our simulation, a conduit is the name given to a part of the karst network between two particular points, called nodes. Nodes are either bifurcation points, which are points where a conduit forks into two other conduits, or dead-end extremities. Each conduit is simulated by a succession of linear segments (Figure 2).

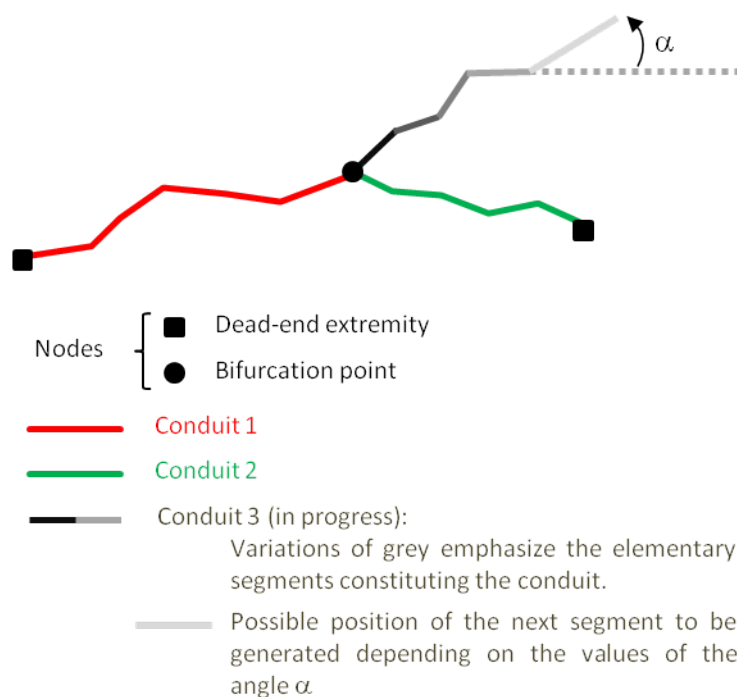


Figure 2: *Schema presenting the notions of conduits, elementary segments and nodes used for the simulation.*

If L-systems are well adaptable to rectilinear and branching objects, the formalisms presented above are not adapted to anastomotic shapes. Lindenmayer [1987] introduced another L-system formalism based on map [Nakamura et al., 1986] to simulate plant cellular tissues. Unfortunately, this formalism is more difficult to adapt to stochastic simulations. Moreover, map L-systems simulate only cyclic structures, which is not fully compatible with the simulation of karst networks, which combine loops and branching curvilinear conduits.

The method presented in this paper combines the branching pattern of classical L-system with the attraction process defined by Rongier et al. [2014b] for the simulation of channel axes. It has been coded in C++ in the ConnectO plugin of Gocad.

### 2.1 Input parameters

To enable some flexibility in the simulation process, several parameters are let to the user's control (Table 2). The karst outlet position  $O(x, y, z)$  is the start of the simulation process, which makes the

network growths to the inlets. A global direction  $\vec{d}$  controls the global orientation of the network. It is the opposite of the direction of karst natural development.

Table 2: *Input parameters for karst network simulation*

Symbols	Parameters
$N$	Number of simulations
$O(x, y, z)$	Coordinates of the karst outlet
$\vec{d}$	Global orientation of karstic network (from outlet to inlets)
$L_C$	Conduit lengths (probability distribution)
$l_s$	Elementary segment length
$\alpha$	Angles between elementary segments (probability distribution)
$n_l$	Maximal number of loops

Conduit lengths  $L_C$ , elementary segment lengths  $l_s$  and angles between the elementary segments  $\alpha$  provide a control on the geometry of the resulting network. Conduit lengths and angles between segments are drawn in probability distributions in order to introduce stochasticity in the resulting geometries.

Finally, the topology of the network is smoothly controlled by the parameter  $n_l$  which is the maximal number of loops that can be generated.

## 2.2 L-system alphabet for karst network simulation

Karst network simulation needs the definition of a L-system, with axiom, production rules and also a specific alphabet. This L-system must simulate the different karstic structures, that is to say conduits, bifurcations (points where a conduit is divided into two conduits) and dead-end passages. All of these structures are represented by symbols in the L-system alphabet; only loops can not be directly symbolized in the alphabet. Table 3 summarizes the alphabet used for karst simulations. Thus, in the L-system formalism, a conduit is a succession of modules  $\{+C\}$  or  $\{-C\}$ , i.e. a succession of elementary segments with a rotation clockwise or counter-clockwise between each of them (Figure 2). This rotation is independent of the previous rotations and leads to various conduit geometries.

Table 3: *L-system alphabet and corresponding geometrical interpretation for karst network simulations*

Symbols	Geometrical interpretation
$C$	Move forward of a length $l_s$ , draw a segment
$T$	Do nothing (represents an on-going conduit extremity)
$D$	Do nothing (represents a dead-end passage extremity)
$W$	Do nothing (represents a waiting conduit extremity)
$M$	Draw a segment between the previous position and the attraction point (to close loop)
$+$	Turn left by an angle $\alpha$ around the vector $\vec{U}$
$-$	Turn right by an angle $\alpha$ around the vector $\vec{U}$
$[$	Start a new conduit and save the position and state of the turtle
$]$	End the conduit and replace the turtle in the latest saved position

## 2.3 Simulation process

The simulation method we propose is performed in two steps. The first step consists in the simulation of an initial network with a branchwork architecture. The second step generates additional loops corresponding to the anastomotic pattern.

### 2.3.1 Simulation of an initial branchwork pattern network

The L-system defined for an initial branchwork network simulation uses an axiom  $\omega$  and seven production rules  $p_1$  to  $p_7$ . It is a parametric L-system (section 1.4), thus, in addition to the input parameters provided by the user (section 2.1), internal variables are used. They regroup global variables:

- $n$ , the number of conduits that are finished, in progress or waiting;
- $w$ , the number of waiting conduits;
- $t$ , the number of in progress conduits, in other words the number of modules  $T$  in the whole L-system string;
- $a$ , the number of loops (anastomoses) already simulated in the karst network ( $a \leq n_l$ );

and variables depending on the conduit being proceeded, used to condition the application of production rules ( $T(i, l_{Ci}, L_{Ci}, e_i)$ ) :

- $i$ , the index of the conduit being proceeded;
- $l_{Ci}$ , the current length of conduit  $i$ , in other words the sum of length of already simulated segments for the conduit  $i$ ;
- $L_{Ci}$ , the conduit length to reach for stopping its growth ( $l_{Ci} \leq L_{Ci}$ );  $L_{Ci}$  is randomly drawn at the creation of the conduit in the probability distribution of  $L_C$  given by the user;
- $e_i$ , an indicator of the kind of conduit extremity for the conduit  $i$  (bifurcation or dead-end passage).

L-system starts with the following axiom  $\omega$ :

$$\omega : T(1, 0, L_{C1}, 1)$$

When there is only one conduit in progress ( $t = 1$ ), two L-system production rules allow the growth of a conduit while the in progress length  $l_{Ci}$  is lower than the length to reach  $L_{Ci}$  :

$$\begin{aligned} p_1 & : T(i, l_{Ci}, L_{Ci}, e_i) : l_{Ci} < L_{Ci}, t = 1 \xrightarrow{0.5} \{+C\}(i, l_{Ci} + l_s, L_{Ci}, rand(\alpha))T(i, l_{Ci}, L_{Ci}, e_i) \\ p_2 & : T(i, l_{Ci}, L_{Ci}, e_i) : l_{Ci} < L_{Ci}, t = 1 \xrightarrow{0.5} \{-C\}(i, l_{Ci} + l_s, L_{Ci}, rand(\alpha))T(i, l_{Ci}, L_{Ci}, e_i) \end{aligned}$$

Each addition of a segment increments the conduit length  $l_{Ci}$  by a value  $l_s$  and is followed by a rotation towards left (if module is  $\{+C\}$ ) or right (if module is  $\{-C\}$ ) by an angle  $rand(\alpha)$  randomly drawn in the angle distribution  $\alpha$  provided by the user. When the cumulated length  $l_{Ci}$  becomes higher than the length  $L_{Ci}$ , the conduit ends with either a bifurcation or a dead-end extremity. The choice between these two possibilities depends on the value of the parameter  $e_i$  of the last module  $T$  of the conduit (drawn in  $]0, 1[$ ), by comparing it with the real number  $E$  defined as follows:

$$E = \begin{cases} 1 - \exp\left(-\frac{w}{n_l}(t-1)\right) & \text{if } n_l > 1 \\ 1 - \exp\left(-(t-1)\right) & \text{otherwise} \end{cases}$$

If  $e_i$  is lower than or equal to  $E$  the extremity of the conduit is a dead-end passage; on the contrary, if  $e_i$  is higher than  $E$ , the extremity is a bifurcation, beginning two new conduits. If  $t = 1$ , we want to exclude a dead-end passage, thus  $E$  will be equal to 0 and guarantee  $e_i > E$ . The ratio  $\frac{w}{n_l}$  favours bifurcation appearance for low values of  $w$  (in that case  $E$  is closer to 0 than 1).  $E$  increases as bifurcations appear and gets closer to 1, favouring dead-end passages. This allows to approach

the wished value of loops. If  $n_l$  is equal to 0 (pure branchwork network), then bifurcation appears randomly. The production rules  $p_3$  and  $p_4$  express these operations:

$$\begin{aligned}
 p_3 & : T(i, l_{C_i}, L_{C_i}, e_i) : l_{C_i} \geq L_{C_i}, e_i \leq E \longrightarrow D \\
 p_4 & : T(i, l_{C_i}, L_{C_i}, e_i) : l_{C_i} \geq L_{C_i}, e_i > E \longrightarrow -[\{-C\}(i, l_s, L_{C_{n+1}} = \text{rand}(L_C), \text{rand}[0, 60]) \\
 & \qquad \qquad \qquad T(n+1, 0, L_{C_{n+1}}, \text{rand}[0, 1])] \\
 & \qquad \qquad \qquad +[\{+C\}(i, l_s, L_{C_{n+2}} = \text{rand}(L_C), \text{rand}[0, 60]) \\
 & \qquad \qquad \qquad T(n+2, 0, L_{C_{n+2}}, \text{rand}[0, 1])]
 \end{aligned}$$

The application of these rules updates global parameters accordingly. If rule  $p_3$  is applied, a conduit in progress is stopped, so  $t$  is decreased by one. If rule  $p_4$  is applied, a conduit in progress is ended but two new conduits are in progress so  $t$  is increased by one.

In the rule  $p_4$ , the modules  $+$  and  $-$  represent the angles between conduit as shown in Figure 3. These angles, between the straight line bore by the last segment of the conduit coming to the bifurcation and the first segment of the conduits coming from the bifurcation, are drawn between 0 and 60 degrees. The distribution of angles given by the user is not used here in order to force the two conduits to drift away from each others. The parameters  $L_{C_{n+1}}, L_{C_{n+2}}$  and  $e_{n+1}, e_{n+2}$  are randomly drawn for each new conduit: parameter  $L_{C_i}$  is drawn in the distribution of conduits lengths  $L_C$  and parameter  $e_i$  is drawn in  $]0, 1]$ .

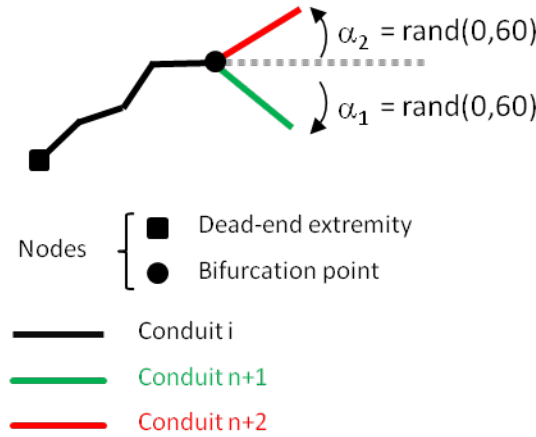


Figure 3: At a bifurcation point, angles  $\alpha_1$  and  $\alpha_2$  are the angles between the dashed straight line and the first segment of the new conduits.  $\alpha_1$  and  $\alpha_2$  are randomly drawn between 0 and 60 degrees.

In order to prepare the second step, which consists in generating loops, some conduits must be on standby, in other words, put in a *waiting* status. These waiting conduits, which will be the seeds of loops in the final karst network, are chosen stochastically by the apparitions of the module  $W$  as a successor of the module  $T$ . Module  $W$  apparitions need to have at least two conduits in progress, otherwise there is no remaining conduit in progress and the karst network simulation is over. Thus,  $p_5, p_6$  and  $p_7$  are only applied if  $t > 1$ . Note also that if  $n_l = 0$  (pure branchwork),  $p_7$  has a probability of 0 and  $p_1$  and  $p_2$  are applied independently of the value of  $t$  (the L-system is reduced to the fourth first rules).

$$\begin{aligned}
 p_5 & : T(i, l_{C_i}, L_{C_i}, e_i) : l_{C_i} < L_{C_i}, t > 1 \xrightarrow{0.48} \{+C\}(i, l_{C_i} + l_s, L_{C_i}, \text{rand}(\alpha))T(i, l_{C_i}, L_{C_i}, e_i) \\
 p_6 & : T(i, l_{C_i}, L_{C_i}, e_i) : l_{C_i} < L_{C_i}, t > 1 \xrightarrow{0.48} \{-C\}(i, l_{C_i} + l_s, L_{C_i}, \text{rand}(\alpha))T(i, l_{C_i}, L_{C_i}, e_i) \\
 p_7 & : T(i, l_{C_i}, L_{C_i}, e_i) : l_{C_i} < L_{C_i}, t > 1 \xrightarrow{0.04} W(i, l_{C_i}, L_{C_i}, 0)
 \end{aligned}$$

The rules  $p_5$  and  $p_6$  are almost the same as rules  $p_1$  and  $p_2$  described above: only the value of their application probabilities are different. If the rule  $p_7$  is applied, the current conduit becomes a waiting

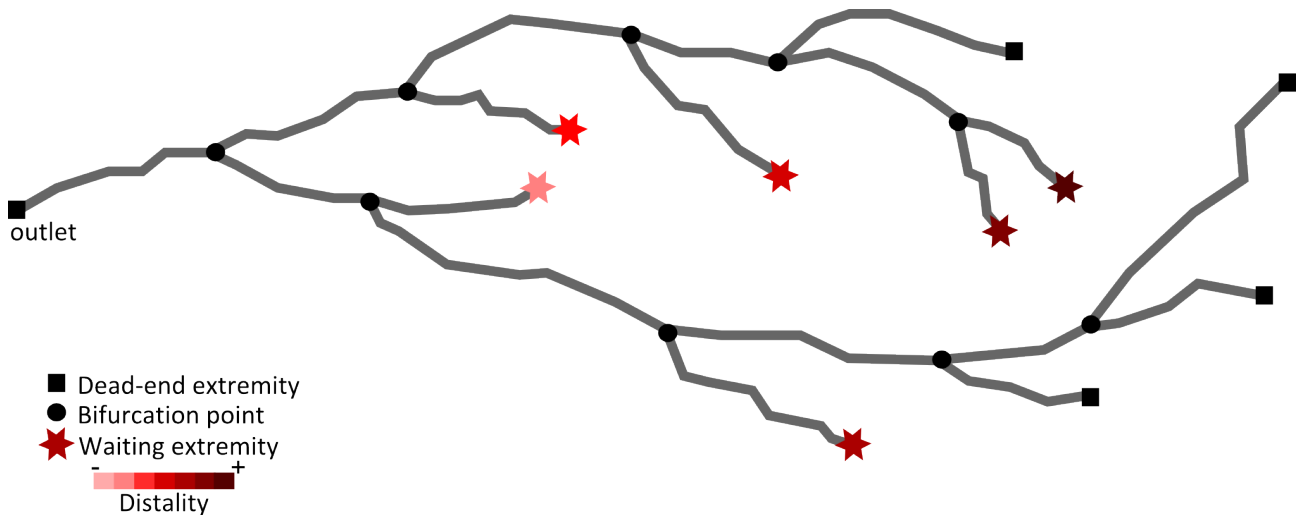


Figure 4: A possible intermediate branchwork pattern network at the end of the first step. The waiting conduits are figured by stars.

conduit because  $W$  is not replaced during the rewriting steps.

The application of rule  $p_7$  updates two global parameters: it increases by one  $w$ , the number of waiting conduits, and it decreases by one  $t$ , the number of in progress conduits.

The seven production rules allow the simulation of an intermediate branchwork karst network with waiting conduits, which are necessary for loop simulations (Figure 4). The first step is stopped when no conduit remains in progress, i.e. when  $t = 0$ .

### 2.3.2 Simulation of loops by developing waiting conduits

The aim of this second step is to generate loops in the karst network. At the beginning of this step, the karst network has a curvilinear branchwork pattern with some waiting conduits (Figure 4). As the karstic network is simulated from outlet to inlets (in the opposite direction of natural karst development), each new conduit propagates oppositely to outlet. Thus, to avoid involuntary crossings, all the waiting extremities (points  $W$  symbolized by stars in Figure 4) are treated one by one from the most distal to the most proximal point  $W$ . The distality of a point  $W$  is defined by the scalar projection of the vector between  $W$  and the outlet onto a line along the vector of the global direction  $\vec{d}$  defined by the user.

To build a loop, a point  $W$  is linked to an attraction point  $A$  representing the conduit extremity position at the end of the conduit growth. The waiting extremity is attracted towards the point  $A$  and the conduit grows until connection is achieved (Figure 5).

The main difficulty lies in the positioning of the attraction point  $A$ . In order to avoid *going back* conduits, only the network conduits that have at least one extremity with a distality higher than that of the point  $W$  are taken into account (Figure 5a). Among these conduits, only those for whom the two segments between the point  $W$  and one of its two extremities do not intersect any other conduits are selected to bore the attraction point  $A$  (Figure 5b). This simplified test prevents a complete test of every elementary segments of the conduits and hence accelerates the process but it could lead to miss the detection of possible intersections. The point  $A$  is randomly chosen on one of those possible conduits (Figure 5b), i.e. in the L-system formalism, a module  $\{\pm C\}$  is chosen and its geometrical position is used as attraction point.

Then, the corresponding  $W$  module in the L-system string is replaced by a  $T$  module. The global parameters are updated:  $w$  is decreased by one and  $t$  is increased by one. Consequently, the simulation of this conduit can restart. Attraction to point  $A$  follows the principle of hard data conditioning in channel simulation already developed with L-system [Rongier et al., 2014b]. Attraction is stopped when the distance between the extremity of the conduit and the point  $A$  is lower than the segment

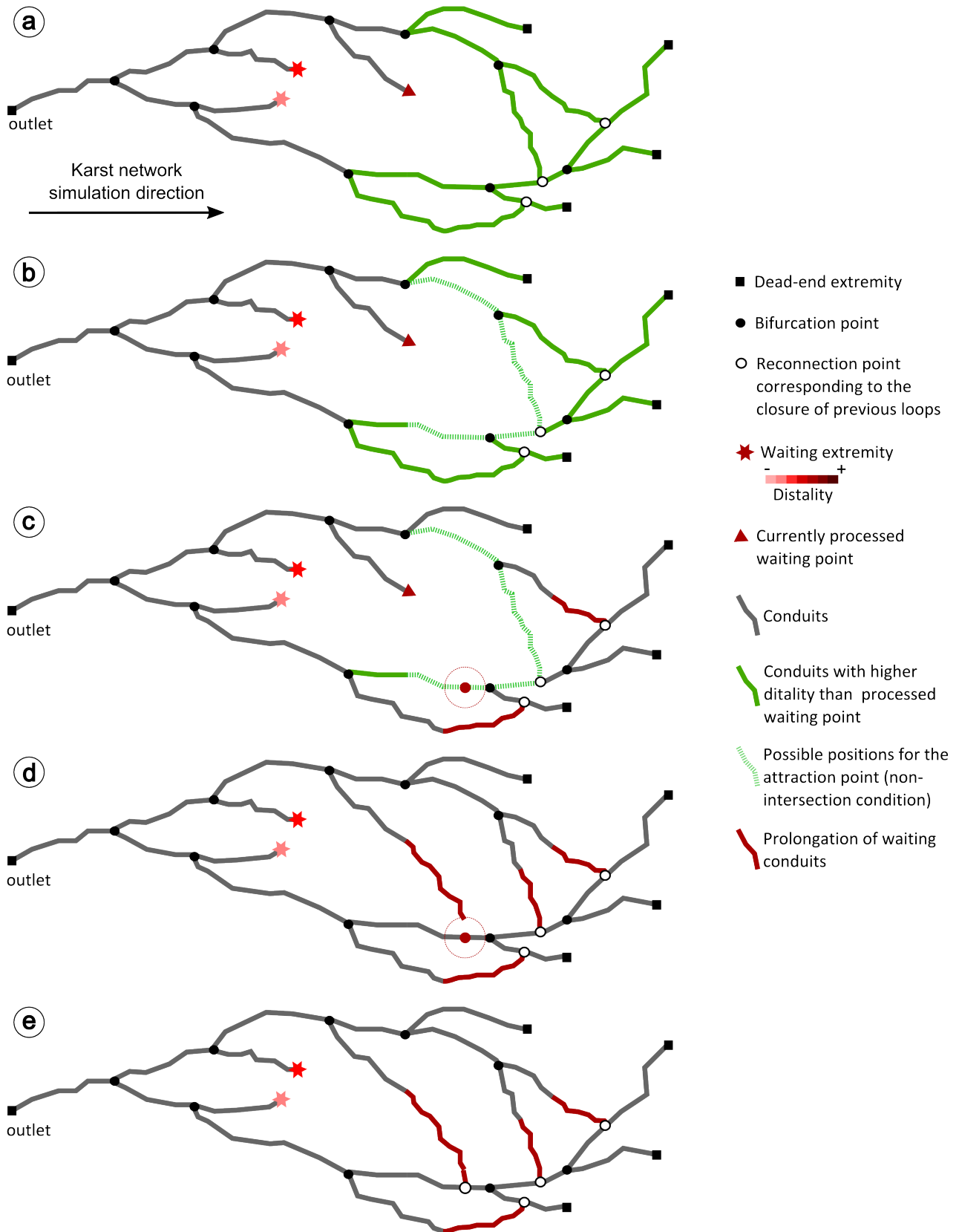


Figure 5: *Loop building. a: Selection of conduits of higher distality than currently processed waiting point. b: Selection of conduits that fulfil the simplified non-intersection condition. c: Random placement of the attraction point A. d: Growth of the processed conduit with hard data conditioning to point A until the conduit reaches the area of conditioning. e: Loop closure.*



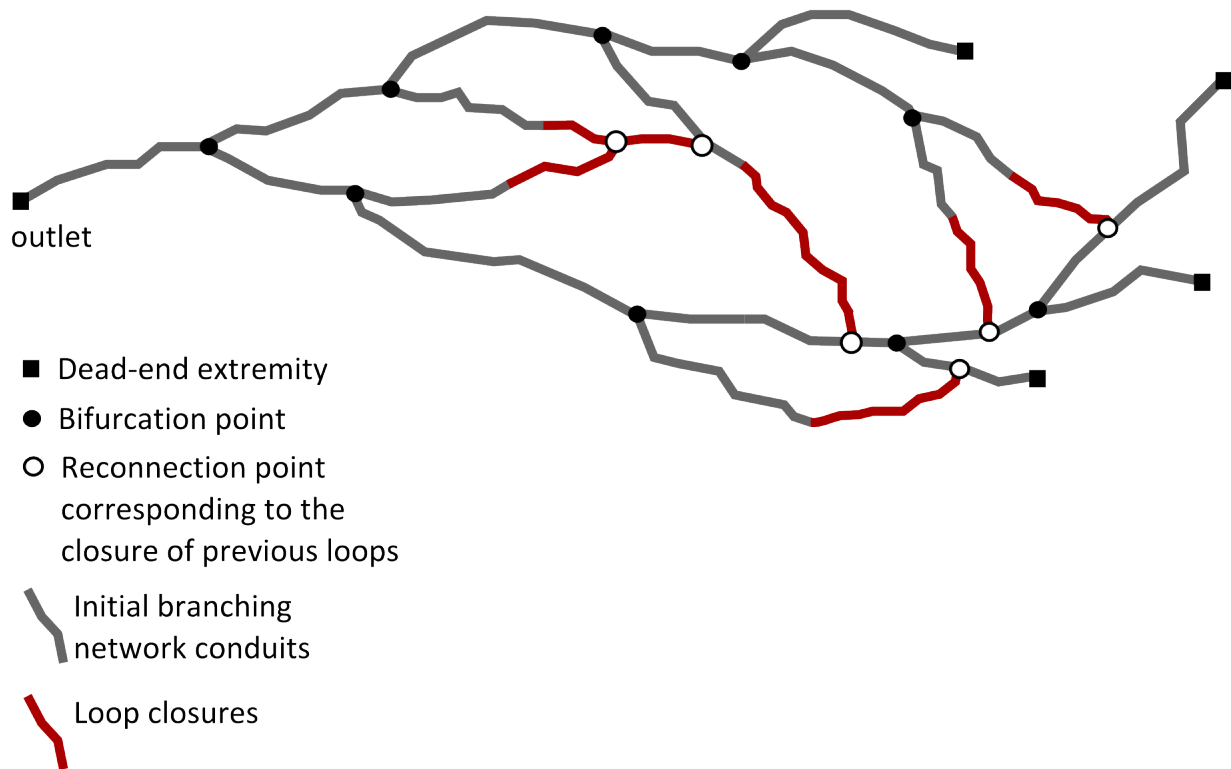


Figure 6: *Final karst network simulation with loops.*

length  $l_s$  (Figure 5c). A last segment is then traced between the extremity of the attracted conduit and point A by replacing the module  $T$  by a module  $M$  (Table 3), leading to the closure of the loop (Figure 5d).

When all the waiting conduits are treated, both parameters  $t$  and  $w$  are equal to 0. The simulation of the karst network is thus ended. The result is a karst network that can mix both branchwork and anastomotic patterns (Figure 6).

### 3 Results and discussion

Even if the method presented above is still at an early stage, interesting results can be shown (Figure 7). Several morphologies of karst networks have been generated. The simulated patterns stretch from pure branchwork karst networks (Figure 7a) to pure anastomotic networks (Figure 7c), with all the combinations between these two extreme poles (Figure 7, b1 and b2), as often encountered in nature [Jaquet et al., 2004].

Nevertheless, several problems appear and need improvements to be solved. In some simulations undesirable intersections between conduits are observable. Indeed, in the current state nothing prevent one conduit from growing towards another one, in particular during the first step of branchwork karst generation. Angles between conduit segments are determined by a combination of the global direction of karst simulation, a random draw in the angle distribution given by the user and the attraction given by the vector in case of loop closure. Thus, the global direction of karst simulation does not favour crossing avoidance, as two conduits starting at the same bifurcation point will grow in the same direction without going away from each others. If it is desirable in the case of anastomoses, it generates overlapping shapes when pure branchwork patterns are wanted (Figure 8). Several solutions are currently worth considering: i) The global direction could be set perpendicular to its initial configuration just after a bifurcation, and then changed back to its initial state. ii) A repulsion constraint could be attached to existing conduits.

A second track of improvement obviously appears in the simulation parametrisation. Indeed, the

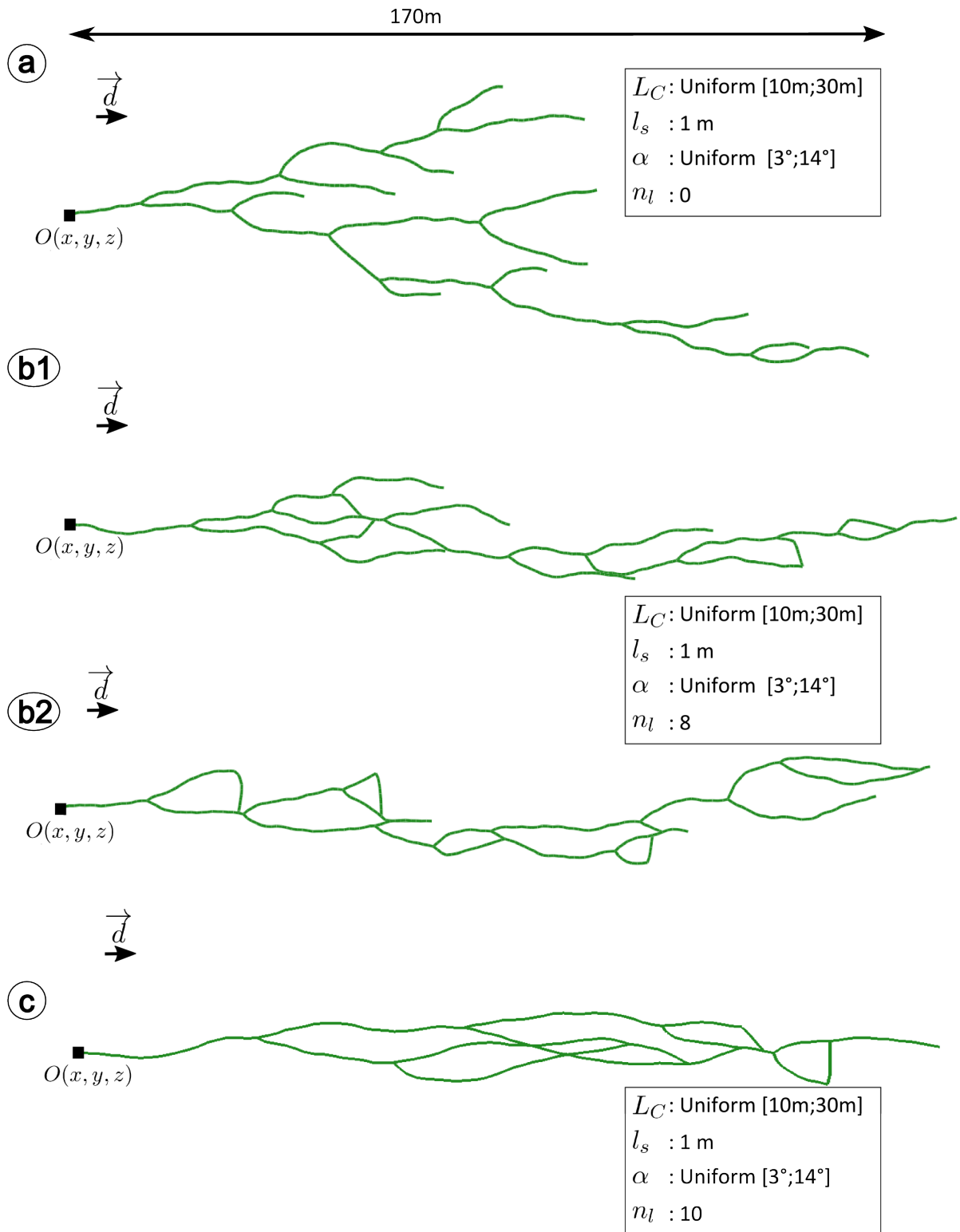


Figure 7: Four examples of simulated networks. All the morphologies can be obtained from pure branchwork pattern network (a) to pure anastomotic pattern network (c) going through karst network composed of a combination of the two patterns (b1 and b2).

maximal number of loops  $n_l$  alone is insufficient to clearly control the topology of the network. It would be appreciable to impose at least the total number of conduits in order to have something close to a ratio between the number of conduits and the number of loops. Howard's parameters [Howard,

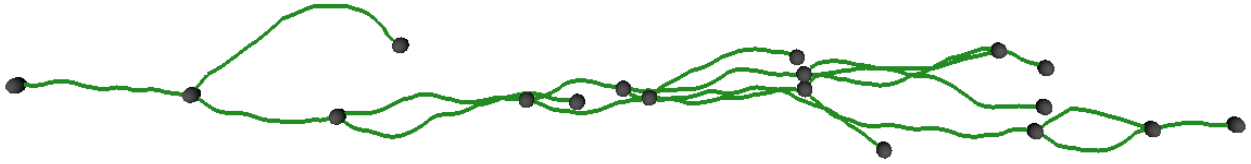


Figure 8: *Karst network simulation showing uncontrollable intersections and overlappings. The grey spheres are located where the reconnections between conduits are controlled, and every conduits crossings without a sphere are uncontrolled. This uncontrollability leads sometimes to networks with bad shapes and geologic unlikelihood.*

1971] could also be used to control the global connectivity of the network [Vigouroux et al., 2010].

Finally, hard data and soft data conditioning should be incorporated in the simulator. Rongier et al. [2014b] have already integrated it in the generation of channel axis using L-systems. An adaptation is required for hard data, with a step to determine what conduit must condition a given data.

## Conclusion and perspectives

This paper presents a new object-based method to simulate karst networks using L-system. The flexibility of this formalism gives the possibility to stochastically generate karst networks composed of a mix of branchwork and anastomotic patterns.

The methodology is based on the definition of a L-system that simulates the stochastic growth of branchwork conduits and on a second step of growing that uses attraction points to constrain conduits to form anastomoses. Encouraging realisations of karst networks have been obtained, going from pure branchwork patterns to pure anastomotic ones. But this work is still at an early stage and some realisations show involuntary intersections between two or more conduits. Several solutions are proposed to solve this problem and would be implemented in the near future. Improving the parametrisation of the simulation and integrating hard and soft data conditioning are also short term perspectives. The simulation of karst networks can be completed by the three dimensions modelling of conduit envelopes using ODSIM (Object-Distance Simulation method) [Henrion et al., 2010, Rongier et al., 2014a].

In a long-term view, it would be interesting to adapt the L-system rules in order to simulate various patterns in a single karst network depending on the geological settings. Indeed, although the developed method is currently an object-based method, the flexibility of the L-system formalism leaves scope for the integration of a genetic dimension in the development of karst networks.

## Acknowledgements

This work was performed in the frame of the RING project at Université de Lorraine. We would like to thank the industrial and academic sponsors of the Gocad Research Consortium managed by ASGA for their support. We also thank Paradigm for providing the SKUA-GOCAD software and API.

## References

- C. Barthélemy and P. Collon-Drouaillet. Simulation of anastomotic karst networks. In *Proc. 33rd Gocad Meeting, Nancy, France*, 2013.
- S. Bauer, R. Liedl, and M. Sauter. Modelling of karst development considering conduit-matrix exchange flow. *IAHS PUBLICATION*, pages 10–15, 2000.

- A. Borghi, P. Renard, and S. Jenni. A pseudo-genetic stochastic model to generate karstic networks. *Journal of Hydrology*, 414:516–529, 2012.
- P. Collon-Drouaillet, V. Henrion, and J. Pellerin. An algorithm for 3d simulation of branchwork karst networks using horton parameters and A\* application to a synthetic case. *Geological Society, London, Special Publications*, 370(1):295–306, 2012.
- V. Henrion, G. Caumon, and N. Cherpeau. Odsim: an object-distance simulation method for conditioning complex natural structures. *Mathematical Geosciences*, 42(8):911–924, 2010.
- A. D. Howard. Quantitative mesures of caves patterns. *Caves and Karst*, 13:7, 1971.
- O. Jaquet, P. Siegel, G. Klubertanz, and H. Benabderrhamane. Stochastic discrete model of karstic networks. *Advances in Water Resources*, 27(7):751–760, July 2004. ISSN 03091708. doi: 10.1016/j.advwatres.2004.03.007.
- G. Kaufmann and J. Braun. Karst aquifer evolution in fractured, porous rocks. *Water Resources Research*, 36(6):1381–1391, 2000. ISSN 1944-7973. doi: 10.1029/1999WR900356.
- A. Lindenmayer. Mathematical models for cellular interactions in development i. filaments with one-sided inputs. *Journal of Theoretical Biology*, 18(3):280–299, Mar. 1968. ISSN 00225193. doi: 10.1016/0022-5193(68)90079-9.
- A. Lindenmayer. An introduction to parallel map generating systems. In *Graph-grammars and their application to computer science*, pages 27–40. Springer, 1987.
- A. Nakamura, A. Lindenmayer, and K. Aizawa. Some systems for map generation. In *The Book of L*, pages 323–332. Springer, 1986.
- A. N. Palmer. Speleogenesis in carbonate rocks. *Evolution of karst: from prekarst to cessation. Postojna-Ljubljana: Založba ZRC*, pages 43–60, 2002.
- E. Pardo-Igúzquiza, P. A. Dowd, C. Xu, and J. J. Durán-Valsero. Stochastic simulation of karst conduit networks. *Advances in Water Resources*, 35:141–150, 2012.
- P. Prezmyslaw and A. Lindenmayer. The algorithmic beauty of plants, 1996.
- G. Rongier, P. Collon-Drouaillet, and M. Filipponi. Simulation of 3d karst conduits with an object-distance based method integrating geological knowledge. *Geomorphology*, 217:152–164, 2014a.
- G. Rongier, P. Collon-Drouaillet, and P. Renard. Channel axis simulation based on Lindenmayer systems. In *Proc. 34th Gocad Meeting, Nancy, France*, pages 1–27, 2014b.
- J. Siemers and W. Dreybrodt. Early development of karst aquifers on percolation networks of fractures in limestone. *Water resources research*, 34(3):409–419, 1998.
- R. Vigouroux, P. Collon-Drouaillet, and V. Henrion. New parameters for the characterization of karst geometry. In *Proceedings of th 30th Gocad Meeting, Nancy, France*, 2010.
- H. Zeng, R. Loucks, X. Janson, G. Wang, Y. Xia, B. Yuan, and L. Xu. Three-dimensional seismic geomorphology and analysis of the ordovician paleokarst drainage system in the central tabei uplift, northern tarim basin, western china. *AAPG bulletin*, 95(12):2061–2083, 2011.

## Appendix A L-system definition

Symbols	Parameters
<b>Input parameters for karst network simulation</b>	
$N$	Number of simulations
$O(x, y, z)$	Coordinates of the karst outlet
$\vec{d}$	Global orientation of karstic network (from outlet to inlets)
$L_C$	Conduit lengths (probability distribution)
$l_s$	Elementary segment length
$\alpha$	Angles between elementary segments (probability distribution)
$n_l$	Maximal number of loops
<b>Global <i>internal</i> parameters</b>	
$n$	the number of conduits that are finished, in progress or waiting
$w$	the number of waiting conduits
$t$	the number of in progress conduits
$a$	the number of loops (anastomoses) already simulated in the karst network
<b>Variables depending on the conduit being proceeded</b>	
$i$	the index of the conduit being proceeded
$l_{Ci}$	the current length of conduit $i$
$L_{Ci}$	the conduit length to reach for stopping its growth
$e_i$	kind of conduit extremity for the conduit $i$ (bifurcation or dead-end passage)

Global parameters values at the beginning:  $n = 1, w = 0, t = 1, a = 0$

Symbols	Geometrical interpretation
$C$	Move forward of a length $l_s$ , draw a segment
$T$	Do nothing (represents an on-going conduit extremity)
$D$	Do nothing (represents a dead-end passage extremity)
$W$	Do nothing (represents a waiting conduit extremity)
$M$	Draw a segment between the previous position and the attraction point (to close loop)
$+$	Turn left by an angle $\alpha$ around the vector $\vec{U}$
$-$	Turn right by an angle $\alpha$ around the vector $\vec{U}$
$[$	Start a new conduit and save the position and state of the turtle
$]$	End the conduit and replace the turtle in the latest saved position

Axiom:  $\omega$  :  $T(1, 0, L, 1)$

Production rules:

$$\begin{aligned}
 p_1 & : T(i, l_{C_i}, L_{C_i}, e_i) : l_{C_i} < L_{C_i}, t = 1 \xrightarrow{0.5} \{+C\}(i, l_{C_i} + l_s, L_{C_i}, \text{rand}(\alpha))T(i, l_{C_i}, L_{C_i}, e_i) \\
 p_2 & : T(i, l_{C_i}, L_{C_i}, e_i) : l_{C_i} < L_{C_i}, t = 1 \xrightarrow{0.5} \{-C\}(i, l_{C_i} + l_s, L_{C_i}, \text{rand}(\alpha))T(i, l_{C_i}, L_{C_i}, e_i) \\
 p_3 & : T(i, l_{C_i}, L_{C_i}, e_i) : l_{C_i} \geq L_{C_i}, e_i \leq E \longrightarrow D \\
 p_4 & : T(i, l_{C_i}, L_{C_i}, e_i) : l_{C_i} \geq L_{C_i}, e_i > E \longrightarrow -[\{-C\}(i, l_s, L_{C_{n+1}} = \text{rand}(L_C), \text{rand}[0, 60]) \\
 & \qquad \qquad \qquad T(n + 1, 0, L_{C_{n+1}}, \text{rand}[0, 1])] \\
 & \qquad \qquad \qquad +[\{+C\}(i, l_s, L_{C_{n+2}} = \text{rand}(L_C), \text{rand}[0, 60]) \\
 & \qquad \qquad \qquad T(n + 2, 0, L_{C_{n+2}}, \text{rand}[0, 1])] \\
 p_5 & : T(i, l_{C_i}, L_{C_i}, e_i) : l_{C_i} < L_{C_i}, t > 1 \xrightarrow{0.48} \{+C\}(i, l_{C_i} + l_s, L_{C_i}, \text{rand}(\alpha))T(i, l_{C_i}, L_{C_i}, e_i) \\
 p_6 & : T(i, l_{C_i}, L_{C_i}, e_i) : l_{C_i} < L_{C_i}, t > 1 \xrightarrow{0.48} \{-C\}(i, l_{C_i} + l_s, L_{C_i}, \text{rand}(\alpha))T(i, l_{C_i}, L_{C_i}, e_i) \\
 p_7 & : T(i, l_{C_i}, L_{C_i}, e_i) : l_{C_i} < L_{C_i}, t > 1 \xrightarrow{0.04} W(i, l_{C_i}, L_{C_i}, 0)
 \end{aligned}$$

with  $E$  defined as follows:

$$E = \begin{cases} 1 - \exp\left(-\frac{w}{n_l}(t-1)\right) & \text{if } n_l > 1 \\ 1 - \exp\left(-(t-1)\right) & \text{otherwise} \end{cases}$$

End conditions:  $t = 0, w = 0$



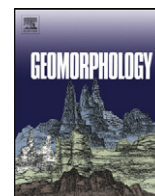
## Appendix E

# Karst conduit simulation with e-ODSIM

**Context** The following article published in *Geomorphology* comes from the master work done under the supervision of Pauline Collon. The article itself was published during the thesis work. The project purpose was to stochastically simulate three-dimensional karst conduits. This method completes the network simulation method defined in the previous appendix, by simulating a conduit envelope around the network.

G. Rongier, P. Collon, M. Filipponi (2014) *Simulation of 3D karst conduits with an object-distance based method integrating geological knowledge*, *Geomorphology* 217, 152–164, DOI: [10.1016/j.geomorph.2014.04.024](https://doi.org/10.1016/j.geomorph.2014.04.024)





# Simulation of 3D karst conduits with an object-distance based method integrating geological knowledge



Guillaume Rongier <sup>a,\*</sup>, Pauline Collon-Drouaillet <sup>a</sup>, Marco Filipponi <sup>b</sup>

<sup>a</sup> GeoRessources UMR7359, Université de Lorraine, CNRS, CREGU, ENSG, 2 Rue du Doyen Marcel Roubault, TSA 70605, 54518 Vandœuvre-Lès-Nancy Cedex, France

<sup>b</sup> Bauen im Karst, Alte Spinnerei, CH-8877 Murg, Switzerland

## ARTICLE INFO

### Article history:

Received 4 July 2013

Received in revised form 2 April 2014

Accepted 22 April 2014

Available online 2 May 2014

### Keywords:

Karst conduit

Shape

Stochastic simulation

Skeleton

Inception feature

## ABSTRACT

Karst conduit shapes have a high influence on fluid flows. As these underground hidden systems are partially inaccessible, their stochastic simulation is an essential tool to assess the uncertainties related to these highly exploited water resources. The object-distance simulation method (ODSIM) is a hybrid dual-scale approach that has been recently proposed to model geological underground structures due to late processes such as dolomitized rocks, mineralized veins or karsts. Using a perturbed Euclidean distance field around a curve representing roughly the conduit centre and called a skeleton, the resulting shapes are globally cylindrical-like 3D envelopes. But at a drain scale, karstic conduits are elongated along weakness planes such as lithostratigraphic horizons, bedding planes, fractures or faults. In addition to those planes the influence of the water table is added. This work presents different improvements of ODSIM methodology for simulating more realistic shapes in the particular case of karst. Firstly, we propose using a custom distance field computed with a fast marching method. Considering the “velocity” field to be proportional to the permeability allows the resulting features to be elongated along the weakness planes. Secondly, to handle specific shapes due to the proximity of the water table, such as trenches or notches, we impose areas of higher velocity between the skeleton and the water table. Finally, we generate a custom random threshold with several variograms and/or distributions depending on the different features integrated in the “velocity” field. Applied on different models, it is shown that the resulting karst conduits have more realistic shapes than those obtained with the previous workflow, while the variability of structures which can be modelled with ODSIM is preserved.

© 2014 Elsevier B.V. All rights reserved.

## 1. Introduction

Karstic systems are underground hydrographic networks made of conduits and caves that have grown by dissolution of the surrounding rocks. They cover approximately 20% of the planet's dry ice-free land (e.g., Ford & Williams, 2007; De Waele et al., 2009) and are therefore important fluid reservoirs, providing water for probably 20 to 25% of the world's population (Ford & Williams, 2007). Development of caves is also responsible for substantial human and financial disasters by causing sinkholes in urbanized zones. These karst features can be dramatic as the surface land usually stays intact until there is insufficient support: the soil suddenly collapses, swallowing everything above (e.g., Brinkmann et al., 2008; Frumkin et al., 2009; Parise et al., 2009). Recent works have shown that karsts may also be a major source of paleoclimate records (e.g., Mongelli, 2002; Horvatinčić et al., 2003; Onac & Constantin, 2008; Kuo et al., 2011). Nowadays human activities are a major threat for karstic environments (e.g., De Waele et al., 2011),

and furthermore climate changes may have a considerable impact on them in the future (e.g., Viles, 2003; Hartmann et al., 2012).

Despite the importance of karstic networks, their location and exact geometry remain poorly known, mainly due to the partial inaccessibility of these underground systems. These networks actually play a major role in the flow regime of most carbonate aquifers and reservoirs (e.g., Lü et al., 2008; Chaojun et al., 2010): their conduits act as preferential flow paths and concentrate the fluids. As conduit shapes result from a complex dissolution process (e.g., Ford & Williams, 2007), a straightforward modelling approach of fluid flows would represent karstic conduits as equivalent to cylindrical tubes. This approach does not take into account the shape variations like abrupt narrowings or enlargements which also greatly impact fluid flows (e.g., Field & Pinsky, 2000; Hauns et al., 2001; Goldscheider, 2008; Morales et al., 2010). Thus, knowing and modelling the shapes of these three-dimensional geological objects could be an important improvement for both water and oil and gas reservoir exploitation. The goal of this paper is to propose a tool to realize such three-dimensional modelling of karstic systems.

Two different contexts of application are examined. First, as large parts of cave systems are still unexplored, three-dimensional stochastic simulations offer a way to better assess the associated uncertainty. However, the current methods focus on the global architecture of the conduit networks (e.g., Borghi et al., 2012; Collon-Drouaillet et al.,

\* Université de Lorraine - ENSG, 2 Rue du Doyen Marcel Roubault, TSA 70605, 54518 Vandœuvre-Lès-Nancy Cedex, France.

E-mail addresses: [guillaume.rongier@gocad.org](mailto:guillaume.rongier@gocad.org) (G. Rongier),

[pauline.collon@univ-lorraine.fr](mailto:pauline.collon@univ-lorraine.fr) (P. Collon-Drouaillet),

[marco.filipponi@bauen-im-karst.info](mailto:marco.filipponi@bauen-im-karst.info) (M. Filipponi).

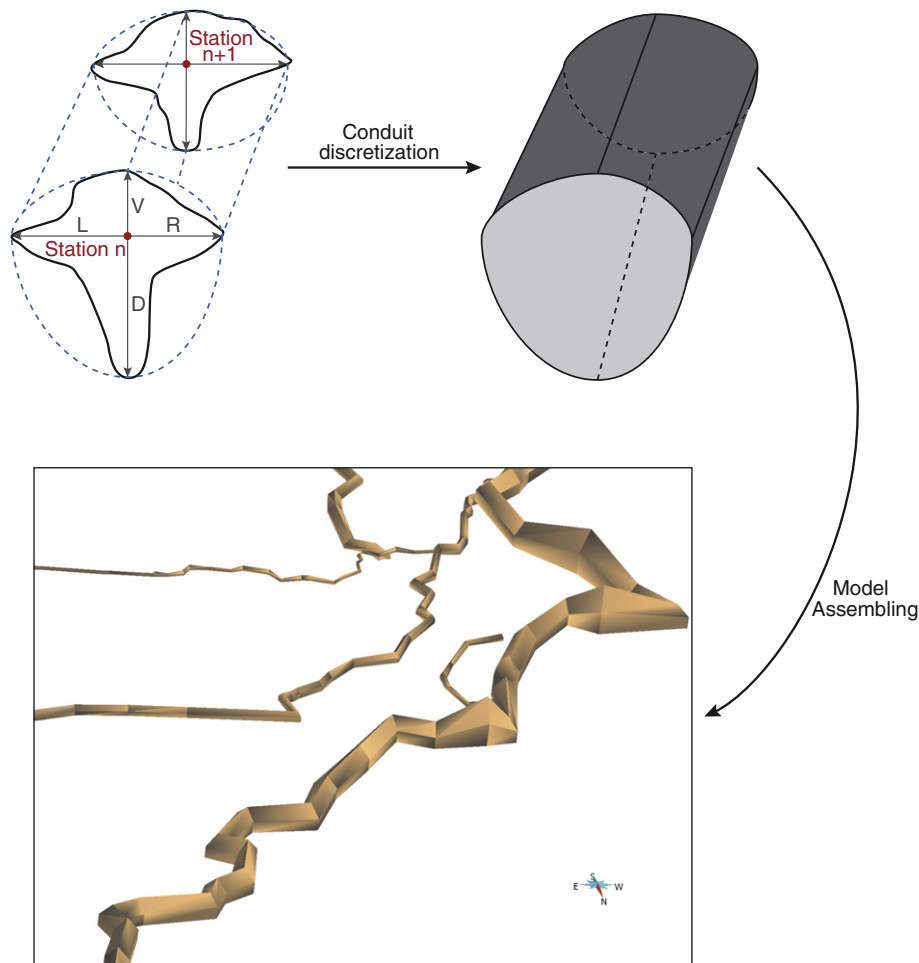


**Fig. 1.** Classical conduit discretization process and 3D “reconstruction” used in common speleological programs (here with GHTopo).

2012; Pardo-Igúzquiza et al., 2012). They stochastically generate several possible skeletons representing roughly the conduit centre and highlighting the uncertainties related to the conduit location. The proposed methodology is complementary to those works by providing volumetric information around those skeletons consistent with local geological settings, highlighting the uncertainties related to the conduit size and shape. Second, it provides a solution to reconstruct the three-dimensional geometry of explored and monitored cave systems. Indeed, new technologies like LiDAR have permitted precise mapping of cave conduits (e.g., Jaillet et al., 2011). But this type of acquisition is time consuming, needs specific equipment and requires a post-treatment of huge amounts of data. It is thus far more adapted to explore and model karst at the drain scale. For larger scales, there are two categories of data: i) two-dimensional maps (plan and/or profile views) which result of a projection of a three-dimensional network on a two-dimensional plane – this is the oldest and most common type of data; ii) three-dimensional information provided by “modern” cave survey. In the latter case, the underground topographic information is given by a sequence of topographic stations, located in order to fit exploration requirements: access easiness, clear sight along the cave passages, etc. At each station only distances to walls are recovered left, right, up and down (LRUD). The numerical treatment of these data leads to a discretization that represents the conduits with elliptical or rectangular section shapes (Fig. 1). Dealing with both categories of data, the 3D reconstruction remains a problem that is currently solved in common speleological programs with a linear interpolation between the various

two-dimensional sections leading to more or less realistic shapes (e.g., Survex,<sup>1</sup> VisualTopo<sup>2</sup> or GHTopo<sup>3</sup>).

In both contexts, few works have been conducted on modelling more realistic 3D karstic conduit shapes (e.g., Labourdette et al., 2007; Henrion et al., 2010; Boggus & Crawfis, 2009). The object-distance simulation method (ODSIM) proposed by (Henrion et al., 2010) generates an envelope along a curve skeleton whose shape is irregular at fine scale but globally cylindrical at the first order. To integrate a geological constraint on the shape, e.g., for the development of hydrothermal dolomites around fractures, they use plane skeletons instead of curves. But the resulting envelope retains a round aspect at the plane extremities. Contrary to geometries generated with this simple approach, karstic shapes are more elongated along given inception features (e.g., Jameson, 1985; Filipponi, 2009) that favour karst conduit development. Thus, depending on the local geological context, the cross-section geometry of karstic conduits varies from circle to lens or “keyhole” (Section 2). These particular shapes are not reproduced by ODSIM (Section 3). In this paper, we propose a new methodology to integrate various geological features influencing conduit shapes by using a custom distance field generated with a fast marching method instead of a Euclidean distance field (Section 4). This involves the creation of a

<sup>1</sup> <http://survex.com/>.

<sup>2</sup> <http://vtopo.free.fr/>.

<sup>3</sup> <http://siliconcavings.chez-alice.fr/>.

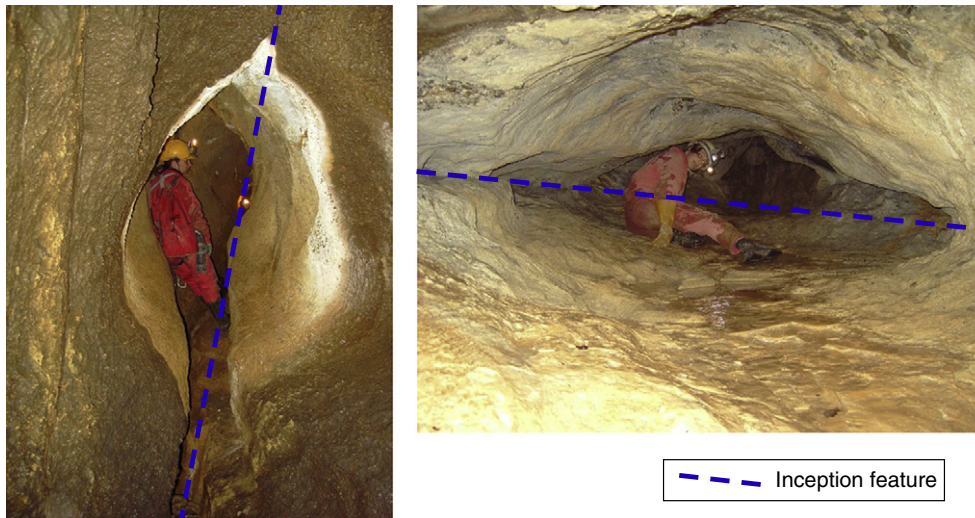


Fig. 2. Examples of karstic conduits showing shapes strongly elongated along inception features (left: Cave O80, Switzerland; right: Grottes aux fées, Switzerland).

“velocity” field that controls the front propagation of the fast marching method (Section 4). This new methodology allows us to simulate specific shapes that are realistic and consistent with geological settings and speleological knowledge of the system (Section 5).

## 2. Geomorphological analysis of the karstic conduits

Because karsts result from fluid circulation and dissolution capacity, the vulnerability to dissolution of the surrounding rocks plays a major role in their genesis. More particularly, karstic networks tend to develop along weakness features – either lithostratigraphic inception features, such as beds or bedding planes, or tectonic inception features, such as fractures or faults (e.g., Jameson, 1985; Lowe, 1992; Faulkner, 2006; Filipponi, 2009). These features are characterized by a strong contrast with the surrounding formations in terms of physical, lithological and/or chemical properties, such as the permeability. This contrast has a major influence on karst genesis (Filipponi, 2009; Filipponi et al., 2010): the inception features favour primary fluid circulations because of it and, thus, primary rock dissolution.

The dissolution process and the path development are not uniform in space due to the three-dimensional nature of the genesis processes and the geometrical anisotropy of the inception features. These features favour a differential dissolution, leading to an elongation of the conduits along them – often with pronounced angles – and explaining their non-cylindrical appearance in cross-section (Fig. 2). The resulting shapes are consequently more or less elliptical depending, for instance, on the dissolution capacity of the fluids or on the contrast in permeability or in carbonate content between the inception feature and the surrounding formations (Filipponi, 2009).

According to various authors, the groundwater table has a major influence on conduit development (e.g., Jameson, 1985; Ford & Williams, 2007; Farrant & Smart, 2011; Jaillet et al., 2011). In the phreatic zone, corresponding to the saturated zone below the water table, the inception features are the most influential factor upon the resulting shapes (Filipponi et al., 2009). The dissolution acts on whole conduits and in all directions. The shapes are then more or less jagged, depending on the fluids, on the surrounding rocks and on the presence of other inception features (Figs. 2, 4.1) (e.g., Jameson, 1985; Lauritzen & Lundberg, 2000; Filipponi, 2009). The vadose zone corresponds to the zone above the current water table. But the observed conduits are usually the result of a long process that has involved a past phreatic development. Keyhole passages are among the most common cross-sectional

conduit geometries that are encountered (Field, 2002). They are characterized by an entrenchment, a canyon passage commonly narrower than the original passage, also called the trench. Indeed, a drop of the water table puts the original conduits in phreatic conditions. The fluids circulating in the conduits with high velocities are led by gravity, incising the floor, generating these typical cross-sectional keyhole shapes (Figs. 3, 4.2) (e.g., Jameson, 1985; Lauritzen & Lundberg, 2000; Filipponi, 2009; Jaillet et al., 2011). Horizontal dissolution notches are less common. They develop at the water table interface when conduits are partially flooded and water level variations are small enough to favour a lateral incision (e.g., Lauritzen & Lundberg, 2000; Ford & Williams, 2007; Farrant & Smart, 2011). Geometrically speaking, notches have a rounder aspect than shapes linked to inception features (Fig. 4.3).

In the following, we explain how these different observed geometries can be integrated in the ODSIM method to improve the realism of simulated karst conduits.

## 3. Principle of the object-distance simulation method

Henrion et al. (2010) proposed an object-distance simulation method (ODSIM) that models a three-dimensional envelope around a



Fig. 3. Example of a keyhole passage (Sieben Hengste Cave System, Switzerland).

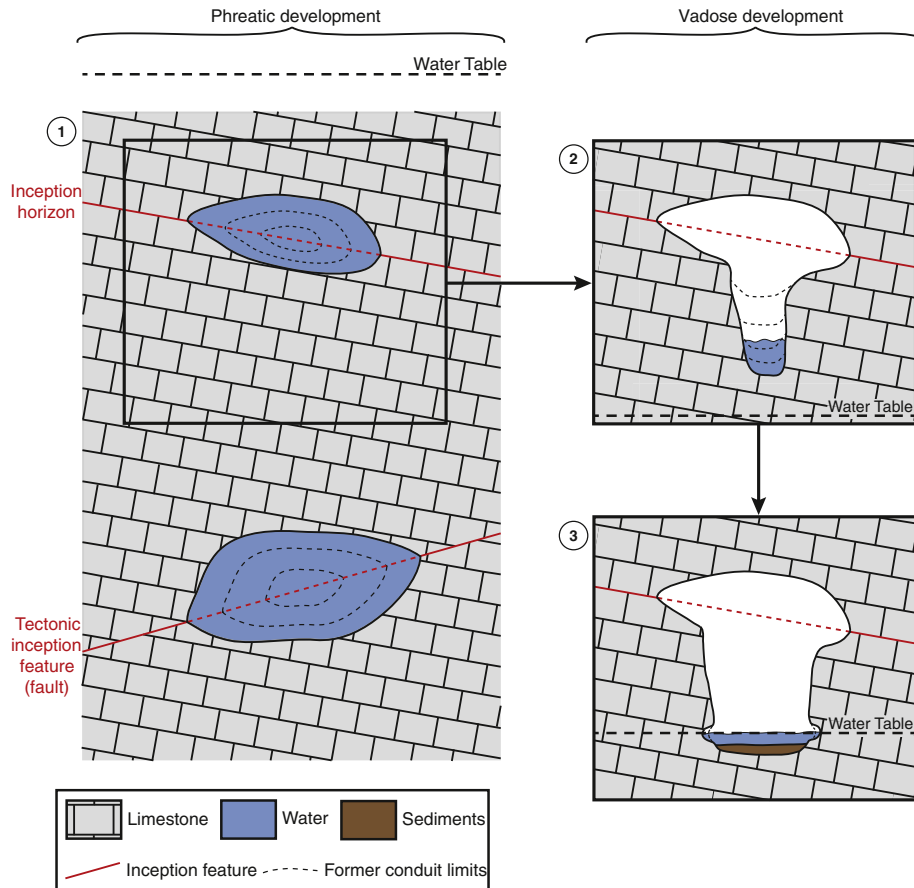


**Fig. 4.** Evolution of a karstic conduit depending on its position relative to the water table: 1. Genesis and growth of two conduits in the phreatic zone following different weakness planes (a lithostratigraphic horizon for the upper one, a fault for the other). 2. Following a fall of the water table, the upper conduit goes through the vadose zone which progressively generates a keyhole passage by cutting a trench. 3. Following a rise of the water table, notches grow at the trench bottom.

skeleton. For the explored parts of a karst, that skeleton can be provided by field data, such as two-dimensional maps or LRUD (Left, Right, Up and Down) data. Otherwise, stochastic simulations can be used to obtain several skeletons and take into account the uncertainties related to the conduit location (e.g., Pardo-Igúzquiza et al., 2011; Borghi et al., 2012; Collon-Drouaillet et al., 2012). The ODSIM method consists of computing a Euclidean distance field around the skeleton and perturbing it using a random threshold (Fig. 5). This threshold can be generated using a sequential Gaussian simulation (SGS) or other stochastic simulation methods (e.g., Deutsch & Journel, 1997; Goovaerts, 1997). As a stochastic simulation method, the SGS can provide an infinity of thresholds. This allows us to build several envelopes for a given skeleton, thus catching the uncertainties around the conduit shape. The perturbation is done using the following indicator function:

$$I_B(p) = \begin{cases} 1 & \text{if } D(p) \leq \varphi(p) \\ 0 & \text{else} \end{cases} \quad (1)$$

$D(p)$  is the 3D distance field computed at each point  $p = [p_x p_y p_z]^T$  of a grid  $G$  and  $\varphi(p)$  is the random threshold. The computed indicator property  $I_B(p)$  is equal to 1 in the geological body, 0 outside. The 3D envelope corresponds to the surface at the interface between the interior and the exterior of the region corresponding to 1, or equivalently to points at a given distance of the network:  $D(p) \leq \varphi(p)$ . In this method, the simulated conduits can be complied with hard data conditioning (like well data or LRUD distances to walls) thanks to an iterative Gibbs sampling algorithm (Geman & Geman, 1984) with inequality constraints (Freulon & de Fouquet, 1993).

With this approach, the only way to avoid a globally cylindrical shape is to use plane skeletons instead of curves. However, the resulting envelope keeps a round aspect at the plane extremities because of the Euclidean distance. Furthermore this approach lacks flexibility when dealing with various and complex shapes, such as those seen in Section 2.

#### 4. Integration of geomorphological information in ODSIM

The proposed methodology keeps the basic principle of ODSIM: the “distance” to an object model controls the first-order features while a random field provides the fine-scale features (Henrion et al., 2010). Our proposal is to play on these two scales. First, by using a custom distance field generated by a fast marching method and constrained to geomorphological information. This allows us to take into account simultaneously various elements involved in the conduit genesis and so influencing the conduit shapes. Second, we propose to build a random threshold by combining different variograms and/or distributions depending on the elements constraining the custom distance field (Fig. 6).

##### 4.1. Using of a custom distance field instead of an Euclidean distance field

The fast marching method (Sethian, 1996; Sethian, 1999a; Sethian, 1999b) concerns the propagation of a front knowing its speed. The principle is to solve the Eikonal equation:

$$|\nabla T| F = 1. \quad (2)$$

$T$  is the time field and  $F$  the velocity field.  $1/F$  gives a slowness field.

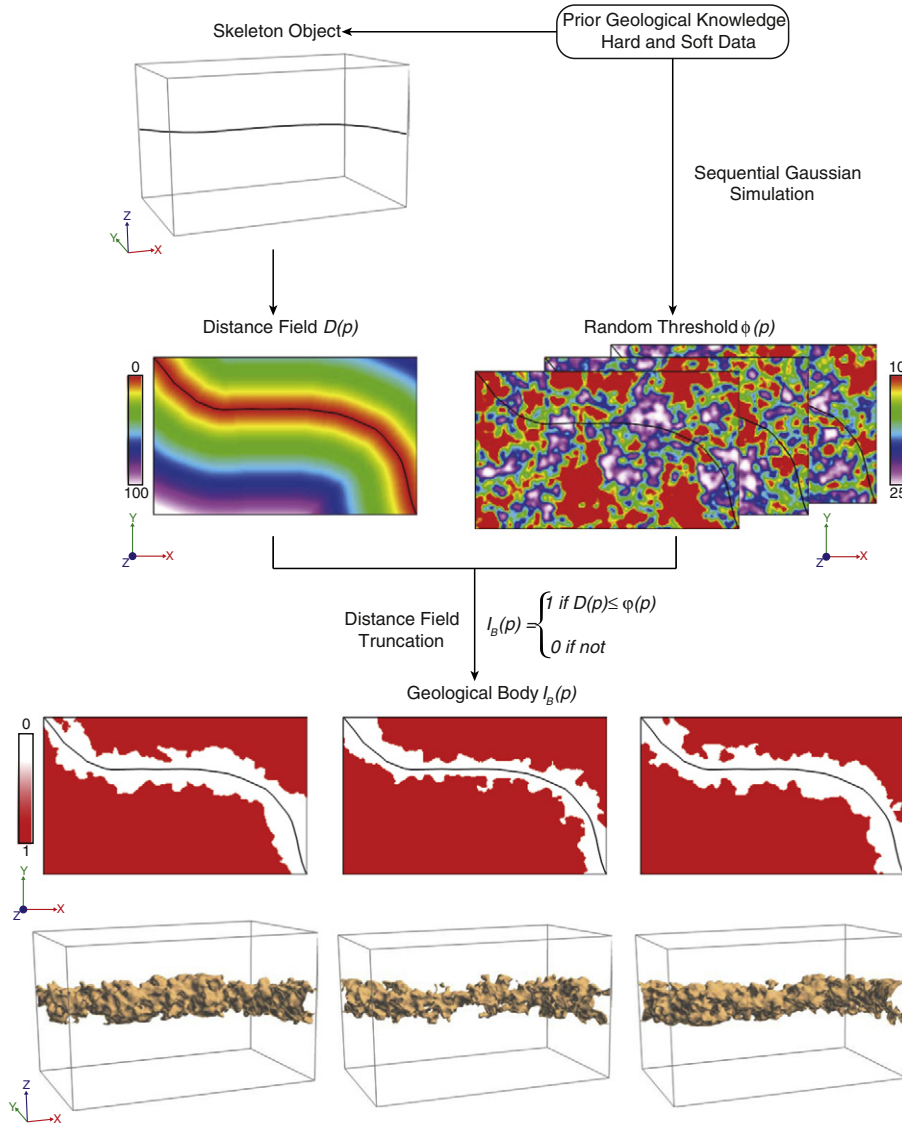


**Fig. 5.** ODSIM workflow (modified from Henrion et al. (2010)) applied to a karstic conduit generation. The distance field  $D(p)$  is truncated with the random threshold  $\varphi(p)$  giving an indicator property  $I_B(p)$  of the karstic conduits and caves.

This method creates a scalar field corresponding to the arrival time  $T(x, y, z)$  at which the propagation front reaches the position  $(x, y, z)$ , depending on a predetermined velocity field (or equivalently a slowness field) (Fig. 7). This velocity field characterizes the speed of the front for each position  $(x, y, z)$ .

In a modelling approach, a convenient aspect is that the choice of the velocity field constrains the evolution of the front and the resulting arrival time field. Putting higher values for inception features in the velocity field constrains the time field in such a way that it contains geomorphological information, providing the custom distance field (Fig. 7). Using a fast marching method gives thereby a greater flexibility to ODSIM. Nevertheless, the property used to compute the velocity field has to be thoughtfully chosen. As underlined by Borghi et al. (2012), contrasts between the values are more important than values themselves when using the fast marching method. The velocity field has to be linked with a property of the medium that respects this contrast rule.

As the notion of contrast controls both the fast marching and the karst genesis, the velocity field is built by using the permeability (or the hydraulic conductivity). This provides emphasis on the weakness planes, and moreover simplifies the choice of the property values.

However, it is not sufficient to model specific structures like those encountered in the vadose zone and specific strategies need to be developed.

#### 4.2. Building the velocity field for the vadose zone

Structures developed in vadose conditions are the result of several speleogenetic phases, corresponding to several water table positions. The goal of our method is not to reproduce each of these phases one after the other as a genetic model would do it. Instead, we propose numerical strategies to reproduce directly final conduit geometries consistent with the speleologist's observations and knowledge.

For reproducing the keyhole geometry, and more specifically the trenches appearing on the conduit floors, we propose to use an "attraction level" with high velocity values similar to those of the inception features. This attraction level may correspond to the present water table. A vertical plane between the skeleton and the attraction level is then considered as a high velocity zone by extending the attraction level values (Fig. 8). This modification constrains the front propagation which goes toward that level.

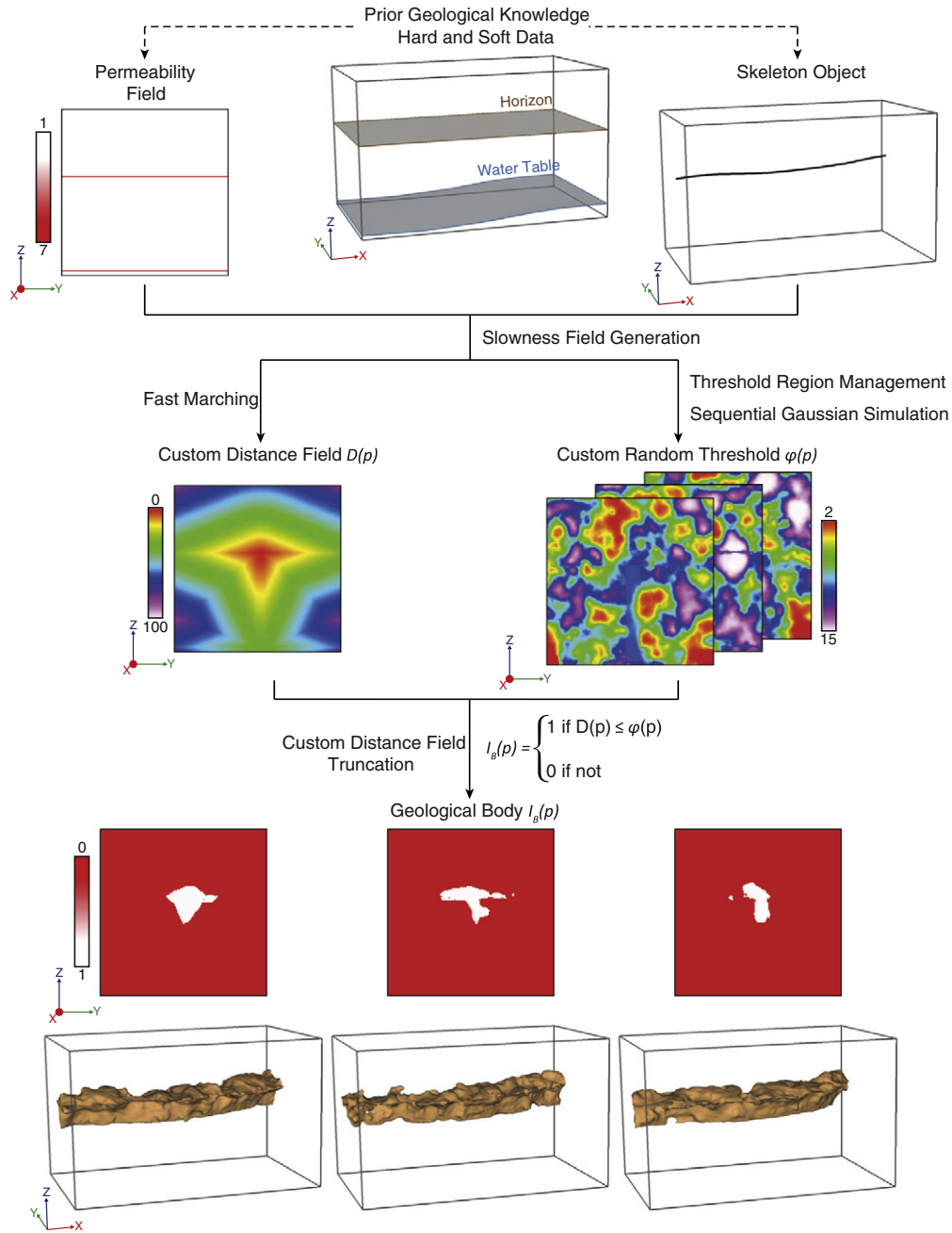


**Fig. 6.** New workflow for ODSIM. The original method is obtained by using a constant velocity or slowness field and the same parameters for the whole threshold. *Slowness field generation* and *fast marching* steps are further detailed in Sections 4.1 and 4.2; *threshold region management* step is detailed in Section 4.3.

To limit the effects of the attraction level on the highest conduits, a parameter representing the maximum allowed distance  $d_{max}$  between the skeleton and the attraction level is added to generate these trenches. Moreover, the distance between the skeleton and the attraction level  $d$  is used to obtain shorter depths for trenches as the conduits move away from the water table. To do that, the permeability values of the attraction level in the vertical plane building the trenches are multiplied by a factor integrating  $d/d_{max}$ , giving the vertical trench plane velocity values  $v$ :

$$v(x_s, y_s, z) = m \times \left( 1 - \frac{d(x_s, y_s, z)}{d_{max}} \right) \times p_w(x_s, y_s, z_w) \quad (3)$$

$(x_s, y_s, z_s)$  is a point of the skeleton,  $(x_w, y_w, z_w)$  is a point of the attraction level,  $z$  is bounded by  $z_s$  and  $z_w$ ,  $m$  is a multiplication factor defined by the user,  $d_{max}$  sizes the zone of influence of the attraction level,  $v$  is the velocity value of the vertical plane at a given point  $(x_s, y_s, z)$ ,  $d$  is the distance between the skeleton and the attraction level at the same horizontal coordinates  $(x_s, y_s)$  and  $p_w$  is the permeability value at the attraction level at the same horizontal coordinates  $(x_s, y_s)$ .

Using  $d$  causes trench depth to evolve smoothly with the distance between the skeleton and the attraction level and avoids sharp enrichment endings on the boundaries of the influence zone (Fig. 9).

If the difference between the velocity values of the attraction level and those of the surrounding formation is not significant, the

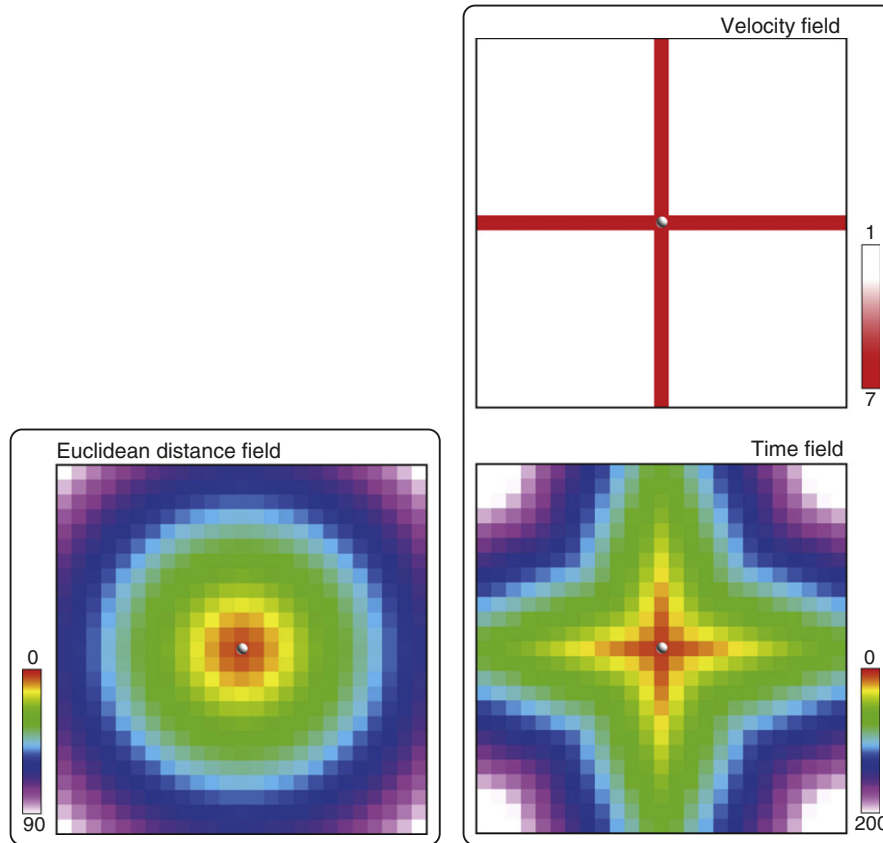


Fig. 7. Comparison between an Euclidean distance field and a field generated by fast marching. Both fields are generated from the central node of the grid, but the time field is constrained by the differences of speed given by the velocity field.

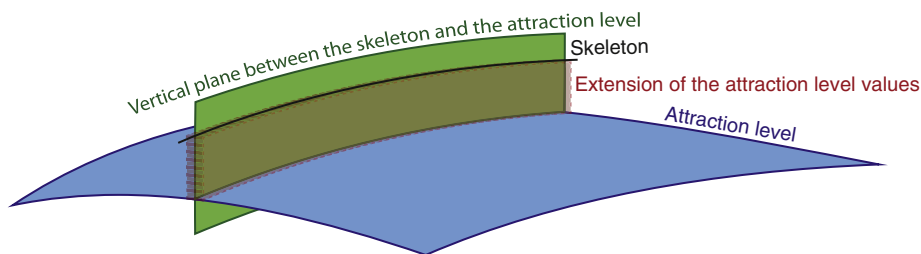


Fig. 8. Foundations for trench modelling: a vertical plane between the skeleton and the attraction level is considered. The values of the attraction level crossed by the plane are extended vertically up to the skeleton.

factor  $(1 - d/d_{max})$  can invert their contrast, leading to lower velocity values for the vertical plane and so a poor front propagation. The multiplication factor  $m$  solves this issue and gives the user a control on the trench depth.

With only one column of cells representing the vertical trench plane in the grid, the resulting trenches are V-shaped and do not show vertical sides or a flat bottom. Thus, several parameters are added to give more control to the propagation of the front and be sure it gives a satisfying shape to the envelope. The main point is to extend the vertical plane sideways, using a width  $w$  and a “beginning distance”  $d_b$  to ensure straighter sides of the trenches (Fig. 10.1).

Notches are often smooth shapes created while the water table is superimposed on the conduits. These features can be easily modelled by thickening the (paleo)water table(s) in the velocity field using a factor  $n$  (Fig. 10.2). The thickening controls the smoothness and the height of the notch shape. The notch depth can be controlled by applying a multiplication factor on the velocity values around the (paleo)water table(s).

#### 4.3. Management of the different scales of perturbations on the envelope

As said before, the velocity field controls the coarse-scale shape of the conduits, but the focus of the ODSIM approach is to combine this

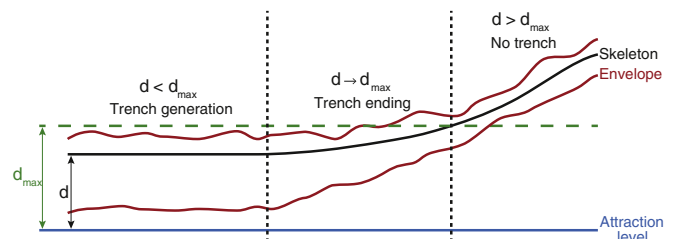


Fig. 9. Consequences on the envelope of the variations of the distance  $d$  between the skeleton and the attraction level, illustrating the impact of the formula (3). The permeability values  $p_w$  are taken from the attraction level and the distance  $d_{max}$  is defined by the user and represents the maximum allowed distance to generate a trench.

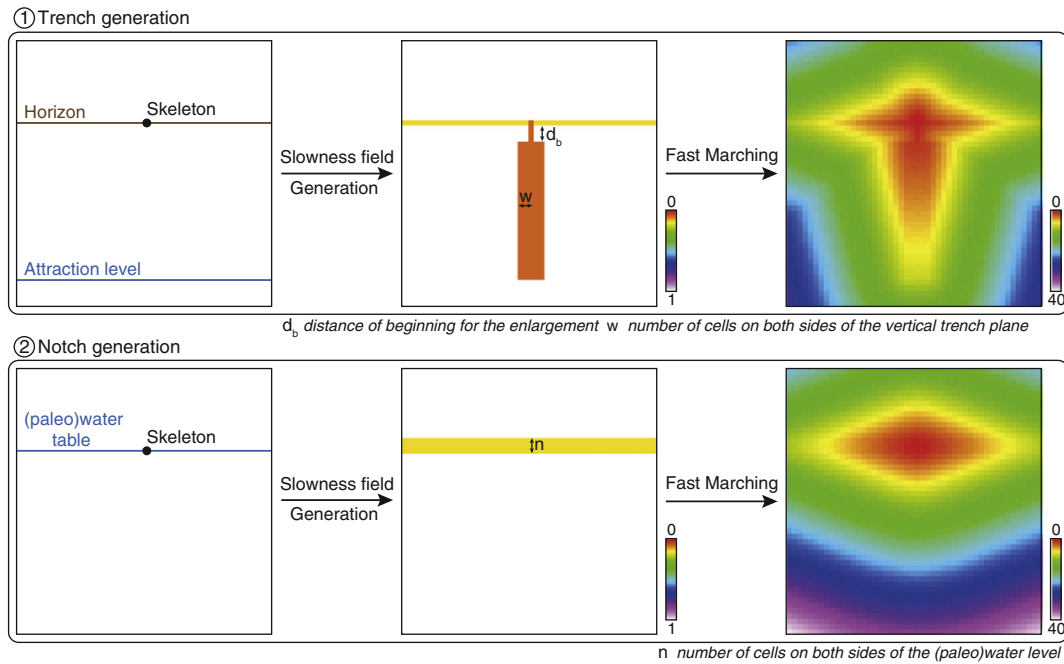


Fig. 10. Modifications of the slowness field allowing the generation of trenches and notches. The global shape of these elements is clearly visible in the field created by fast marching.

field with a random threshold that perturbs this “perfect” geometry by introducing fine-scale variability and also allows hard data conditioning. In their paper, Henrion et al. (2010) have proposed to introduce a locally variable mean into the sequential Gaussian simulation in order to accommodate a spatial trend. But this kind of modification would equally affect roof, walls and floors of the conduits by a progressive growing or narrowing.

Considering cave conduit geometries, it appears that these fine-scale variabilities are not identically affecting the roof, the walls or the floor. Due to many different factors, like breaking-down, mechanical and chemical erosion, it is common to have more variabilities along a roof than, particularly, on the bottom of a trench. Thus, conduit irregularities are not symmetrical and, moreover, their variations do not range between the same extrema (Fig. 11). Such differences between conduit ceiling, floor and/or sides can be noticed in several conduits, such as in



Fig. 11. Example of a passage with different scales of perturbation: the top and the floor of the conduit are roughly flat whereas its sides are more wavy (Mammoth Cave, US).

the Abracurrie Main Chamber, Nullarbor, Australia (James et al., 2012) or in the Clearwater Cave, Gunung Mulu, Sarawak (Farrant & Smart, 2011).

To model a smooth trench floor, for instance, we propose to separate the grid in two areas: the first one contains the vertical trench planes – with eventually an extension around the planes to avoid trench side protuberances to develop below the trench floor when using very high perturbations, and the second one the rest of the grid. Then two distinct variograms and/or distributions are defined in each area. The sequential Gaussian simulation generating the random threshold has to preserve a continuous resulting field between those areas (Fig. 12).

Increasing the range of the variogram used on the trench planes smoothes their bottom while preserving small scale perturbation on the trench sides. Reducing the amplitude of the values used for the probability density function (PDF) on the trench planes avoids obtaining a large range of variation for the conduits at the bottom (Fig. 13). The same method can be applied to reduce the roughness along weakness planes. Eventually, the use of several variogram models and/or distributions for each element controlling the shape gives differential perturbations of the envelope.

## 5. Results and discussion

These extensions of ODSIM have been implemented as a plugin of the GOCAD geomodelling software<sup>4</sup> and written in C++. It should be noted that this work can be developed in another modelling software, in a numerical computing environment such as MATLAB or Scilab as well as in a stand-alone application. The methodology has been tested on two synthetic cases. By using synthetic cases, we can easily demonstrate the new possibilities (cylinder, lens, keyholes, ...) offered by the method in a few examples, without falling into a controversial context. To better illustrate the independence between the skeleton simulation and the three-dimensional envelop modelling, the same karstic skeleton is used

<sup>4</sup> <http://www.pdgm.com/products/GOCAD>.



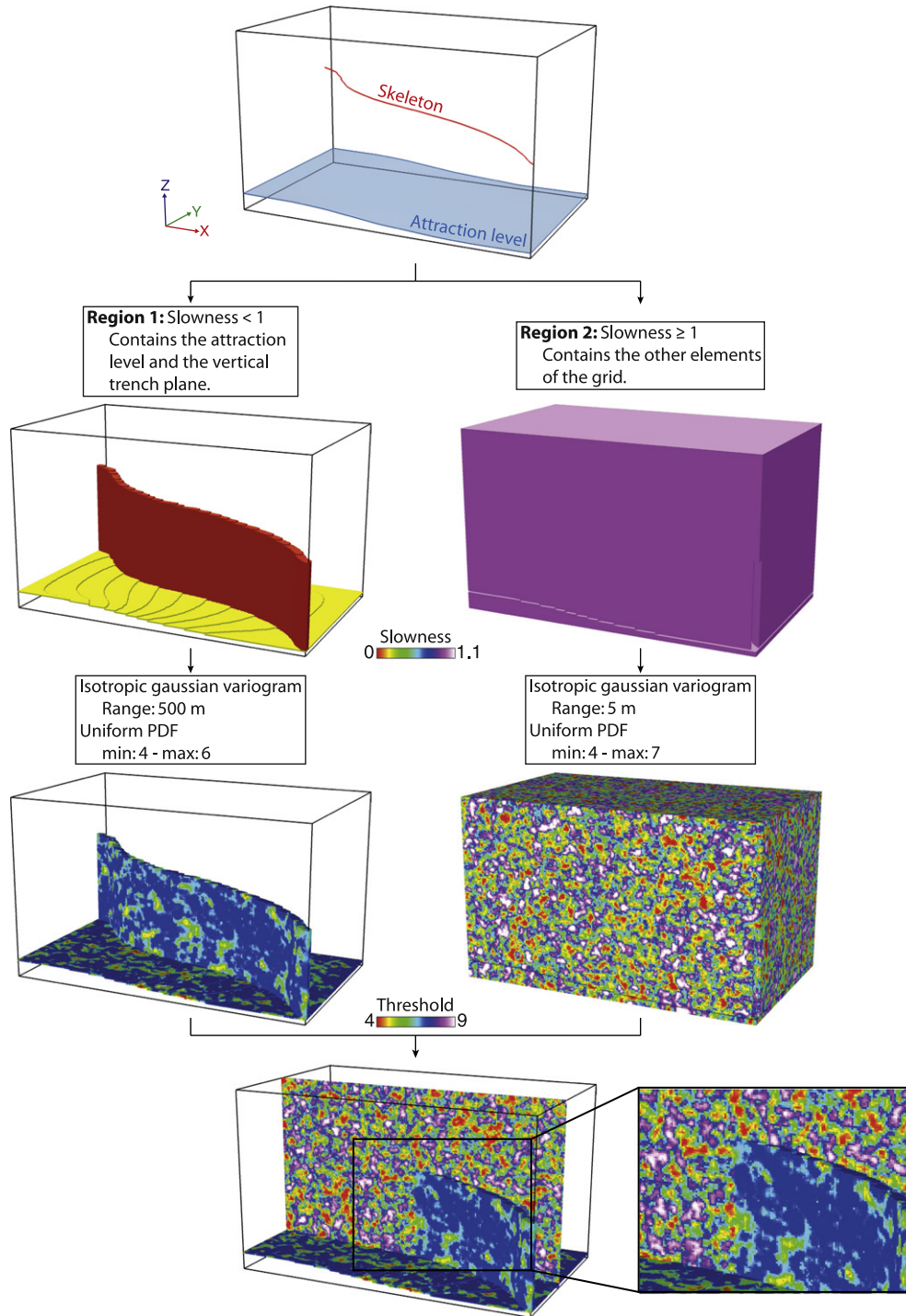


**Fig. 12.** Threshold generation example: the principle is to separate the structures with different perturbation types using their values in the slowness field. Here only two areas are created: the last screenshot shows the region 1 together with a section along the whole  $x$  axis, showing elements of the region 2. The enlargement on the right shows the continuity between the features of the two areas despite the two different distributions and variograms. This continuity is essential for obtaining good quality envelopes.

in the following examples. Inception features, water table and attraction level are modelled with triangulated surfaces. For the threshold simulations, a regular structural grid has been used. Both examples are supposed to be the expression of two genetic phases: i) an initial phreatic phase that is visible on the final shapes through an elongation along inception features; ii) and a second phase that results from a lowering of the water table. In the first example, to illustrate trench modelling capacities, an attraction level has been introduced at the water table level. The

distance  $d_{\max}$  has been chosen to limit entrenchments to the lowest conduit (Fig. 14). The various parameters used in this simulation are presented in Table 1 (Example 1). In the second example, we wanted to test the capacity of the method to reproduce notches (Fig. 15). A water table is thus introduced at the same altitude as the lowest conduits. It is duplicated into an attraction level to simultaneously develop trenches on the upper conduit, superposed to the inception elongation features. Detailed parameters are presented in Table 1 (Example 2).

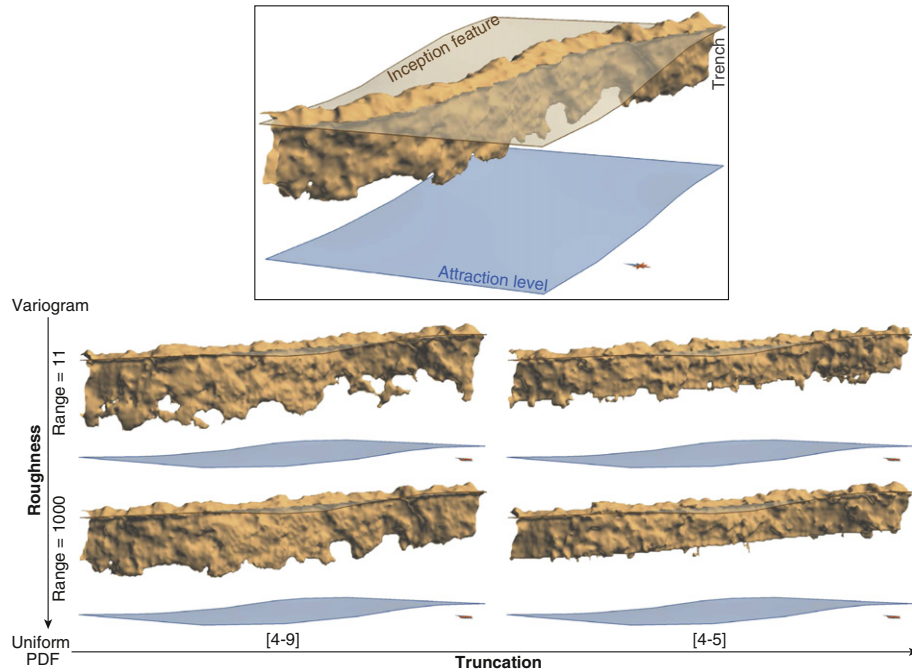


**Fig. 13.** Impact of the variogram and distribution used to generate the threshold: side view of the resulting envelopes. The given parameters are those of the weakness planes and the trench plane, the rest of the grid having a variogram range of 11 m and a uniform PDF of [4–9]. The velocity field values are 5 for the previous planes and 1 in the rest of the grid.

The resulting envelopes reflect the various coarse-scale karstic shapes that are now possible to model with this new methodology: i) lengthening and sharp incision along inception features (stratigraphical and tectonic); ii) realistic symmetric round shapes for the vertical conduits; iii) trenches superposed on a cylindrical or lens shape for keyhole passages; and iv) longitudinal notches. All these features can be combined. What trenches concern, depth variations follow the position of the conduits relatively to the attraction level: the further from the attraction level the conduits are, the lower is the trench depth. Their bottom is smoother than the shapes linked to the inception features thanks to the combined use of different variograms and distributions in the random threshold generation. Notch representations are more like a

rounding of the lateral carving although they can be more “marked” in the caves. The result remains useful in representing large notches. Generally, the proposed methodology offers an interesting list of solutions to simulate or reconstruct realistic three-dimensional karstic conduits. In this dual-scale geostatistical simulation method, the coarse-scale features can be modelled by an adapted and modular combination of a skeleton representation of the studied object and geological/speleological constraints defined by the user.

This results in a custom velocity field representing the coarse-scale geometries. A solution is proposed for managing the different fine-scale features depending on the same geological/speleological constraints. The Gibbs sampler with inequality constraints algorithm – which is

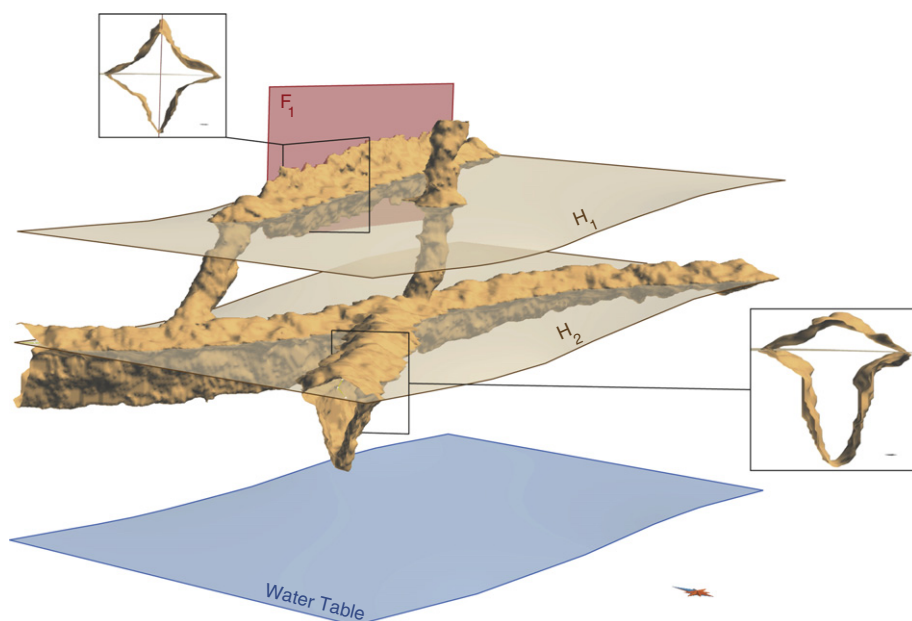


**Fig. 14.** Simulated envelope obtained by using two stratigraphic inception features ( $H_1$  and  $H_2$ ), one tectonic inception feature (fault  $F_1$ ) and an attraction level. Complex three-dimensional karst features such as trenches or elongated shapes are successfully reproduced.

**Table 1**  
Summary of parameters used to create the two synthetic models.

	Example 1	Example 2
GRID PARAMETERS		
Grid size (in cell)	250 × 150 × 150	250 × 150 × 150
Cell size (in m)	1 × 1 × 1	1 × 1 × 1
FAST MARCHING PARAMETERS		
<b>Initial slowness field</b>		
$H_1$ slowness value	0.2	0.2
$H_2$ slowness value	0.2	–
$F_1$ slowness value	0.2	0.2
Water table slowness value	0.2	0.2
Matrix slowness value	1	1
<b>Trench parameters</b>		
$d_{max}$ (in m)	70	70
$d_b$ (in cell)	4	4
$w$ (in cell)	1	1
<b>Notch parameters</b>		
$n$ (in cell)	–	1
THRESHOLD PARAMETERS		
<b>Low slowness region (Slowness &lt; 1)</b>		
<i>Variogram</i>		
Type	Gaussian	Gaussian
Range (in m)	500	500
<i>Distribution</i>		
Type	Uniform	Uniform
Min–Max	4–6	4–6
<b>High slowness region (Slowness = 1)</b>		
<i>Variogram</i>		
Type	Gaussian	Gaussian
Range (in m)	7	7
<i>Distribution</i>		
Type	Uniform	Uniform
Min–Max	4–7	4–7

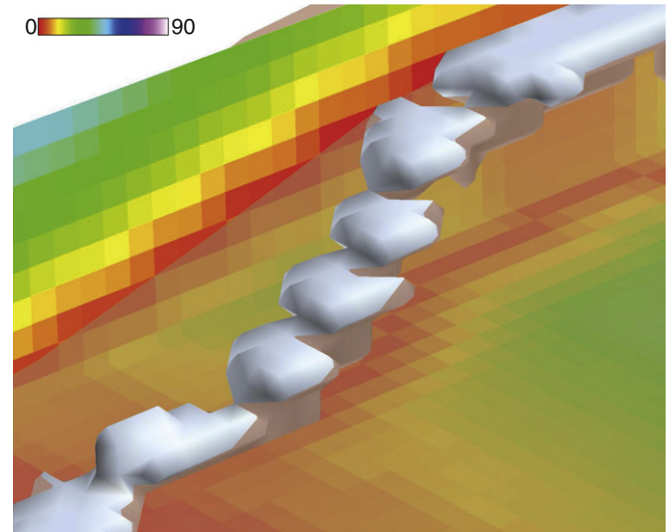


**Fig. 16.** Insufficient grid resolution leading to a non-continuous karstic conduit simulation. The colours correspond to the custom distance field and the transparent surface represents the weakness plane.

already available in the method (Henrion et al., 2010) – complements this toolbox by allowing hard data conditioning. Some further work is required to quantitatively validate the method capacity to reproduce realistic shapes. Several solutions could be explored:

- Compare a cave already modelled using a LiDAR survey or 2D sections and maps with several simulated conduits. Due to the stochastic nature of the process, the direct assessment of the real and simulated passage fit is worthless: a simulated conduit can be geomorphologically

consistent even if it does not fit the real conduit. Some indicators have to be developed to capture the entire three-dimensional characteristics of a conduit, such as, for instance, the conduit volume or the ratio of conduit surface area to conduit volume. Those indicators are then used to compare the real conduit and the simulated ones.

- Compare the simulated shapes for the unknown parts of a network with the conditioned shapes in the known parts based on statistical or fractal-based principles such as introduced by Curl (1986) (e.g., Pardo-Iguzquiza et al., 2011).

Despite these encouraging results, some limitations appear. First, the grid resolution can have a significant impact on the results. Indeed the introduction of the inception features in a velocity property corresponds to their rasterization in the grid. Stratigraphic inception horizons have a thickness of some centimetres to some decimetres (Filipponi, 2009), and conduits may be very stretched along them. Moreover, tectonic inception features induce very thin shapes at the intersection with the conduit. This means that shape modelling requires high grid resolutions,

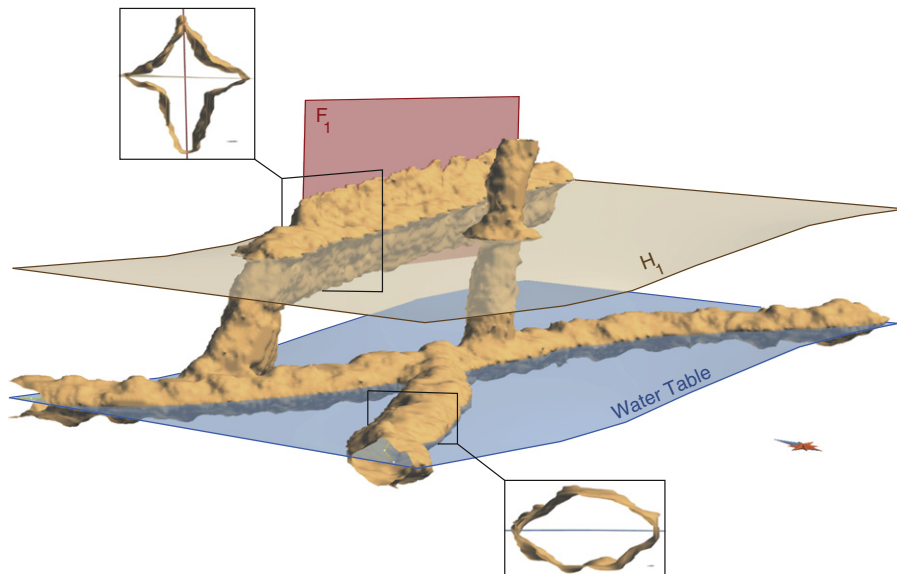


**Fig. 15.** Simulated envelope obtained by using one stratigraphic inception feature ( $H_1$ ), one tectonic inception feature (fault  $F_1$ ) and an attraction level superimposed on a water table at the same level as the lowest conduits. Complex three-dimensional karst features such as notches, trenches or elongated shapes are successfully reproduced.

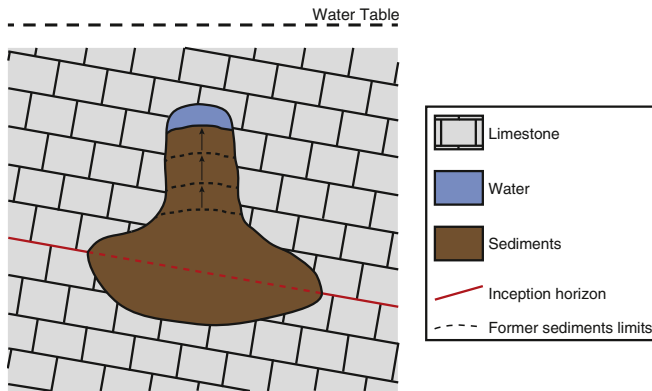


**Fig. 17.** Principle of the development of the paragenetic conduits: sediments progressively fill the cavity and block the downward dissolution, which favours an upward dissolution propagation.

at least to represent the global shape of the conduits in an acceptable way (Fig. 16). Another solution would be to have a non-regular grid organized along inception features. Second, the increase of the degrees of freedom in the process has a direct consequence on the increase of user choices and parameters, even if many features can be integrated directly in the custom distance field. But this last limitation is directly linked to the complexity of the studied case and difficult to avoid. Nevertheless, perhaps a new alternative could be found that avoids the use of the  $d_b$  and  $w$  parameters in the trench modelling process.

As for perspectives, a modelling method for other shapes could be studied. For instance paragenetic caves are made of conduits developed in the phreatic zone shaped like upside-down trenches, displaying an upward entrenchment of conduits (Fig. 17) (Renault, 1958; Pasini, 1967; Renault, 1968). They could probably be modelled with the same principle as trenches, but upturned. Another common geometry, partially linked to breakdowns, is strike-oriented passages (e.g., Palmer, 2012) that have a polygonal shape following horizons, with many perpendicular angles (Fig. 18). Even if various scales of variability are introduced in the simulated conduits through the threshold field, small-scale features such as scallops can still not be clearly and deliberately represented. On the other hand, larger scale features, such as conduit loops, are not linked to the conduit shape but to the network and should be introduced by the skeleton.

In a broader perspective, tests are required to assess the impact of these shapes on flow simulations. Modelling sediments could also be interesting considering their impact on fluid flows and on speleogenesis (Farrant & Smart, 2011). Finally, the entire methodology could be adapted to other underground processes, such as hydrothermal alteration, or be used to study the usefulness and applicability of the method in sinkhole prevention.

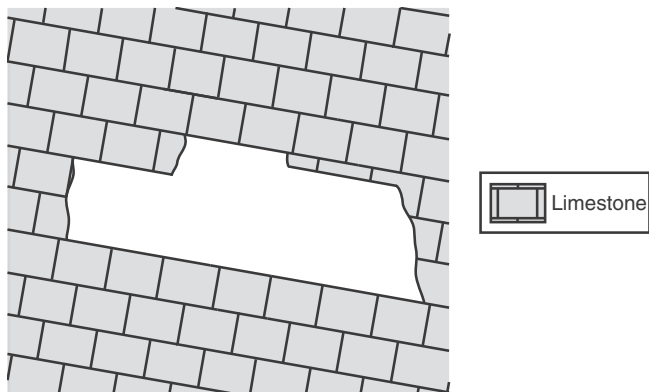


**Fig. 18.** A strike-oriented passage: the conduit shape follows lithostratigraphic horizons.

## 6. Conclusions

These improvements of ODSIM allow the stochastic generation of karst conduit envelopes around a skeleton by taking into account local geological information, especially inception features and (paleo)water table. It consequently contributes to the global workflow of stochastic karst generation, complementing the methods that stochastically generate skeletons representing the general network by introducing geomorphologically consistent conduit shapes. Various classic conduit shapes can be simulated, such as elongated or keyhole passages, while preserving the original capacities of ODSIM. Some other particular shapes still need to be taken into account to allow their simulation. Applying this method on synthetic cases gives quite satisfying results. The simulated shapes finely reproduce the most common conduit geometries while controlling the different scales and areas of shape perturbations. However, a confrontation to real data still needs to be carried out; first to validate the application to the reconstruction of explored and monitored conduits, then to validate more objectively the method's capacity to generate realistic conduits.

## Acknowledgements

We would like to thank the industrial and academic members of the GOCAD Consortium,<sup>5</sup> especially Paradigm for providing the GOCAD Software and API, ASGA (Association Scientifique pour la Géologie et ses Applications) and the French National Scientific Research Center CNRS - GeoResources for their support. We would also like to thank the reviewers, including Ph. Häuselmann, for constructive comments which helped improve this paper. This work was performed in the framework of the "Investissements d'avenir" Labex RESSOURCES21 (ANR-10-LABX-21).

## References

- Boggus, M., Crawfis, R., 2009. Explicit generation of 3D models of solution caves for virtual environments. *Proceedings of the 2009 International Conference on Computer Graphics and Virtual Reality*, pp. 85–90.
- Borghi, A., Renard, P., Jenni, S., 2012. A pseudo-genetic stochastic model to generate karstic networks. *J. Hydrol.* 414–415, 516–529.
- Brinkmann, R., Parise, M., Dye, D., 2008. Sinkhole distribution in a rapidly developing urban environment: Hillsborough County, Tampa Bay area, Florida. *Eng. Geol.* 99, 169–184.
- Chaojun, Z., Chengzao, J., Benliang, L., Xiuyu, L., Yunxiang, L., 2010. Ancient karsts and hydrocarbon accumulation in the middle and western parts of the North Tarim uplift, NW China. *Pet. Explor. Dev.* 37, 263–269.
- Collon-Drouaillet, P., Henrion, V., Pellerin, J., 2012. An algorithm for 3D simulation of branchwork karst networks using Horton parameters and A-star. Application to a synthetic case. *Geol. Soc. Lond. Spec. Publ.* 370, 12. <http://dx.doi.org/10.1144/SP370.3>.
- Curl, R.L., 1986. Fractal dimensions and geometries of caves. *Math. Geol.* 18, 765–783.
- Deutsch, C.V., Journel, A.G., 1997. *GSLIB: Geostatistical Software Library and User's Guide (Applied Geostatistics)*. Oxford University Press, USA.
- De Waele, J., Gutiérrez, F., Parise, M., Plan, L., 2011. Geomorphology and natural hazards in karst areas: a review. *Geomorphology* 134, 1–8.
- De Waele, J., Plan, L., Audra, P., 2009. Recent developments in surface and subsurface karst geomorphology: an introduction. *Geomorphology* 106, 1–8. <http://dx.doi.org/10.1016/j.geomorph.2008.09.023>.
- Farrant, A.R., Smart, P.L., 2011. Role of sediment in speleogenesis; sedimentation and paragenesis. *Geomorphology* 134, 79–93.
- Faulkner, T., 2006. Tectonic inception in Caledonide marbles. *Acta Geol.* 35, 7–21.
- Field, M.S., 2002. A lexicon of cave and karst terminology with special reference to environmental karst hydrology. National Center for Environmental Assessment, Washington Office, Office of Research and Development, US Environmental Protection Agency.
- Field, M.S., Pinsky, P.F., 2000. A two-region nonequilibrium model for solute transport in solution conduits in karstic aquifers. *J. Contam. Hydrol.* 44, 329–351.
- Filipponi, M., 2009. *Spatial Analysis of Karst Conduit Networks and Determination of Parameters Controlling the Speleogenesis along Preferential Lithostratigraphic Horizons*. Ph.D. Thesis École Polytechnique Fédérale de Lausanne, Suisse.
- Filipponi, M., Jeannin, P.Y., Tacher, L., 2009. Evidence of inception horizons in karst conduit networks. *Geomorphology* 106, 86–99.
- Filipponi, M., Jeannin, P.Y., Tacher, L., 2010. Understanding cave genesis along favourable bedding planes. The role of the primary rock permeability. *Z. Geomorphol. Suppl.* 54, 91–114.

<sup>5</sup> <http://www.gocad.org>.

- Ford, D., Williams, P., 2007. *Karst Hydrogeology and Geomorphology*. John Wiley and Sons, Ltd.
- Freulon, X., de Fouquet, C., 1993. Conditioning a Gaussian model with inequalities. In: Soares, A. (Ed.), *Geostatistics Tróia '92*. Springer Netherlands, Number 5 in Quantitative Geology and Geostatistics, pp. 201–212.
- Frumkin, A., Karkanas, P., Bar-Matthews, M., Barkai, R., Gopher, A., Shahack-Gross, R., Vaks, A., 2009. Gravitational deformations and fillings of aging caves: the example of Qesem karst system, Israel. *Geomorphology* 106, 154–164.
- Geman, S., Geman, D., 1984. Stochastic relaxation, Gibbs distributions, and the Bayesian restoration of images. *IEEE Transactions on Pattern Analysis and Machine Intelligence* pp. 721–741.
- Goldscheider, N., 2008. A new quantitative interpretation of the long-tail and plateau-like breakthrough curves from tracer tests in the artesian karst aquifer of Stuttgart, Germany. *Hydrogeol. J.* 16, 1311–1317.
- Goovaerts, P., 1997. *Geostatistics for natural resources evaluation*. Applied Geostatistics Oxford University Press, New York.
- Hartmann, A., Lange, J., Aguado, A.V., Mizyed, N., Smiatek, G., Kunstmann, H., 2012. A multi-model approach for improved simulations of future water availability at a large Eastern Mediterranean karst spring. *J. Hydrol.* 468–469, 130–138.
- Hauns, M., Jeannin, P.Y., Atteia, O., 2001. Dispersion, retardation and scale effect in tracer breakthrough curves in karst conduits. *J. Hydrol.* 241, 177–193.
- Henrion, V., Caumon, G., Cherpeau, N., 2010. ODSIM: an object-distance simulation method for conditioning complex natural structures. *Math. Geosci.* 42 (8), 911–924.
- Horvatinić, N., Krajar Bronić, I., Obelić, B., 2003. Differences in the  $^{14}\text{C}$  age,  $\delta^{13}\text{C}$  and  $\delta^{18}\text{O}$  of Holocene tufa and speleothem in the Dinaric karst. *Palaeogeogr. Palaeoclimatol. Palaeoecol.* 193, 139–157.
- Jaillet, S., Sadier, B., Arnaud, J., Azéma, M., Boche, E., Cailhol, D., Filippini, M., Roux, P.L., Varrel, E., 2011. Topographie, représentation et analyse morphologique 3D de drains, de conduits et de parois du karst. *Images et modèles 3D en milieux naturels*. pp. 119–130.
- James, J.M., Contos, A.K., Barnes, C.M., 2012. Nullarbor caves, Australia. In: White, William B., Culver, David C. (Eds.), *Encyclopedia of Caves*, second edition. Elsevier Science, pp. 568–576.
- Jameson, R.A., 1985. Structural segments and the analysis of flow paths in the North Canyon of Snedegar Cave, Friars Hole Cave System. Master's Thesis West Virginia University, Morgantown.
- Kuo, T.S., Liu, Z.Q., Li, H.C., Wan, N.J., Shen, C.C., Ku, T.L., 2011. Climate and environmental changes during the past millennium in central western Guizhou, China as recorded by Stalagmite ZJD-21. *J. Asian Earth Sci.* 40, 1111–1120.
- Labourdette, R., Lascu, I., Mylroie, J., Roth, M., 2007. Process-like modeling of flank-margin caves: from genesis to burial evolution. *J. Sediment. Res.* 77, 965–979.
- Lauritzen, S.E., Lundberg, J., 2000. *Solutional and erosional morphology. Speleogenesis: Evolution of Karst Aquifers*: Huntsville, Ala National Speleological Society pp. 408–426.
- Lowe, D.J., 1992. *The Origin of Limestone Caverns: An Inception Horizon Hypothesis*. Ph.D. Thesis Manchester Polytechnic, United Kingdom.
- Lü, X., Yang, N., Zhou, X., Yang, H., Li, J., 2008. Influence of Ordovician carbonate reservoir beds in Tarim Basin by faulting. *Sci. China Ser. D Earth Sci.* 51, 53–60.
- Mongelli, G., 2002. Growth of hematite and boehmite in concretions from ancient karst bauxite: clue for past climate. *Catena* 50, 43–51.
- Morales, T., Uriarte, J.A., Olazar, M., Antigüedad, I., Angulo, B., 2010. Solute transport modelling in karst conduits with slow zones during different hydrologic conditions. *J. Hydrol.* 390, 182–189.
- Onac, B.P., Constantin, S. (Eds.), 2008. *Archives of climate and environmental change in karst*. Quaternary International, 187.
- Palmer, A.N., 2012. Solution caves in regions of moderate relief. In: White, William B., Culver, David C. (Eds.), *Encyclopedia of Caves*, second edition. Elsevier Science, pp. 733–743.
- Pardo-Igúzquiza, E., Dowd, P.A., Chaoshui, X., Durán-Valsero, J.J., 2012. Stochastic simulation of karst conduit networks. *Adv. Water Resour.* 35, 141–150. <http://dx.doi.org/10.1016/j.advwatres.2011.09.014>.
- Pardo-Igúzquiza, E., Durán-Valsero, J.J., Rodríguez-Galiano, V., 2011. Morphometric analysis of three-dimensional networks of karst conduits. *Geomorphology* 132, 17–28.
- Parise, M., De Waele, J., Gutiérrez, F., 2009. Current perspectives on the environmental impacts and hazards in karst. *Environ. Geol.* 58, 235–237.
- Pasini, G., 1967. Nota preliminare sul ruolo speleogenetico dell'erosione "antigravitativa". *Le Grotte d'Italia*. . . 4 pp. 75–90.
- Renault, P., 1958. *Éléments de spéléomorphologie karstique*. *Ann. Spéol.* 13, 23–48.
- Renault, P., 1968. Contribution à l'étude des actions mécaniques et sédimentologiques dans la spéléogénèse. 3e partie: les facteurs sédimentologiques. *Ann. Spéol.* 23, 529–596.
- Sethian, J., 1996. A fast marching level set method for monotonically advancing fronts. *Proc. Natl. Acad. Sci.* 93, 1591–1595.
- Sethian, J., 1999a. Fast marching methods. *SIAM Rev.* 41, 199–235.
- Sethian, J., 1999b. *Level Set Methods and Fast Marching Method*. Cambridge University Press, Cambridge, United Kingdom.
- Viles, H.A., 2003. Conceptual modeling of the impacts of climate change on karst geomorphology in the UK and Ireland. *J. Nat. Conserv.* 11, 59–66.

# Bibliography

- S. I. Aanonsen, G. Nævdal, D. S. Oliver, A. C. Reynolds, B. Vallès, and others. The Ensemble Kalman Filter in Reservoir Engineering – A Review. *SPE Journal*, 14(03):393–412, 2009. doi: 10.2118/117274-PA. (Cited page 34)
- J. D. Abad, O. E. Sequeiros, B. Spinewine, C. Pirmez, M. H. Garcia, and G. Parker. Secondary Current of Saline Underflow In A Highly Meandering Channel: Experiments and Theory. *Journal of Sedimentary Research*, 81(11): 787–813, 2011. doi: 10.2110/jsr.2011.61. (Cited page 18)
- V. Abreu, M. Sullivan, C. Pirmez, and D. Mohrig. Lateral accretion packages (LAPs): an important reservoir element in deep water sinuous channels. *Marine and Petroleum Geology*, 20(6-8):631–648, 2003. doi: 10.1016/j.marpetgeo.2003.08.003. (Cited pages xi, 2, 18, 20, 23, and 158)
- G. J. J. Aleva. Indonesian fluvial cassiterite placers and their genetic environment. *Journal of the Geological Society*, 142(5):815–836, 1985. doi: 10.1144/gsjgs.142.5.0815. (Cited page 2)
- D. Allard and H. Group. On the Connectivity of Two Random Set Models: The Truncated Gaussian and the Boolean. In A. Soares, editor, *Geostatistics Tróia '92*, number 5 in Quantitative Geology and Geostatistics, pages 467–478. Springer Netherlands, 1993. ISBN 978-0-7923-2157-6 978-94-011-1739-5. doi: 10.1007/978-94-011-1739-5\_37. (Cited page 34)
- F. O. Alpak, M. D. Barton, and S. J. Naruk. The impact of fine-scale turbidite channel architecture on deep-water reservoir performance. *AAPG Bulletin*, 97(2):251–284, 2013. doi: 10.1306/04021211067. (Cited pages 12 and 13)
- Z. Anka, M. Séranne, M. Lopez, M. Scheck-Wenderoth, and B. Savoye. The long-term evolution of the Congo deep-sea fan: A basin-wide view of the interaction between a giant submarine fan and a mature passive margin

## Bibliography

- (ZaiAnGo project). *Tectonophysics*, 470(1–2):42–56, 2009. doi: 10.1016/j.tecto.2008.04.009. (Cited pages [xxvii](#) and [5](#))
- P. Anquez, G. Rongier, and P. Collon. Stochastic simulations of karst networks with Lindenmayer systems. In *Proc. 35th Gocad Meeting*, Nancy, France, 2015. (Cited page [197](#))
- D. A. Armitage, T. McHargue, A. Fildani, and S. A. Graham. Postavulsion channel evolution: Niger Delta continental slope. *AAPG Bulletin*, 96(5): 823–843, 2012. doi: 10.1306/09131110189. (Cited page [24](#))
- R. W. C. Arnott. Stratal architecture and origin of lateral accretion deposits (LADs) and conterminuous inner-bank levee deposits in a base-of-slope sinuous channel, lower Isaac Formation (Neoproterozoic), East-Central British Columbia, Canada. *Marine and Petroleum Geology*, 24(6-9):515–528, 2007. doi: 10.1016/j.marpetgeo.2007.01.006. (Cited page [158](#))
- G. B. Arpat and J. Caers. A Multiple-scale, Pattern-based Approach to Sequential Simulation. In O. Leuangthong and C. V. Deutsch, editors, *Geostatistics Banff 2004*, number 14 in Quantitative Geology and Geostatistics, pages 255–264. Springer Netherlands, 2004. ISBN 978-1-4020-3515-9 978-1-4020-3610-1. (Cited page [31](#))
- O. Babak and C. V. Deutsch. An intrinsic model of coregionalization that solves variance inflation in collocated cokriging. *Computers & Geosciences*, 35(3): 603–614, Mar. 2009. doi: 10.1016/j.cageo.2008.02.025. (Cited page [167](#))
- N. Babonneau, B. Savoye, M. Cremer, and B. Klein. Morphology and architecture of the present canyon and channel system of the Zaire deep-sea fan. *Marine and Petroleum Geology*, 19(4):445–467, 2002. doi: 10.1016/S0264-8172(02)00009-0. (Cited pages [xxvii](#) and [5](#))
- N. Babonneau, B. Savoye, M. Cremer, and M. Bez. Sedimentary Architecture in Meanders of a Submarine Channel: Detailed Study of the Present Congo Turbidite Channel (Zaiango Project). *Journal of Sedimentary Research*, 80(10):852–866, 2010. doi: 10.2110/jsr.2010.078. (Cited page [119](#))
- C. Barthélemy and P. Collon-Drouaillet. Simulation of Anastomotic Karst Networks. In *Proc. 32nd Gocad Meeting*, page 13, Nancy, 2013. (Cited page [47](#))
- R. T. Beaubouef. Deep-water leveed-channel complexes of the Cerro Toro Formation, Upper Cretaceous, southern Chile. *AAPG Bulletin*, 88(11):1471–1500, 2004. doi: 10.1306/06210403130. (Cited page [11](#))

- B. J. Bluck, J. D. Ward, and M. C. J. D. Wit. Diamond mega-placers: southern Africa and the Kaapvaal craton in a global context. *Geological Society, London, Special Publications*, 248(1):213–245, 2005. doi: 10.1144/GSL.SP.2005.248.01.12. (Cited page 2)
- M. D. Blum and T. E. Törnqvist. Fluvial responses to climate and sea-level change: a review and look forward. *Sedimentology*, 47:2–48, 2000. doi: 10.1046/j.1365-3091.2000.00008.x. (Cited page 2)
- J. B. Boisvert, M. J. Pyrcz, and C. V. Deutsch. Multiple Point Metrics to Assess Categorical Variable Models. *Natural Resources Research*, 19(3):165–175, 2010. doi: 10.1007/s11053-010-9120-2. (Cited pages [xiii](#), [39](#), and [69](#))
- C. E. Bond, A. D. Gibbs, Z. K. Shipton, and S. Jones. What do you think this is? “Conceptual uncertainty” in geoscience interpretation. *GSA today*, 17(11):4, 2007. doi: 10.1130/GSAT01711A.1. (Cited page [xliv](#))
- A. H. Bouma. Key controls on the characteristics of turbidite systems. *Geological Society, London, Special Publications*, 222(1):9–22, 2004. doi: 10.1144/GSL.SP.2004.222.01.02. (Cited page 4)
- A. H. Bouma, P. H. Kuenen, and F. P. Shepard. *Sedimentology of some flysch deposits: a graphic approach to facies interpretation*, volume 168. Elsevier Amsterdam, 1962. (Cited page 7)
- A. Braathen, K. Baelum, H. H. Christiansen, T. Dahl, O. Eiken, H. Elvebakk, F. Hansen, T. H. Hanssen, M. Jochmann, T. A. Johansen, H. Johnsen, L. Larsen, T. Lie, J. Mertes, A. Mørk, M. B. Mørk, W. Nemec, S. Olaussen, V. Oye, K. Rød, G. O. Titlestad, J. Tveranger, and K. Vagle. The Longyearbyen CO<sub>2</sub> Lab of Svalbard, Norway – Initial assessment of the geological conditions for CO<sub>2</sub> sequestration. *Norwegian Journal of Geology*, 92:353–376, 2012. (Cited pages [xi](#), [xxxvii](#), [xxxviii](#), and [26](#))
- J. W. Brandt and V. R. Algazi. Continuous skeleton computation by Voronoi diagram. *CVGIP: Image Understanding*, 55(3):329–338, 1992. doi: 10.1016/1049-9660(92)90030-7. (Cited page 46)
- J. C. Brice. Evolution of Meander Loops. *Geological Society of America Bulletin*, 85(4):581–586, 1974. doi: 10.1130/0016-7606(1974)85<581:EOML>2.0.CO;2. (Cited page 141)
- S. G. Buck. The Saaiplaas Quartzite Member: A Braided System of Gold- and Uranium-Bearing Channel Placers within the Proterozoic Witwatersrand



## Bibliography

- Supergroup of South Africa. In J. D. Collinson and J. Lewin, editors, *Modern and Ancient Fluvial Systems*, pages 549–562. Blackwell Publishing Ltd., 1983. ISBN 978-1-4443-0377-3. (Cited pages [xxvii](#) and [2](#))
- K. M. Campion, A. R. G. Sprague, and M. D. Sullivan. *Architecture and Lithofacies of the Capistrano Formation (Miocene-Pliocene)*, San Clemente, California. Annual Fieldtrip Guidebook, Pacific Section SEPM, Book 100, 2005. ISBN 1-878861-93-X. (Cited pages [xxvii](#) and [8](#))
- C. Camporeale, P. Perona, A. Porporato, and L. Ridolfi. On the long-term behavior of meandering rivers. *Water resources research*, 41(12):W12403, 2005. doi: 10.1029/2005WR004109. (Cited pages [177](#) and [201](#))
- C. Camporeale, P. Perona, A. Porporato, and L. Ridolfi. Hierarchy of models for meandering rivers and related morphodynamic processes. *Reviews of Geophysics*, 45(1):RG1001, 2007. doi: 10.1029/2005RG000185. (Cited pages [xvii](#) and [160](#))
- M. A. Carson and M. F. Lapointe. The inherent asymmetry of river meander planform. *The Journal of Geology*, pages 41–55, 1983. doi: 10.1086/628743. (Cited page [141](#))
- G. Caumon, P. Collon-Drouaillet, C. Le Carlier de Veslud, S. Viseur, and J. Sausse. Surface-Based 3D Modeling of Geological Structures. *Mathematical Geosciences*, 41(8):927–945, 2009. doi: 10.1007/s11004-009-9244-2. (Cited page [xliv](#))
- S. Chatterjee and R. Dimitrakopoulos. Pattern-based Simulation using Self Organized Maps. In *Geomatrix'12, International Conference on Geospatial Technologies and Applications*, pages 1–3, Indian Institute of Technology Bombay (IITB), 2012. (Cited page [31](#))
- A. Comunian, P. Renard, and J. Straubhaar. 3D multiple-point statistics simulation using 2D training images. *Computers & Geosciences*, 40(0):49–65, 2012. doi: 10.1016/j.cageo.2011.07.009. (Cited page [39](#))
- N. D. Cornea, D. Silver, and P. Min. Curve-skeleton properties, applications, and algorithms. *Visualization and Computer Graphics, IEEE Transactions on*, 13(3): 530–548, 2007. doi: 10.1109/TVCG.2007.1002. (Cited pages [47](#) and [207](#))
- R. K. Corney, J. Peakall, D. R. Parsons, L. Elliott, J. L. Best, R. E. Thomas, G. M. Keevil, D. B. Ingham, and K. J. Amos. Reply to discussion of Imran et al. on “The orientation of helical flow in curved channels” by Corney et

- al., *Sedimentology*, 53, 249–257. *Sedimentology*, 55(1):241–247, 2008. doi: 10.1111/j.1365-3091.2007.00925.x. (Cited pages 17, 33, and 160)
- R. K. T. Corney, J. Peakall, D. R. Parsons, L. Elliott, K. J. Amos, J. L. Best, G. M. Keevil, and D. B. Ingham. The orientation of helical flow in curved channels. *Sedimentology*, 53(2):249–257, 2006. doi: 10.1111/j.1365-3091.2006.00771.x. (Cited pages 17, 33, and 160)
- T. F. Cox and M. A. Cox. *Multidimensional scaling*. Chapman and Hall, London, 1994. ISBN 978-1-58488-094-3. (Cited pages xiv, 54, and 55)
- B. T. Cronin, A. Hurst, H. Celik, and I. Türkmen. Superb exposure of a channel, levee and overbank complex in an ancient deep-water slope environment. *Sedimentary Geology*, 132(3-4):205–216, May 2000. doi: 10.1016/S0037-0738(00)00008-7. (Cited page 12)
- A. Crosato. Effects of smoothing and regriding in numerical meander migration models. *Water Resources Research*, 43(1):W01401, 2007. doi: 10.1029/2006WR005087. (Cited pages 176, 177, and 199)
- S. De Iaco. On the use of different metrics for assessing complex pattern reproductions. *Journal of Applied Statistics*, 40(4):808–822, 2013. doi: 10.1080/02664763.2012.754853. (Cited pages xiii and 39)
- S. De Iaco and S. Maggio. Validation Techniques for Geological Patterns Simulations Based on Variogram and Multiple-Point Statistics. *Mathematical Geosciences*, 43(4):483–500, 2011. doi: 10.1007/s11004-011-9326-9. (Cited pages 39 and 204)
- J. De Leeuw. Applications of convex analysis to multidimensional scaling. In *Recent Developments in Statistics*, pages 133–146. J.R. Barra, F. Brodeau, G. Romier and B. Van Cutsem, Amsterdam, north holland publishing company edition, 1977. (Cited page 56)
- J. De Leeuw and W. J. Heiser. Convergence of correction matrix algorithms for multidimensional scaling. *Geometric representations of relational data*, pages 735–752, 1977. (Cited page 56)
- J. De Leeuw and W. J. Heiser. Multidimensional scaling with restrictions on the configuration. *Multivariate analysis*, 5:501–522, 1980. (Cited page 56)
- J. De Leeuw and P. Mair. Multidimensional scaling using majorization: SMA-COF in R. *Journal of Statistical Software*, 31(3):1–30, 2009. (Cited page 57)

## Bibliography

- M. E. Deptuck, G. S. Steffens, M. Barton, and C. Pirmez. Architecture and evolution of upper fan channel-belts on the Niger Delta slope and in the Arabian Sea. *Marine and Petroleum Geology*, 20(6-8):649–676, 2003. doi: 10.1016/j.marpetgeo.2003.01.004. (Cited pages [xxvii](#), [xxxi](#), [8](#), [9](#), [23](#), and [159](#))
- M. E. Deptuck, Z. Sylvester, C. Pirmez, and C. O’Byrne. Migration-aggradation history and 3-D seismic geomorphology of submarine channels in the Pleistocene Benin-major Canyon, western Niger Delta slope. *Marine and Petroleum Geology*, 24(6-9):406–433, 2007. doi: 10.1016/j.marpetgeo.2007.01.005. (Cited pages [13](#) and [34](#))
- C. Deutsch and T. Tran. FLUVSIM: a program for object-based stochastic modeling of fluvial depositional systems. *Computers & Geosciences*, 28(4):525–535, 2002. doi: 10.1016/S0098-3004(01)00075-9. (Cited pages [xxviii](#), [30](#), [38](#), [84](#), [146](#), [150](#), [151](#), and [152](#))
- C. V. Deutsch. Fortran programs for calculating connectivity of three-dimensional numerical models and for ranking multiple realizations. *Computers & Geosciences*, 24(1):69–76, 1998. doi: 10.1016/S0098-3004(97)00085-X. (Cited pages [xiii](#), [xxviii](#), [39](#), [41](#), [46](#), and [204](#))
- C. V. Deutsch and T. A. Hewett. Challenges in reservoir forecasting. *Mathematical Geology*, 28(7):829–842, 1996. doi: 10.1007/BF02066003. (Cited page [38](#))
- C. V. Deutsch and A. G. Journel. *GSLIB: Geostatistical Software Library and User’s Guide*. Oxford University Press, New York, 1992. ISBN 978-0-19-510015-0. (Cited pages [xxviii](#), [xliii](#), [27](#), [28](#), [38](#), [84](#), and [166](#))
- C. V. Deutsch and L. Wang. Hierarchical object-based stochastic modeling of fluvial reservoirs. *Mathematical Geology*, 28(7):857–880, 1996. doi: 10.1007/BF02066005. (Cited pages [30](#) and [32](#))
- R. M. Dorrell, S. E. Darby, J. Peakall, E. J. Sumner, D. R. Parsons, and R. B. Wynn. Superelevation and overspill control secondary flow dynamics in submarine channels. *Journal of Geophysical Research: Oceans*, 118(8):3895–3915, 2013. doi: 10.1002/jgrc.20277. (Cited pages [20](#), [33](#), and [160](#))
- L. Droz, T. Marsset, H. Ondréas, M. Lopez, B. Savoye, and F.-L. Spy-Anderson. Architecture of an active mud-rich turbidite system: The Zaire Fan (Congo–Angola margin southeast Atlantic) Results from ZaiAngo 1 and 2 cruises. *AAPG Bulletin*, 87(7):1145–1168, 2003. doi: 10.1306/03070300013. (Cited pages [xxvii](#) and [5](#))

- L. Droz, T. Marsset, B. Dennielou, N. Babonneau, B. Savoye, and M. Bez. Avulsion phenomenon: process and consequences on fan evolution. A new perspective from the Zaire (Congo) Turbidite System (ZaiAngo Project, Ifremer/Total). In *10th International Congress of the Brazilian Geophysical Society*, 2007. doi: 10.1190/sbgf2007-450. (Cited pages 10 and 24)
- A. Einstein. The Cause of the Formation of Meanders in the Courses of Rivers and of the So-Called Baer's Law. *Die Naturwissenschaften*, 14:223–224, 1926. (Cited page 16)
- D. J. Evans and R. A. Chadwick. *Underground Gas Storage: Worldwide Experiences and Future Development in the UK and Europe*. Geological Society of London, 2009. ISBN 978-1-86239-272-4. (Cited page xxxvii)
- J. Feder. Plex languages. *Information Sciences*, 3(3):225–241, July 1971. doi: 10.1016/S0020-0255(71)80008-7. (Cited page 151)
- D. V. Fitterman, C. M. Menges, A. M. Al Kamali, and F. Essa Jama. Electromagnetic mapping of buried paleochannels in eastern Abu Dhabi Emirate, U.A.E. *Geoexploration*, 27(1-2):111–133, 1991. doi: 10.1016/0016-7142(91)90018-8. (Cited pages xi, xxxvii, and 2)
- R. D. Flood and J. E. Damuth. Quantitative characteristics of sinuous distributary channels on the Amazon Deep-Sea Fan. *Geological Society of America Bulletin*, 98(6):728–738, 1987. doi: 10.1130/0016-7606(1987)98<728:QCOSDC>2.0.CO;2. (Cited page 6)
- M. Gainski, A. G. MacGregor, P. J. Freeman, and H. F. Nieuwland. Turbidite reservoir compartmentalization and well targeting with 4D seismic and production data: Schiehallion Field, UK. *Geological Society, London, Special Publications*, 347(1):89–102, 2010. doi: 10.1144/SP347.7. (Cited pages xxvii, xxxix, xl, 14, 34, and 158)
- A. Galli, H. Beucher, G. L. Loc'h, B. Doligez, and H. Group. The Pros and Cons of the Truncated Gaussian Method. In M. Armstrong and P. A. Dowd, editors, *Geostatistical Simulations*, number 7 in Quantitative Geology and Geostatistics, pages 217–233. Springer Netherlands, 1994. ISBN 978-90-481-4372-6 978-94-015-8267-4. doi: 10.1007/978-94-015-8267-4\_18. (Cited pages 29, 38, and 84)
- W. E. Galloway. Siliciclastic slope and base-of-slope depositional systems: component facies, stratigraphic architecture, and classifica-

## Bibliography

- tion. *AAPG bulletin*, 82(4):569–595, 1998. doi: 10.1306/1D9BC5BB-172D-11D7-8645000102C1865D. (Cited page 9)
- A. García-Gil, E. Vázquez-Suñe, M. M. Alcaraz, A. S. Juan, J. Á. Sánchez-Navarro, M. Montlleó, G. Rodríguez, and J. Lao. GIS-supported mapping of low-temperature geothermal potential taking groundwater flow into account. *Renewable Energy*, 77:268–278, 2015. doi: 10.1016/j.renene.2014.11.096. (Cited page xxxvii)
- R. Gaujoux and C. Seoighe. A flexible R package for nonnegative matrix factorization. *BMC Bioinformatics*, 11(1):367, 2010. doi: 10.1186/1471-2105-11-367. (Cited page 57)
- M. Genesseeux, A. Mauffret, and G. Pautot. Les glissements sous-marins de la pente continentale niçoise et la rupture de câbles en mer Ligure (Méditerranée occidentale). *Comptes Rendus de l'Académie des Sciences de Paris*, 290(14):959–962, Jan. 1980. (Cited page 3)
- F. Giorgio Serchi, J. Peakall, D. B. Ingham, and A. D. Burns. A unifying computational fluid dynamics investigation on the river-like to river-reversed secondary circulation in submarine channel bends. *Journal of Geophysical Research: Oceans*, 116(C6):C06012, 2011. doi: 10.1029/2010JC006361. (Cited page 18)
- J. Gómez-Hernández and X.-H. Wen. To be or not to be multi-Gaussian? A reflection on stochastic hydrogeology. *Advances in Water Resources*, 21(1): 47–61, 1998. doi: 10.1016/S0309-1708(96)00031-0. (Cited page 38)
- J. C. Gower. Some distance properties of latent root and vector methods used in multivariate analysis. *Biometrika*, 53(3-4):325–338, 1966. doi: 10.1093/biomet/53.3-4.325. (Cited page 55)
- E. Gringarten and C. V. Deutsch. Teacher's Aide Variogram Interpretation and Modeling. *Mathematical Geology*, 33(4):507–534, 2001. doi: 10.1023/A:1011093014141. (Cited page 167)
- S.-A. Grundvåg, E. P. Johannessen, W. Helland-Hansen, and P. Plink-Björklund. Depositional architecture and evolution of progradationally stacked lobe complexes in the Eocene Central Basin of Spitsbergen. *Sedimentology*, 61(2): 535–569, 2014. doi: 10.1111/sed.12067. (Cited pages xxvii and xxxviii)
- F. B. Guardiano and R. M. Srivastava. Multivariate Geostatistics: Beyond Bivariate Moments. In A. Soares, editor, *Geostatistics Tróia*

- '92, number 5 in *Quantitative Geology and Geostatistics*, pages 133–144. Springer Netherlands, 1993. ISBN 978-0-7923-2157-6 978-94-011-1739-5. (Cited pages 29, 38, and 170)
- M. C. Hanna, D. Uffen, S. Emsley, and T. Inks. Reliable Geophysics. *CSEG recorder*, April 2015:53–59, 2015. (Cited pages xxvii and xli)
- M. M. Hassanpour, M. J. Pyrcz, and C. V. Deutsch. Improved geostatistical models of inclined heterolithic strata for McMurray Formation, Alberta, Canada. *AAPG Bulletin*, 97(7):1209–1224, 2013. doi: 10.1306/01021312054. (Cited pages 30, 146, 149, 150, 151, and 205)
- J. C. Hernández Del Pozo, I. Ocete, R. García, and R. Carmona. Locating hidden river courses via geo-technical investigation? Application in the city of Granada, Spain. *Natural Hazards and Earth System Science*, 5(6):911–923, 2005. doi: 10.5194/nhess-5-911-2005. (Cited page 2)
- E. J. Hill and C. M. Griffiths. Describing and generating facies models for reservoir characterisation: 2D map view. *Marine and Petroleum Geology*, 26(8):1554–1563, 2009. doi: 10.1016/j.marpetgeo.2008.09.004. (Cited pages 85, 149, and 151)
- A. D. Howard. Modeling channel migration and floodplain sedimentation in meandering streams. *Lowland floodplain rivers: geomorphological perspectives*, pages 1–41, 1992. (Cited page 177)
- A. D. Howard and A. T. Hemberger. Multivariate characterization of meandering. *Geomorphology*, 4(3-4):161–186, 1991. doi: 10.1016/0169-555X(91)90002-R. (Cited pages 102 and 197)
- S. Ikeda, G. Parker, and K. Sawai. Bend theory of river meanders. Part 1. Linear development. *Journal of Fluid Mechanics*, 112:363–377, 1981. doi: 10.1017/S0022112081000451. (Cited pages 16, 32, 160, and 198)
- J. Imran, G. Parker, and C. Pirmez. A nonlinear model of flow in meandering submarine and subaerial channels. *Journal of Fluid Mechanics*, 400:295–331, Dec. 1999. doi: 10.1017/S0022112099006515. (Cited pages 16, 33, and 160)
- J. Imran, M. A. Islam, H. Huang, A. Kassem, J. Dickerson, C. Pirmez, and G. Parker. Helical flow couplets in submarine gravity underflows. *Geology*, 35(7):659–662, 2007. doi: 10.1130/G23780A.1. (Cited page 17)

## Bibliography

- J. Imran, M. A. Islam, and A. Kassem. “The orientation of helical flow in curved channels” by Corney et al., *Sedimentology*, Vol. 53, pp. 249–257 – discussion. *Sedimentology*, 55(1):235–239, 2008. doi: 10.1111/j.1365-3091.2007.00924.x. (Cited pages 17, 33, and 160)
- M. A. Islam, J. Imran, C. Pirmez, and A. Cantelli. Flow splitting modifies the helical motion in submarine channels. *Geophysical Research Letters*, 35(22), 2008. doi: 10.1029/2008GL034995. (Cited page 17)
- A. K. Jain. *Fundamentals of digital image processing*, volume 3. Prentice-Hall Englewood Cliffs, 1989. ISBN 978-0-13-336165-0. (Cited page 46)
- M. Janocko, M. B. J. Cartigny, W. Nemeč, and E. W. M. Hansen. Turbidity current hydraulics and sediment deposition in erodible sinuous channels: Laboratory experiments and numerical simulations. *Marine and Petroleum Geology*, 41:222–249, 2013a. doi: 10.1016/j.marpetgeo.2012.08.012. (Cited pages xxviii, 18, 19, 20, and 21)
- M. Janocko, W. Nemeč, S. Henriksen, and M. Warchoř. The diversity of deep-water sinuous channel belts and slope valley-fill complexes. *Marine and Petroleum Geology*, 41:7–34, 2013b. doi: 10.1016/j.marpetgeo.2012.06.012. (Cited pages 2, 7, and 8)
- E. Johannessen, T. Henningsen, N. Bakke, T. Johansen, B. Ruud, P. Riste, H. Elvebakk, M. Jochmann, G. Elvebakk, and M. Woldengen. Palaeogene clinof orm succession on Svalbard expressed in outcrops, seismic data, logs and cores. *First Break*, 29(1768), 2011. doi: 10.3997/1365-2397.2011004. (Cited pages xxvii and xxxviii)
- E. P. Johannessen and R. J. Steel. Shelf-margin clinof orms and prediction of deepwater sands. *Basin Research*, 17(4):521–550, 2005. doi: 10.1111/j.1365-2117.2005.00278.x. (Cited pages xxvii and xxxviii)
- H. Johannesson and G. Parker. Secondary Flow in Mildly Sinuous Channel. *Journal of Hydraulic Engineering*, 115(3):289–308, 1989. doi: 10.1061/(ASCE)0733-9429(1989)115:3(289). (Cited page 16)
- A. Journel and F. Alabert. New method for reservoir mapping. *Journal of Petroleum technology*, 42(2):212–218, 1990. doi: 10.2118/18324-PA. (Cited page 38)
- A. Journel and T. Zhang. The Necessity of a Multiple-Point Prior Model. *Mathematical Geology*, 38(5):591–610, 2006. doi: 10.1007/s11004-006-9031-2. (Cited page 31)

- P. Jussel, F. Stauffer, and T. Dracos. Transport modeling in heterogeneous aquifers: 1. Statistical description and numerical generation of gravel deposits. *Water Resources Research*, 30(6):1803–1817, 1994. doi: 10.1029/94WR00162. (Cited pages [xxxvii](#) and [2](#))
- G. M. Keevil, J. Peakall, J. L. Best, and K. J. Amos. Flow structure in sinuous submarine channels: Velocity and turbulence structure of an experimental submarine channel. *Marine Geology*, 229(3-4):241–257, 2006. doi: 10.1016/j.margeo.2006.03.010. (Cited page [17](#))
- M. King and M. Mark. Flow Simulation of Geologic Models. *SPE Reservoir Evaluation & Engineering*, 2(4):351–367, 1999. doi: 10.2118/57469-PA. (Cited page [38](#))
- R. Kinoshita. An investigation of channel deformation of the Ishikari River. Publication no. 36. *Natural Resources Division, Ministry of Science and Technology of Japan*, 1961. (Cited page [141](#))
- B. Kneller and C. Buckee. The structure and fluid mechanics of turbidity currents: a review of some recent studies and their geological implications. *Sedimentology*, 47:62–94, 2000. doi: 10.1046/j.1365-3091.2000.047s1062.x. (Cited page [3](#))
- V. Kolla. A review of sinuous channel avulsion patterns in some major deep-sea fans and factors controlling them. *Marine and Petroleum Geology*, 24(6-9):450–469, 2007. doi: 10.1016/j.marpetgeo.2007.01.004. (Cited pages [xi](#), [8](#), [9](#), [18](#), [23](#), [30](#), and [209](#))
- V. Kolla, P. Bourges, J.-M. Urruty, and P. Safa. Evolution of Deep-Water Tertiary Sinuous Channels Offshore Angola (West Africa) and Implications for Reservoir Architecture. *AAPG Bulletin*, 85(8):1373–1405, 2001. doi: 10.1306/8626CAC3-173B-11D7-8645000102C1865D. (Cited pages [xxviii](#), [xxxi](#), [25](#), [141](#), and [144](#))
- V. Kolla, H. W. Posamentier, and L. J. Wood. Deep-water and fluvial sinuous channels—Characteristics, similarities and dissimilarities, and modes of formation. *Marine and Petroleum Geology*, 24(6-9):388–405, June 2007. doi: 10.1016/j.marpetgeo.2007.01.007. (Cited pages [10](#) and [24](#))
- P. D. Komar. The channelized flow of turbidity currents with application to Monterey Deep-Sea Fan Channel. *Journal of Geophysical Research*, 74(18):4544–4558, Aug. 1969. doi: 10.1029/JC074i018p04544. (Cited page [3](#))



## Bibliography

- A. A. Konstantinovskii. Perspectives of the discovery of complex (gold and platinum group metal) paleoplacers in the eastern Baltic Shield. *Lithology and Mineral Resources*, 40(1):9–20, 2005. doi: 10.1007/s10987-005-0002-3. (Cited page 2)
- R. Labourdette. Integrated three-dimensional modeling approach of stacked turbidite channels. *AAPG Bulletin*, 91(11):1603–1618, 2007. doi: 10.1306/06210706143. (Cited pages xi, 2, 12, and 13)
- R. Labourdette. ‘LOSCS’ Lateral Offset Stacked Channel Simulations: Towards geometrical modelling of turbidite elementary channels. *Basin Research*, 20(3):431–444, 2008. doi: 10.1111/j.1365-2117.2008.00361.x. (Cited pages xvii, 160, 161, 199, and 200)
- R. Labourdette and M. Bez. Element migration in turbidite systems: Random or systematic depositional processes? *AAPG Bulletin*, 94(3):345–368, 2010. doi: 10.1306/09010909035. (Cited pages xxviii and 22)
- R. Labourdette, J. Poncet, J. Seguin, F. Temple, J. Hegre, and A. Irving. Three-dimensional modelling of stacked turbidite channels in West Africa: impact on dynamic reservoir simulations. *Petroleum Geoscience*, 12(4):335–345, 2006. doi: 10.1144/1354-079306-705. (Cited pages 13, 34, 38, and 158)
- E. Lajeunesse, L. Malverti, P. Lancien, L. Armstrong, F. Métivier, S. Coleman, C. E. Smith, T. Davies, A. Cantelli, and G. Parker. Fluvial and submarine morphodynamics of laminar and near-laminar flows: a synthesis. *Sedimentology*, 57(1):1–26, 2010. doi: 10.1111/j.1365-3091.2009.01109.x. (Cited pages xxviii and 16)
- W. B. Langbein and L. B. Leopold. *River meanders – Theory of minimum variance*. US Government Printing Office, 1966. ISBN 978-1-288-97435-1. (Cited page 141)
- D. K. Larue and J. Hovadik. Why Is Reservoir Architecture an Insignificant Uncertainty in Many Appraisal and Development Studies of Clastic Channelized Reservoirs? *Journal of Petroleum Geology*, 31(4):337–366, 2008. doi: 10.1111/j.1747-5457.2008.00426.x. (Cited pages 13, 108, and 113)
- T. C. Lee, R. L. Kashyap, and C. N. Chu. Building Skeleton Models via 3-D Medial Surface Axis Thinning Algorithms. *CVGIP: Graphical Models and Image Processing*, 56(6):462–478, 1994. doi: 10.1006/cgip.1994.1042. (Cited page 47)

- D. Leitner, S. Klepsch, G. Bodner, and A. Schnepf. A dynamic root system growth model based on L-Systems. *Plant and Soil*, 332(1-2):177–192, 2010. doi: 10.1007/s11104-010-0284-7. (Cited page 84)
- J. Lin. Divergence measures based on the Shannon entropy. *Information Theory, IEEE Transactions on*, 37(1):145–151, 1991. doi: 10.1109/18.61115. (Cited page 53)
- A. Lindenmayer. Mathematical models for cellular interactions in development I. Filaments with one-sided inputs. *Journal of Theoretical Biology*, 18(3):280–299, 1968. doi: 10.1016/0022-5193(68)90079-9. (Cited pages xvi and 84)
- Y. Liu and A. Journel. Improving Sequential Simulation with a Structured Path Guided by Information Content. *Mathematical Geology*, 36(8):945–964, 2004. doi: 10.1023/B:MATG.0000048800.72104.de. (Cited page 31)
- S. Longay, A. Runions, F. Boudon, and P. Prusinkiewicz. Treesketch: interactive procedural modeling of trees on a tablet. In *Proceedings of the international symposium on sketch-based interfaces and modeling*, pages 107–120. Eurographics Association, 2012. doi: 10.2312/SBM/SBM12/107-120. (Cited page 104)
- S. Lopez. *Modélisation de réservoirs chenalisés méandri-formes : une approche génétique et stochastique*. PhD thesis, Ecole Nationale Supérieure des Mines de Paris, 2003. (Cited pages xvii, 33, 38, 146, 160, 197, 198, 201, 202, 205, and 208)
- D. R. Lowe. Sediment gravity flows; II, Depositional models with special reference to the deposits of high-density turbidity currents. *Journal of Sedimentary Research*, 52(1):279–297, 1982. doi: 10.1306/212F7F31-2B24-11D7-8648000102C1865D. (Cited page 7)
- S. M. Luthi and S. S. Flint. The application of outcrop-based research boreholes for reservoir modelling: potential, challenges and pitfalls. *Geological Society, London, Special Publications*, 387(1):233–246, 2014. doi: 10.1144/SP387.6. (Cited page xxxviii)
- R. V. Macauley and S. M. Hubbard. Slope channel sedimentary processes and stratigraphic stacking, Cretaceous Tres Pasos Formation slope system, Chilean Patagonia. *Marine and Petroleum Geology*, 41:146–162, 2013. doi: 10.1016/j.marpetgeo.2012.02.004. (Cited page 7)

## Bibliography

- K. L. Maier, A. Fildani, T. R. McHargue, C. K. Paull, S. A. Graham, and D. W. Caress. Punctuated Deep-Water Channel Migration: High-Resolution Subsurface Data from the Lucia Chica Channel System, Offshore California, U.S.A. *Journal of Sedimentary Research*, 82(1):1–8, 2012. doi: 10.2110/jsr.2012.10. (Cited pages [xxviii](#), [23](#), and [24](#))
- J.-L. Mallet. Space-Time Mathematical Framework for Sedimentary Geology. *Mathematical Geology*, 36(1):1–32, 2004. doi: 10.1023/B:MATG.0000016228.75495.7c. (Cited pages [xxx](#), [93](#), and [94](#))
- G. Mariethoz. *Geological stochastic imaging for aquifer characterization*. PhD thesis, Université de Neuchâtel, 2009. (Cited page [44](#))
- G. Mariethoz and J. Caers. *Multiple-point Geostatistics: Stochastic Modeling with Training Images*. John Wiley & Sons, 2014. (Cited page [xliii](#))
- G. Mariethoz, P. Renard, and J. Straubhaar. The Direct Sampling method to perform multiple-point geostatistical simulations. *Water Resources Research*, 46(11):W11536, 2010. doi: 10.1029/2008WR007621. (Cited pages [29](#), [39](#), [59](#), and [170](#))
- G. Mariethoz, A. Comunian, I. Irrazaval, and P. Renard. Analog-based meandering channel simulation. *Water Resources Research*, 50(2):836–854, 2014. doi: 10.1002/2013WR013730. (Cited pages [32](#), [200](#), and [205](#))
- J. H. Martin. A review of braided fluvial hydrocarbon reservoirs: the petroleum engineer’s perspective. *Geological Society, London, Special Publications*, 75(1):333–367, 1993. doi: 10.1144/GSL.SP.1993.075.01.20. (Cited pages [xxxvii](#) and [2](#))
- M. Mayall and C. O’Byrne. Reservoir Prediction and Development Challenges in Turbidite Slope Channels. In *Offshore Technology Conference*, Houston, Texas U.S.A., 2002. doi: 10.4043/14029-MS. (Cited pages [11](#), [14](#), and [158](#))
- M. Mayall, E. Jones, and M. Casey. Turbidite channel reservoirs – Key elements in facies prediction and effective development. *Marine and Petroleum Geology*, 23(8):821–841, 2006. doi: 10.1016/j.marpetgeo.2006.08.001. (Cited pages [xi](#), [xxxvii](#), [2](#), [6](#), [8](#), [11](#), [13](#), [14](#), and [34](#))
- P. J. McCabe, D. L. Gautier, M. D. Lewan, and C. Turner. The future of energy gases. USGS Numbered Series Circular 1115, Dept. of the Interior, U.S. Geological Survey, USGS Map Distribution ; U.S. G.P.O., 1993. (Cited page [xxxvii](#))

- T. McHargue, M. Pyrcz, M. Sullivan, J. Clark, A. Fildani, B. Romans, J. Covault, M. Levy, H. Posamentier, and N. Drinkwater. Architecture of turbidite channel systems on the continental slope: Patterns and predictions. *Marine and Petroleum Geology*, 28(3):728–743, 2011. doi: 10.1016/j.marpetgeo.2010.07.008. (Cited pages [xi](#), [xxviii](#), [6](#), [7](#), [12](#), [23](#), [33](#), [129](#), and [160](#))
- E. Meerschman, G. Pirot, G. Mariethoz, J. Straubhaar, M. V. Meirvenne, and P. Renard. A Practical Guide to Performing Multiple-Point Statistical Simulations with the Direct Sampling Algorithm. *Computers & Geosciences*, 52:307–324, 2012. doi: 10.1016/j.cageo.2012.09.019. (Cited pages [39](#) and [174](#))
- G. V. Middleton and M. A. Hampton. Sediment gravity flows: mechanics of flow and deposition. In G. Middleton and A. Bouma, editors, *Turbidites and Deep-water Sedimentation*, page 38. Pacific Section Society of Economic Paleontologists and Mineralogists, Los Angeles, 1973. (Cited page [3](#))
- J. M. Moore, A. D. Howard, W. E. Dietrich, and P. M. Schenk. Martian Layered Fluvial Deposits: Implications for Noachian Climate Scenarios. *Geophysical Research Letters*, 30(24):2292, 2003. doi: 10.1029/2003GL019002. (Cited page [2](#))
- T. Mulder and J. Alexander. The physical character of subaqueous sedimentary density flows and their deposits. *Sedimentology*, 48(2):269–299, 2001. doi: 10.1046/j.1365-3091.2001.00360.x. (Cited page [3](#))
- T. Mulder and S. Etienne. Lobes in deep-sea turbidite systems: State of the art. *Sedimentary Geology*, 229(3):75–80, 2010. doi: 10.1016/j.sedgeo.2010.06.011. (Cited page [10](#))
- A. E. Mulligan, R. L. Evans, and D. Lizarralde. The role of paleochannels in groundwater/seawater exchange. *Journal of Hydrology*, 335(3-4):313–329, 2007. doi: 10.1016/j.jhydrol.2006.11.025. (Cited page [2](#))
- E. Mutti and W. R. Normark. An Integrated Approach to the Study of Turbidite Systems. In P. Weimer and M. H. Link, editors, *Seismic Facies and Sedimentary Processes of Submarine Fans and Turbidite Systems*, Frontiers in Sedimentary Geology, pages 75–106. Springer New York, 1991. ISBN 978-1-4684-8278-2 978-1-4684-8276-8. doi: 10.1007/978-1-4684-8276-8\_4. (Cited page [6](#))
- R. Mvech and P. Prusinkiewicz. Visual models of plants interacting with their environment. In *Proceedings of the 23rd annual conference on Computer graphics and interactive techniques*, pages 397–410, 1996. doi: 10.1145/237170.237279. (Cited pages [84](#) and [92](#))

## Bibliography

- T. Nakajima, J. Peakall, W. D. McCaffrey, D. A. Paton, and P. J. P. Thompson. Outer-Bank Bars: A New Intra-Channel Architectural Element within Sinuous Submarine Slope Channels. *Journal of Sedimentary Research*, 79(12):872–886, 2009. doi: 10.2110/jsr.2009.094. (Cited pages 22, 158, 195, and 197)
- W. R. Normark, H. Posamentier, and E. Mutti. Turbidite systems: State of the art and future directions. *Reviews of Geophysics*, 31(2):91–116, 1993. doi: 10.1029/93RG02832. (Cited page 6)
- D. S. Oliver. Conditioning Channel Meanders to Well Observations. *Mathematical Geology*, 34(2):185–201, 2002. doi: 10.1023/A:1014464202497. (Cited pages 32 and 205)
- D. S. Oliver and Y. Chen. Recent progress on reservoir history matching: a review. *Computational Geosciences*, 15(1):185–221, 2010. doi: 10.1007/s10596-010-9194-2. (Cited page 34)
- M. P. O’Neill and A. D. Abrahams. Objective identification of meanders and bends. *Journal of Hydrology*, 83(3):337–353, 1986. doi: 10.1016/0022-1694(86)90160-5. (Cited page 198)
- F. Oriani and P. Renard. Binary upscaling on complex heterogeneities: The role of geometry and connectivity. *Advances in Water Resources*, 64:47–61, 2014. doi: 10.1016/j.advwatres.2013.12.003. (Cited page 44)
- R. Ostermeier. Compaction Effects on Porosity and Permeability: Deepwater Gulf of Mexico Turbidite. *Journal of Petroleum Technology*, 53(02):68–74, 2001. doi: 10.2118/66479-JPT. (Cited page 26)
- W. Palubicki, K. Horel, S. Longay, A. Runions, B. Lane, R. Měch, and P. Prusinkiewicz. Self-organizing Tree Models for Image Synthesis. In *ACM SIGGRAPH 2009 Papers*, SIGGRAPH ’09, pages 58:1–58:10, New York, NY, USA, 2009. ACM. ISBN 978-1-60558-726-4. doi: 10.1145/1576246.1531364. (Cited page 84)
- Paradigm. SKUA® Software Suite by Paradigm®. <http://www.pdgm.com/products/skua-gocad/>, 2015. (Cited page 57)
- G. Parker, Y. Shimizu, G. V. Wilkerson, E. C. Eke, J. D. Abad, J. W. Lauer, C. Paola, W. E. Dietrich, and V. R. Voller. A new framework for modeling the migration of meandering rivers. *Earth Surface Processes and Landforms*, 36(1):70–86, 2011. doi: 10.1002/esp.2113. (Cited page 198)

- M. Parquer, J. Ruiu, G. Caumon, P. Collon, and G. Rongier. Towards more genetics concepts and data integration in channel simulation. In *Proc. 35th Gocad Meeting*, Nancy, France, 2015. (Cited pages 154, 161, and 202)
- J. Peakall, B. McCaffrey, and B. Kneller. A Process Model for the Evolution, Morphology, and Architecture of Sinuous Submarine Channels. *Journal of Sedimentary Research*, 70(3):434–448, 2000. doi: 10.1306/2DC4091C-0E47-11D7-8643000102C1865D. (Cited pages 22, 24, and 158)
- L. Piegl and W. Tiller. *The NURBS book*. Springer, London, 1995. ISBN 978-3-642-59223-2. (Cited page 94)
- D. J. W. Piper and W. R. Normark. Sandy Fans-From Amazon to Hueneme and Beyond. *AAPG Bulletin*, 85(8):1407–1438, Jan. 2001. doi: 10.1306/8626CACD-173B-11D7-8645000102C1865D. (Cited page 4)
- D. J. W. Piper, P. Cochonat, and M. L. Morrison. The sequence of events around the epicentre of the 1929 Grand Banks earthquake: initiation of debris flows and turbidity current inferred from sidescan sonar. *Sedimentology*, 46(1): 79–97, 1999. doi: 10.1046/j.1365-3091.1999.00204.x. (Cited page 3)
- C. Pirmez and J. Imran. Reconstruction of turbidity currents in Amazon Channel. *Marine and Petroleum Geology*, 20(6-8):823–849, June 2003. doi: 10.1016/j.marpetgeo.2003.03.005. (Cited page 3)
- H. W. Posamentier. Depositional elements associated with a basin floor channel-levee system: case study from the Gulf of Mexico. *Marine and Petroleum Geology*, 20(6-8):677–690, 2003. doi: 10.1016/j.marpetgeo.2003.01.002. (Cited pages xxviii, 22, 24, 26, and 158)
- M. J. Pranter and N. K. Sommer. Static connectivity of fluvial sandstones in a lower coastal-plain setting: An example from the Upper Cretaceous lower Williams Fork Formation, Piceance Basin, Colorado. *AAPG Bulletin*, 95(6): 899–923, 2011. doi: 10.1306/12091010008. (Cited pages xxxvii and 2)
- A. Prélat, D. M. Hodgson, and S. S. Flint. Evolution, architecture and hierarchy of distributary deep-water deposits: a high-resolution outcrop investigation from the Permian Karoo Basin, South Africa. *Sedimentology*, 56(7):2132–2154, 2009. doi: 10.1111/j.1365-3091.2009.01073.x. (Cited page 10)
- A. Prélat, J. A. Covault, D. M. Hodgson, A. Fildani, and S. S. Flint. Intrinsic controls on the range of volumes, morphologies, and dimensions of submarine lobes. *Sedimentary Geology*, 232(1-2):66–76, 2010. doi: 10.1016/j.sedgeo.2010.09.010. (Cited pages xxviii and 11)

## Bibliography

- P. Prusinkiewicz. Graphical applications of L-systems. In *Proceedings of graphics interface*, volume 86, pages 247–253, 1986. (Cited page 88)
- P. Prusinkiewicz and A. Lindenmayer. *The Algorithmic Beauty of Plants*. Springer-Verlag, New York, NY, USA, 1996. ISBN 978-1-4613-8476-2. (Cited pages xxx, 84, 87, 92, and 93)
- P. Prusinkiewicz, M. James, and R. Měch. Synthetic topiary. In *Proceedings of the 21st annual conference on Computer graphics and interactive techniques*, pages 351–358. ACM, 1994. doi: 10.1145/192161.192254. (Cited page 91)
- P. Prusinkiewicz, L. Mündermann, R. Karwowski, and B. Lane. The use of positional information in the modeling of plants. In *Proceedings of the 28th annual conference on Computer graphics and interactive techniques*, pages 289–300, 2001. doi: 10.1145/383259.383291. (Cited page 207)
- M. Pyrcz, J. Boisvert, and C. Deutsch. ALLUVSIM: A program for event-based stochastic modeling of fluvial depositional systems. *Computers & Geosciences*, 35(8):1671–1685, 2009. doi: 10.1016/j.cageo.2008.09.012. (Cited pages xiii, xvii, 33, 38, 84, 94, 146, 160, 164, 197, 199, 205, and 208)
- M. J. Pyrcz and C. V. Deutsch. *Geostatistical reservoir modeling*. Oxford university press, 2014. (Cited page xliii)
- M. J. Pyrcz, T. McHargue, J. Clark, M. Sullivan, and S. Strebelle. Event-Based Geostatistical Modeling: Description and Applications. In P. Abrahamsen, R. Hauge, and O. Kolbjørnsen, editors, *Geostatistics Oslo 2012*, number 17 in Quantitative Geology and Geostatistics, pages 27–38. Springer Netherlands, Jan. 2012. ISBN 978-94-007-4152-2 978-94-007-4153-9. (Cited page 32)
- R Core Team. *R: A Language and Environment for Statistical Computing*. R Foundation for Statistical Computing, Vienna, Austria, 2012. ISBN 3-900051-07-0. (Cited page 57)
- C. R. Rao. Differential metrics in probability spaces. *Differential geometry in statistical inference*, 10:217–240, 1987. doi: doi:10.1214/lnms/1215467062. (Cited page 53)
- H. G. Reading and M. Richards. Turbidite systems in deep-water basin margins classified by grain size and feeder system. *AAPG bulletin*, 78(5):792–822, 1994. (Cited page 4)

- P. Renard, J. Straubhaar, J. Caers, and G. Mariethoz. Conditioning Facies Simulations with Connectivity Data. *Mathematical Geosciences*, 43(8):879–903, 2011. doi: 10.1007/s11004-011-9363-4. (Cited pages 34, 40, and 43)
- M. Richards, M. Bowman, and H. Reading. Submarine-fan systems i: characterization and stratigraphic prediction. *Marine and Petroleum Geology*, 15(7): 689–717, 1998. doi: 10.1016/S0264-8172(98)00036-1. (Cited page 4)
- G. Rongier, P. Collon, P. Renard, and J. Ruiiu. Channel simulation using L-system, potential fields and NURBS. In *Proc. 35th Gocad Meeting*, Nancy, France, 2015. (Cited pages xv and xxvii)
- I. L. Rozovskii. *Flow of water in bends of open channels*. Academy of Sciences of the Ukrainian SSR (translated from Russian by the Israel Program for Scientific Translations, Jerusalem, 1961), Kiev, 1957. (Cited page 16)
- J. Ruiiu, G. Caumon, and S. Viseur. Semiautomatic interpretation of 3D sedimentological structures on geologic images: An object-based approach. *Interpretation*, 3(3):SX63–SX74, 2015a. doi: 10.1190/INT-2015-0004.1. (Cited pages 32, 108, and 162)
- J. Ruiiu, G. Caumon, and S. Viseur. Modeling Channel Forms and Related Sedimentary Objects Using a Boundary Representation Based on Non-uniform Rational B-Splines. *Mathematical Geosciences*, pages 1–26, 2015b. doi: 10.1007/s11004-015-9629-3. (Cited pages 30, 86, 94, 96, 130, 155, 161, 162, and 208)
- T. Salles. *Modélisation numérique du remplissage sédimentaire des canyons et chenaux sous-marins par approche génétique*. PhD thesis, Université Bordeaux 1, Bordeaux, 2006. (Cited pages xxviii, 3, and 17)
- C. Scheidt and J. Caers. Representing Spatial Uncertainty Using Distances and Kernels. *Mathematical Geosciences*, 41(4):397–419, 2009. doi: 10.1007/s11004-008-9186-0. (Cited page 39)
- Schlumberger. Petrel E&p Software Platform. <http://www.software.slb.com/products/platform/Pages/petrel.aspx>, 2015. (Cited page 58)
- J. Schwenk, S. Lanzoni, and E. Foufoula-Georgiou. The life of a meander bend: connecting shape and dynamics via analysis of a numerical model. *Journal of Geophysical Research: Earth Surface*, page 2014JF003252, 2015. doi: 10.1002/2014JF003252. (Cited pages 176, 177, and 201)



## Bibliography

- J. Serra. *Image Analysis and Mathematical Morphology*. Academic Press, Inc., Orlando, FL, USA, 1983. ISBN 978-0-12-637240-3. (Cited page 46)
- G. Shanmugam. Ten turbidite myths. *Earth-Science Reviews*, 58(3-4):311–341, 2002. doi: 10.1016/S0012-8252(02)00065-X. (Cited page 3)
- G. Shanmugam and R. J. Muiola. Submarine fans: Characteristics, models, classification, and reservoir potential. *Earth-Science Reviews*, 24(6):383–428, 1988. doi: 10.1016/0012-8252(88)90064-5. (Cited pages 10 and 11)
- G. Shanmugam, T. D. Spalding, and D. H. Rofheart. Process sedimentology and reservoir quality of deep-marine bottom-current reworked sands (sandy contourites); an example from the Gulf of Mexico. *AAPG Bulletin*, 77(7): 1241–1259, 1993. (Cited pages xxvii and 7)
- R. N. Shepard. The analysis of proximities: Multidimensional scaling with an unknown distance function. I. *Psychometrika*, 27(2):125–140, 1962a. doi: 10.1007/BF02289630. (Cited page 39)
- R. N. Shepard. The analysis of proximities: Multidimensional scaling with an unknown distance function. II. *Psychometrika*, 27(3):219–246, 1962b. doi: 10.1007/BF02289621. (Cited page 39)
- L. E. Shmaryan and C. V. Deutsch. Object-based modeling of fluvial/deepwater reservoirs with fast data conditioning: methodology and case studies. In *SPE annual technical conference*, pages 877–886, 1999. doi: 10.2118/56821-MS. (Cited page 32)
- A. Shtuka, P. Samson, and J. L. Mallet. Petrophysical simulation within an object-based reservoir model. In *European 3-D reservoir modelling conference*, pages 47–56, 1996. (Cited pages 32 and 40)
- J. W. Snedden. Channel-body basal scours: Observations from 3D seismic and importance for subsurface reservoir connectivity. *Marine and Petroleum Geology*, 39(1):150–163, 2013. doi: 10.1016/j.marpetgeo.2012.08.013. (Cited page 2)
- A. R. G. Sprague, M. D. Sullivan, K. M. Campion, G. N. Jensen, F. J. Goulding, T. R. Garfield, D. K. Sickafoose, C. Rossen, D. C. Jennette, R. T. Beaubouef, V. Abreu, J. A. Ardill, M. L. Porter, and F. B. Zelt. The Physical Stratigraphy of Deep-Water Strata: A Hierarchical Approach to the Analysis of Genetically Related Stratigraphic Elements for Improved Reservoir Prediction. In *AAPG Annual Meeting*, Houston, Texas, USA, 2002. (Cited pages 6 and 7)

- D. a. V. Stow and A. J. Bowen. A physical model for the transport and sorting of fine-grained sediment by turbidity currents. *Sedimentology*, 27(1):31–46, 1980. doi: 10.1111/j.1365-3091.1980.tb01156.x. (Cited page 3)
- J. Straubhaar. MPDS technical reference guide. Technical report, Centre d’hydrogéologie et géothermie, University of Neuchâtel, Neuchâtel, 2011. (Cited page 59)
- J. Straubhaar, P. Renard, G. Mariethoz, R. Froidevaux, and O. Besson. An Improved Parallel Multiple-point Algorithm Using a List Approach. *Mathematical Geosciences*, 43(3):305–328, Mar. 2011. doi: 10.1007/s11004-011-9328-7. (Cited pages xxviii, 28, 29, and 59)
- S. Strebelle. Conditional Simulation of Complex Geological Structures Using Multiple-Point Statistics. *Mathematical Geology*, 34(1):1–21, 2002. doi: 10.1023/A:1014009426274. (Cited pages xiii, 29, 39, and 84)
- S. Strebelle and N. Remy. Post-processing of Multiple-point Geostatistical Models to Improve Reproduction of Training Patterns. In O. Leuangthong and C. V. Deutsch, editors, *Geostatistics Banff 2004*, number 14 in Quantitative Geology and Geostatistics, pages 979–988. Springer Netherlands, 2005. ISBN 978-1-4020-3515-9 978-1-4020-3610-1. doi: 10.1007/978-1-4020-3610-1\_102. (Cited page 31)
- S. Strebelle, K. Payrazyan, and J. Caers. Modeling of a Deepwater Turbidite Reservoir Conditional to Seismic Data Using Principal Component Analysis and Multiple-Point Geostatistics. *SPE Journal*, 8(3), 2003. doi: 10.2118/85962-PA. (Cited pages 34 and 108)
- L. Streit, P. Federl, and M. Sousa. Modelling Plant Variation Through Growth. *Computer Graphics Forum*, 24(3):497–506, Sept. 2005. doi: 10.1111/j.1467-8659.2005.00875.x. (Cited page 84)
- L. Stright, J. Stewart, K. Champion, and S. Graham. Geologic and seismic modeling of a coarse-grained deep-water channel reservoir analog (Black’s Beach, La Jolla, California). *AAPG Bulletin*, 98(4):695–728, 2014. doi: 10.1306/09121312211. (Cited pages xxvii, 7, and 8)
- E. J. Sumner, J. Peakall, R. M. Dorrell, D. R. Parsons, S. E. Darby, R. B. Wynn, S. D. McPhail, J. Perrett, A. Webb, and D. White. Driven around the bend: Spatial evolution and controls on the orientation of helical bend

## Bibliography

- flow in a natural submarine gravity current. *Journal of Geophysical Research: Oceans*, 119(2):898–913, 2014. doi: 10.1002/2013JC009008. (Cited pages 20, 33, and 160)
- P. Tahmasebi, A. Hezarkhani, and M. Sahimi. Multiple-point geostatistical modeling based on the cross-correlation functions. *Computational Geosciences*, 16(3):779–797, 2012. doi: 10.1007/s10596-012-9287-1. (Cited pages 31 and 39)
- P. Tahmasebi, M. Sahimi, and J. Caers. MS-CCSIM: Accelerating pattern-based geostatistical simulation of categorical variables using a multi-scale search in Fourier space. *Computers & Geosciences*, 67:75–88, June 2014. doi: 10.1016/j.cageo.2014.03.009. (Cited page 204)
- P. J. Talling. On the triggers, resulting flow types and frequencies of subaqueous sediment density flows in different settings. *Marine Geology*, 352:155–182, 2014. doi: 10.1016/j.margeo.2014.02.006. (Cited page 3)
- P. J. Talling, R. B. Wynn, D. G. Masson, M. Frenz, B. T. Cronin, R. Schiebel, A. M. Akhmetzhanov, S. Dallmeier-Tiessen, S. Benetti, P. P. E. Weaver, and others. Onset of submarine debris flow deposition far from original giant landslide. *Nature*, 450(7169):541–544, 2007. doi: 10.1038/nature06313. (Cited page 3)
- P. J. Talling, J. Allin, D. A. Armitage, R. W. Arnott, M. J. Cartigny, M. A. Clare, F. Felletti, J. A. Covault, S. Girardclos, E. Hansen, and others. Key future directions for research on turbidity currents and their deposits. *Journal of Sedimentary Research*, 85(2):153–169, 2015. doi: 10.2110/jsr.2015.03. (Cited page 2)
- X. Tan, P. Tahmasebi, and J. Caers. Comparing Training-Image Based Algorithms Using an Analysis of Distance. *Mathematical Geosciences*, 46(2):149–169, 2014. doi: 10.1007/s11004-013-9482-1. (Cited pages xiii, 39, and 69)
- J. Taylor-Hell. Incorporating Biomechanics into Architectural Tree Models. In *18th Brazilian Symposium on Computer Graphics and Image Processing, 2005. SIBGRAPI 2005*, pages 299–306, Oct. 2005. doi: 10.1109/SIBGRAPI.2005.32. (Cited pages 84 and 104)
- V. Teles, G. de Marsily, and E. Perrier. Sur une nouvelle approche de modélisation de la mise en place des sédiments dans une plaine alluviale pour en représenter l’hétérogénéité. *Comptes Rendus de l’Académie des Sciences*

- *Series IIA - Earth and Planetary Science*, 327(9):597–606, 1998. doi: 10.1016/S1251-8050(99)80113-X. (Cited pages [xvii](#), [161](#), and [195](#))
- W. S. Torgerson. Multidimensional scaling: I. Theory and method. *Psychometrika*, 17(4):401–419, 1952. doi: 10.1007/BF02288916. (Cited pages [39](#), [54](#), and [55](#))
- W. S. Torgerson. *Theory and methods of scaling*. John Wiley & Sons, New York, 1958. ISBN 978-0-471-87945-9. (Cited pages [54](#) and [55](#))
- T. T. Tran. Improving variogram reproduction on dense simulation grids. *Computers & Geosciences*, 20(7):1161–1168, 1994. doi: 10.1016/0098-3004(94)90069-8. (Cited page [69](#))
- N. Tyler. New oil from old fields. *Geotimes*, 33(7):8–10, 1988. (Cited page [2](#))
- S. Viseur. *Simulation stochastique basée-objet de chenaux*. PhD thesis, Institut National Polytechnique de Lorraine, Vandoeuvre-lès-Nancy, France, 2001. (Cited pages [xiii](#), [xvii](#), [30](#), [32](#), [38](#), [84](#), [94](#), [150](#), [151](#), [152](#), [160](#), and [195](#))
- H. Wadell. Volume, shape, and roundness of quartz particles. *The Journal of Geology*, pages 250–280, 1935. (Cited page [46](#))
- A. W. Western, G. Blöschl, and R. B. Grayson. Toward capturing hydrologically significant connectivity in spatial patterns. *Water Resources Research*, 37(1): 83–97, Jan. 2001. doi: 10.1029/2000WR900241. (Cited page [44](#))
- H. E. Wheeler. Time-stratigraphy. *AAPG Bulletin*, 42(5):1047–1063, Jan. 1958. (Cited page [93](#))
- H. Wickham. *ggplot2: elegant graphics for data analysis*. Springer, 2009. ISBN 978-0-387-98141-3. (Cited page [57](#))
- L. Wietzerbin. *Modélisation et paramétrisation d’objets naturels de formes complexes en trois dimensions. Application à la simulation stochastique de la distribution d’hétérogénéités au sein des réservoirs pétroliers*. PhD thesis, Institut National Polytechnique de Lorraine, Vandoeuvre-lès-Nancy, France, 1994. (Cited pages [30](#) and [94](#))
- D. R. Wilson and T. R. Martinez. Improved heterogeneous distance functions. *Journal of Artificial Intelligence Research*, 6:1–34, 1997. doi: 10.1613/jair.346. (Cited page [52](#))

## Bibliography

- R. B. Wynn, B. T. Cronin, and J. Peakall. Sinuous deep-water channels: Genesis, geometry and architecture. *Marine and Petroleum Geology*, 24(6-9):341–387, 2007. doi: 10.1016/j.marpetgeo.2007.06.001. (Cited pages 4, 6, 7, and 209)
- L. Yang, W. Hou, C. Cui, and J. Cui. GOSIM: A multi-scale iterative multiple-point statistics algorithm with global optimization. *Computers & Geosciences*, 89:57–70, 2016. doi: 10.1016/j.cageo.2015.12.020. (Cited page 204)
- Y. Yin, S. Wu, C. Zhang, S. Li, and T. Yin. A reservoir skeleton-based multiple point geostatistics method. *Science in China Series D: Earth Sciences*, 52(1): 171–178, 2009. doi: 10.1007/s11430-009-5004-x. (Cited page 39)
- J. H. Youngson and D. Craw. Variation in placer style, gold morphology, and gold particle behavior down gravel bed-load rivers; an example from the Shotover/Arrow-Kawarau-Clutha River system, Otago, New Zealand. *Economic Geology*, 94(5):615–633, 1999. doi: 10.2113/gsecongeo.94.5.615. (Cited pages xxxvii and 2)



## **Connectivité de corps sédimentaires chenalisés : stratégies d'analyse et de simulation en modélisation de subsurface**

**Résumé** Les chenaux sont des structures sédimentaires clés dans le transport et le dépôt de sédiments depuis les continents jusqu'aux planchers océaniques. Leurs dépôts perméables permettent la circulation et le stockage de fluides. Comme illustré avec les systèmes turbiditiques, le remplissage de ces chenaux est très hétérogène. Son impact sur la connectivité des dépôts perméables est amplifié par les variations d'organisation spatiale des chenaux. Mais du fait de l'aspect lacunaire des données, l'architecture de ces structures souterraines n'est que partiellement connue. Dans ce cas, les simulations stochastiques permettent d'estimer les ressources et les incertitudes associées. De nombreuses méthodes ont été développées pour reproduire ces environnements. Elles soulèvent deux questions capitales : comment analyser et comparer la connectivité de simulations stochastiques ? Comment améliorer la représentation de la connectivité dans les simulations stochastiques de chenaux et réduire les incertitudes ?

La première question nous a conduits à développer une méthode pour comparer objectivement des réalisations en se concentrant sur la connectivité. L'approche proposée s'appuie sur les composantes connexes des simulations, sur lesquelles sont calculés plusieurs indicateurs. Une représentation par positionnement multidimensionnel (MDS) facilite la comparaison des réalisations. Les observations faites grâce au MDS sont ensuite validées par une carte de chaleur et les indicateurs. L'application à un cas synthétique de complexes chenaux/levées montre les différences de connectivité entre des méthodes et des valeurs de paramètres différentes. En particulier, certaines méthodes sont loin de reproduire des objets avec une forme de chenaux.

La seconde question amène deux principaux problèmes. Premièrement, il apparaît difficile de conditionner des objets très allongés, comme des chenaux, à des données de puits ou dérivées de données sismiques. Nous nous appuyons sur une grammaire formelle, le système de Lindenmayer, pour simuler stochastiquement des objets chenaux conditionnés. Des règles de croissance prédéfinies contrôlent la morphologie du chenal, de rectiligne à sinueuse. Cette morphologie conditionne les données au fur et à mesure de son développement grâce à des contraintes attractives ou répulsives. Ces contraintes assurent le conditionnement tout en préservant au mieux la morphologie. Deuxièmement, l'organisation spatiale des chenaux apparaît peu contrôlable. Nous proposons de traiter ce problème en intégrant les processus qui déterminent l'organisation des chenaux. Un premier chenal est simulé avec un système de Lindenmayer. Puis ce chenal migre à l'aide d'une simulation gaussienne séquentielle ou d'une simulation multipoints. Cette approche reproduit les relations complexes entre des chenaux successifs sans s'appuyer sur des modèles physiques partiellement validés et au paramétrage souvent contraignant.

L'application de ces travaux à des cas synthétiques démontre le potentiel de ces approches. Elles ouvrent des perspectives intéressantes pour mieux prendre en compte la connectivité dans les simulations stochastiques de chenaux.

**Mots-clés** chenal turbiditique connectivité composante connexe simulation stochastique système de Lindenmayer migration de chenaux

---

## **Connectivity of channelized sedimentary bodies: analysis and simulation strategies in subsurface modeling**

**Abstract** Channels are the main sedimentary structures for sediment transportation and deposition from the continents to the ocean floor. The significant permeability of their deposits enables fluid circulation and storage. As illustrated with turbiditic systems, those channel fill is highly heterogeneous. Combined with the spatial organization of the channels, this impacts significantly the connectivity between the permeable deposits. The scarcity of the field data involves an incomplete knowledge of these subsurface reservoir architectures. In such environments, stochastic simulations are used to estimate the resources and give an insight on the associated uncertainties. Several methods have been developed to reproduce these complex environments. They raise two main concerns: how to analyze and compare the connectivity of a set of stochastic simulations? How to improve the representation of the connectivity within stochastic simulations of channels and reduce the uncertainties?

The first concern leads to the development of a method to objectively compare realizations in terms of connectivity. The proposed approach relies on the connected components of the simulations, on which several indicators are computed. A multidimensional scaling (MDS) representation facilitates the realization comparison. The observations on the MDS are then validated by the analysis of the heatmap and the indicators. The application to a synthetic case study highlights the difference of connectivity between several methods and parameter values to model channel/levee complexes. In particular, some methods are far from representing channel-shaped bodies.

Two main issues derive from the second concern. The first issue is the difficulty to simulate a highly elongated object, here a channel, conditioned to well or seismic-derived data. We rely on a formal grammar, the Lindenmayer system, to stochastically simulate conditional channel objects. Predefined growth rules control the channel morphology to simulate straight to sinuous channels. That morphology conditions the data during its development thanks to attractive and repulsive constraints. Such constraints ensure the conditioning while preserving at best the channel morphology. The second issue arises from the limited control on the channel organization. This aspect is addressed by taking into account the evolution processes underlying channel organization. An initial channel is simulated with a Lindenmayer system. Then that channel migrates using sequential Gaussian simulation or multiple-point simulation. This process reproduces the complex relationships between successive channels without relying on partially validated physical models with an often constraining parameterization.

The applications of those various works to synthetic cases highlight the potentiality of the approaches. They open up interesting prospects to better take into account the connectivity when stochastically simulating channels.

**Keywords** turbiditic channel connectivity connected component stochastic simulation Lindenmayer system channel migration